Journal of Research of the National Bureau of Standards Vol. 47, No. 3, September 1951 Research Paper 2236

First Dissociation Constant of Phosphoric Acid From 0° to 60° C; Limitations of the Electromotive Force Method for Moderately Strong Acids

Roger G. Bates

An accurate determination by the electromotive-force method of the dissociation constant of an acid as strong as the first acidic group of phosphoric acid requires that the hydrogen-ion concentration be established with greater accuracy than is usually attainable. The uncertain quantity is the activity coefficient of hydrochloric acid in the particular mixture under study. It is shown that the calculation of this coefficient by the Debye-Hückel equation, which affords an adequate estimate of the small hydrogen-ion correction in buffer solutions composed of weak acids, fails to yield the desired accuracy for mixtures in which the acid is dissociated to an appreciable extent. In order to determine the common logarithm of the first dissociation constant of phosphoric acid with an accuracy believed to be ±0.005 unit, the hydrogen-ion concentration of some of the buffer mixtures studied was kept at low levels by use of a large excess of potassium dihydrogen phosphate. Other solutions contained formic acid instead of hydrochloric acid, thereby lowering the hydrogen-ion concentration still further. In addition, particular attention was given to a choice of reasonable values for the activity coefficient used to estimate the hydrogen-ion correction.

By these means the first dissociation constant, K_1, of phosphoric acid was calculated from emf measurements of 71 phosphate buffer solutions, together with supplementary data from the literature for 18 additional solutions. The result from 0° to 60° C is given by

$$-\log K_1 = \frac{799.31}{T} - 4.5535 + 0.013486\,T,$$

where T is the temperature in °K. The changes of heat content, entropy, and heat capacity for the dissociation of 1 mole of aqueous phosphoric acid in the standard state were found to be −7,650 j, −66.8 j deg^{-1}, and −154 j deg^{-1}, respectively, at 25° C.

1. Introduction

Experience has proved that the electromotive-force method is well suited to the accurate determination of the dissociation constants of many weak acids and bases in aqueous solution. However, it is not generally recognized that the accuracy obtainable by this method diminishes with increasing strength of the acid or base. When approximately 10 percent or more of a weak acid is dissociated in solution, the uncertainty in establishing the true concentrations of the ionic and molecular species becomes so large that an exact determination of the dissociation constant is no longer possible.

Some years ago the author undertook to measure the electromotive force of a series of cells of the type

$$\mathrm{Pt;\ H_2\ (g,\ 1\ atm),\ KH_2PO_4\ (\mathit{xm}),\ HCl\ (\mathit{m})\ AgCl;\ Ag} \qquad \text{(Cell I)}$$

where m is molality, in an attempt to extend the investigation of Nims [1][1] to other temperatures and buffer ratios. It was found to be impossible to obtain an accurate value for the first dissociation constant of phosphoric acid by analysis of the data for mixtures in which $1 < x < 3$. At the time it appeared unlikely that the dissociation constant of an acid as strong as the first acidic group of phosphoric acid could be fixed with an accuracy of 0.01 in the common logarithm by this emf method, and the study was accordingly abandoned. The cause of the difficulty was readily apparent; the activity coefficient of hydrochloric acid in the buffer solutions must be known accurately in order to obtain the hydrogen-ion concentration and, consequently, the molalities of phosphoric acid and primary phosphate ion from which the buffer ratio is computed. This activity coefficient cannot readily be determined exactly, and use is usually made of estimated values, calculated perhaps by some form of the Debye-Hückel equation. This device is completely adequate for acids so weak that the total contribution of the hydrogen ion is small but is unsatisfactory, in general, when the pH of the buffer solution lies below 2.5 to 3.0.

It was realized later that two possibilities of reducing the hydrogen-ion concentration might be feasible, and the investigation was resumed. The first and simpler approach is to increase the value of x as greatly as is consistent with adequate buffer capacity and to estimate the activity coefficient from independent data. The second is to substitute a weak acid of known strength for the hydrochloric acid which, together with potassium dihydrogen phosphate, forms the buffer solutions, at the same

[1] Figures in brackets indicate the literature references at the end of this paper.

957570—51

time adding neutral chloride to furnish the desired concentration of that ion. This latter procedure complicates the analysis of the data, for the hydrogen-ion concentration is then fixed by two dissociative equilibria instead of one. However, it is possible to evaluate the constant for one of these equilibria when that for the other is known [2, 3, 4].

The results of both approaches are presented. Data for 46 mixtures of potassium dihydrogen phosphate and hydrochloric acid, in which x varied from 1.2 to 6, are reported. Twenty-five mixtures of potassium dihydrogen phosphate and formic acid (ratios 5:1 and 8:1) with added potassium chloride were also studied. The combined data, as well as those for 18 solutions studied by Nims [1], were used to evaluate K_1 for phosphoric acid from 0° to 60° C with an estimated accuracy of ± 0.005 unit and to demonstrate the manner in which the accuracy of the electromotive-force method depends upon the strength of the acid studied.

2. Experimental Procedures and Results

Two different preparations of potassium dihydrogen phosphate were used. The first was prepared from reagent-grade salt by two recrystallizations from water. The salt was dried at 110° to 130°. A determination of the loss in weight suffered by weighed samples on ignition to metaphosphate indicated that the dried salt retained less than 0.02 percent of water. This portion of salt was used to prepare the 32 solutions grouped in series 1 through 4 (see table 1). The second preparation, from which the solutions of series 5 through 7 were made, was NBS Standard Sample 186–Ib.

The potassium chloride was a fused sample free of bromide [5]. Reagent-grade 90-percent formic acid was distilled twice in an all-glass still. Only the middle fraction was retained for redistillation or for use in the preparation of the solutions. Hydrochloric acid was diluted to a concentration of 6 molar and distilled in a similar fashion. An approximately 0.1-molar solution of the distilled acid was standardized gravimetrically by weighing silver chloride. The specific conductance of the water used in preparing the buffer solutions did not exceed 1.0×10^{-6} ohm^{-1} cm^{-1}. In view of the low pH of all of the buffer solutions, no special precautions were taken to exclude carbon dioxide, although dissolved air was removed by passage of nitrogen through the solutions before the cells were filled. In other respects, the experimental procedure was essentially the same as that followed in the determination of the second dissociation constant of phosphoric acid [6].

The solutions prepared from potassium dihydrogen phosphate and hydrochloric acid were grouped into five series according to the ratio of the molalities of the two components, that is, $m_{KH_2PO_4}$:m_{HCl}. This ratio was 1.2414:1 for series 1; 1.2683:1 for series 2; 1.5581:1 for series 3; 2.184:1 for series 4; and 6:1 for series 5. The cells containing the aqueous mixtures of potassium dihydrogen phosphate and formic acid can be represented as follows:

$$\text{Pt; } H_2 \text{ (g, 1 atm), } KH_2PO_4 \text{ } (xm), \text{ HCOOH } (m), \text{ KCl } (m_{Cl}=0.005), \text{ AgCl; Ag.} \qquad \text{(Cell II)}$$

The molality of potassium chloride was 0.005 in each solution, but the ratio of the molality of potassium dihydrogen phosphate to that of formic acid was 5:1 in series 6 and 8:1 in series 7.

The measured electromotive force of each cell was corrected to a hydrogen partial pressure of 1 atm in the usual way. The pwH value of each of the 71 buffer solutions at each temperature of measurement was computed by the defining equation [2]

$$\text{pwH} \equiv -\log (f_H f_{Cl} m_H) = \frac{(E-E^\circ)\boldsymbol{F}}{2.3026\ RT} + \log m_{Cl}, \quad (1)$$

in which f represents a molal activity coefficient; E and E° are the electromotive force and standard potential, respectively, of the cell at the appropriate absolute temperature, T; and R and $\boldsymbol{F}$ are the gas constant and the faraday. Values of E° and $2.3026RT/\boldsymbol{F}$ in absolute volts are summarized in an earlier publication [7]. The pwH values are listed in table 1.

3. Calculation of the Dissociation Constant: Series 1 to 5.

3.1. The Conventional Electromotive-Force Method

Inasmuch as the hydrogen-ion concentration in the buffer solutions of series 1 to 5 can be expressed in terms of the first dissociation equilibrium of phosphoric acid, pwH can be related directly through the mass law with K_1, the first dissociation constant, and the molalities and activity coefficients of phosphoric acid and primary phosphate ion. Making the substitution in eq 1 and rearranging gives the formal expression for log K_1:

$$-\log K_1 = \text{pwH} + \log \frac{m_{H_3PO_4}}{m_{H_2PO_4^-}} + \log \frac{f_{H_3PO_4} f_{Cl}}{f_{H_2PO_4^-}}, \quad (2)$$

This substitution is the basis of the method of determining the dissociation constant, as outlined by Roberts [8] and by Harned and Ehlers [9]. The solutions of series 1 to 5 (cell I) were composed of hydrochloric acid, m moles /1,000 g of water, and potassium dihydrogen phosphate, xm moles/1,000 g of water. Because of the appreciable dissociation of the phosphoric acid formed, the reaction between these two components is incomplete, and at equilibrium

$$m_{H_3PO_4} = m - m_H, \quad (3)$$

and

$$m_{H_2PO_4^-} = m(x-1) + m_H. \quad (4)$$

The hydrogen-ion concentration needed to compute the concentrations of the two phosphate species

[2] For convenience, the charges carried by hydrogen (H^+) and chloride (Cl^-) ions will not be indicated. Likewise, m_H will represent the total concentration of hydrogen ion, whether hydrated or not.

can be obtained, in principle, either from the mass law by successive arithmetical approximations with a provisional dissociation constant or from pwH. In both cases activity coefficients must be estimated, and simplicity favors the latter:

$$-\log m_{\mathrm{H}} = \mathrm{pwH} + \log f_{\mathrm{H}} f_{\mathrm{Cl}}. \qquad (5)$$

Inasmuch as it is not possible to obtain the exact value of $f_{\mathrm{H}} f_{\mathrm{Cl}}$, it is convenient to define an "apparent" m_{H}, namely m'_{H}, that approaches the true m_{H} at low ionic strengths:

$$-\log m'_{\mathrm{H}} = \mathrm{pwH} - \frac{2A\sqrt{\mu}}{1+Ba^*\sqrt{\mu}}. \qquad (5a)$$

The Debye-Hückel equation has been substituted for $\log f_{\mathrm{H}} f_{\mathrm{Cl}}$ on the right-hand side of eq 5a; A and B are constants at a particular temperature [10],

TABLE 1. pwH *from 0° to 50° for aqueous mixtures of potassium dihydrogen phosphate and hydrochloric acid and for aqueous mixtures of potassium dihydrogen phosphate, formic acid, and potassium chloride*

$m_{KH_2PO_4}$	pwH at (°C)—												
	0°	5°	10°	15°	20°	25°	30°	35°	40°	45°	50°	55°	60°
Series 1. KH_2PO_4:HCl=1.2414:1													
0.13818	1.7960	1.8072	1.8180	1.8294	1.8418	1.8529	1.8729	1.8891	1.9050	1.9233	1.9415	1.9583	1.9772
.12289	1.8236	1.8337	1.8439	1.8556	1.8678	1.8784	1.8955	1.9119	1.9278	1.9462	1.9637	1.9825	2.0027
.08765	1.8899	1.8993	1.9091	1.9195	1.9309	1.9436	1.9557	1.9701	1.9835	1.9999	2.0166	2.0363	2.0544
.04705	2.0219	2.0307	2.0389	2.0484	2.0568	2.0683	2.0813	2.0945	2.1065	2.1219	2.1367	2.1521	2.1680
.02870	2.1331	2.1414	2.1491	2.1572	2.1665	2.1763	2.1880	2.1997	2.2123	2.2264	2.2402	2.2539	2.2682
.02427	2.1733	2.1815	2.1886	2.1967	2.2050	2.2143	2.2252	2.2367	2.2482	2.2619	2.2751	2.2884	2.3024
.010572	2.3877	2.3939	2.3996	2.4053	2.4121	2.4192	.....	.....	.....	.....	.....	.....	.....
Series 2. KH_2PO_4:HCl=1.2683:1													
0.14117	1.8099	1.8197	1.8303	1.8428	1.8552	1.8693	.....	.....	.....	.....	.....	.....	.....
.11333	1.8595	1.8690	1.8796	1.8915	1.9029	1.9155	.....	.....	.....	.....	.....	.....	.....
.08642	1.9113	1.9206	1.9296	1.9440	1.9502	1.9638	.....	.....	.....	.....	.....	.....	.....
.06759	1.9620	1.9709	1.9801	1.9907	2.0010	2.0123	2.0267	2.0425	2.0577	2.0743	2.0908	2.1079	2.1250
.05386	2.0102	2.0184	2.0270	2.0374	2.0470	2.0587	2.0714	2.0863	2.1001	2.1160	2.1325	2.1491	2.1661
.03196	2.1221	2.1295	2.1372	2.1461	2.1551	2.1662	2.1774	2.1902	2.2021	2.2179	2.2317	2.2468	2.2628
.015488	2.2978	2.3038	2.3097	2.3171	2.3236	2.3322	2.3417	2.3525	2.3632	2.3755	2.3880	2.4004	2.4128
.011046	2.3688	2.3926	2.3976	2.4037	2.4106	2.4189	2.4269	2.4356	2.4449	2.4562	2.4671	2.4779	2.4883
Series 3. KH_2PO_4:HCl=1.5581:1													
0.17343	.....	.....	.....	.....	.....	2.0139	2.0334	2.0532	2.0727	2.0945	2.1165	2.1382	2.1603
.13787	1.9825	1.9958	2.0066	2.0206	2.0351	2.0497	2.0696	2.0899	2.1084	2.1301	2.1500	2.1710	2.1934
.11447	2.0139	2.0256	2.0363	2.0498	2.0634	2.0771	2.0966	2.1148	2.1332	2.1545	2.1727	2.1938	2.2157
.09439	2.0437	2.0555	2.0667	2.0798	2.0916	2.1058	2.1259	2.1450	2.1631	2.1826	2.2009	2.2205	2.2417
.05590	2.1352	2.1463	2.1548	2.1664	2.1775	2.1892	2.2047	2.2218	2.2372	2.2551	2.2712	2.2895	2.3085
.04646	2.1685	2.1771	2.1871	2.1977	2.2089	2.2209	2.2382	2.2571	2.2734	2.2921	2.3023	2.3204	2.3394
.04230	2.1865	2.1974	2.2048	2.2161	2.2274	2.2385	2.2562	2.2733	2.2886	2.3059	2.3189	2.3360	2.3559
.019571	2.3437	2.3506	2.3602	2.3692	2.3790	2.3885	2.4013	2.4156	2.4276	2.4416	2.4536	2.4681	2.4834
Series 4. KH_2PO_4:HCl=2.184:1													
0.2437	2.1600	2.1758	2.1902	2.2079	2.2256	2.2451	2.2641	2.2855	2.3075	2.3331	2.3605	2.3865	2.4131
.18880	2.1875	2.2033	2.2164	2.2340	2.2516	2.2703	2.2896	2.3078	2.3263	2.3539	2.3804	2.4053	2.4314
.17753	2.1970	2.2107	2.2246	2.2412	2.2583	2.2764	2.2963	2.3171	2.3359	2.3636	2.3860	2.4127	2.4388
.11627	2.2450	2.2580	2.2700	2.2860	2.3031	2.3189	2.3384	2.3576	2.3741	2.3988	2.4252	2.4481	2.4732
.10961	2.2494	2.2622	2.2744	2.2898	2.3054	2.3233	2.3438	2.3509	2.3801	2.4045	2.4283	2.4524	2.4776
.07075	2.3048	2.3174	2.3286	2.3433	2.3577	2.3736	2.3908	2.4080	2.4275	2.4494	2.4712	2.4933	2.5163
.06118	2.3264	2.3396	2.3476	2.3614	2.3747	2.3898	2.4071	2.4259	2.4457	2.4662	2.4877	2.5075	2.5316
.04076	2.3857	2.3942	2.4043	2.4174	2.4305	2.4437	2.4592	2.4737	2.4923	2.5122	2.5328	2.5527	2.5734
.019761	.....	.....	.....	.....	.....	2.5649	.....	.....	.....	.....	.....	.....	.....
Series 5. KH_2PO_4:HCl=6:1 *													
0.3638	.....	.....	.....	.....	.....	2.8645	.....	.....	.....	.....	.....	.....	.....
.3008	2.7762	2.7921	2.8083	2.8259	2.8468	2.8685	2.8921	2.9168	2.9419	2.9693	2.9967	.....	.....
.2435	.....	.....	.....	.....	.....	2.8756	.....	.....	.....	.....	.....	.....	.....
.2403	2.7850	2.7966	2.8139	2.8331	2.8542	2.8757	2.8980	2.9220	2.9466	2.9746	3.0001	.....	.....
.19788	.....	.....	.....	.....	.....	2.8835	.....	.....	.....	.....	.....	.....	.....
.18084	2.7953	2.8094	2.8255	2.8442	2.8631	2.8839	2.9026	2.9267	2.9505	2.9780	3.0034	.....	.....
.13710	.....	.....	.....	.....	.....	2.8959	.....	.....	.....	.....	.....	.....	.....
.13590	.....	.....	.....	.....	.....	2.8980	.....	.....	.....	.....	.....	.....	.....
.11932	2.8157	2.8291	2.8438	2.8611	2.8793	2.8995	2.9169	2.9394	2.9626	2.9894	3.0135	.....	.....
.10348	.....	.....	.....	.....	.....	2.9104	.....	.....	.....	.....	.....	.....	.....
.09540	.....	.....	.....	.....	.....	2.9133	.....	.....	.....	.....	.....	.....	.....
.08354	.....	.....	.....	.....	.....	2.9219	.....	.....	.....	.....	.....	.....	.....
.05932	.....	.....	.....	.....	.....	2.9431	.....	.....	.....	.....	.....	.....	.....
.05927	2.8655	2.8778	2.8904	2.9053	2.9216	2.9404	2.9576	2.9789	2.9992	3.0234	3.0463	.....	.....

* The 5 solutions for which pwH from 0° to 50° is listed make up series 5a; the remainder are in series 5b.

TABLE 1. pwH *from 0° to 50° for aqueous mixtures of potassium dihydrogen phosphate and hydrochloric acid and for aqueous mixtures of potassium dihydrogen phosphate, formic acid, and potassium chloride*—Continued

$m_{KH_2PO_4}$	pwH at (°C)—												
	0°	5°	10°	15°	20°	25°	30°	35°	40°	45°	50°	55°	60°
Series 6. KH_2PO_4:HCOOH=5:1; KCl=0.005*m*													
0.3018						3.3886							
.2417	3.3526					3.3872					3.4542		
.19889						3.3833							
.19227						3.3848							
.16137						3.3899							
.14376						3.3919							
.12916											3.4617		
.12892	3.3561												
.12694						3.3896							
.11013						3.3938							
.09861						3.3946							
.09320						3.3945							
.08812											3.4695		
.08791	3.3629												
.08357						3.3994							
.06736						3.4056							
.06688											3.4764		
.06669	3.3714												
.05390											3.4840		
.05371	3.3812												
Series 7. KH_2PO_4:HCOOH=8:1; KCl=0.005*m*													
0.3867						3.5121							
.19031						3.5121							
.12885						3.5148							
.09564						3.5197							
.06442						3.5338							

and a^* is the ion-size parameter. The ionic strength, μ, of these mixtures is given by [3]

$$\mu = x\,m + m_H. \tag{6}$$

The Debye-Hückel equation suggests that the last term of eq 2 will be zero, or nearly so, in the region of low ionic strengths. Terms of this sort are indeed found to be small at low concentrations and to vary linearly with ionic strength in the region of moderate concentrations. The evaluation of log K_1 is accordingly made by extrapolation to infinite dilution of the apparent log K_1, or log K_1', derived from the following equation:

$$-\log K_1' = \text{pwH} + \log \frac{m - m_H'}{m(x-1) + m_H'}. \tag{7}$$

3.2. Limitations of the Conventional Method as Applied to Moderately Strong Acids

The procedure outlined in the foregoing section may be termed "the conventional emf method." The choice of a^* in eq 5a is somewhat arbitrary, being guided only by our knowledge of what constitutes a "reasonable" ion size, for the magnitude of this parameter is often of the same order as the ionic diameter in angstrom units. If $-\log K$ for the acid exceeds 3, the particular choice of a^*, within the reasonable range 2 to 8, is of little concern, for m_H is small compared to m, and relatively large errors in m_H' alter the last term of eq 7 but slightly. However, when the acid is as strong as the first dissociation step of phosphoric acid, for which $-\log K_1$ is about 2.12 [1], m_H' is quite large and the choice of a^* becomes an important consideration.

Figure 1 demonstrates the failure of the extrapolation lines computed with various values of a^* to converge at an ionic strength of zero. The open circles are the data at 25° for series 1, the most acidic solutions included in the study. The values of a^* (eq 5a) are indicated at the right of each line. When $a^*=0$, the last term of eq 5a reduces to the Debye-Hückel limiting law. The dots in figure 1 were computed from the data of series 5a at 25°. The ratio of phosphate to hydrochloric acid is considerably higher than in series 1. Accordingly m_H' is smaller, and the choice of a^* has less effect upon the result. It is unlikely that the difficulty could be resolved and the lines made to converge by obtaining data at lower ionic strengths, for the degree of dissociation of the phosphoric acid would be inevitably increased. Furthermore, still higher ratios of primary phosphate to hydrochloric acid might introduce uncertainties in the extrapolation, and it seems advisable to avoid them.

3.3. Estimation of the Activity Coefficient

Various possible means of choosing the correct extrapolation line were next considered. Up to this point the determination of the dissociation constant

[3] $\mu = \frac{1}{2}\Sigma m_i z_i^2$, where m_i and z_i are, respectively, the molality and charge of the ion of species i.

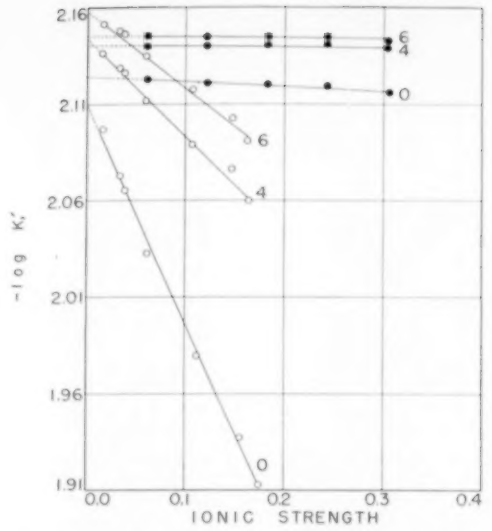

FIGURE 1. *Effect of a^* on the extrapolation at two different ratios of potassium dihydrogen phosphate to hydrochloric acid.*

The value of a^* used appears beside each line. Circles represent data of series 1; dots are for series 5a.

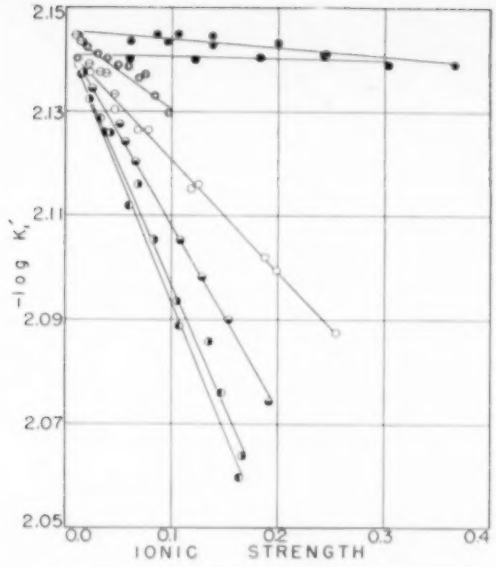

FIGURE 2. *Plot of $-\log K_1'$ at 25° as a function of ionic strength.*

A value of 4 was used for a^* in equation 5a. ◐=series 1; ◑=series 2; ◒=series 3; ○=series 4; ⊖=Nims series 1; @Nims series 2,3; ●=series 5a; ○=series 5b.

is completely rigorous, and it is unfortunate that a partially nonthermodynamic step need be introduced. As eq 5 suggests, different extrapolation lines with different intercepts exist because the correct value of $f_H f_{Cl}$ in each buffer solution is unknown. Unfortunately, the required activity coefficients cannot readily be determined. Nevertheless, the most probable range of a^* (eq 5a) can be narrowed somewhat in the light of the values that have been found to describe the behavior of the activity coefficient of hydrochloric acid and $f_H f_{Cl}$ in other mixtures of similar composition. Thus log $f_H f_{Cl}$ in aqueous solutions of hydrochloric acid with ionic strengths less than 0.2 is represented by the last term of eq 5a with $a^*=6.0$. If the hydrochloric acid is replaced partially or even completely by alkali chloride without altering the ionic strength, the activity coefficient term, $f_H f_{Cl}$, decreases [11].[4] To represent these new, lower activity coefficients, a lower value of a^* is necessary. Accordingly, a^* for $f_H f_{Cl}$ is found to approach a limit of 4.6 to 5.4 in pure solutions of sodium chloride and potassium chloride with ionic strengths of 0.2 or less. The principles of ionic interaction lead us to expect, in this instance, a larger specific effect of cations than of anions. Hence, it is possible that the activity coefficient of hydrochloric acid in a mixture of the acid and primary potassium phosphate does not differ greatly from that in a pure solution of potassium chloride. The most probable range of a^* can be fixed at 4 to 6 and a value of 5 chosen as a first approximation.

[4] Except possibly with lithium chloride, for which some measurements show a small increase.

Two separate calculations of $-\log K_1'$ were made at 0°, 25°, and 50° by eq 7. A value of 4 for a^* (eq 5a) was used for the first and 6 for the second. The data of series 1 to 5 were supplemented by those of Nims [1], who studied three series of six solutions each. The ratios of the molalities of potassium dihydrogen phosphate to hydrochloric acid in the latter were, respectively, 2.071:1 (series N1); 3.102:1 (series N2); and 3.079:1 (series N3). Two or three approximations were necessary in computing log K_1', as the contribution of the hydrogen ion to the total ionic strength was considerable. The extrapolation lines for $a^*=4$ are shown in figure 2.

4. Calculation of the Dissociation Constant: Series 6 and 7

In order to reduce the hydrogen-ion concentration below the level in the mixtures containing 6 moles of potassium dihydrogen phosphate to 1 of hydrochloric acid (series 5), two series of solutions were prepared from potassium dihydrogen phosphate and formic acid. Each buffer solution was also 0.005 molal with respect to potassium chloride. The formal expression relating the product of the dissociation constants for the two acids to the emf or pwH has been derived in another article [4]:

$$-1/2 \log K_1K_F = \text{pwH} + 1/2 \log \frac{m_{H_3PO_4} m_{HFo}}{m_{H_2PO_4^-} m_{Fo^-}} + 1/2 \log \frac{f_{H_3PO_4} f_{HFo} f_{Cl}^2}{f_{H_2PO_4^-} f_{Fo^-}}. \quad (8)$$

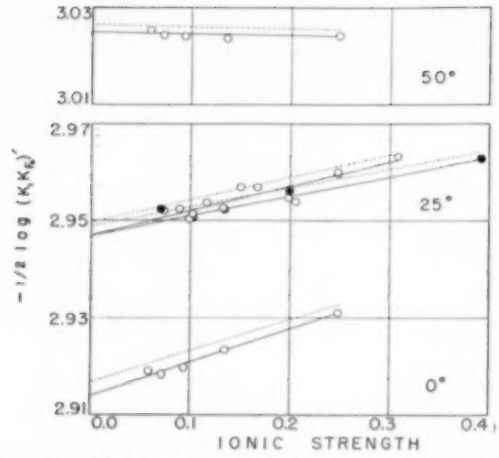

FIGURE 3. *Plot of $-\frac{1}{2}$ log $(K_1K_F)'$ at 0°, 25°, and 50° as a function of ionic strength.*

Circles (series 6) and dots (series 7) were calculated from the experimental data, using $a^*=4$, and the solid lines were fitted to them. The broken lines indicate the shift that would result from using $a^*=6$.

Inasmuch as K_F, the dissociation constant of formic acid (HFo), is well known from 0° to 60° [12, 13], the value of K_1 can be derived from the product, K_1K_F.

If m_1 represents the molality of potassium dihydrogen phosphate and m_2 that of formic acid,

$$m_{H_2PO_4} = m_{Fo^-} - m_H, \tag{9}$$

$$m_{HFo} = m_2 - m_{Fo^-}, \tag{10}$$

and

$$m_{H_2PO_4^-} = m_1 + m_H - m_{Fo^-}. \tag{11}$$

Furthermore, the last term of eq 8, which becomes zero at infinite dilution, is a linear function of ionic strength at low and moderate concentrations. Hence, log K_1K_F can be evaluated conveniently by extrapolation to infinite dilution of the apparent quantity, log $(K_1K_F)'$, computed by the equation

$$-\log (K_1K_F)' = \text{pwH} + 1/2 \log \frac{(m_2 + m'_H - m'_{Fo^-}) - m_2 m'_H/m'_{Fo^-}}{m_1 + m'_H - m'_{Fo^-}}. \tag{12}$$

The calculation of the formate molality rests on the assumed equality of $f_H f_{Cl}$ and $f_H f_{Fo^-}/f_{HFo}$ at moderate concentrations and is hence given the prime mark denoting an apparent or inexact quantity:

$$m'_{Fo^-} = m_2 y/(1+y), \tag{13a}$$

where

$$\log y = \text{pwH} + \log K_F. \tag{13b}$$

Equation 5a is used once more to compute m'_H, the apparent hydrogen-ion concentration, and the ionic strength is given by

$$\mu = m_1 + m'_H + m_{Cl} = m_1 + m'_H + 0.005. \tag{14}$$

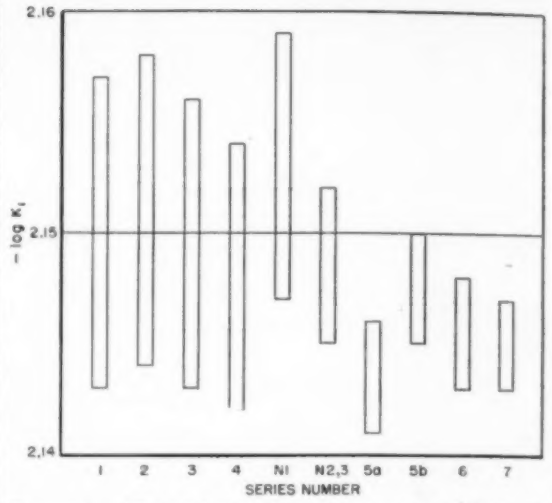

FIGURE 4. *Effect of choice of a^* on the value of $-\log K_1$ at 25° obtained from 10 groups of solutions.*

It should be emphasized that m'_H, m'_{Fo}, and log $(K_1K_F)'$ approach the true m_H, m_{Fo^-}, and log K_1K_F as the solution becomes more and more dilute.

The data of series 6 and 7 were used to calculate $-1/2$ log $(K_1K_F)'$ in the manner described above. As before, two different values of a^*, 4 and 6, were used to obtain m'_H by eq 5a. Two successive approximations were sufficient to establish consistent values of m'_H and μ. The dissociation constant of formic acid, K_F, was taken to be 1.638×10^{-4} at 0°, 1.772×10^{-4} at 25°, and 1.650×10^{-4} at 50° [13]. The results for series 6 are shown as open circles in figure 3 and those for series 7 as dots. The plotted points have been calculated from the experimental data, using $a^*=4$, and the solid lines fitted to them. The broken lines indicate the shift that would result from using $a^*=6$. The intercepts are listed in table 2. The difference is about 0.002 to 0.003 in $-1/2$ log K_1K_F, or about 0.005 in log K_1. The uncertainty in a^* is expected to have a smaller effect on the results of series 7 (8:1 ratio of primary phosphate to formic acid) than on series 6 (5:1 ratio).

TABLE 2. *Summary of $-\frac{1}{2}$ log K_1K_F for two values of the ion-size parameter*

t	Series 6		Series 7	
	$a^*=4$	$a^*=6$	$a^*=4$	$a^*=6$
°C				
0	2.914$_2$	2.916$_8$	-------	-------
25	2.947$_6$	2.949$_3$	2.947$_9$	2.949$_9$
50	3.025$_8$	3.026$_8$	-------	-------

5. The Dissociation Constant at 25°

Table 3 summarizes the values of the first dissociation constant computed from all seven series and the data of Nims [1], a total of 81 buffer solutions. The series are arranged in the table from top to bottom in the order of decreasing acidity, and it is evident, both in the table and in figure 4, that the uncertainty of the determination decreases in the same way. For $a^*=4$, the 10 groups of solutions furnish about the same value of $-\log K_1$. The mean of these is 2.144, and the mean deviation from this figure is only 0.0014. For $a^*=6$, the values of $-\log K_1$ display a general downward trend with increasing ratio of phosphate salt to acid. It is not believed that the constancy indicates the correctness of a value of 4 for a^*, as the parameter usually changes somewhat with buffer ratio. The lower end of each bar in figure 4 corresponds to $a^*=4$, the upper end to $a^*=6$.

The mean of the 20 values of $-\log K_1$ given in table 3 was chosen as the best estimate of $-\log K_1$ that could be made. This average figure of 2.148 ± 0.005 at 25° is considerably higher than 2.124 found by Nims [1] with $a^*=0$, that is, by computing $f_{H_2}f_{Cl}$ in eq 5 from the Debye-Hückel limiting law. Noyes and Eastman [14] have reported the conductance of seven solutions of phosphoric acid of molalities ranging from 0.0002 to 0.1. From these data, Sherrill and Noyes [15] derived a value of 2.081 for $-\log K_1$ at 18°. In a later recalculation, Lugg [16] obtained 2.09. This figure is in good agreement with 2.096 given by Nims for 18° [1]. Mason and Culvern [17] have recently extended the conductance measurements at 25°. From their data for the dilute solutions, together with those of Noyes and Eastman, they obtained 2.126 for $-\log K_1$ at 25°. However, there is some indication that their data, treated independently, would yield a value near 2.140.

Bjerrum and Unmack have calculated the first dissociation constant of phosphoric acid from measurements of the emf of hydrogen-calomel cells at 18°, 25°, and 37° [18]. Their results are compared in the following table with those of Nims [1] and those reported here.

	18°	25°	37.5°
Bjerrum and Unmack	2.120	2.161	2.235
Nims	2.096	2.124	2.185
Bates	2.119	2.148	2.209

The value given by Bjerrum and Unmack at 37° has been corrected to 37.5° by addition of 0.003. By the analysis of titration curves for phosphoric acid in the presence of alkali chlorides, Hentola obtained 2.172 for $-\log K_1$ at 25° [19].

TABLE 3. *Summary of $-\log K_1$ at 25° for two values of the ion-size parameter*

Series	$-\log K_1$ for—		$\Delta(\log K_1)$
	$a^*=4$	$a^*=6$	
1	2.143	2.157	0.014
2	2.144	2.158	.014
3	2.143	2.156	.013
4	2.142	2.154	.012
Nims 1	2.147	2.159	.012
Nims 2, 3	2.145	2.152	.007
5a	2.141	2.146	.005
5b	2.145	2.150	.005
6	2.143	2.148	.005
7	2.143	2.147	.004
Mean	2.148		

6. The Temperature Coefficient of log K_1

Although the choice of the correct K_1 at 25° was dependent upon a partly arbitrary selection of a^* (eq 5a), the temperature coefficient of log K_1 was found to be substantially unaffected by this selection. In other words, the difference between log K_1 at 0° and 50° was practically the same whether a^* were 4 or 6, as shown in table 4, where log K_0 − log K_t is tabulated for seven groups of solutions. The figures in parentheses are the values calculated with 6 for a^*, and the others were obtained with $a^*=4$. The values of log K_1 at each temperature were derived by the methods described earlier in this paper. The average difference at each temperature, given in the last column, was combined with 2.148, the value of

TABLE 4. *Change of the first dissociation constant of phosphoric acid with temperature calculated with $a^*=4$; values for $a^*=6$ appear in parentheses*

t	log K_0 − log K_t from series—							Average log K_0 − log K_t
	1	2	3	4	Nims 2, 3	5a	6	
°C								
0	0(0)	0(0)	0(0)	0(0)	0(0)	0(0)	0(0)	0(0)
5	0.018	0.018	0.015	0.016	.....	0.016	.....	0.0166
10	.033	.033	.031	.032	.....	.031	.....	.0320
15	.051	.050	.051	.051	.....	.050	.....	.0506
20	.071	.070	.071	.071	.....	.070	.....	.0706
25	.091(0.090)	.091(0.090)	.091(0.090)	.092(0.092)	0.088(0.087)	.094(0.093)	0.100(0.100)	.0924(0.0917)
30	.116	.113	.118	.117	.....	.111	.....	.1150
35	.138	.139	.147	.141	.....	.136	.....	.1402
40	.169	.168	.171	.168	.....	.162	.....	.1676
45	.196	.193	.198	.195	.....	.191	.....	.1946
50	.225(0.222)	.222(0.222)	.223(0.222)	.224(0.221)	.220(0.218)	.218(0.216)	.225(0.223)	.2223(0.2205)
55	.251	.252	.252	.252	.....	.....	.....	.2522
60	.282	.282	.281	.282	.....	.....	.....	.2816

$-\log K_1$ at 25°, to obtain $-\log K_1$ at the other 12 temperatures. The following equation, the constants of which were determined by the method of least squares, represents the "observed" $\log K_1$ from 0° to 60° with an average deviation of ±0.0005:

$$-\log K_1 = \frac{799.31}{T} - 4.5535 + 0.013486T. \quad (15)$$

The observed and calculated values are summarized in the second and third columns of table 5, and K_1 is given in the last column.

TABLE 5. *Summary of $-\log K_1$ and K_1 from 0° to 60°*

t	$-\log K_1$ (observed)	$-\log K_1$ (calculated eq 15)	$K_1 \times 10^3$
°C			
0	2.056	2.0565	8.79
5	2.073	2.0713	8.45
10	2.088	2.0880	8.17
15	2.107	2.1068	7.82
20	2.127	2.1266	7.46
25	2.148	2.1483	7.11
30	2.171	2.1714	6.75
35	2.196	2.1961	6.37
40	2.224	2.2222	5.97
45	2.251	2.2494	5.61
50	2.277	2.2780	5.28
55	2.308	2.3078	4.92
60	2.338	2.3386	4.59

7. Thermodynamic Quantities

The changes of free energy, $\Delta F°$, of heat content, $\Delta H°$, of entropy, $\Delta S°$, and of heat capacity, $\Delta C°_p$, for the first dissociation process in the standard state were calculated from eq 15 and the usual formulas [20]. The results are given in table 6. In view of the relatively large uncertainty in the value of $-\log K_1$, the accuracy of $\Delta F°$ is estimated to be about ±30 j mole $^{-1}$. On the other hand, the temperature coefficient at 25° seems rather well established, and accordingly $\Delta H°$, $\Delta S°$, and $\Delta C°_p$ are believed accurate within 150 j mole $^{-1}$, 0.5 j deg $^{-1}$ mole $^{-1}$, and 5 j deg $^{-1}$ mole $^{-1}$, respectively, at 25°. The uncertainty in the temperature coefficient of $\log K_1$ is considerably larger near the ends of the temperature range covered by the measurements than in the middle. Hence, these three thermodynamic quantities are given only for temperatures from 15° to 45°.

TABLE 6. *Thermodynamic quantities for the process:* $H_3PO_4 = H^+ + H_2PO_4^-$ *in aqueous solution*

t	$\Delta F°$	$\Delta H°$	$\Delta S°$	$\Delta C°_p$
°C	*j mole^{-1}*	*j mole^{-1}*	*j deg^{-1}mole^{-1}*	*j deg^{-1}mole^{-1}*
0	10,752			
5	11,034			
10	11,319			
15	11,618	−6,136	−61.6	−149
20	11,932	−6,986	−64.2	−151
25	12,261	−7,650	−66.8	−154
30	12,600	−8,426	−69.4	−157
35	12,956	−9,216	−72.0	−159
40	13,328	−10,018	−74.5	−162
45	13,705	−10,832	−77.1	−164
50	14,087			
55	14,500			
60	14,906			

The value of $\Delta H°$ at 25°, −7,650 j mole^{-1}, is to be compared with −7,420 j mole^{-1} derived from the emf data of Nims [1, 13] and with −8,160 j mole^{-1} from the calorimetric data of Pitzer [21]. Pitzer chose −7,870 j mole^{-1} as a "best value." For the entropy change on dissociation, the measurements of Nims lead to $\Delta S° = -65.7$ j deg^{-1} mole^{-1} at 25° and those of Pitzer to −66.9. The latter figure is in excellent agreement with −66.8 j deg^{-1} mole^{-1} obtained in this investigation.

8. References

[1] L. F. Nims, J. Am. Chem. Soc. **56,** 1110 (1934).
[2] R. G. Bates, J. Am. Chem. Soc. **70,** 1579 (1948).
[3] R. G. Bates and G. D. Pinching, J. Research NBS **43,** 519 (1949) RP2043.
[4] R. G. Bates, J. Am. Chem. Soc. **73,** 2259 (1951).
[5] G. D. Pinching and R. G. Bates, J. Research NBS **37,** 311 (1946) RP1749.
[6] R. G. Bates and S. F. Acree, J. Research NBS **30,** 129 (1943) RP1524.
[7] R. G. Bates and G. D. Pinching, J. Research NBS **42,** 419 (1949) RP1982.
[8] E. J. Roberts, J. Am. Chem. Soc. **52,** 3877 (1930).
[9] H. S. Harned and R. W. Ehlers, J. Am. Chem. Soc. **54,** 1350 (1932).
[10] G. G. Manov, R. G. Bates, W. J. Hamer, S. F. Acree, J. Am. Chem. Soc. **65,** 1765 (1943).
[11] H. S. Harned, J. Am. Chem. Soc. **57,** 1865 (1935).
[12] H. S. Harned and N. D. Embree, J. Am. Chem. Soc. **56,** 1042 (1934).
[13] H. S. Harned and B. B. Owen, The physical chemistry of electrolytic solutions, 2d ed., chapter 15 (Reinhold Publishing Corp., New York, N. Y., 1950).
[14] A. A. Noyes and G. W. Eastman, Carnegie Institution of Washington Publication No. 63, p. 239 (1907).
[15] M. S. Sherrill and A. A. Noyes, J. Am. Chem. Soc. **48,** 1861 (1926).
[16] J. W. H. Lugg, J. Am. Chem. Soc. **53,** 4 (1931).
[17] C. M. Mason and J. B. Culvern, J. Am. Chem. Soc. **71,** 2387 (1949).
[18] N. Bjerrum and A. Unmack, Kgl. Danske Videnskab. Selskab., Math.-fys. Medd. **9,** No. 1 (1929).
[19] Y. Hentola, Kemian Keskuliiton Julkaisuja **13,** No. 2 (1946).
[20] H. S. Harned and R. A. Robinson, Trans. Faraday Soc. **36,** 973 (1940).
[21] K. S. Pitzer, J. Am. Chem. Soc. **59,** 2365 (1937).

WASHINGTON, February 26, 1951.

Journal of Research of the National Bureau of Standards Vol. 47, No. 3, September 1951 Research Paper 2237

Determination of Ash in GR-S Synthetic Rubbers and Latices

Frederic J. Linnig, Lewis T. Milliken, and Ralph I. Cohen

Rapid methods are described for the determination of the ash content of GR-S synthetic rubbers and latices. Filter paper and filter pulp are used to prevent either material from overrunning the edge of the crucible when introduced into the furnace at the ashing temperature. Water is used to facilitate the burning of the carbonaceous residue obtained in ashing GR-S latex. These procedures have been put into use in the control testing of GR-S production. They are as precise as older methods of ashing and far less time-consuming. The techniques employed should be applicable to other organic materials.

1. Introduction

The determination of ash is an important factor in controlling the quality of GR-S synthetic rubbers and latices and in assuring the consumer that his material meets the requirements of the specification. Methods used in ashing natural rubber [4, 8, 9],[1] natural rubber latex [7, 8, 9, 18], and other similar organic compounds [1, 2, 3, 5, 6] call for distillation of the dry sample by gradually raising the temperature of the specimen from room temperature to a point somewhat below the ignition temperature of the gases formed. The carbonaceous residue is then ashed to constant weight at temperatures varying from 400° to 550° C, depending on the substance tested. This distillation procedure is too time consuming for control testing. Introduction of GR-S rubber into a muffle furnace at the final ashing temperature, as suggested by one of the plant laboratories [17], yields satisfactory results with many samples. However, when applied to certain samples of GR-S rubber, particularly those coagulated with alum, this procedure yields results that may be low by as much as 30 percent. These low results are due to loss of material that froths and overruns the edge of the crucible during the early stages of the pyrolysis. In addition, when GR-S latex is ashed according to the procedure used for natural rubber latex, the carbonaceous residue formed on distillation may be removed only at temperatures that cause appreciable loss of inorganic material. Accordingly, techniques were developed for safely introducing either undried latex or rubber into the furnace at the ashing temperature, and for facilitating through the use of a washing treatment, the removal of the carbonaceous material formed in ashing GR-S latex. These techniques have been adopted for use in the official methods of the Government synthetic rubber program [10, 12, 13], and should be applicable to other organic materials that may give rise to difficulties in ashing.

2. Procedure

GR-S. The sample to be tested is mill-massed on a laboratory rubber mill and sheeted. A 2- to 5-g specimen of the sheeted rubber is weighed to the nearest milligram and wrapped in a single sheet of 15-cm "ashless" filter paper by spreading it along a chord of the circle midway between the center and the edge. The paper is rolled into a tight cylinder around the rubber, and the ends of the filter paper are folded over the sample. The resulting roll is then folded over once or twice on itself and placed in a porcelain or aluminum crucible that has a volume of from 30 to 60 ml, and that has been ignited to constant weight (±0.2 mg) at 550° C plus or minus 25° C. The crucible containing the wrapped specimen is placed directly into a muffle furnace maintained at 550° C. plus or minus 25° C. The door of the furnace is closed and should not be reopened until combustion of the carbonaceous material is nearly complete (30 to 60 min.). After the carbon appears to have burned completely, the crucible is removed from the furnace, cooled to room temperature in a desiccator, and weighed. As a check for the complete removal of carbon, the specimen may be reheated for 30-min. intervals until it has attained constant weight within ±0.2 mg.

A correction should be made for the ash content of the filter paper when the effect is greater than 0.01 percent of the weight of the specimen.

GR-S Latex. A circle of ashless filter paper 9 cm in diameter is folded into the form of a cone, and inserted into a 60-ml porcelain crucible previously ignited to constant weight (±0.2 mg) at 550° C plus or minus 25° C. A small quantity of dry ashless filter pulp (0.25 to 0.50 g) is pressed down into the bottom of the cone, and the crucible and its contents are weighed to the nearest milligram in a weighing bottle or friction top metal container. Five milliliters of latex, previously filtered through an 80-mesh stainless steel wire screen, are poured into the cone and the crucible, and its contents are reweighed to the nearest milligram. The crucible and its contents are placed directly into a muffle furnace maintained at 550° C plus or minus 25° C. The door of the furnace is closed and should not be reopened for 45 to 60 min. The crucible is then removed and allowed to cool until it may be touched by hand (about 10 min.). Two to five drops of distilled water are added to the ash, the actual number depending upon the quantity of residue present. Sufficient time should be allowed between

[1] Figures in brackets indicate the literature references at the end of this paper.

drops for the water to be absorbed by the residue before the next drop is added. An unabsorbed excess of water should be avoided, since it will cause spattering of the residue upon the side of the crucible during ashing, thus making subsequent washes more difficult. The dampened residue is ashed for one-half hour, and the alternate wetting and ashing procedures are repeated until all of the carbon appears to have been burned. The crucible and its contents are cooled to room temperature in a desiccator and weighed. As a check for the complete removal of carbon, the wetting and ashing techniques may be repeated again until the crucible and its contents have reached constant weight within ± 0.5 mg. This usually requires from two to five washes and a total time of 2 to 4 hours, depending upon the latex tested.

3. Discussion of Techniques

3.1. Temperature of Ashing

A temperature of 550° C was chosen to allow for the fairly rapid burning of both uncompounded GR–S and GR–S latex with a minimum loss of inorganic material through decomposition or volatilization. Reducing the temperature of the furnace below this point greatly slows down the rate of ashing. Lower temperatures are necessary only when the method is applied to certain compounded stocks containing appreciable quantities of materials that decompose or volatilize at this temperature [14]. The furnace door should be kept closed to prevent rapid burning and glowing of the specimen at temperatures that may be above the furnace temperature. Loss from explosion of the distilling gases during the early stages of the pyrolysis is prevented by the filter paper that appears to be intact at this time.

3.2. Choice of Crucible

Both aluminum [2] [16] and porcelain crucibles have been found satisfactory for use in the determination of ash in GR–S. Aluminum crucibles are more suitable for rapid routine testing because they are (1) much less expensive; (2) more uniform in weight (approximately 5.2 g for those used in this work); (3) more rapidly cooled. The crucibles used in this work have straight sides and a relatively large base. Consequently, they are more stable and the wrapped specimen remains on the bottom of the crucible even when it tends to uncurl.

However, only porcelain crucibles may be used in ashing GR–S latices. Figure 1 shows the results obtained when both porcelain and aluminum crucibles are used. It was believed that the observed increase in the weight of the residue in the aluminum crucibles on repeated wetting and ashing resulted from a reaction between the aluminum and the water in the presence of the alkaline residue obtained from ashing the soap in the latex. Tests made by wetting pure sodium carbonate with water and heating as directed in the procedure lend support to this view.

[2] The aluminum crucibles used here were obtained on special order from The Aluminum Company of America in accordance with "drawing (Alcoa) FR-9747–X, capacity $3^{5}/_{16}$ cu. in., 28 gage material, $1^{25}/_{64}$ in. overall height, 1.675 in. diameter, beveled at bottom." The price at the time of purchase was approximately $14.00 a thousand.

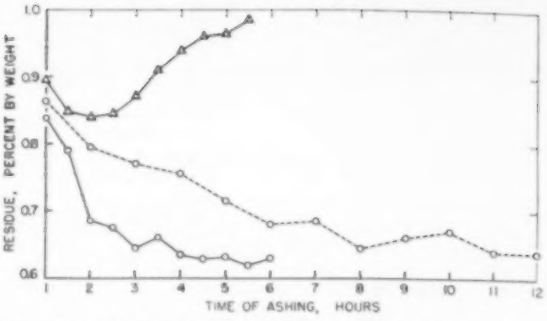

FIGURE 1. *Effect of wetting residues of GR–S latex and reheating for different periods of time in porcelain and aluminum crucibles.*

○, Porcelain crucibles; △, aluminum crucibles; ____, one-half-hour periods; ----, 1-hour periods.

3.3. Use of Filter Paper and Pulp

In addition to preventing loss from explosion the use of filter paper allows all types of GR–S polymers to be ashed without loss from frothing when introduced into the furnace at the ashing temperature. This technique has been used in ashing volatile metallo-organic compounds [11]. Oxalic acid or ammonium oxalate placed over the specimen in the crucible help to prevent "boiling over" of the polymer, but are not as satisfactory as filter paper. Rubber charred with nitric acid or treated with sulfuric acid or ammonium sulfate prior to ashing does not effervesce, but the resulting values are different from those obtained by the slow-ashing procedures [4, 8]. In addition, the ash obtained when the specimen is wrapped in filter paper is quite porous and fluffy, and can be readily extracted or dissolved for further analysis.

GR–S latex may be ashed without previously drying the specimen if ashless filter pulp is used to absorb the liquid and to prevent the spattering that would otherwise occur during the first few minutes in the furnace. Not only is a fluffy residue obtained, but the cone prevents the residue from adhering to the walls of the crucible. The washing and burning of the carbonaceous material are thus facilitated.

3.4. Washing of the Ash

It is believed that the slow and incomplete ashing of GR–S latex is due to a protective layer of salt that covers the carbon formed when the polymeric portion of the latex is burned. It is probable that treating the residue with small portions of water removes at least part of this coating of salt, permitting an additional portion of the carbon to be burned. Qualitative tests indicate the presence of carbonate resulting from ashing the soap present in the original latex. Since the coagulated polymer contains but

little soap, GR–S may be ashed within 1 hour without the washing treatment. Nitric acid, sulfuric acid, hydrochloric acid, and aqueous solutions of oxalic acid have been used to wash the residue. Only one treatment with any of the mineral acids is required to yield a carbon-free ash, but since these acids alter the composition of the ash, the resulting values though reproducible are different from those obtained when no treatment is used. Since oxalic acid offered no advantage over water, water was chosen. This technique of wetting the carbonaceous residues with water to facilitate burning is simpler than a number of previous methods [1, 5, 6].

Figure 1 shows the effect of using two different periods of heating between water washes. Apparently, the use of one-half-hour heating periods reduces the time required for ashing by 50 percent. Further reduction of the heating periods is not helpful.

4. Results

In order to determine the over-all precision of the tests when used over an extended period, duplicate determinations were made daily for 5 to 10 days on samples of GR–S and GR–S latex. The particular samples of GR–S used were chosen because of their marked tendency to overrun the edge of the crucible when rapidly ashed without the use of filter paper. The samples of GR–S latex used were chosen because they characterize differences in latex types that might effect either the final results or the ease of testing. Both porcelain and aluminum crucibles were used in testing the GR–S rubber samples so that the values obtained might be compared. For further comparison the same rubber samples were tested according to the slow-ashing process [4, 8] without previous extraction.

The results of these tests are given in tables 1 and 2. An analysis of variance [15] made of the data showed a significant, but small, day-to-day variability for the tests used on both the rubber and latex. This variability was not sufficiently large to affect appreciably the values for the over-all precision, s_r, that is, the standard deviation of a single random determination given in the tables. The values of s_r for each of the tests are of the same order of magnitude as that obtained when GR–S is analyzed by the older slow-ashing process. In addition, the data obtained for GR–S rubber indicate at least as good retention of material by the new process as by the old. A similar comparison for GR–S latex cannot be made, since the older slow-ashing methods are not applicable to this material. Though the ash is not necessarily identical with the inorganic material originally present in the sample, because of the decomposition of soaps, etc., the residue represents the original adequately for specification purposes.

TABLE 1. *Ash content of GR–S synthetic rubber samples*

Procedure		X–243AC [a]		X–346AC [a]		X–452AC [a]	
		Porcelain crucibles	Aluminum crucibles	Porcelain crucibles	Aluminum crucibles	Porcelain crucibles	Aluminum crucibles
		Percent	*Percent*	*Percent*	*Percent*	*Percent*	*Percent*
Present	Mean	0.778	0.770	0.536	0.545	0.496	0.502
	High	.83	.80	.55	.58	.56	.54
	Low	.74	.72	.50	.52	.45	.46
	s_r [b]	.025	.022	.016	.018	.029	.022
	No. of determinations	10	10	10	10	20	20
Slow-ashing	Mean	0.749	....	0.504	....	0.509	....
	High	.78	....	.56	....	.56	....
	Low	.72	....	.46	....	.47	....
	s_r [b]	[c]	....	[c]	....	.026	....
	No. of determinations	20	....	16	....	30	....

[a] These designations apply to samples of alum-coagulated GR–S used as reference lots in the control testing of this type of GR–S production in the government synthetic rubber plants.

[b] s_r represents the standard deviation of a single random determination including both within-day and day-to-day variability.

[c] These determinations were made over too short a period to permit a reliable estimate of s_r.

TABLE 2. *Ash content of different types of GR–S synthetic rubber latices* [a]

	Types—			
	I	III	V	X–478 [b]
	Percent	*Percent*	*Percent*	*Percent*
Mean	0.318	0.762	0.465	0.529
High	.35	.80	.52	.57
Low	.27	.71	.40	.50
s_r [c]	.028	.028	.028	.022
Number of determinations	15	16	16	10

[a] The designations given are for different types of commercially available latices. Types I, III, and V were tested simultaneously.

[b] GR–S latex polymerized at 41° F.

[c] s_r represents the standard deviation of a single random determination including both within-day and day-to-day variability.

[d] This value of s_r was calculated from the pooled data obtained with the three types of latex tested simultaneously.

5. References

[1] Am. Soc. Testing Materials, ASTM 1949 Standards, Part 5, Designation D 128–47, p. 758.

[2] Am. Soc. Testing Materials, ASTM 1949 Standards, Part 5, Designation D 377–47T, p. 152.

[3] Am. Soc. Testing Materials, ASTM 1949 Standards, Part 5, Designation D 584–47, p. 380.

[4] Am. Soc. Testing Materials, ASTM 1949 Standards, Part 6, Designation D 297–43T, p. 816.

[5] Association of Official Agricultural Chemists, Official and Tentative Methods of Analysis of the Association of Official Agricultural Chemists, Designation 6.107, p. 73 (1945).

[6] Association of Official Agricultural Chemists, Official and Tentative Methods of Analysis of the Association of Official Agricultural Chemists, Designation 10.5, p. 107 (1945).

[7] British Standards Institution, British standard methods of testing latex, raw rubber, and unvulcanized compounded rubber, Bull. BS 902, p. 9 (June 1940).

[8] British Standards Institution, British standard methods of testing latex, raw rubber, and unvulcanized compounded rubber, Bull. BS 902, p. 20 (June 1940).

[9] British Standards Institution, British Standard methods of testing vulcanized rubber, Bull. BS 903, p. 55 (Oct. 1950).

[10] R. I. Cohen, L. T. Milliken, and F. J. Linnig, The determination of ash in GR–S latices, unpublished report to Office of Rubber Reserve (May 8, 1950).

[11] W. F. Hillebrand and G. E. F. Lundell, Applied inorganic analysis, p. 317, 1st ed. (John Wiley and Sons, Inc., New York, N. Y., 1929).

[12] L. T. Milliken, The use of aluminum crucibles for the determination of ash in GR–S, unpublished report to Office of Rubber Reserve (July 24, 1947).

[13] L. T. Milliken and F. J. Linnig, Determination of ash in alum-coagulated GR–S, unpublished Report to Office of Rubber Reserve (Feb. 21, 1949).

[14] J. R. Scott, J. Rubber Research **14,** 150 (1945).

[15] G. W. Snedecor, Statistical methods, 4th ed. (The Collegiate Press, Ames, Iowa, 1946).

[16] J. R. Todd, Government Evaluation Laboratories, Akron, Ohio, Private communication (March 12, 1946).

[17] U. S. Rubber Co., Agent, Office of Rubber Reserve, Institute, West Virginia, private communication (April 25, 1944).

[18] G. H. Vila, Vanderbilt rubber handbook, 9th ed., p. 263 (R. T. Vanderbilt Co., New York, N. Y., 1948).

WASHINGTON, August 31, 1950.

Glass Spheres for the Measurement of the Effective Opening of Testing Sieves[1]

Frank G. Carpenter[2] and Victor R. Deitz

It is shown that the "effective" opening of testing sieves is generally somewhat larger than the average opening or the nominal opening. A method of measuring the effective opening by means of a calibrated mixture of glass spheres is described. Glass beads of the type used for highway markings were a suitable source of glass spheres for sizes from 80 to 1,000 microns (U. S. Sieves No. 170 through 18). Details are given for the selection of the spheres, the preparation of the desired mixture of spheres, subdivision of the samples, the measurement of the diameters, and the calculation of the weight-size distribution. From a statistical analysis of the calibration data, both the reproducibility and accuracy of the method were found in general to be about 1 percent.

1. Introduction

The specifications for practically every powdered or granular material of commerce prescribe maximum and/or minimum *limits* of the particle sizes. In addition, a knowledge of the *distribution* of particle sizes is often required, both for control purposes and in research. In order to test materials for conformity with specifications, or to measure the particle size distribution, testing sieves are used by many industries. Sieve analyses obtained by different laboratories (for example, those of the buyer and seller) often show considerable disagreement. The discrepancy in some cases is due to inadequate sampling procedures, but when good representative samples, or even the same sample are used, differences frequently occur.

The sieving operation consists of agitating the material on a sieve of known opening until substantially all the particles that are small enough to pass the openings have passed. The shaking process can be carried out in a satisfactorily reproducible manner so that the error from this source can be made satisfactorily low [1].[3] The weights of the fractions retained by the various sieves can be determined without appreciable errors. On the other hand, the evaluation of the size of the openings of testing sieves may be one of the largest sources of error in sieve analysis. Consideration of this error is the subject of this paper.

Specifications [2] for testing sieves allow a manufacturing tolerance in the average size of the opening from ± 2 to ± 7 percent, depending upon the size of the opening. These tolerances are rather wide but are satisfactory if only a rough idea of the particle size is desired or if it is desired that a certain material be finer or coarser than some stated size. If an accurate particle size distribution is required, especially with material with a narrow range of particle sizes, then these tolerances are so large as to render the sieves almost useless without an individual calibration to determine the effective opening of each sieve.

1.1. Effective Sieve Opening

The difficulties encountered in the evaluation of sieve openings arise from three sources, none of which appear to have received sufficient attention. First, all the openings of a sieve are rarely of the same size. Rather, the sizes of openings are distributed according to some probability law. The over-sized particles can pass the larger holes and, thus, the openings that are effective are somewhat larger than the average opening. Second, the separation achieved by a sieve is not complete, but instead some under-sized particles always remain on the top of the sieve. The sieve opening is thus effectively somewhat smaller than the average opening. Third, the opening is effective in three dimensions, and the plane defined by the sieve cloth may not coincide with the plane defined by the effective opening. The effective opening will thus be larger than the average opening, which is measured by the projection on the plane of the sieve cloth.

The first and second of these phenomena are acting in opposite directions, and the effects of one might nullify the effects of the other. However, the manner and speed of shaking affect both; therefore, the effective opening is not a constant for a given sieve but depends also upon the way the sieve is used. The general dependence of the effective sieve opening on time of shaking is illustrated in figure 1. Assume that a sieve with an opening size distribution given in figure 1, A, is to be used to separate into two fractions a material with the particle size distribution given in figure 1, B. After a very short time of shaking, the particle size distributions in the fractions passing and retained are as illustrated in figure 1, C. The separation is very incomplete with large amounts of under-sized particles retained. After a longer shaking time the distributions given in figure 1, D, may be achieved, and the effective size of the sieve may be defined as the point at which the curves cross, which is also the point at which the curves are the steepest. Figure 1, E, illustrates the effect of an infinitely long shaking time. As the shaking progresses it is seen that the effective opening becomes larger. It becomes evident that the effective opening depends upon the time of shaking. In addition, the type of shaking motion would have a similar effect. Any method of calibration for effec-

[1] This investigation is sponsored as a joint research project undertaken by the Bone Char Research Project, Inc., and the National Bureau of Standards.

[2] Research Associate at the National Bureau of Standards, representing the Bone Char Research Project, Inc.

[3] Figures in brackets indicate the literature references at the end of this paper.

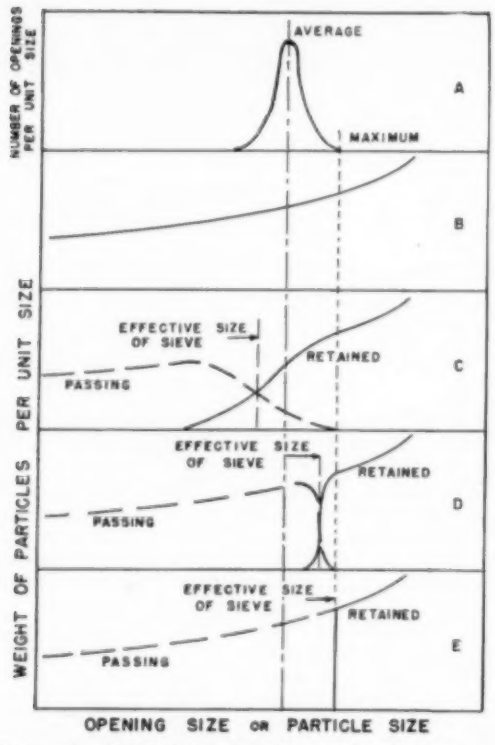

FIGURE 1. *Effect of time of shaking on the effective sieve opening.*

A, Opening-size distribution; B, particle-size distribution before sieving; C, particle-size distribution after very short time of shaking; D, particle-size distribution after long time of shaking; E, particle-size distribution after infinite time of shaking.

tive opening must necessarily take these two effects into account.

If all the openings of the sieve were exactly the same size, the shaking time required to reach a condition similar to figure 1, D, would be considerably shortened. It is to be noted, however, that even in perfectly uniform sieves the effective opening is not equal to the average opening unless the shaking is continued for an infinite time.

The usual method of calibrating sieve openings [3] consists in making measurements on a magnified projection of the sieve cloth. Observations by this method are rapid, and the openings may be inspected for uniformity during these measurements. This method, however, has two serious disadvantages. First, the average opening is measured, taking no account of the difference between average and effective opening. Second, the calibration requires special equipment and skilled operators. Weber and Moran [4] suggested that the projection method be used to measure a large number of openings, and the effective opening be determined by use of an empirical relation between the statistical parameters and the effective opening. This method requires the same special equipment and even more skilled operators.

Fagerholt [5] showed that the effective size of the sieve after a shaking period of time, t, is equal to the average diameter of particles that passed by continued shaking under the same conditions during the interval of time t to $3t$. This conclusion is based on assumptions that are not strictly true. For practical purposes this method is much too involved, because it requires an independent particle-size determination for each sieve for each sieve analysis. It offers a way, however, for determining the effective size of the sieve for very irregularly shaped particles.

2. New Method of Calibrating Testing Sieves

The authors in a previous paper [1] pointed out that the effective opening can be determined directly and simply by measuring the sizes of spheres that will just pass. In that paper exploratory work was described on the use of a calibrated sample of glass spheres for measuring the effective opening of testing sieves.

2.1. Particle Shapes

It is recognized that the sieve openings are square or slightly rectangular in shape and that irregularly shaped particles can pass through even though one of the dimensions of the particle, or "an average" of all dimensions, is considerably larger than the diameter of the opening. This is especially true for needle-like shapes. The average diameter of irregular particles that pass a sieve cannot be considered equal to the diameter of spheres that pass the sieve. The glass spheres used in this work were only intended to measure the opening of the sieve. The calculation of some "average" diameter of particles, which deviate from a spherical shape, is a separate problem that introduces factors not directly related to the methods for evaluating effective sieve openings.

2.2. Rectangular Openings

If the openings are rectangular rather than square, then the "effective" size for irregularly shaped particles will be increased, but the effective size for spheres will be the same as for a square with the same dimension as the minimum side. For this reason, sieves that are to be used with needle-like particles must be examined independently for squareness of holes. Fortunately, the openings of most testing sieves made in recent years are essentially square in shape.

2.3. Uniformity of Openings

The method of calibrating testing sieves by use of glass spheres takes into account the effect of nonuniformity, but it does not measure directly the uniformity of the openings. If there is reason to suspect that the sieve openings are not sufficiently uniform, they should be checked independently either by the usual projection method or by the method proposed by the authors in a previous paper [1]. The latter

is based on the effect of uniformity of openings on the sieving rate. The amount of nonuniformity that can be tolerated in testing sieves was considered in [1]. Sieves that do not appear obviously deformed, are usually sufficiently uniform so that the glass sphere method of calibration will correct for the small amount of nonuniformity that does exist.

3. Selection of Glass Spheres

The spherical shape was chosen primarily to eliminate any doubt or question about "average" diameter or the orientation of the particle in passing the opening. The spheres were not intended to be representative of the particles to be used on the sieves, nor is their diameter to be considered equal to the average diameter of irregular particles that might be sieved on the same sieve.

Glass was chosen because its hardness minimizes abrasion and because spheres of glass are readily available. Glass beads of the type used for projection screens were used by Gooden and Updike [7] as a source for spheres of 100-μ diameter. Glass beads of the type used for highway markings [4] are a suitable source of glass spheres for sizes from 80 to 1,000μ (sieves No. 170 through 18). Larger and smaller sizes of glass spheres are being made for other purposes, and a wider range of sieve sizes could be covered if desired.

3.1. Separation of Spherical Particles

The glass beads for highway markings as purchased are not all spherical, nor are the sizes continuous. It was necessary to separate the spherical particles from the elliptical, tear drop, dumbell, and jagged pieces. The spherical shapes were effectively separated from the other shapes by rolling the particles down an incline. The spheres roll true, whereas nonspheres either roll in circles or not at all. The apparatus used is shown in figure 2. It consists essentially of a smooth flat disk about 20 in. in diameter, turning at about 3 rpm and tilted slightly. Only one sieve fraction can be separated at a time. For the larger sizes (about 1,000 μ) the inclination of the disk is only a few degrees from the horizontal, but for the finer sizes (100μ) inclinations up to 30° from the horizontal are required. It is desirable that the particles roll over as many times as possible; therefore, a disk 30 or 40 in. in diameter would be desirable for particles larger than 1,000 μ. For the larger spheres, a disk made of ordinary window glass is an acceptable material for the separation. No difficulty is experienced in cutting it to the desired shape, as it need not be perfectly round. It can be fastened to the turntable by means of a very viscous stopcock grease. For the smaller particles, glass has a serious disadvantage in that it rapidly builds up static electric charges. A polished copper plate is generally more satisfactory, however, and in these experiments a polished copper plate

[4] Suitable beads have been obtained from: Cataphote Corp., Toledo, Ohio; Potters Bros., Inc., Ozone Park, N. Y.; Minnesota Mining & Manufacturing Co., St. Paul, Minn.

FIGURE 2. *Apparatus employed to separate spheres from the original mixture.*

one-sixteenth in. thick was used on particles smaller than about 500 μ.

The particles were fed onto the rotating disk in a thin stream. For the finest sizes the number rate of feed was quite large, and a 2-mm glass stopcock made a suitable gate. For the larger sizes only three or four pieces at a time could be fed without undue interference. A stopcock is unsuited at this low rate, and instead a cardboard tube with a notch in one side was supported to just touch the surface of the plate. The motion of the plate beneath the tube caused the particles to roll out of the notch in the tube one layer high and three or four wide (depending on the width and height of the notch). A gentle blast of air was directed into the stream of particles immediately after they were fed onto the plate. This dislodged any that stuck behind a nonspherical piece and started all particles rolling.

The spherical particles immediately rolled off the plate into a suitable hopper, while the nonspherical particles either did not roll at all or rolled more slowly or in curved paths and were carried by the turning disk and fell into the discard hopper. A strong blast of air was used to dislodge the particles that did not roll. Figure 3 shows the spherical particles, and figure 4 the discarded particles. About 10 lb of 74 to 149 μ (No. 100 to No. 200 sieves) material was separated in 20 hours on the apparatus described. About 5 percent of this particular material was discarded. In some lots, particularly in the larger sizes, 50 percent was discarded. The larger sizes separated more quickly.

Measurements of the sphere diameters showed that on the average the major and minor axes of the projections of the spheres differed by more than 2 or 3 percent only in 4 percent of the beads. Only one

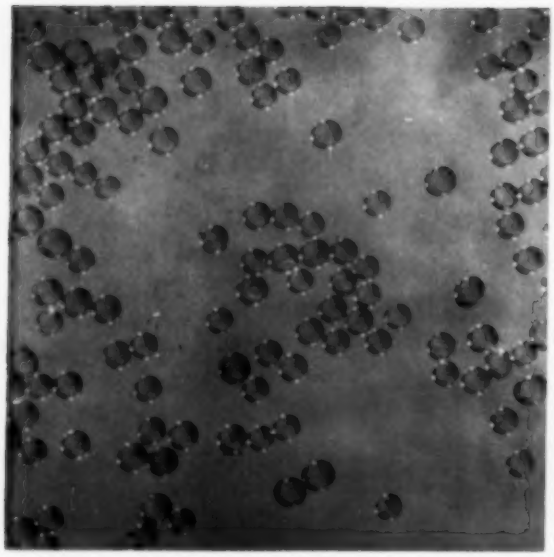

FIGURE 3. *Spherical particles separated from mixture.*

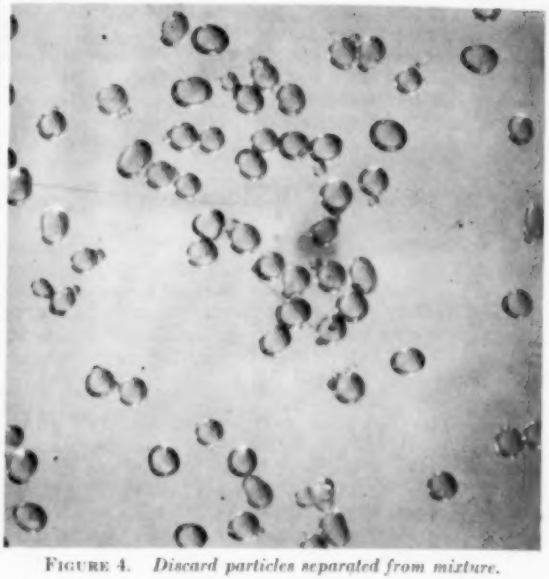

FIGURE 4. *Discard particles separated from mixture.*

bead in 14,000 was observed whose major axis was more than 1.5 times the minor axis. At least 90 percent of the beads could be considered spherical within the accuracy of the measurements.

3.2. Continuous Size Distribution

In order to obtain spheres of a continuous size distribution the material selected as spheres was carefully sieved into the closest sieve fractions ($\sqrt[4]{2}$ series), and then equal weights of each fraction were used in the final mixture. This procedure produces a logarithmic particle size distribution. This distribution was chosen because the precision of the measurement of the sieve openings is the same for all sizes.

The details of the manufacturing process for these glass beads were not known. Various lots as received from the manufacturers were found to contain a discontinuous distribution of particle sizes. It is not known whether this resulted from the manufacturing process or from a subsequent particle size separation. For example, one lot of spheres was examined in which the 350- to 500-μ sieve fraction (No. 45 to No. 35) consisted entirely of spheres ranging from 350 to 400 μ and from 440 to 500 μ. There were no spheres at all in the size range 400 to 440 μ. The No. 40 sieve has a nominal opening of 420 μ, and this lot consisted of equal weights of No. 35 to No. 40 fraction and No. 40 to No. 45 fraction. The sieves indicated a smooth continuous particle size distribution, but closer measurement revealed the discontinuity. For this reason it was necessary to obtain spheres from several manufacturers in different lots and to mix them so as to obtain a fairly continuous particle size distribution. The continuity was checked by withdrawing a sample and applying a condensed version of the calibration procedure to be explained in a later paragraph. The use of a mixture of many different lots of spheres produces a calibration curve with many minor fluctuations.

4. Preparation of Samples

A convenient total weight of spheres in the final calibrated sample is about 100 g. The total number of samples prepared in lot 3 was 256 (equal to 2^8) which required about 56 lb of glass spheres having a continuous range of sizes in the proper proportions. After lot 3 had been assembled and the preliminary check calibration indicated that the particle size distribution would be satisfactory, the individual samples were prepared. The "Boerner Sampler" [6] was used as the sample reduction device.[5] It is a riffle-type apparatus with a funnel, gate, and chute attached above the compartments, which are arranged circularly. The combination of gate and chute makes it impossible to feed too fast or to feed at the wrong angle. It has been found to give at least as good results as any known sample-reducing device or technique. As an additional precaution to neutralize any errors of the sampling device, careful attention was paid to the side the sampler from which the sample emerged. Although 256 samples were desired, 512 samples were first made; these were recombined in pairs so that the final sample represented equal quantities of material from each side of the sampler. Figure 5 illustrates the process for only four samples.

[5] Acknowledgment is gratefully made to Lawrence Zeleny, Grain Branch, Production and Marketing Administration, U. S. Department of Agriculture, for the loan of these samplers.

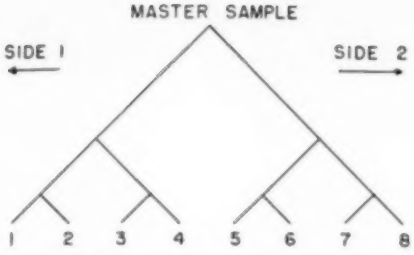

SAMPLE NO.	TIMES FROM	
	SIDE 1	SIDE 2
1	3	0
2	2	1
3	2	1
4	1	2
5	2	1
6	1	2
7	1	2
8	0	3
1 PLUS 8	3	3
2 PLUS 7	3	3
3 PLUS 6	3	3
4 PLUS 5	3	3

FIGURE 5. *Method employed to subdivide mixture of spheres into individual calibration samples.*

4.1. Selection of Samples for Calibration

It was recognized that the essential problem in calibration was adequate sampling. The spheres were divided into 256 samples by the best means available, but it must be admitted that all 256 samples may not be identical. Every twenty-fifth sample in the orderly arrangement of numbers given to the samples was chosen as a sample of the 256, making 10 in all. Each of these 10 samples contain approximately 10 million spheres, therefore, they must be further sampled to obtain a practical number small enough to measure. Because spheres of approximately the same size do not tend to segregate and present an easier problem of measurement, each of the 10 samples was separated into 14 sieve fractions.

The spheres for the actual measurement were mounted on a gelatine-coated microscope slide. In order to make sure that an adequate sample was obtained from each sieve fraction, four different slides were prepared, each slide representing particles from a different portion of the sample container. Twenty-five particles chosen at random from each slide were measured. A total of 1,400 particles in each sample was measured; altogether 14,000 particles were measured for the 10 samples.

4.2. Measurement of Diameters

The apparatus for the measurement consisted of a projection microscope with its accompanying light source and screen. The measurements were made on the projection of the image of the particles on the screen. The magnifications and projection distances were arranged so that the projections of the particles were between 6 and 30 cm in diameter. Two different microscope objectives were used, 16 and 32 mm, according to the magnification desired. The ocular was 7.5 power with a scale mounted inside. The measurements were made in air. A carbon arc and condenser lens system were used for illumination. The magnifications were checked at frequent intervals throughout the measurements by the use of two different stage micrometers. Both of these stage, micrometers have been calibrated at this Bureau and the observations obtained are accurate to within 1 μ.

In order to speed the measurement, a scale was drawn on a separate piece of paper that could be moved about the screen. The distance between the microscope and the image was adjusted so that the graduations on the hand scale exactly coincided with the projected scale in the eye piece. The hand scale could then be moved about, and several heads near the center of the screen could be measured very rapidly. Two people working together measured 25 particles in about 2 minutes. Counting the time required for changing slides, preparing samples, and relaxation to prevent eyestrain, 300 or 400 particles were measured per hour. When nonspherical particles were encountered, the minimum diameter was measured. This was done because it was desired to know the size of the hole through which a particle passes rather than the average size of the particle.

The individual diameters were measured to the nearest 2 to 5 percent, depending upon the part of the scale in use. More precise measurements could have been made. However, since sampling rather than measurement is the factor that limits the accuracy, greater precision was unnecessary and would have greatly lengthened the subsequent work of computation. As it was, 88 points were obtained in the range 60 to 1200 μ, averaging about five points within the range between each pair of sieves of the $\sqrt[4]{2}$ series.

5. Computation

The measurements of the diameter of each sphere were recorded in terms of the projected scale reading. Since it was desired to calculate the weight fraction finer than each size, the first step was to determine the diameter frequency distribution within the 100 spheres representing one sieve fraction of one sample. The actual diameter for each size was evaluated by multiplying the scale reading by the magnification factor. These computations give a number-size distribution. On the assumption that all the particles were of the same density and same shape, the weight is proportional to the number of particles and to their diameter cubed. The weight fraction of spheres of diameter, d, in the sieve fraction thus becomes $nd^3/\Sigma nd^3$. If w is the weight of the sieve fraction and Σw the total weight of the sample, then w/Σ w is the weight fraction of the sieve fraction in the total sample. The weight fraction (f) of spheres of diameter d in the total sample is

$$f=\frac{nd^3}{\Sigma nd^3}\times\frac{w}{\Sigma w}.$$

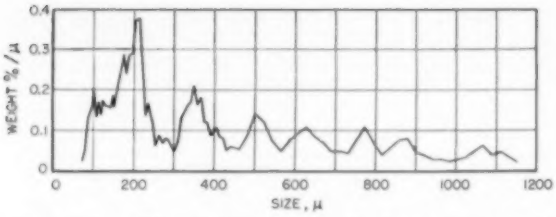

FIGURE 6. *Differential particle-size distribution curve of mixture of spheres.*

Calibrated glass spheres, lot 3.

5.1. Sample Computation

Typical data are given in table 1 for one sieve fraction of one sample. Each diameter recorded in table 1 is the mean of the size range; for example, measurements between 1.875 and 1.925 are recorded as 1.90. The frequency distribution, diameters, and the computations leading to the weight fractions are given in table 2.

The differential type of particle size distribution (expressed by weight fraction per unit size range as a function of size) is obtained by dividing each f by its corresponding size range. The integral type of particle size distribution (expressed by weight fraction finer as a function of size) is obtained by summing the f's. The particle size associated with the sum of the fractions finer is the smaller limiting diameter of the size range. This is in contrast to the mean of the size range used in the above expression for f and in the differential type of particle size distribution.

These computations were repeated for each fraction of the ten samples, and the values were averaged to obtain the final calibration. The calibration is given graphically in figures 6 and 7.

5.2. Evaluation of Sieve Opening

In order to evaluate the sieve opening with a sample of the spheres, the entire sample is placed on the sieve or sieves in question. The sieves are shaken with the calibrated spheres in the same manner as will be used with the unknown material. The spheres are then carefully brushed from each sieve and the weight fraction finer than each sieve evaluated. The effective size of the sieve is then read directly from the calibration curve (fig. 7). Care must be exercised to avoid loss of the spheres in order that the sample can be used again. Expeience has shown that the fines are most easily lost; therefore, if the total weight of the sample decreases slightly with repeated use, it may be assumed that the loss is in the finest sizes. The particular operation in which there is most chance of losing particles is the transfer from the sieve to the weighing container. The loss of particles in this operation can be minimized by inverting the sieve into a deep funnel and removing the contents with a stiff brush. The stem of the funnel should fit snugly into the receiver.

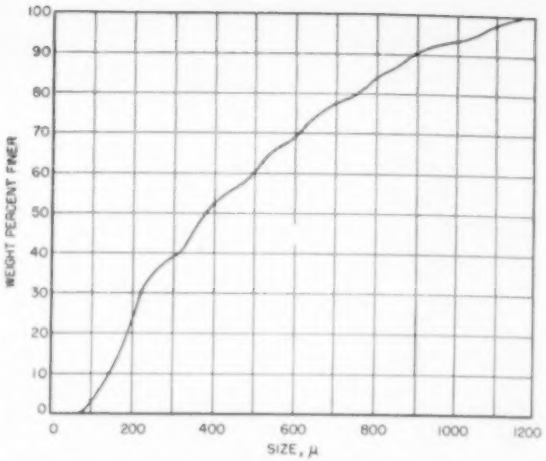

FIGURE 7. *Integral particle-size distribution curve of mixture of spheres.*

Calibrated glass spheres, lot 3.

TABLE 1. *Typical data obtained for observations of particle diameters*

Measured diameters of individual particles on microscope slide—			
1	2	3	4
2.00	1.80	1.95	1.90
2.05	1.95	1.85	1.70
1.80	1.85	2.10	1.80
1.80	1.85	1.85	1.75
1.80	1.85	1.75	1.80
1.90	1.80	1.75	1.80
1.95	1.80	1.90	1.85
1.75	1.80	1.86	1.80
1.90	1.90	1.90	1.80
1.97	1.80	1.95	1.85
2.05	1.80	2.00	1.90
1.90	1.85	1.80	1.80
2.05	1.90	1.90	1.95
1.80	1.85	1.65	2.00
1.75	1.80	1.90	1.80
2.00	2.00	1.75	1.75
2.00	1.80	1.95	1.70
1.80	1.90	1.75	1.85
1.85	1.85	1.80	1.80
2.00	1.85	1.85	1.95
1.90	1.90	1.95	2.05
1.80	1.80	1.85	1.95
1.85	1.90	1.80	2.00
1.85	1.85	1.85	1.75
1.80	1.90	1.90	1.85

Identification number of sample: 100
Sieve fraction: through 20 on 25
Weight of fraction: $w = 8.78$ g
Total weight of sample: $\Sigma w = 106.51$ g
Magnification factor: 1 unit = 419 μ

5.3. Application to Sieve Analysis

One of the most disturbing features of sieve analyses is the inability to obtain the same results with the same sample using different sets of sieves that have been considered identical. The small variations in the sieve openings inherent in the manufacture of the sieves are the cause of this trouble. In order to

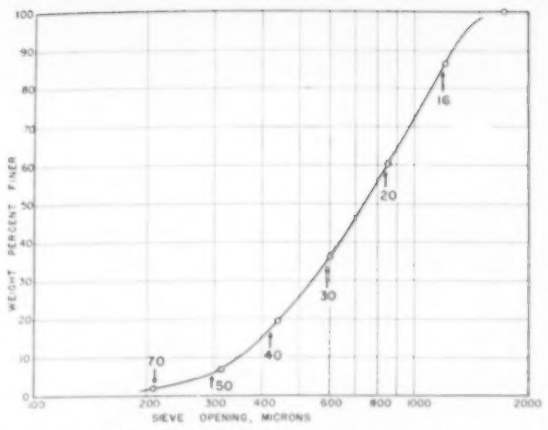

FIGURE 8. *Corrections of sieve analysis to nominal sieve opening, bone char 32; arrow indicates nominal sieve opening.*

TABLE 2. *Computation of weight fraction from measured diameters of 100 particles*

Measured diameter, scale units	Diameter, d	Number, n	d^3	nd^3	f
	μ				
2.10	879.9	1	6812×10^3	6812×10^3	0.0011
2.05	859.9	4	6337	25348	.0040
2.00	838.0	8	5885	47080	.0074
1.95	817.1	9	5454	96166	.0151
1.90	796.1	17	5045	85765	.0135
1.85	775.2	20	4658	93160	.0146
1.80	754.2	29	4290	124410	.0195
1.75	733.3	9	3942	35478	.0056
1.70	712.3	2	3614	7228	.0011
1.65	691.4	1	3304	3304	.0005
		$\Sigma=100$		$\Sigma=524751$	$\Sigma=.0824$

$$\frac{w}{\Sigma w}=\frac{8.78}{106.51}=0.0824 \text{ (see table 1)}$$

$$f=\frac{nd^3}{\Sigma nd^3}\times\frac{w}{\Sigma w}=\frac{nd^3}{524{,}751\times10^3}\times0.0824=1.5709\times10^{-12}\,nd^3$$

reduce the results of any sieve analysis to that which would be obtained if sieves with nominal sized openings were used, it is only necessary to plot the results as cumulative percentage finer (or coarser) as a function of the calibrated opening of the sieve. Such a plot for a bone char (char 32) is shown in figure 8. From this curve the cumulative percentage finer (or coarser) than the nominal openings can be obtained (at points indicated by arrows); hence the corrected sieve analysis may be calculated. In this way sieve analyses made at different laboratories with different sets of sieves may be reported with reference to the same sieve openings.

6. Evaluation of Errors

The errors inherent in the method of measuring the effective size of the openings of testing sieves by means of calibrated glass spheres arise from three sources. First, a *dividing error* occurs when the samples are prepared. Second, a *sieving error* occurs when the samples are used. Third, a *calibration error* occurs in the sampling and measuring involved in the calibration process. The magnitude of each each of these errors has been determined and, also, their effect on the over-all reproducibility and accuracy of the method.

The dividing error can be considered in two parts. One is due to the inaccuracies of the sample-reducer, and the other arises from the use of only a relatively limited number of particles. It is possible to estimate the error of the latter by the application of statistics. If n is the number of particles of one size remaining in the final sample after three or more separations on the sample divider, then according to statistical theory (appendix 1), the standard deviation associated with this number is approximately $\sqrt{n}$. The error in the determination of size of particle from this cause can be readily evaluated (appendix 2) and is listed in table 3.

TABLE 3. *Errors in the measurement of effective openings of testing sieves by means of glass spheres*

U. S. Standard Sieve No.	Standard deviation		
	Dividing	Sieving	Calibration
	Microns	*Microns*	*Microns*
18	3.56	2.6	2.8
20	1.40	3.5	2.0
25	1.42	2.3	1.5
30	0.74	1.2	1.24
35	.30	2.4	1.14
40	.46	2.0	1.07
45	.15	3.1	0.98
50	.23	0.7	.88
60	.10	1.6	.79
70	.04	1.2	.69
80	.04	0.8	.66
100	.03	.3	.65

Because of the good construction of the sampling device and the additional precautions that were observed, it is reasonable to assume that the error arising from the inaccuracies of the sampling device is small. Indeed, it can be shown that this error is so small that it exerts no appreciable influence on the final sum of all errors (appendix 3).

The error due to sieving depends upon the particular sieving method employed. In order to obtain some idea of the error that might be encountered, one sample was sieved nine times, using the particular procedure used in this laboratory.[6] The standard deviations representing the variations among these nine sievings are also listed in table 3. These variations are due to sieving alone because the same sample, the same sieves, and the same calibration curve were used.

The variation among the calibrations of the ten different samples is a measure of the sum of the dividing and calibration errors. The dividing error has already been determined and can be subtracted [7] from the sum to yield the calibration error alone (appendix 4). This error is also listed in table 3.

[6] The sieves were shaken for 8 min in an old style (two eccentric) Ro-Tap operating at 117 taps/min.

[7] The variance (standard deviation squared) is additive.

It is noted that each of the errors are of the same order of magnitude, indicating that any additonal precautions in the sample dividing or calibration would have been wasted effort unless some method of sieving with less error could have been found.

The accuracy and reproducibility of the glass sphere method of calibrating testing sieves are tabulated in table 4. The values listed are the maximum variations that might reasonably be expected and are taken as three times the standard deviations. The accuracy is measured by the sum [7] of the calibration and dividing errors and is an indication of the precision with which the size of the spheres is known.

There are two types of reproducibility. The variation to be expected when the same sieve is calibrated several times with the same sample of glass spheres is that due to the sieving error. If different samples of glass spheres are used, then the dividing error is included also.

As a general summary in regard to errors it can be stated that both the accuracy and reproducibility of a glass sphere calibration is about 1 percent of the size of the sieve opening. This is significantly better than the 2- to 7-percent variation allowed in the present specifications for testing sieves. Even more important, however, the glass spheres measure the effective opening (for particles not too far from spherical) rather than the average opening.

TABLE 4. *Reproducibility and accuracy of the calibration process*

The values listed are the maximum variation to be expected (three times the standard deviation)

U. S. Standard Sieve No.	Nominal opening	Reproducibility		Accuracy
		Using same calibration sample	Using different samples	
	Microns	*Microns*	*Microns*	*Microns*
18	1,000	7.8	13.3	13.5
20	840	10.5	11.4	7.5
25	710	6.9	8.1	6.3
30	590	3.6	4.2	4.4
35	500	7.2	7.3	3.5
40	420	6.0	6.1	3.4
45	350	9.1	9.1	2.9
50	297	2.1	2.2	2.8
60	250	4.8	4.8	2.4
70	210	3.7	3.7	2.1
80	177	2.4	2.4	2.0
100	149	0.9	0.9	1.9

7. References

[1] F. G. Carpenter and V. R. Deitz, Methods of sieve analysis with particular reference to bone char, J. Research NBS **45,** 328 (1950) RP2143.

[2] Standard specifications for sieves for testing purposes, ASTM E11–39, ASA No. 23.1–1939, NBS Letter Circular 584 (1940).

[3] Standard specifications for sieves, NBS Letter Circular 584 (1940).

[4] M. Weber and R. F. Moran, A precise method for sieving analyses, Ind. Eng. Chem., Anal. Ed. **10,** 120 (1938).

[5] G. Fagerholt, Particle size distribution of products ground in tube mill (in English) **227** pp. (G. E. C. Gads, Copenhagen, Denmark, 1945).

[6] E. G. Boerner, A device for sampling grain, seeds, and other material, U. S. Dept. of Agriculture Bulletin No. 207 (1915).

[7] E. L. Gooden and R. L. Updike, Preparation of standard powders for reference in particle size measurement, Ind. Eng. Chem., Anal. Ed. **18,** 802 (1946).

8. Appendix 1

Acknowledgment is made to J. M. Cameron and John Mandel of the Bureau for the derivation leading to the following results.

A large number of particles is split into two groups as evenly as possible. Each of these groups is again divided into two groups as evenly as possible, and so on. After k such splitting operations, 2^k subgroups are formed.

If there were N particles in the original aggregate, one would expect each subgroup to have $N/2^k=n$ particles. But, due to randomness in the partitioning, the actual number of particles observed will vary about this expected number. As few as zero could be found or as many as N.

Assuming that each particle has an equal chance of going into either group at each partition, the probability that a particle be found in a particular subgroup is $1/2^k$, and the numbers of particles in the subgroups will be binominally distributed. From the mathematics of the binomial distribution, the standard deviation of the number of particles found in the various subgroups is

$$\sigma=\sqrt{N\frac{1}{2^k}\left(1-\frac{1}{2^k}\right)}=\sqrt{n\left(1-\frac{1}{2^k}\right)}.$$

It may be noted that for values of k greater than 3 the value of the factor in parenthesis is practically one, hence, the standard deviation becomes

$$\sigma=\sqrt{n} \qquad (\text{for } k>3).$$

9. Appendix 2

In weight units the standard deviation is $\sigma_w=\sqrt{n\rho sd^3}$, where ρ is the particle density (2.6 g/cm³ for glass), s is the shape factor ($s=\pi/6$ for spheres), and d is the particle diameter. If w is the weight of a fraction of particles all of the same size then the number of particles is obtained by

$$n=\frac{w}{\rho sd^3}.$$

The standard deviation in weight units thus becomes

$$\sigma_w=\sqrt{\frac{w}{\rho sd^3}}\,\rho sd^3=\sqrt{w\rho sd^3}.$$

The weight fraction is obtained by dividing by the total weight of all the fractions.

$$\sigma_f=\frac{\sigma_w}{\Sigma w}=\sqrt{\frac{w\rho sd^3}{\Sigma w}}.$$

Since the error is small, to a first approximation the ratio of error in weight fraction units to the error in size units is equal to the slope of the calibration curve at that point. That is, $\sigma_f/\sigma_s=df/ds$ where df/ds is the slope of integral type particle size distribution curve (fig. 7) and is equal to the differential particle size distribution given in figure 6. The standard deviation in size units can thus be expressed in terms of easily measurable quantities as

$$\sigma_s=\sqrt{\frac{w\rho sd^3}{\Sigma w}}\Big/\frac{df}{ds}.$$

This quantity is tabulated in table 3 for each of the sieve fractions.

10. Appendix 3.

In the course of the calibration procedure the 10 samples were all sieved. Nine of these samples were sieved with the same set of sieves and in the same manner. The variance among these sieve analyses is listed in table 5, column 5, and is the sum of dividing and sieving errors. No calibration error is involved because all sievings are referred to the same calibration curve. According to statistical theory, when errors are independent, their variances (standard deviation squared) are additive. In table 5 are listed the variances due to dividing error (col. 2), sieving error (col. 3), and their sum (col. 4). The sums are compared to the measured combined errors from the nine different samples (col. 5) by taking the ratios, and applying the F test, (col. 6). In no case does the value of F indicate a highly significant difference between the two. On one-half the sieves column 4 is larger, and on the other half column 5 is larger. Altogether, this indicates that there is really no difference between the two columns.

TABLE 5. *Variance due to dividing and sieving*

U. S. Standard Sieve No.	Dividing	Sieving	Dividing +sieving calculated	Dividing +sieving observed	F* Col. 5 / Col. 4
1	2	3	4	5	6
	μ^2	μ^2	μ^2	μ^2	
18	12.7	6.9	19.6	30.8	1.57
20	1.96	12.5	14.5	16.0	1.11
25	2.02	5.3	7.3	19.2	1.40
30	0.55	1.4	2.0	7.8	3.94
35	.09	5.9	6.0	3.6	0.60
40	.21	3.9	4.1	2.9	.70
45	.02	9.3	9.3	2.3	.24
50	.05	0.51	0.56	1.96	3.50
60	.01	2.50	2.51	1.00	0.40
70	0	1.53	1.53	0.49	.32
80	0	0.62	0.62	.25	.40
100	0	.09	.09	.16	1.78

* For 8 and 8 degrees of freedom, F at 1-percent level = 6.03, F at 5-percent level = 3.44.

Column 5 includes errors due to inaccuracies in the sample divider, while column 4 does not. This indicates, therefore, that the error due to the sample divider is so small as to be negligible.

11. Appendix 4

The variance among the calibrations of the 10 different samples is a measure of the sum of the dividing and calibrating errors. It is listed in column 2 of table 6 and is composed of two parts, one due to dividing the samples (col. 3) and the other due to the calibration procedure. A subtraction yields the variance due to calibration alone (col. 4). This is the variance among the 10 samples. The variance of the mean from the true value is one-tenth of the variation among the 10 samples and is listed in column 5. The sum of the dividing variance and calibration variance of the mean is listed in column 6. This is a measure of the precision and in this case, considering the whole procedure, it is a measure of the accuracy.

TABLE 6. *Variance due to dividing and calibration errors*

U. S. Standard Sieve No.	Dividing + calibration measured	Dividing	Calibration	Calibration variance of the mean	Dividing + calibration variance of the mean
1	2	3	4	5	6
	μ^2	μ^2	μ^2	μ^2	μ^2
18	80.4	12.7	77.7	7.77	20.5
20	43.6	2.0	41.6	4.16	6.2
25	25.0	2.0	23.0	2.30	4.3
30	16.9	0.6	15.4	1.54	2.1
35	13.0	.1	12.9	1.29	1.39
40	11.6	.2	11.4	1.14	1.34
45	9.6	.0	9.6	0.96	1.96
50	7.8	.1	7.7	.77	0.87
60	6.3	0	6.3	.63	.63
70	4.8	0	4.8	.48	.48
80	4.4	0	4.4	.44	.44
100	4.0	0	4.0	.40	.40

WASHINGTON, November 24, 1950.

Journal of Research of the National Bureau of Standards Vol. 47, No. 3, September 1951 Research Paper 2239

Precise Topography of Optical Surfaces[1]

James B. Saunders

The unit of length usually used in measuring optical surface features, by interference of light, is one-half the wavelength of the monochromatic light that is used. A method is described in which the unit of length is a much smaller fraction of the wavelength. Topographic maps of optical surfaces are made in which the contour interval is less than one-thirtieth the wavelength. The smallness of the unit depends upon the quality of the surfaces. Irregularities, too small to be detected with the Fizeau or two-beam fringes, are made to appear very prominent. Surface markings, caused by the final polishing actions, can be made to stand out in bold relief.

The accuracy of results that may be obtained with any type of interferometer depends upon the accuracy with which one can locate a line in the fringe field, along which the order of interference is constant. The intensity of light in a direction normal to these lines, in a set of two-beam or Fizeau [2] type of interference fringes, is a smooth mathematical function without abrupt changes, whereas for multiple beam or Fabry-Perot [3] type fringes it has sharp maxima and minima for transmitted and reflected light, respectively. The accuracy attainable with the two types of fringes is roughly proportional to the ratio of fringe separation to fringe width, the fringe width being defined here as the width at one-half maximum intensity.

Accurate contour maps of one surface relative to a standard surface of known shape are obtained by photographing the interference fringes, produced by these two surfaces, with monochromatic light. The contour intervals are one-half wavelength. As in geodesy, the smaller the contour interval the more detail is revealed in the contour map and the narrower the lines the more detail is revealed along the line. With broad fringes, of the two-beam type, irregularities of several hundredths of a wavelength can be completely hidden in or between the dark broad lines. An irregularity of several tenths of a wavelength can be completely invisible if it falls within the area between two adjacent Fabry-Perot fringes that appears uniformly illuminated. The one-half wavelength interval is, therefore, inadequate for representing local irrregularities on high-quality optical surfaces.

This paper describes a procedure whereby very narrow fringes are used for producing contour maps of optical surfaces with contour intervals of a small fraction of a wavelength. These intervals can be made as small as the narrowness of the fringes will permit. If m resolved fringes can be equally spaced between two of the original fringes, the separation of which corresponds to one-half wavelength or to one order of interference, then the contour intervals will be $[1/2(m+1)]\lambda$. Values of m as large as 19 have been used, for which the intervals are $\lambda/40$.

The usual procedure in precision measurements on glass optical surfaces is to place the unknown close to and almost parallel to a standard surface of known shape, with a thin air wedge between, and to observe the fringes produced by the interference of monochromatic light reflected normally from these two surfaces. Figure 1 shows a set of two-beam interference fringes, observed by reflection with a Fizeau viewing instrument, which one might have under observation for the purpose of measuring the deviation of an unknown surface from a standard plane surface. The orders of interference corresponding to each fringe, although not usually known, are indicated by the numerals. The exact position of the lines that represent the loci of integral orders of interference, are only known to lie somewhere within the darker portion of the fringes. This locus for fringe number 3 is indicated by the narrow solid line. Usually, as will be shown later, these lines are not as smooth [4] as the much broader fringes appear to be. The assumption that this line lies at the center of the dark fringe is usually false and, consequently, results based on this assumption are in error by the amount of displacement of the line from the center; which can amount to over a tenth of the separation between adjacent fringes. Even if one could locate the lines of integral orders, he would still be unable to measure the change in order of interference along a straight line such as the one shown dotted in figure 1, for the purpose of surface measurement. The change in order of interference along this straight line is an accurate measure of the deviation of the unknown surface from a plane, but if the shape of the surface between the fringes is unknown one has no way of determining the fractional orders of interference at points on this straight

[1] This work was done as part of a research project sponsored by the Air Force. The paper was presented at the March 1950 meeting of the Optical Society of America (Abstract, J. Opt. Soc. Am. **40**, 258 (Apr. 1950)). Since then the author's attention has been called to a paper by Takemara Sakurai and Kôrô Shishido at the Research Institute of Scientific Measurements, on "Test of an optical flat by the Fabry-Perot etalon" and published in the Scientific Report of the Research Institute, Tôhoku University, [A], **I**, No. 1 (May 1949).

[2] Fizeau, Compt. rend. **54**, 1237 (1862).

[3] C. Fabry and A. Perot, Ann. Chim. Phys. **12**, 459 (1897).

[4] The irregular serrations along the edges of the fringes are a good indication of the shape of the lines of constant orders. In fact, the location of lines of constant order (although not integral) are most accurately locatable along the margin of the fringes where the density gradients are a maximum. This is the most accurate means, known to the author for locating lines of integral differences in order of interference for surface measurements.

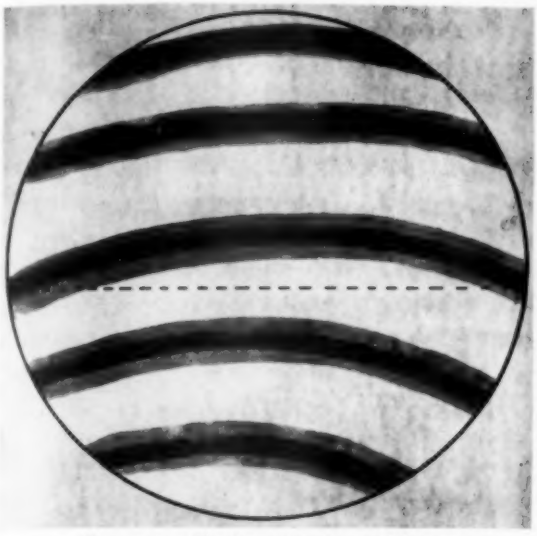

FIGURE 1. *Two-beam interference fringes.*

line that are not also on the lines of integral orders. Linear interpolation, for points not on a fringe, can be in error by several tenths of an order. The measurement of deviations of a surface from a plane, by measuring the change in order of interference along this line, is in error both from the inability to locate the lines of integral orders of interference and also from interpolation based on the false assumption that the order of interference varies linearly with the displacement of the point from the adjacent fringes. Unless a fringe passes through the center of a surface, the deviation of the surface at this point, relative to others, cannot be accurately measured.

The accuracy of measurements on the deviations of the unknown surface from an arbitrarily chosen reference plane, along any one of the lines of integral orders such as the narrow solid line in fringe 3, is limited only by the accuracy with which the line can be located. The deviation of the surface at any point on this line, from a plane through the indicated straight line (which is coincident with neither of the reflecting surfaces but intersecting the unknown surface at the two ends of fringe 3) and making an angle θ with the standard reference plane, is equal to the product of θ and the perpendicular distance of the point to the straight line where θ equals one-half the wavelength of the light used divided by the fringe separation. The fringe separation is defined as the average distance between the centers of adjacent fringes and is the separation that would be obtained if the unknown was replaced by a true plane, placed in the position of the arbitrarily chosen reference plane. The value for θ should be constant for all computations, although the observed fringes may neither be parallel nor equally spaced. The use of different values for fringe separation is equivalent to measuring deviations from different planes at various angles to the standard.

If both the standard and the unknown are coated with a uniformly thin coat of highly reflecting metal, such as silver or aluminum, the fringes in which the lines of integral orders of interference are located become narrower. The narrowness of these fringes, relative to their separation, increases with the reflectance of the surfaces and also with decreasing angle of incidence. The decrease in width of these narrow line fringes, relative to their separation, increases the accuracy of locating the lines of integral order of interference. With modern methods of metal deposition and with smooth surfaces that are almost parallel to each other, fringes may be obtained whose width, at one-half the maximum intensity, are only one-fiftieth part of their separation.[5] With such narrow fringes, deviations can be measured to better than one-hundredth of a wavelength. These narrow-line or Fabry-Perot type fringes are dark by reflected light and bright with a dark background, with transmitted light. Figure 2, A, shows a set of two-beam fringes produced by reflected light, and B shows a graph of multiple reflection fringes, formed by the same surfaces by transmitted light after applying the thin coat of aluminum. Note the increased accentuation of detail along these narrow fringes over that shown by the broad ones.

When measuring surface features to one-hundredth of a fringe, the mechanical errors in the micrometer (assuming a micrometer eyepiece to be used) and personal errors of settings become large unless the changes in order of interference with movement of the cross hair, are relatively small. This requires that the fringes have considerable separations. At least two fringes must appear on the surface in order to determine the unit of deviation of a fringe from a straight line corresponding to a known unit of deviation of the surface from a plane. This unit is usually one-half the wavelength of the monochromatic light being used. Figure 3, A, shows such a set of fringes, formed by the same surface that was used for figure 2, B. Further enhancement of detail along the fringes in figure 3, A, over those of figure 2, B, is obvious. This is partially due to the decrease in width of the fringes relative to their separation, caused by making the wedge between the plates smaller and, consequently, reducing the angle of incidence that favors the narrowing of these fringes.

In order to further enhance irregularities along a fringe and still be able to measure the magnitude of the corresponding deviations in the surface, a multiple spectral line source, such as the mercury arc for instance, may be used. Each spectral line produces its own set of fringes. If the absolute orders of interference of each and all of the fringes are known, the separation of the surfaces along the fringes is known and, consequently, the change in separation of the surfaces between two adjacent fringes of different colors is also known, although this difference in separation may be only a small

[5] S. Tolansky, Multiple-beam interferometry of surfaces and films (Oxford at the Clarendon Press, 1948).

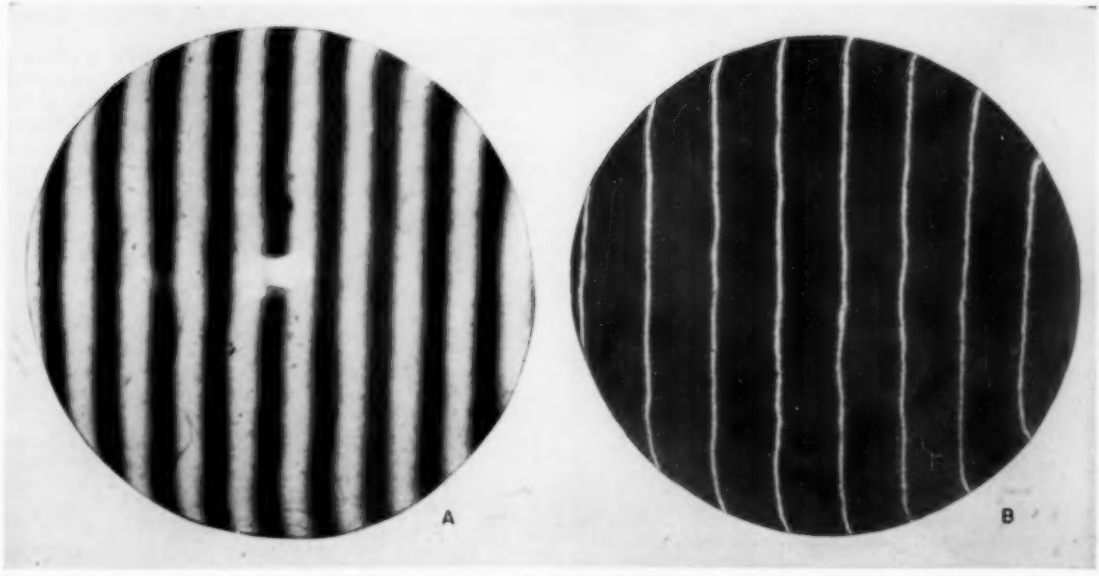

FIGURE 2. *Equal-thickness interference fringes.*

A, Two-beam fringes produced by reflected light; B, Multiple-beam fringes produced by transmitted light.

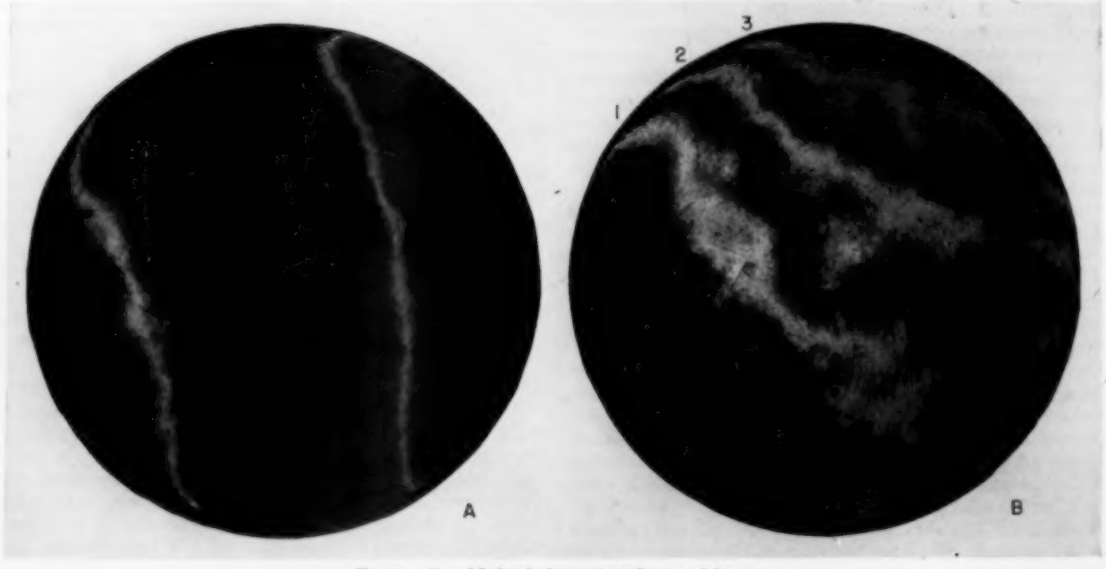

FIGURE 3. *Multiple-beam interference fringes.*

A, Single spectral line. Note increase enhancement of surface detail. B, Multiple spectral line. One order of each of three lines shown on plate. Wedge too small to include other lines. Note further enhancement of surface detail.

fraction of the unit of length, one-half wavelength. The thickness and angle of the air wedge between the surfaces may now be adjusted so that one of two or more closely spaced fringes of different color pass through the center of the surface and one or more of the others just inside the edge. The surfaces are then as near parallel as is practicable, thus favoring the attainment of the narrowest fringe possible, relative to fringe separation, and measurements may be made at all radial distances. Still greater enhancement of the irregularities is thereby attained, and two or more fringes are available for quantitative evaluation of these irregularities. Figure 3, B, shows a set of fringes, produced by a mercury source, in which the total change in order of interference across the plate is less than three-tenths of a unit ($\lambda/2=0.27\mu$).

Maximum enhancement of surface irregularities is obtained by adjusting the surfaces to as near parallelism as is possible and the separation near to some integral number of half wavelengths. If one had two plane reflecting surfaces (the existence of which is doubted by the author) these could be placed parallel to each other, which is the condition for fringes of infinite width. If the separation is now adjusted to some value in the neighborhood of where the resultant interference produces maximum variation of intensity with change in separation, then small deviations in phase, caused by irregularities of only a few angstroms, such as may be produced by the individual particles of the polishing compound, become quite visible. Figure 4 shows the abovementioned surfaces (actually both surfaces contribute equally) in which the parallelism and separation are most favorable to the revelation of small surface detail. Note the fiber-like appearance in the darker regions where maximum enhancement of detail occurs. Quantitative measurements of these finer irregularities have not yet been attempted.

The manner of determining absolute orders of interference may be described by means of figure 5 The large circularly enclosed fringe system represents a set that might be under observation. The colors of the fringes are indicated by R for red, Y for yellow, G for green, B for blue, and V for violet. The wavelengths of the light, forming the fringes, are identified usually by the color of the corresponding fringes. The small circularly enclosed fringe system represents the same fringes as those shown in the large circle. They are straight as if formed by parallel surfaces and are inserted to show the relationship between the fringes in the large circle and the lines, which correspond to fringes, in the chart above. If we assume the surfaces that form this fringe system to be extended in the direction of their decreasing separation to their line of intersection, and one could observe the fringe system in this extended area, one would find and could identify the zero order of interference for each set (color) of fringes, all of which coincide. Extending from the zero order fringe, one would observe equally spaced red fringes (assuming plane surfaces), the order of which could be identified by counting from the zero order.

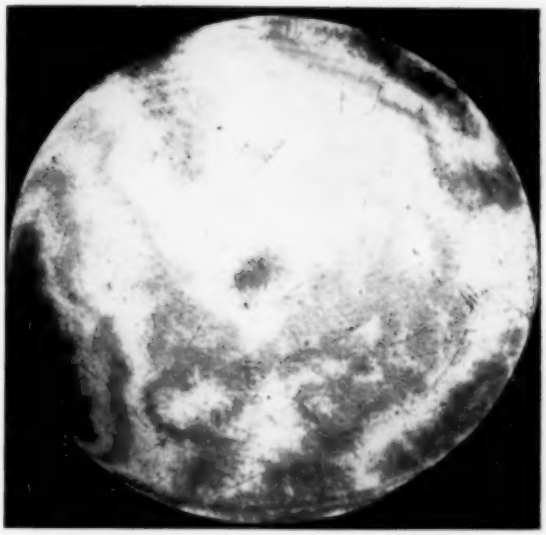

FIGURE 4. *Multiple-beam interference fringes.*

Surfaces are as near parallel as the surfaces will permit (maximum enhancement of detail). Note fabric-like marks, believed to be due to final polishing action.

Thus the numbers associated with the vertical lines indicates the order of interference for all the visible colors in the source, and their positions correspond to the positions of the fringes. One sees on this chart, in the neighborhood of 3.3-μ separation of the plates, that several fringes fall in a space corresponding to 0.12-μ increase in separation of the plates. This space corresponds to a change of only 0.36 in the order of interference for this red spectral line. If the maximum and minimum separations of the plates are adjusted to 3.2 and 3.4 μ, respectively, the particular set of fringes that correspond to the lines falling in this range on the chart can be seen on the plates. We therefore have a fringe system in which the increase in separation of the surfaces from one fringe of a given color to another fringe of a different color is a small fraction of the conventional unit, $\frac{1}{2}\lambda$, that is usually used for this type of measurement. Furthermore, the width of the bright line fringes, relative to separation of adjacent orders, is made smaller by the two surfaces being made nearer parallel than is practical when using monochromatic light. The narrower the fringes, relative to separation of adjacent orders, the more concentrated a cluster or grouping of fringes can be used, without overlapping. Figure 3, B, shows a constellation or group of fringes whose separations correspond to an increase in separation of the surfaces of 270 A from fringe 1 to 2, and 225 A from 2 to 3.

When an optical flat is placed on an unknown surface with only an air film separator, the weight of the top plate forces the air film to become relativerly thin, but the plates will not come into absolute contact at any point. Usually, small particles of dust will prevent the air film from becoming as

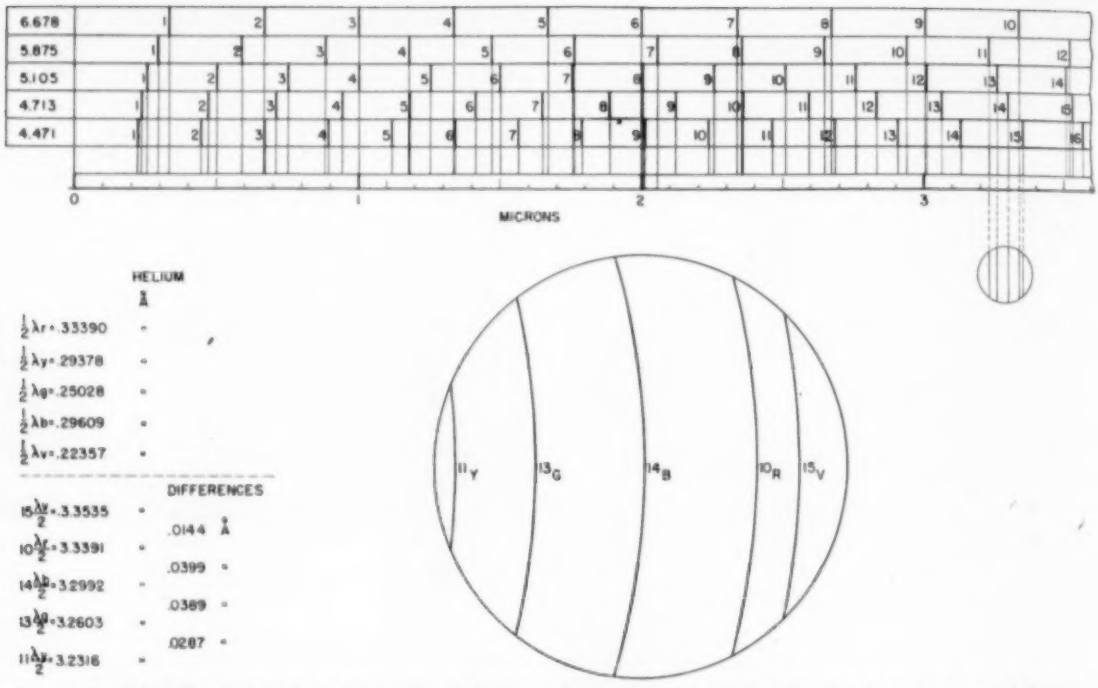

FIGURE 5. *Chart showing how the absolute order of interference is identified from the relative distribution of colored fringes produced by a multiple line source.*

thin as would be attained in their absence The usual range in thickness, for circular surfaces of 4-in. diameter and free from dust, is from 8 to 9μ. For larger surfaces this range may extend to 10μ. The range, 0 to 3.6μ, shown in figure 5 is not practical but was used for explanatory purposes only. The practical range is from 6 to 9μ and is shown in figure 6 for several different light sources. If one has access to different sources he may choose a constellation most suitable for a given film-thickness range.

A more elegant topographic map of an optical surface, relative to a standard, can be obtained by using monochromatic light and photographing the image of a given fringe in several different positions on a single film; the shift in the fringe system being accomplished by changing the optical separation of the surfaces. There are several different ways of changing the optical separation, only one of which will be described in detail. The interferometer plates are enclosed in an airtight chamber (see fig. 7) in which the pressure of the enclosed gas may be controlled at will. The collimator and collector lenses form the windows to the chamber. A gas line, connected to a manometer through a two-way stop cock, permits either compression by a compressor, or evacuation by a vacuum pump. A needle valve in the line, not shown, facilitates control of the pressure in the chamber.

According to the law of Gladstone and Dale, the index of refraction of a gas varies linearly with the density. For a constant temperature of 25° C, which was maintained during this experiment, the density is directly proportional to pressure, to a close approximation. The relation between refractive index and pressure, is $n-1=P(n_0-1)/760$ where n is the refractive index of the gas, P is the pressure in millimeters of mercury, and n_0 is the refractive index of the gas at 760 mm pressure and at 25° C.

If Δn is the change in n for a given change of ΔP in P, it may be shown that the corresponding change in order of interference, ΔN, at a point where the separation of the surfaces is L, is

$$\Delta N=\frac{2L\Delta n}{\lambda}=\frac{2L}{\lambda}\frac{(n_0-1)}{760}\Delta P.$$

From this relation one may compute the separation, L, that is necessary in order to get a chosen change in order of interference for any desired pressure range. For instance, suppose the available pressure range to be 1 atm or 760 mm of mercury and the desired change in order of interference to be one (the maximum practical change for this work), then $\Delta P=760$, and $\Delta N=1$. Consequently,

$$L=\frac{\lambda}{2(n_0-1)},$$

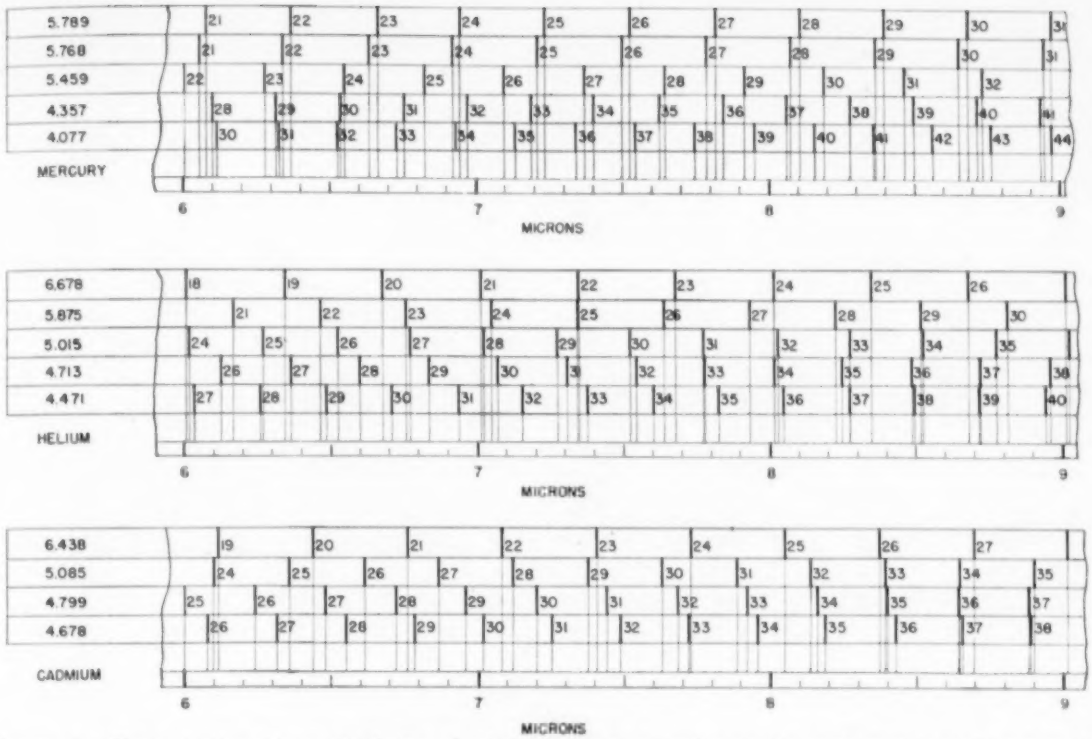

FIGURE 6. *Charts showing relative distribution of colored fringes for normal separation of plates when placed one on the other for test.*

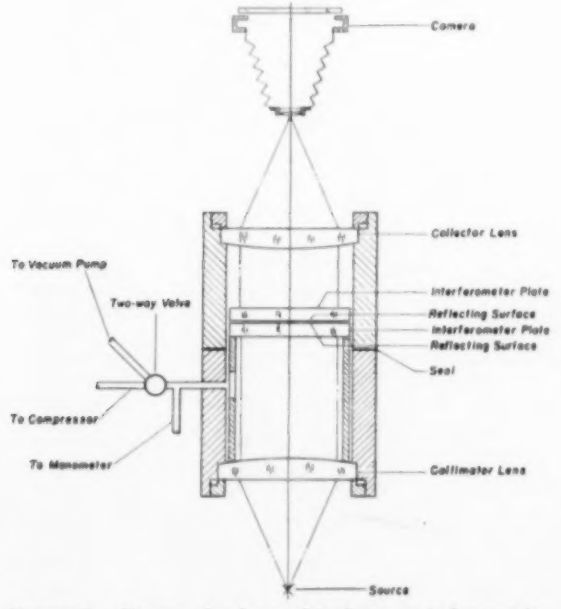

FIGURE 7. *Vacuum chamber used to change optical separation without changing the geometrical separation of two interferometer plates.*

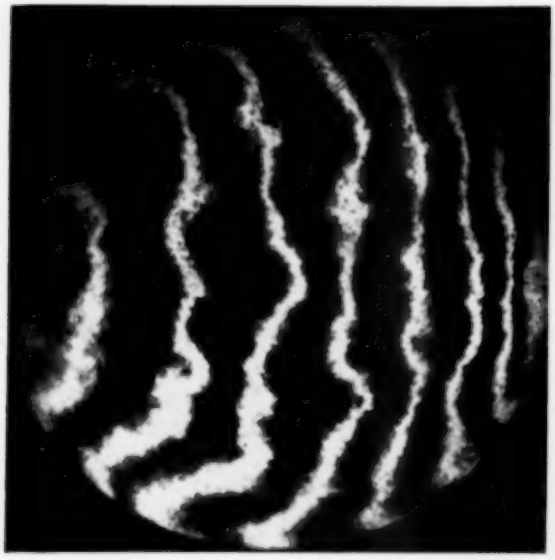

FIGURE 8. *Topographic map of one optical surface, relative to a standard, produced by photographing a given fringe (order of interference) successively, as it was moved across the plate, by controlled evacuation of air wedge between the plates.*

Total movement corresponds to a change of one-half order of interference.

FIGURE 9. *Same photograph as in figure 3, B, with inserted drawing, for surface measurement.*

If, for instance, the light to be used is the green line of mercury, for which $\frac{1}{2}\lambda = 2.7 \times 10^{-5}$ cm and $n_0 - 1$ is 2.8×10^{-4}, then L equal 0.96 mm. Consequently, with this separation, pressure range and light source, a fringe can be made to take on any position between the positions of this fringe and that of one of its adjacent neighbors at the extremes of the pressure range. If there is more than one fringe on the plate and one wishes to interpolate nine additional, equally spaced fringes, between each of the adjacent original fringes, thus completely filling the photographed field with fringes whose separations are one-tenth that of the original set, then it will be necessary to change the pressure in steps of 76 mm for nine times, or a total of nine-tenths of an atmosphere. If the wedge between the surfaces is such as to give a maximum change in order of interference of one-half, then one-half-atm change in pressure is sufficient to move the center of a fringe completely across the surface. If, for this wedge, one wishes to photograph 10 fringes on the plate, the necessary change in pressure will be nine-twentieths of an atmosphere. It is, of course, essential that this pressure range be within that available, which in this particular case is 0 to 760 mm.

Figure 8 represents a topographic map with contour intervals of approximately 170 A, or one-thirtieth of a wavelength of cadmium green light. The separation of the two surfaces was 0.82 mm, and the change in separation, in terms of interference fringes, was approximately one-half fringe (1,300 A).

To illustrate the application of these smaller-than-one-half-wavelength-unit topographic maps to quantitative determination of surface features, measurements have been made on the deviations of one of the surfaces used to produce figure 3, B, relative to the other. For this discussion one surface will be assumed a true plane (called the reference surface) and the other (called the unknown) to have all the irregularities corresponding to the irregularities shown in this fringe pattern. Lines and points have been inserted in figure 3, B, and reproduced as figure 9.

The deviations of the unknown from a true reference plane, for several points along the lines *AEB* and *CFD* have been computed and are plotted in figure 10. The chosen reference plane is an imaginary plane that passes through points *A* and *B* (consequently including all points on the straight line *AB*) and making an angle θ with the reference surface approximating the average angle between the two reflecting surfaces. The unknown surface and the chosen reference plane are made as near parallel to each other as the irregularities in the unknown will permit. The value of θ is obtained from circle *ABDC*, which is concentric with respect to the center of the plates, the straight line *AB*, and the perpendicular projections of points *C* and *D* on line *AB*. Circle *ABDC* must intersect at least two locatable lines, such as *AEB* and *CFD*, along each of which the order of interference is constant, and between which the change in separation of the reflecting surfaces is known. The line *AEB* is the lower edge of fringe 2, and line *CFD* is the lower edge of fringe 1. The change in separation of the plates between these two lines is approximately equal to that between the centers of the corresponding fringes

and, as was given previously, equal to 270 A. The magnitude of θ is taken to be $2d/(Y_1+Y_2)$, where d equals the change in separation of the plates between fringes 1 and 2, Y_1 equals the normal distance of the point C from the straight line AB, and Y_2 equals the normal distance of point D from AB. This choice for θ is entirely arbitrary and in no way affects the computed shape of the unknown surface.

To correlate the data shown in figure 10 with the topographic map (fig. 9) from which it was derived, the designated points in figure 9 are labeled likewise in the graph. Thus, the ordinate of point E in figure 10 is the deviation of the unknown at point E of figure 9. The lower branch of solid curve $2R$, figure 10, represents deviations along the right-hand portion of line 2 figure 9, and the upper branch, $2L$ having the circled points, corresponds to the left-hand portion of this line.

These measurements are not limited to points along a single fringe or line, but may be made at any point along any fringe that appears on the photograph. The deviation of the unknown from the chosen reference plane, at a point on any other line, such as point F on line 1, is equal to $Y_4\theta - Nd$, where Y_4 is the normal distance between point F and line AB, and N is the difference in order of interference between F and any point on line 2. Thus, measurements may be made at all points along each and every contour line shown.

The plot shown in figure 10 does not give any better idea of the shape of the unknown surface than the contour map from which it was derived. The values are, however, better defined numerically.

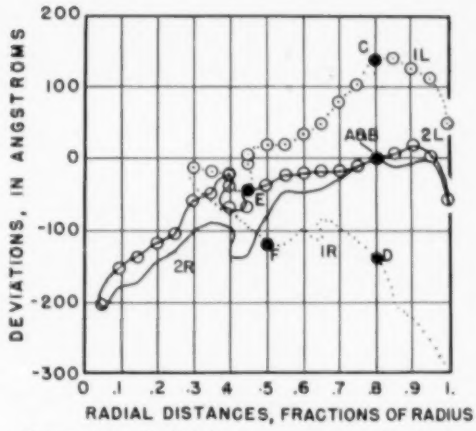

FIGURE 10. *Radial distances, fractions of radius.*
Radius equals one-half diameter of plates.

The failure of all computed points to fall on a single smooth curve indicates that the unknown surface is not a figure of revolution about its center. The appearance of more than two values of a given radial distance and on a single line is due to local depressions or elevations. The irregular shape of the curves also indicates the degree of local irregularities in the surface. These local irregularities represent deviations approximating 50 A, in some cases.

WASHINGTON, January 2, 1951.

Journal of Research of the National Bureau of Standards Vol. 47, No. 3, September 1951 Research Paper 2240

Hydrodynamics of Cathode Films

Garbis H. Keulegan

A hydrodynamical theory of the cathode diffusion layer based on the assumption of a uniform density reduction at the cathode surface is presented. By means of an approximate solution for the flow and the diffusion equations, the layer dimensions, the velocity distributions, and the densities are determined. Further derivations from the solutions directly applicable to results obtained by the freezing method are effected. The data of Brenner on copper and nickel baths are considered. Using the observed values of the density reductions at the cathode surface, the maximum width of the layer, the average densities for a given distance from the cathode, and the mobilities of the cations are determined and compared with the observations. The agreement between observed and computed values is regarded as fairly satisfactory.

1. Introduction

Neither the cognizance of the phenomenon representing the subject matter of the present paper, nor the statement of the basic causes producing it is original with us. Some 12 years ago, W. Blum, Chief of the Electrodeposition Section, National Bureau of Standards, described to us the cathode film phenomenon as a thin layer of moving material very close to the cathode surface and as being caused by the continued reduction of the densities due to electrodeposition. Since the phenomenon in question is also partly hydrodynamical in nature, he suggested that we should prepare a theoretical study with a view to determining the density distributions in cathode films.

Blum's first thought was that the film might constitute a seat of discontinuity in densities, since to the naked eye a line of demarcation between the contiguous layers of liquid near the cathode surface is distinctly visible. The line of demarcation should be due to the different indices of refractions of the liquid layers on the two sides of the line. Thus, according to these ideas the flow near the cathode surface is in one or two layers having dissimilar densities with sharp discontinuities. But, despite the appearance of the region close to the cathode surface, the opinion was ventured on our part that the exsitence of the sharp discontinuities could not be shown on the basis of purely hydrodynamical reasoning. The basis for this opinion was the belief that the phenomenon in question was essentially similar to the type of flow encountered when a heated vertical plate in the presence of cold air sets up convection currents. Since experience in this particular case does not show any discontinuities in temperatures, it might be expected that density discontinuities would not be present in the cathode plate problem. Unfortunately, due to other pressing work at that time, it was impossible to proceed with a mathematical solution of this interesting problem.

About 3 years ago, Blum repeated his request for an analytical study of the problem, since he was planning to resume the experimental investigation of cathode films. The computations that appear in this paper were completed shortly after the receipt of this request. Meanwhile two other papers on the subject, one by Agar [1][1] and the other by Wagner [2], were published. Since the present work proceeds on a mathematical basis different from these two papers and since the work was conceived with a view of interpreting the results of A. Brenner, a member of the staff of the Bureau, on cathode film densities, it is hoped that some interest in the results achieved will develop.

In the present treatment it is assumed that the reduction of densities over the vertical cathode surface is constant. On the whole the treatment is self-contained and is given in full detail. In general, the results shown are approximate and sufficient, it is believed, to evaluate average densities in a vertical plane parallel to the cathode surface. In a future publication it is proposed to investigate the problem of cathode films with the basic assumption that the density gradient at the cathode surface is constant and uniform, rather than the density.

2. Molecular Character of Electric Conduction in Solutions

Certain fundamental relations of electrochemical import that will be considered during the course of the analysis are based on the ideas of Larmor [3] in the matter of electrolytic conduction.

Taking an idealized situation it will be supposed that the electrolytic solution is a binary system and that ionization is complete. In each portion of the solution the number of the positive ions and the negative ions is the same and the conditions are steady, that is, independent of time. At a point of the solution let the number of ions of each kind per unit volume be n. Measuring positive y horizontally away from the plane cathode surface toward the anode, let a section normal to y be selected. Let dN_1 be the number of the cations and dN_2 the number of anions crossing the section per unit area during time dt. The motions of the ions are due in

[1] Figures in brackets indicate the literature references at the end of this paper.

part to the electrical force dP/dy, P being the electrical potential, and in part to the forces producing diffusion. If U_1 be the specific mobility of the cations and k_1 the coefficient of diffusion of these ions,

$$dN_1=\left(nU_1\frac{dP}{dy}+k_1\frac{dn}{dy}\right)dt, \tag{1}$$

and for the anions, in similar manner,

$$dN_2=\left(nU_2\frac{dP}{dy}-k_2\frac{dn}{dy}\right)dt. \tag{2}$$

Since there is no accumulation of electricity at a point, the relation between the electrical current intensity, I, and the motion of the ions will be

$$se(dN_1+dN_2)=Idt, \tag{3}$$

where se is the charge on each ion. Applying the principle of continuity of the ionic flows,

$$\frac{1}{2}\frac{d}{dy}\left(\frac{dN_1}{dt}-\frac{dN_2}{dt}\right)=\frac{dn}{dt}. \tag{4}$$

On the other hand, the current intensity remaining constant, from eq 3

$$\frac{d^2N_1}{dy\,dt}+\frac{d^2N_1}{dy\,dt}=0, \tag{5}$$

and this together with eq 4 gives

$$\frac{d^2N_1}{dy\,dt}=\frac{dn}{dt}, \tag{6}$$

and

$$\frac{d^2N_2}{dy\,dt}=-\frac{dn}{dt}. \tag{7}$$

Differentiating eq 1 and 2 with respect to y and using the relations just given,

$$\frac{dn}{dt}=U_1\frac{d}{dy}\left(n\frac{dP}{dy}\right)+k_1\frac{d^2n}{dy^2}, \tag{8}$$

and

$$\frac{dn}{dt}=-U_2\frac{d}{dy}\left(n\frac{dP}{dy}\right)+k_2\frac{d^2n}{dy^2}. \tag{9}$$

Multiply the first of these by U_2, the second by U_1, and adding the resulting equations, one obtains

$$\frac{dn}{dt}=\frac{k_2U_1+k_1U_2}{U_1+U_2}\frac{d^2n}{dy^2}. \tag{10}$$

Now the form of this equation is exactly the form of the diffusion equation of an ordinary nonelectrolytic solution. Hence, the changes in the concentrations of an electrolyte proceed with the diffusitivity constant

$$D=\frac{k_2U_1+k_1U_2}{U_1+U_2}. \tag{11}$$

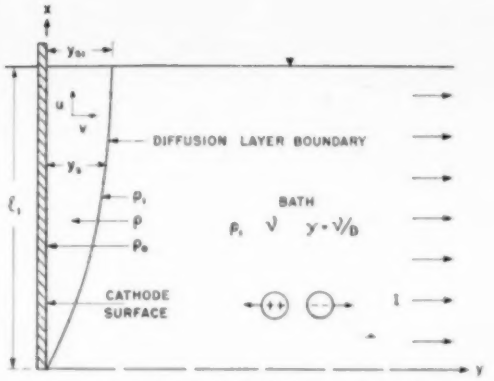

FIGURE 1. *Geometrical and physical quantities relating to the diffusing layer.*

As this relation holds good however slight the electric current may be, it may be supposed that the relation holds in the limit when the current is nil. Therefore, D is the ordinary coefficient of diffusion of the solution, and thus a relation exists connecting this coefficient with the ionic quantities, that is, with the specific mobilities and the coefficients of diffusion of the two ions.

If the relations

$$k_1=CU_1 \text{ and } k_2=CU_2 \tag{12}$$

exist, where C is a constant independent of the concentration of the ions, then

$$D=\frac{2U_1U_2}{U_1+U_2}C. \tag{13}$$

Now, from the theory of electrolytic diffusion by Nernst [4] we have

$$D=\frac{2U_1U_2}{U_1+U_2}RT, \tag{14}$$

where T is the absolute temperature and R the gas constant. Accordingly, the constant C in eq 13 may be identified with the product RT in eq 14.

3. The Equations of Motion and of Diffusion

Taking the case of a plane cathode surface, held vertically, a point at the lower edge may be chosen as the origin of the rectangular coordinate system (x,y) (see fig. 1). The positive x axis is drawn vertically upward and the positive y axis normal to the surface and into the electrolyte body. Denoting the velocity components along the x and the y axes by u and v, respectively, the equations of motion are

$$u\frac{\partial u}{\partial x}+v\frac{\partial u}{\partial y}=-\frac{1}{\rho}\frac{\partial p}{\partial x}-g+\nu\frac{\partial^2u}{\partial y^2}, \tag{15}$$

and

$$0 = -\frac{1}{\rho}\frac{\partial p}{\partial y}, \tag{16}$$

where p is the pressure, ν the kinematic viscosity of the solution, ρ the density, and g the constant of gravitational acceleration. These are the equations of motion used in viscous boundary layer theory.

The pressure must be expressed in terms of the densities. Denoting the density of the electrolytic bath at points far removed from the cathode surface by ρ_1, the density near the surface may be expressed by the relation

$$\rho = \rho_1 - \Delta\rho, \tag{17}$$

where $\Delta\rho$ is the deficiency of the density in the layer. The greatest reduction of density is at the cathode surface, that is at the plane $y = 0$. Let the average value of $\Delta\rho$ over the entire length of the cathode surface be denoted by $\Delta\rho_m$. The study of the densities in the layer is done conveniently, as will be seen later, by considering the ratio

$$\alpha = \frac{\Delta\rho}{\Delta\rho_m}. \tag{18}$$

Another quantity important for the analysis is the effective gravity

$$g\frac{\Delta\rho_m}{\rho_1} = G. \tag{19}$$

Now, the second boundary layer equation, eq 16, states that in the layer next to the cathode surface the pressure along a horizontal plane remains constant. Moreover, all motions being nil in the main body of the bath solution, the pressures are hydrostatic and hence

$$p = p_0 - \rho_1 g x, \tag{20}$$

where p_0 is the pressure at points in the horizontal plane passing through the origin. Thus,

$$\frac{1}{\rho}\frac{\partial p}{\partial x} = -g\frac{\rho_1}{\rho}. \tag{21}$$

Remembering that $\Delta\rho$ is a small quantity and making use of the relations in eq 18 and 19, we have

$$-\frac{1}{\rho}\frac{\partial p}{\partial x} - g = G\alpha, \tag{22}$$

and thus eq 15 reduces to

$$u\frac{\partial u}{\partial x} + v\frac{\partial u}{\partial y} = \nu\frac{\partial^2 u}{\partial y^2} + G\alpha. \tag{23}$$

This is the equation of motion that is appropriate to the problem at hand. To this must be added the conditions of continuity,

$$\frac{\partial u}{\partial x} + \frac{\partial v}{\partial y} = 0. \tag{24}$$

Next will be considered the equation of diffusion. In the presence of convective currents, the diffusion equation takes the form

$$\frac{\partial n}{\partial t} + u\frac{\partial n}{\partial x} + v\frac{\partial n}{\partial y} = D\left(\frac{\partial^2 n}{\partial x^2} + \frac{\partial^2 n}{\partial y^2}\right), \tag{25}$$

where n is the number of particles of the diffusing material per unit volume. This relation reduces to Fick's equation when convective currents are absent. Although the equation is well known, it may be helpful to give a derivation in order to clarify the ideas involved. Neither the name of the investigator giving the first derivation nor the manner of derivation is known to us.

Consider a parallelepiped of sides dx, dy, and 1. Let the number of particles crossing the face at x perpendicular to the x axis during time dt be

$$N_{11}\,dy\,dt, \qquad N_{11} = -D\frac{\partial n}{\partial x} + nu,$$

and the face at $x + dx$ be

$$N_{12}\,dy\,dt = \left(N_{11} + \frac{\partial N_{11}}{\partial x}dx\right)dy\,dt.$$

Similarly, let the number of particles crossing the face at y perpendicular to the y axis be

$$N_{21}\,dx\,dt, \qquad N_{21} = -D\frac{\partial n}{\partial y} + nv,$$

and the face at $y + dy$ be

$$N_{22}\,dy\,dt = \left(N_{21} + \frac{\partial N_{21}}{\partial y}dy\right)dx\,dt,$$

so the accumulation of the particles in the parallelepiped is

$$-\left(\frac{\partial N_{11}}{\partial x} + \frac{\partial N_{21}}{\partial y}\right)dx\,dy\,dt.$$

But the accumulation is also

$$\frac{\partial n}{\partial t}dx\,dy\,dt.$$

Hence,

$$\frac{\partial n}{\partial t} = -\frac{\partial N_{11}}{\partial x} - \frac{\partial N_{21}}{\partial y},$$

or

$$\frac{\partial n}{\partial t} = D\left(\frac{\partial^2 n}{\partial x^2} + \frac{\partial^2 n}{\partial y^2}\right) - u\frac{\partial n}{\partial x} - v\frac{\partial n}{\partial y} - n\left(\frac{\partial u}{\partial x} + \frac{\partial v}{\partial y}\right).$$

The last term in the right-hand number vanishes because of the incompressibility of the solution. This now proves the general equation of diffusion given by eq 25. A tacit assumption of the derivation is that the ratio of the volume of the diffusive

particles to the volume of the solution is a small fraction. Stated otherwise, the result is valid for small concentrations.

The diffusion equation is much simplified when applied to the cathode film boundary layer. First, the concentrations do not vary appreciably with time. Second, the layer being very thin and comparatively very long, the quantity $\partial^2 n/\partial x^2$ is small in comparison with $\partial^2 n/\partial y^2$. Accordingly, eq 25 becomes

$$u\frac{\partial n}{\partial x}+v\frac{\partial n}{\partial y}=D\frac{\partial^2 n}{\partial y^2},$$

and since n is proportional to α, also

$$u\frac{\partial \alpha}{\partial x}+v\frac{\partial \alpha}{\partial y}=D\frac{\partial^2 \alpha}{\partial y^2}. \tag{26}$$

This is the diffusion equation appropriate to the problem at hand. Equations 23, 24, and 26 govern the movement of liquid and the distribution of the densities in the cathode film subject to the boundary conditions.

4. Boundary Conditions

The boundary conditions to be considered are of two kinds. One kind relates to the velocities and the other to the densities, the latter having electrochemical implications.

The boundary conditions to be assigned to velocity components are the most obvious ones. The solution or the liquid of the film being viscous, u and v vanish at the cathode surface; that is

$$u=v=0, \qquad y=0. \tag{27}$$

To state the condition for the velocities at large distances away from the cathode surface it is necessary to introduce first the concept of the boundary layer thickness (see fig. 1). The boundary layer thickness, y_s, is such that the density of the solution at this distance from the cathode differs only imperceptibly from the density of the bath. Since the movement of liquid in general is nil in the main portion of the bath, a second condition for the velocities is

$$u=o, \qquad y=y_s. \tag{28}$$

It is obvious that the thickness y_s of the boundary layer at the lower edge of the cathode surface, that is at $x=0$, vanishes. This means that the liquid moving upward in the film must be replenished by a later and horizontal movement of the bath solution into the film region. Hence

$$v>0, \qquad y=y_s. \tag{29}$$

The assumption of vanishing velocities in the bath in the vertical direction is an idealization. Under the actual conditions of experimentation, arbitrary movements in the bath may be present even when forced agitation is not resorted to. Since the movement of liquid in the film next to the cathode surface is upward and in the film next to the anode downward, it is obvious that a circulation is induced in the bath liquid. Due to accidental variations of temperature at places the regularity of the circulatory motion will be disturbed and will give rise to weak eddying motions. These will be most noticeable near the upper surface of the bath and close to the cathode. Such accidental disturbances can be imagined to have only minor effects on the main motion in the film and thus will be ignored.

The boundary conditions that are to be assigned to the densities are not obvious, especially the one relating to the value of the densities at the cathode surface. Regarding this, it seems that two different statements may be made depending on whether the transmitted electric current is of the limiting value or is inferior to this limiting value. Taking the case of weak electric currents, we may consider the question of the densities at the cathode surface as follows:

Assume that the ionic system is binary and ionization is complete. Since at the cathode surface, that is at $y=0$, $dN_2/dt=0$, eq 3 gives

$$\frac{dN_1}{dt}=\frac{I}{se},$$

and thus eq 1 and 2 now become

$$\frac{I}{se}=nU_1\frac{dP}{dy}+k_1\frac{dn}{dy},$$

and

$$0=nU_2\frac{dP}{dy}-k_2\frac{dn}{dy},$$

where n is the number of ions of each kind per unit volume. Eliminating the potential gradient between these two equations and making use of eq 11,

$$D\frac{dn}{dy}=\frac{U_2}{U_1+U_2}\frac{I}{se}. \tag{30}$$

This is the relation between the electric current intensity and the gradient of n at the cathode surface.

It is desirable that the quantity n in eq 30 be replaced by c, the latter being defined as the gram equivalent of the salt per cubic centimeter of the solution. In a unit cube there are n cations and n anions each of ionic valence s, and the system is completely ionized. Introducing N, the Avogadro number, the molar concentration is n/N and hence the concentration in gram equivalent of the salt per cubic centimeter of the solution is

$$c=\frac{ns}{N},$$

and eq 30 now becomes

$$D\frac{dc}{dy}=\frac{U_2}{U_1+U_2}\cdot\frac{I}{\epsilon N}. \tag{31}$$

Since eN is the universal constant F, with the numerical value $F=96450$, and with the dimensions coulomb per gram equivalent,

$$D\frac{dc}{dy}=\frac{U_2}{U_1+U_2}\frac{I}{F} \tag{32}$$

The same condition may be expressed in terms of densities instead of concentrations. For the majority of electrolyte solutions the variation of densities with the concentration is linear; that is

$$\frac{dc}{d\rho}=m. \tag{33}$$

For copper sulphate $m=1.32\times10^{-2}$ gram equivalent per gram; and for nickel chloride $m=1.71\times10^{-2}$ gram equivalent per gram. Equation 32 may now be written as

$$mD\frac{d\rho}{dy}=\frac{U_2}{U_1+U_2}\frac{I}{F}, \qquad y=0. \tag{34}$$

This is the relation between the intensity of the electric current and the gradient of the density at a point of the cathode surface. It is the only relation that may be derived on the basis of simple concepts of an electrochemical nature. Accordingly, we are not certain of the state of the densities at the cathode surface for the present.

Two simplifying assumptions may be made. First, it may be supposed that the current intensity is uniform at the cathode surface. The resulting boundary condition would be that the density gradient is uniform at the cathode surface. Second, it may be supposed that the density is constant at the cathode surface. For the present analysis we shall adopt the second alternative simply for the reason that the corresponding analysis may be completed with ease. Thus it will be supposed that,

$$\Delta\rho=\Delta\rho_m, \qquad y=0,$$

and

$$\Delta\rho=0, \qquad y=\infty.$$

In view of eq 18

$$\alpha=1, \qquad y=0, \tag{35}$$

and

$$\alpha=0, \qquad y=\infty. \tag{36}$$

The set of equations 27, 28, 35, and 36 constitute the boundary conditions to be considered in solving the set of equations 23, 24, and 26.

Since the relation implied in eq 34 is valid for all conditions, it may be used to consider average effects. Expressing ρ in terms of α through the use of eq 18, multiplying the two sides of the resulting equation by dx, and integrating between $x=0$ and $x=l_1$, where l_1 is the length of immersion of the cathode surface,

$$-mD\Delta\rho_m\int_0^{l_1}\left(\frac{d\alpha}{dy}\right)dx=\frac{U_2}{U_1+U_2}\frac{Il_1}{F}, \tag{37}$$

where now I is the average intensity of the electric current measured in amperes per square centimeter. We shall use this relation to compute the transport number of copper ions taking our data from the results of the Brenner experiments.

5. The Dimensional Form of the Basic Equations

The solution of the basic equations subject to the boundary conditions indicated above will be greatly simplified if the equations are changed into forms involving dimensionless quantities only. The clue to the proper course of analysis may be found in the method of Blasius for treating the viscous boundary layer of plates in a current of air.

The limiting values of the densities and the velocities being uniform at the boundaries of the cathode film or of the diffusion layer, it is to be expected that the distribution of the velocities and of the density reductions in different normal sections are affine to each other. The affinities will be established by the introduction of the characteristic length δ and the characteristic velocity U, both of which are functions of x only.

Introducing the stream function ψ, such that

$$u=\frac{\partial\psi}{\partial y}, \qquad v=-\frac{\partial\psi}{\partial x}, \tag{38}$$

the condition of incompressibility, eq 24, is automatically satisfied. In terms of the stream function the equation of motion, eq 23, and the equation of diffusion, eq 26, transform to

$$\frac{\partial\psi}{\partial y}\cdot\frac{\partial^2\psi}{\partial y\partial x}-\frac{\partial\psi}{\partial x}\cdot\frac{\partial^2\psi}{\partial y^2}=\nu\frac{\partial^3\psi}{\partial y^3}+G\alpha, \tag{39}$$

and

$$\frac{\partial\psi}{\partial y}\cdot\frac{\partial\alpha}{\partial x}-\frac{\partial\psi}{\partial x}\cdot\frac{\partial\alpha}{\partial y}=D\frac{\partial^2\alpha}{\partial y^2}. \tag{40}$$

Introducing the new variables

$$\eta=y/\delta, \tag{41}$$

and

$$H=\frac{\psi}{U\delta}, \tag{42}$$

and remembering that U and δ are functions of x only, we have, first

$$\frac{\partial}{\partial y}=\frac{\partial\eta}{\partial y}\cdot\frac{d}{d\eta}=\frac{1}{\delta}\frac{d}{d\eta}, \tag{43}$$

and

$$\frac{\partial}{\partial x}=\frac{\partial\eta}{\partial x}\frac{d}{d\eta}=-\frac{\eta}{\delta}\frac{d\delta}{dx}\frac{d}{d\eta}, \tag{44}$$

and hence

$$\frac{\partial\psi}{\partial x}=H\frac{d}{dx}(U\delta)-U\frac{d\delta}{dx}\eta\frac{dH}{d\eta}, \tag{45}$$

$$\frac{\partial \psi}{\partial y} = U \frac{dH}{d\eta}, \tag{46}$$

$$\frac{\partial^2 \psi}{\partial x \partial y} = \frac{dU}{dx}\frac{dH}{d\eta} - \frac{U\eta}{\delta}\frac{d\delta}{dx}\frac{d^2H}{d\eta^2}, \tag{47}$$

$$\frac{\partial^2 \psi}{\partial y^2} = \frac{U}{\delta}\frac{d^2H}{d\eta^2}, \tag{48}$$

and

$$\frac{\partial^3 \psi}{\partial y^3} = \frac{U}{\delta^2}\frac{d^3H}{d\eta^3}. \tag{49}$$

Substituting these expressions in eq 39 and 40,

$$-U\frac{dU}{dx}\left(\frac{dH}{d\eta}\right)^2 + \frac{U}{\delta}\frac{d}{dx}(U\delta)\cdot H\frac{d^2H}{d\eta^2} + \nu\frac{U}{\delta^2}\frac{d^3H}{d\eta^3} + G\alpha = 0, \tag{50}$$

and

$$\frac{\gamma}{\delta}\frac{d}{dx}(U\delta)\,H\frac{d\alpha}{d\eta} + \frac{\nu}{\delta^2}\frac{d^2\alpha}{d\eta^2} = 0, \tag{51}$$

where

$$\gamma = \frac{\nu}{D}. \tag{52}$$

Now eq 50 and 51 will be freed of the differential operators involving x if one can write

$$M_1 U\frac{dU}{dx} = M_2\frac{U}{\delta}\frac{d}{dx}(U\delta) = \frac{\nu U}{\gamma\delta^2} = G \tag{53}$$

and

$$\frac{M_2}{\delta}\frac{d}{dx}(U\delta) = \frac{\nu}{\gamma\delta^2}, \tag{54}$$

where M_1 and M_2 are numerical constants. In view of these provisional relations, the two equations simplify to

$$\gamma\frac{d^3H}{d\eta^3} + \frac{1}{M_2}H\frac{d^2H}{d\eta^2} - \frac{1}{M_1}\left(\frac{dH}{d\eta}\right)^2 + \alpha = 0, \tag{55}$$

and

$$\frac{H}{M_2}\frac{d\alpha}{d\eta} + \frac{d^2G}{d\eta^2} = 0. \tag{56}$$

In fact, the provisional equations 53 and 54, determine the dependence of the characteristic velocity U and the characteristic length δ on the variable x. The provisional equations 53 and 54 imply

$$M_1\delta\frac{dU}{dx} = M_2\frac{d}{dx}(U\delta), \tag{57}$$

$$M_2\delta\frac{d}{dx}(U\delta) = \frac{\nu}{\gamma}, \tag{58}$$

and

$$\nu U = \gamma\delta^2 G. \tag{59}$$

It is now obvious that U and δ each are single power terms of x. Assuming

$$U = Ax^r, \tag{60}$$

$$\delta = Bx^s, \tag{61}$$

where A and B are constants involving the physical characteristics of the electrolytic solution. Substituting these expressions in eq 57, 58, and 59, comparing the powers of x and the coefficients for the individual equations, the comparisons yield

$$M_1 r = M_2(s+r), \tag{62}$$

$$M_2(s+r)AB^2 = \nu/\gamma \tag{63}$$

$$2s + r - 1 = 0, \tag{64}$$

$$r = 2s, \tag{65}$$

and

$$\nu A = \gamma B^2 G. \tag{66}$$

Equations 64 and 65, yield $r = 1/2$ and $s = 1/4$. Equation 62 now yields

$$2M_1 - 3M_2 = 0.$$

For simplicity subject to the last derived equations, we may put $M_1 = 1/2$ and $M_2 = 1/3$.

Substituting the values of the constants A and B that are obtained from eq 63 and 66 into eq 60 and 61, there results

$$U = 2G^{1/2}x^{1/2}, \tag{67}$$

and

$$\delta = \left(\frac{4\nu^2}{G\gamma^2}\right)^{1/4}x^{1/4}, \tag{68}$$

which are the functions showing the dependence of the characteristic velocity U and the characteristic length δ on the independent variable x.

Substituting the values of M_1 and M_2 as found above into eq 55 and 56, these simplify into

$$\gamma\frac{d^3H}{d\eta^3} + 3H\frac{d^2H}{d\eta^2} - 2\left(\frac{dH}{d\eta}\right)^2 + \alpha = 0, \tag{69}$$

and

$$\frac{d^2\alpha}{d\eta^2} + 3H\frac{d\alpha}{d\eta} = 0, \tag{70}$$

which are the equation of motion and the equation of diffusion expressed in dimensionless forms.

In terms of the new variables, the velocity components u and v are, using eq 38, 45, and 46,

$$u = U\frac{dH}{d\eta}, \tag{71}$$

and

$$-v = \frac{d}{dx}(U\delta)H - U\frac{d\delta}{dx}\eta\frac{dH}{d\eta}, \tag{72}$$

and the boundary conditions are

$$\left.\begin{aligned} H=0, \quad \frac{dH}{d\eta}=0, \quad \eta=0, \\ \frac{dH}{d\eta}=0, \quad \eta=\infty, \\ \alpha=1, \quad \eta=0, \\ \alpha=0, \quad \eta=\infty. \end{aligned}\right\} \tag{73}$$

The two equations 69 and 70 become the basic equations for the problem of temperature variation of a heated plate placed vertically in a cool air bath, when

$$\alpha=\frac{T-T_1}{T_0-T_1}, \tag{74}$$

where T is the temperature near the plate, T_0 the temperature of the plate, and T_1 that of the cool air, and the parameter γ is replaced by

$$\sigma=\nu/k, \tag{75}$$

where k is the thermometric conductivity.

Goldstein [5] has discussed the Pohlhausen solution of the heated plate problem and the equations considered are similar to eqs 69 and 70, when allowances are made for the variations in some of the coefficients. Thus, in the two basically different phenomena of the diffusion layer near a cathode plate and of the conduction layer near a heated plate, the corresponding parameters γ and σ play identical roles. The latter is well known as the Prandtl number. The former will be called the diffusion parameter for the present, since it is a dimensionless number expressing the ratio of the kinematic viscosity to the coefficient of diffusion. In forming the numerical value of γ, both D and ν must be expressed in square centimeters per second.

6. An Approximate Solution of the Basic Equations

Since an approximate solution is adequate for the present objectives, it is hardly necessary to effect a rigorous solution of the two equations, 69 and 70. To prepare the way for the approximate solution, it is necessary to introduce the boundary layer thickness y_s, which is a function of x. To the distances y and y_s correspond the parametric distances η and η_s, such that

$$\eta=y/\delta \text{ and } \eta_s=y_s/\delta. \tag{76}$$

We introduce the ratio

$$\theta=\eta/\eta_s=y/y_s. \tag{77}$$

It is obvious that the quantity θ will serve as the independent variable in the place of η. Indeed, the basic equations 69 and 70 transform to

$$\gamma\frac{d^3H}{d\theta^3}+3\eta_s H\frac{d^2H}{d\theta^2}-2\eta_s\left(\frac{dH}{d\theta}\right)^2+\eta_s^3\alpha=0, \tag{78}$$

and

$$\frac{d^2\alpha}{d\theta^2}+3\eta_s H\frac{d\alpha}{d\theta}=0, \tag{79}$$

with the boundary conditions

$$\left.\begin{aligned} H=0, \quad \theta=0, \\ \frac{dH}{d\theta}=0, \quad \theta=0, \\ \frac{dH}{d\theta}=0, \quad \theta=1, \\ \alpha=1, \quad \theta=0, \\ \alpha=0, \quad \theta=1, \end{aligned}\right\} \tag{80}$$

in place of the set shown by eq 73.

It is obvious, intuitively, that the space rate of change of the velocity components, $\partial u/\partial y$ and $\partial v/\partial y$, each vanish at large distances from the cathode surface. These conditions are fulfilled likewise quite approximately at distances equaling or exceeding y_s. This observation suggests the additional boundary conditions

$$\left.\begin{aligned} \frac{d^2H}{d\theta^2}=0, \quad \theta=1, \\ \frac{d\alpha}{d\theta}=0, \quad \theta=1, \end{aligned}\right\} \tag{81}$$

the first of these resulting from eq 48. All the boundary conditions of eqs 80 and 81 are satisfied if it is assumed that

$$\alpha=1-\sin\frac{\pi}{2}\theta, \tag{82}$$

and

$$H=\frac{A_1}{\pi}\left[\frac{5}{4}-\cos\pi\theta-\frac{1}{4}\cos 2\pi\theta\right]. \tag{83}$$

The above analysis involves the quantities A_1 and η_s, which at present are not known. For the determination of their values the differential equations 78 and 79 are at our disposal. Multiplying these equations by $d\theta$, integrating between the limits $\theta=0$ and $\theta=1$, and making use of the boundary conditions, the result is

$$-\gamma\left(\frac{d^2H}{d\theta^2}\right)_0-5\eta_s\int_0^1\left(\frac{dH}{d\theta}\right)^2d\theta+\eta_s^3\int_0^1\alpha d\theta=0, \tag{84}$$

and

$$\left(\frac{d\alpha}{d\theta}\right)_0+3\eta_s\int_0^1\alpha\,\frac{dH}{d\theta}\,d\theta=0, \tag{85}$$

after resorting to the rules of integration by parts. Introducing the values of α and H from eq 82 and 83 and effecting the integrations, we find

$$-2\pi\gamma A_1-\frac{25}{8}\,\eta_s A_1^2+\eta_s^3\left(\frac{\pi-2}{\pi}\right)=0,$$

$$-\frac{\pi}{2}+\frac{14}{5}\,\eta_s\frac{A_1}{\pi}=0,$$

and hence

$$\eta_s^4=\frac{5\pi^4}{14(\pi-2)}\left(\gamma+\frac{125}{448}\,\pi\right), \tag{86}$$

and

$$A_1=\frac{5\pi^2}{28\eta_s}. \tag{87}$$

The expressions for η_s and A_1 as given by eq 86 and 87, respectively, and the expressions for α and H as given by eq 82 and 83, respectively, constitute the first approximate solution of the diffusion layer problem based on the assumption that the reduction of densities, or concentrations, at the cathode surface is uniform.

7. Thickness of the Cathode Diffusion Layer

Inasmuch as the diffusion parameter $\gamma=\nu/D$ is ordinarily a very large quantity, it is sufficient to write in the place of eq 86

$$\eta_s^4=\frac{5\pi^4\gamma}{14(\pi-2)}. \tag{88}$$

Introducing the value of y_s from eq 76 and the value of δ from eq 68, we find first

$$y_s=\left[\frac{5\pi^4\gamma}{14(\pi-2)}\right]^{1/4}\left[\frac{4\nu^2}{G\gamma^2}\right]^{1/4}x^{1/4},$$

and next introducing the value of G from eq 19

$$y_s=3.33\left(\frac{\rho_1\nu^2}{g\Delta\rho_m\gamma}\right)^{1/4}x^{1/4}. \tag{89}$$

This is the expression that gives the thickness of the diffusion layer along the cathode surface (See fig. 2). The thickness is not uniform, but increases from the zero value at the lower edge of the cathode surface to a maximum at the upper end of the cathode surface still in contact with the electrolyte. The rate of increase of the thickness, however, is very gradual due to the fact that the thickness if proportional to the one fourth power of x, the distance from the lower end of the cathode. Again at a chosen point x the thickness of the layer

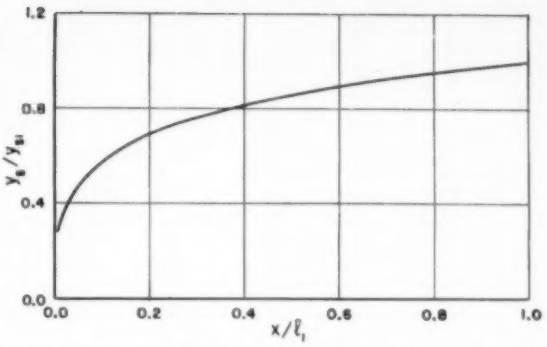

FIGURE 2. *Shape of the boundary of the diffusion layer.*

decreases when $\Delta\rho_m$, the maximum reduction of the density at the cathode surface, is increased. Since the decrease of density at the cathode surface is proportional to the electrical current density, when the latter is inferior to its limiting value, it is to be expected that a decrease in the intensity of current will cause the thickness of the diffusion layer to be augmented.

Having established the magnitude of the diffusion layer thickness, it is of interest to inquire next into the normal density gradient at the cathode surface. The variation of the density gradient will be best understood if it is expressed in terms of the average density gradient, the averaging being made over the entire cathode surface. In view of eq 18, the quantity

$$\left(\frac{\partial\alpha}{\partial y}\right)_0\Big/\overline{\left(\frac{\partial\alpha}{\partial y}\right)_0}=R, \tag{90}$$

where the numerator on the left-hand side refers to local values at the point x and the denominator to the average values, is the ratio to be considered. Since

$$\frac{\partial\alpha}{\partial y}=\frac{\partial\alpha}{\partial\theta}\cdot\frac{\partial\theta}{\partial y},$$

we have from eq 77 and 82

$$\left(\frac{\partial\alpha}{\partial y}\right)_0=-\frac{\pi}{2y_s},$$

or

$$\left(\frac{\partial\alpha}{\partial y}\right)_0=-\frac{c_1}{x^{1/4}}, \tag{91}$$

where

$$c_1=\frac{\pi}{6.66}\left(\frac{\rho_1\nu^2}{g\Delta\rho_m\gamma}\right)^{-1/4}. \tag{92}$$

Accordingly, the average value over the length l_1 of the cathode surface is

$$\overline{\left(\frac{\partial\alpha}{\partial y}\right)_0}=-\frac{4}{3}\,\frac{c_1}{l_1^{1/4}}, \tag{93}$$

and the desired ratio is

$$R=\frac{3}{4}\left(\frac{l_1}{x}\right)^{1/4}, \tag{94}$$

which gives the proportionate variation of the normal density gradient over the cathode surface. The variation is shown graphically in figure 3. In the section of the cathode from $x/l_1=0.2$ to $x/l_1=1.0$ the ratio is nearly constant. This circumstance assures the utility of the present solutions even for the case in which the normal concentration gradient is strictly constant over the entire surface of the cathode, provided that one deals with the average values of the densities in the planes close and parallel to the cathode surface.

If the diffusion layer thickness at $x=l_1$, that is at the upper end of the cathode surface just in contact with the bath, be denoted by y_{s1}, then the average value of the normal density gradient, expressed in terms of the maximum density reduction, is

$$\overline{\left(\frac{\partial \alpha}{\partial y}\right)}_0=-\frac{2.1}{y_{s1}}. \tag{95}$$

Use will be made, subsequently, of this relation.

8. Velocitus in the Diffusion Layer

Consider first the velocity component u, that is the component parallel to the surface of the cathode. Now,

$$u=U\frac{dH}{d\eta}, \tag{71}$$

where

$$U=2G^{1/2}x^{1/2}. \tag{67}$$

Since

$$\frac{dH}{d\eta}=\frac{dH}{d\theta}\cdot\frac{d\theta}{d\eta},$$

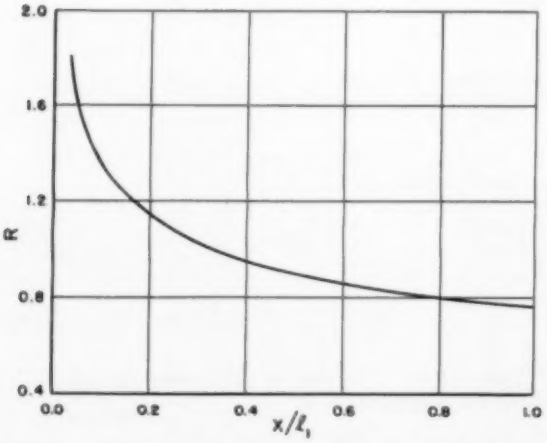

FIGURE 3. *Variation of the density gradient along the cathode surface.*

eq 71 may serve, in view of eq 77, 83, and 87, to give the distribution of the velocities in a normal section of the diffusion layer. There is, however, another method for representing the velocity distribution. Moving away from the cathode surface in a normal section, u is zero at the cathode surface, increases to a maximum value u_m, and then decreases to zero at the limit of the boundary layer, that is at $y=y_s$. Thus, the distribution of the velocity may be obtained also by considering the ratio u/u_m. Now

$$u_m=U\left(\frac{dH}{d\eta}\right)_m. \tag{96}$$

In terms of the variable θ,

$$\left(\frac{dH}{d\eta}\right)_m=\frac{1}{\eta_s}\left(\frac{dH}{d\theta}\right)_m. \tag{97}$$

If θ_1 be the value of θ that makes u a maximum, we have from eq 83,

$$\eta_s\left(\frac{dH}{d\eta}\right)_m=A_1\left[\sin\pi\theta_1+\frac{1}{2}\sin 2\pi\theta_1\right].$$

The value of $\theta_1=\frac{1}{3}$ satifies the relation.

$$\cos\ \pi\theta_1+\cos\ 2\pi\theta_1=0.$$

This makes

$$\sin\ \pi\theta_1+\frac{1}{2}\sin 2\pi\theta_1=1.299,$$

and therefore

$$\left(\frac{dH}{d\theta}\right)_m=1.299\,A_1 \tag{98}$$

Substituting into eq 96, from eq 98, 97, 88, and 67 gives

$$u_m=0.82\left(\frac{G}{\gamma}\right)^{1/2}x^{1/2},$$

or using eq 19,

$$\frac{u_m}{\sqrt{gx}}=0.82\left(\frac{\Delta\rho_m}{\rho_1\gamma}\right)^{1/2}. \tag{99}$$

Accordingly, the maximum value of u in a normal section changes from one section to another and increases with the one-half power of the distance from the lower end of the cathode.

Since,

$$u/u_m=(dH/d\eta)/(dH/d\eta)_m.$$

and introducing the relations in the equations 97 and 98, the distribution of the velocity component u in a normal section in the diffusion layer becomes

$$u/u_m=0.77\left[\sin\pi\frac{y}{y_s}+\frac{1}{2}\sin 2\pi\frac{y}{y_s}\right]. \tag{100}$$

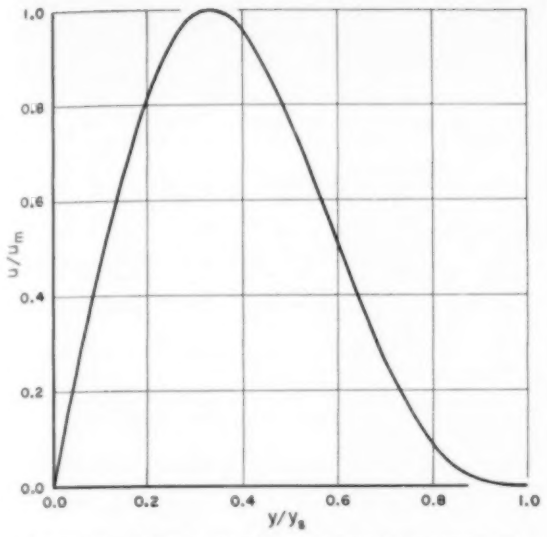

FIGURE 4. *Distribution of the vertical velocity component.*

The graphical representation of the distribution is given in figure 4.

Next consider v, the velocity component normal to the cathode surface. The velocity can be written from eq 72 as

$$v=-U\frac{d\delta}{dx}\left[3H-\eta\frac{dH}{d\eta}\right]. \tag{101}$$

The magnitude of v is largest at the liquid boundary of the diffusion layer. Let v_m be this largest value. This occurs at $\eta=\eta_s$. Let H_s be the value of H at $\eta=\eta_s$ or at $\theta=1$. At $\eta=\eta_s$, $dH/d\eta=0$, and thus

$$v_m=-3\frac{d\delta}{dx}H_sU, \tag{102}$$

where

$$H_s=2A_1/\pi. \tag{103}$$

In view of the values of U and δ from eq 67 and 68,

$$U\frac{d\delta}{dx}=\frac{1}{2}(4\nu^2G)^{1/4}x^{-1/4}\gamma^{-1/2}.$$

Substituting the above result in eq 102 and also introducing the value of A_1 from eq 87,

$$v_m=-1.013(\nu^2G)^{1/4}\gamma^{-3/4}x^{-1/4}. \tag{104}$$

Accordingly, the liquid of the bath moves horizontally into the cathode diffusion layer. The velocity with which the liquid approaches the cathode surface is variable along the length of the cathode surface, the maximum value occurring at the lower end of the cathode surface. After a certain elevation is reached the variation in the value of v_m ceases to be pronounced.

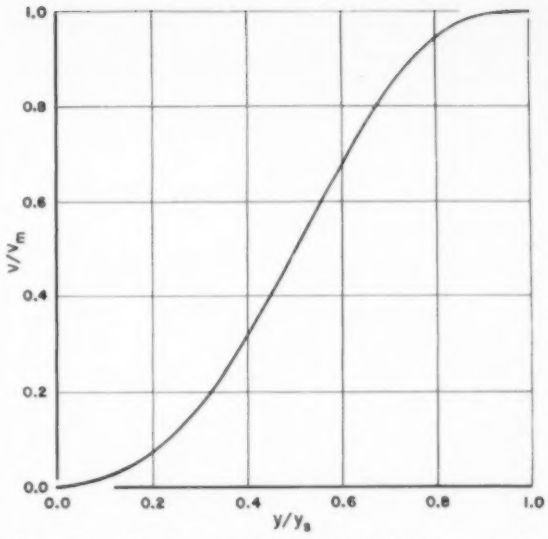

FIGURE 5. *Distribution of the horizontal velocity component.*

The representation of the distribution of v in a normal section of the layer is most conveniently done by considering the ratio v/v_m. Now,

$$\frac{v}{v_m}=\frac{1}{H_s}\left[H-\frac{\eta}{3}\frac{dH}{d\eta}\right],$$

or in terms of θ,

$$\frac{v}{v_m}=\frac{1}{H_s}\left[H-\frac{\theta}{3}\frac{dH}{d\theta}\right].$$

This gives, in view of eq 83 and 103,

$$\frac{v}{v_m}=\frac{5}{8}-\frac{1}{2}\cos\pi\theta-\frac{1}{8}\cos 2\pi\theta-\frac{\pi\theta}{6}\sin\pi\theta-\frac{\pi\theta}{12}\sin 2\pi\theta. \tag{105}$$

The graphical representation of the distribution is shown in figure 5.

9. The Brenner Freezing Method and the Laminar Mean Densities

In the Brenner method [6] the electrolytic solution near a cylindrical cathode is suddenly frozen, successive layers of the solid of 0.003- to 0.004-inch thickness are carved off on a lathe, and the compositions of the layers are determined. Thus, in this method the average concentration or the average density of a lamina of thickness dy_1, of distance y_1 from the cathode and of length l_1 are determined. Accordingly, if theoretical results are to be compared with the observed results of the Brenner experiments, it becomes necessary to derive a formula giving the average value of densities of a lamina of distance y_1 from the cathode surface,

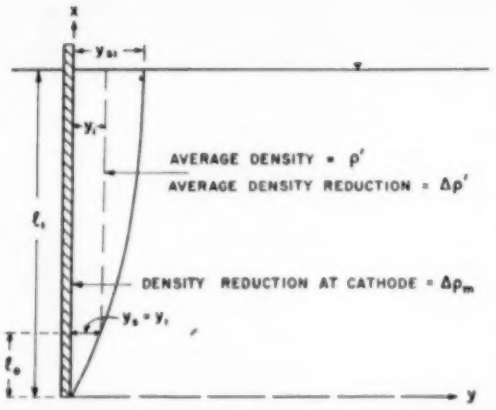

FIGURE 6. *Geometrical and physical quantities relating to the diffusion layer in Brenner's tests.*

Let the average density reduction in the lamina of length l_1 and of distance y_1 from the cathode surface be denoted by $\Delta\rho'$. Mathematically,

$$\Delta\rho' = \frac{1}{l_1}\int_0^{l_1} \Delta\rho \, dx. \tag{106}$$

Let l_0 be the value of x for which the boundary layer thickness equals y_1 (see fig. 6). Obviously, for values of $x < l_0$, $\Delta\rho = 0$, and thus,

$$\Delta\rho' = \frac{1}{l_1}\int_{l_0}^{l_1} \Delta\rho \, dx. \tag{107}$$

Since, according to the present solutions, the density reduction at $y = y_1$ is given by the relation

$$\Delta\rho = \Delta\rho_m\left(1 - \sin\frac{\pi}{2}\frac{y_1}{y_s}\right) \tag{108}$$

(from eq 82), then

$$\Delta\rho' = \Delta\rho_m\left[\frac{1}{l_1}\int_{l_0}^{l_1} dx - \frac{1}{l_1}\int_{l_0}^{l_1} \sin\frac{\pi}{2}\frac{y_1}{y_s}\, dx\right]. \tag{109}$$

It must be remembered in effecting the integration of the second integral of the right-hand member, that y_1 is held constant. Putting

$$y_1/y_s = \beta,$$

and

$$y_1/y_{s1} = \beta_1, \tag{110}$$

It is seen from the law of the layer thickness, eq 89, that

$$l_1 = l_0/\beta_1^4, \tag{111}$$

$$x = l_0/\beta^4, \tag{112}$$

and thus,

$$dx = -4l_0 d\beta/\beta^5. \tag{113}$$

Accordingly, in terms of the new variable β,

$$\Delta\rho' = \Delta\rho_m\left[1 - \beta_1^4 + 4\beta_1^4\int_1^{\beta_1} \sin\frac{\pi}{2}\beta\,\frac{d\beta}{\beta^5}\right. \tag{114}$$

For convenience, we may write

$$F(\beta_1) = \beta_1^4 - 4\beta_1^4\int_1^{\beta_1} \sin\frac{\pi}{2}\beta\,\frac{d\beta}{\beta^5} \tag{115}$$

and hence,

$$\Delta\rho'/\Delta\rho_m = 1 - F(\beta_1). \tag{116}$$

Since $\beta_1 = y_1/y_{s1}$, we have also

$$\Delta\rho'/\Delta\rho_m = 1 - F(y_1/y_{s1}). \tag{117}$$

This is the desired formula that will be used in analyzing the experimental data of Brenner. It involves the average reduction of density over a lamina, the average maximum reduction of density at the cathode surface, the distance of the lamina from the cathode, and the maximum thickness of the diffusion layer. The determination of the function $F(\beta_1)$ was carried out by replacing the term $\sin(\pi/2)\beta$ appearing in the integrand by a power series in β and then effecting the integration. The results of this determination are given in table 1.

10. An Analysis of the Results Obtained by Brenner with the Freezing Method

The comparison between the results of the present analytical theory of the cathode diffusion layer and the results of the Brenner experiments on the reduction of the densities in the diffusion layer will be carried out along the following lines. First, from the observed values of the reduction of density at the cathode surface, $\Delta\rho_m$, the maximum thickness of the diffusion layer, y_{s1}, will be computed and compared with the observations. Second, using the same observed values of $\Delta\rho_m$, the ration $\Delta\rho'/\Delta\rho_m$ will be computed for the distance y_1, and these will be compared with the observations. Third, $\Delta\rho_m$ will be computed from a consideration of the electric current intensities used in the expeiments and will be compared with the observations.

TABLE 1. *Numerical values of the function* $F(y_1/y_{s1})$

y_1/y_{s1}	$F(y_1/y_{s1})$	y_1/y_{s1}	$F(y_1/y_{s1})$
0	0.0000	0.6	0.8526
0.1	.2070	.7	.9388
.2	.4024	.8	.9840
.3	.5708	.9	.9796
.4	.7099	1.0	1.0000
.5	.8180		

The Brenner [6] results relate to electrolytic baths of copper sulfate and nickel sulfate. The baths actually used were not pure binary systems, but this fact will be ignored. The complete data from the Brenner tests are collected in table 2. The

TABLE 2. *Diffusion layer densities of the Brenner test*

Distance from cathode, y_1	Normality, N	Density, ρ'	Current intensity, I	Metallic ion
cm	*Gram equiv/liter*	*g/cm³*	*amp/cm²*	
3.69×10^{-2}	1.274	1.1009	0.04	Copper
11.16	1.522	1.1174		
18.79	1.800	1.1381		
27.63	1.920	1.1465		
37.63	1.931	1.1473		
3.83	1.741	1.132	0.01	Nickel
11.18	1.885	1.142		
21.05	1.971	1.149		
32.46	1.985	1.150		
44.12	1.985	1.150		
3.83	1.561	1.118	0.02	Nickel
12.36	1.724	1.130		
21.05	1.872	1.139		
30.00	1.935	1.146		
40.00	1.959	1.148		
3.83	1.382	1.105	0.04	Nickel
12.36	1.694	1.128		
21.05	1.900	1.143		
30.00	1.947	1.147		
40.00	1.981	1.149		

concentrations in the original data are in terms of the normalities. The densities as derived from the normality values are added. The average densities ρ' taken from the table are plotted against y_1 in figure 7, and smooth curves are drawn through the points of observation. The extreme values ρ_0 and ρ_1 of the densities are read from the curves. The differences $(\rho_1-\rho_0)$ give $\Delta\rho_m$, the average maximum reduction of densities at the cathode surfaces. The difference $(\rho_1-\rho')$, where ρ' is the observed value of the densities corresponding to the distance y_1 gives $\Delta\rho'$, the average reduction of the densities corresponding to the distance y_1. All these quantities, together with the ratio $\Delta\rho'/\Delta\rho_m$, are entered in table 3.

From the observed values of $\Delta\rho_m$ and ρ_1 the maximum layer thickness, y_{z1}, may be computed from the theoretical formula in eq 89. However, the use of eq 89 for this purpose requires that the parametric diffusion number, γ, be known. This number involves the ratio of the kinematic viscosity μ, to the diffusion constant D, for each of the two electrolytic solutions. The viscosities of the electrolytes may be determined from the normalities using the Arrhenius [7] formula,

$$\mu=\mu_1{}^N,$$

where μ_1 is the specific viscosity of a normal solution referred to the solvent at the same temperature, μ is the specific viscosity of the solution having the normality N. Wagner [8] gives $\mu_1=1.358$ for copper sulfate and $\mu_1=1.361$ for nickel sulfate at the temperature 25° C. The normalities of the bath solutions in the Brenner tests being 2 and the densities about $\rho=1.151$, the kinematic viscosities of the two solutions are practically equal and so $\mu=0.0144$ cm²/sec. Regarding the diffusion coefficient D, the Thovert [9] values for copper sulfate may be supposed to apply as well to nickel sulfate. For copper sulfate at a temperature of 17° C, $N=1.95$, the diffusion coefficient is $D=2.66\times10^{-6}$ cm²/sec. Hence the value

$$\gamma=0.572\times10^4$$

may be used for the two solutions. As regards the cathode immersion length l_1, we take it to be 10 cm, this being the value communicated to the author orally by Brenner.

Using the above-mentioned values of the pertinent quantities the magnitudes of the maximum layer thickness were computed from eq 85, and these are shown in table 4. Also there are given in the table the observed values of the same quantity as read from the curves in figure 7. At instances equalling the maximum layer thicknesses the average densities equal the bath densities. There is some difficulty

TABLE 3. *Reductions in the diffusion layer densities of the Brenner tests*

Distance from cathode, y_1	Reduction of density at cathode, $\Delta\rho_m$	Reduction of density in layer, $\Delta\rho'$	Theoretical maximum layer thickness, y_{z1}	Proportionate density reduction, $1-\Delta\rho'/\Delta\rho_m$	Proportionate distance from cathode, y_1/y_{z1}	Current intensity, I	Metallic ion
cm	*g/c cm³*	*g/c cm³*	*cm*			*amp/cm²*	
0.00	0.061	0.061	0.0302	0.00	0.00	0.04	Copper
3.69×10⁻²		.047		.23	.12		
11.16		.031		.49	.37		
18.79		.010		.84	.62		
27.63		.002		.97	.91		
37.63		.000		1.00	1.25		
0.00	0.025	.025	0.0382	0.00	0.00	0.01	Nickel
3.83		.018		.28	.10		
11.18		.008		.68	.29		
21.05		.001		.96	.55		
32.46		.000		1.00	.85		
44.12		.000		1.00	1.15		
0.00	0.040	.040	0.0347	0.00	0.00	0.02	Nickel
3.83		.030		.25	.11		
12.36		.018		.55	.35		
21.05		.009		.77	.61		
30.00		.002		.95	.86		
40.00		.000		1.00	1.15		
0.00	0.059	.059	0.0315	0.00	0.00	0.04	Nickel
3.83		.044		.25	.12		
12.36		.021		.64	.39		
21.05		.006		.90	.65		
30.00		.002		.97	.95		
40.00		.000		1.00	1.26		

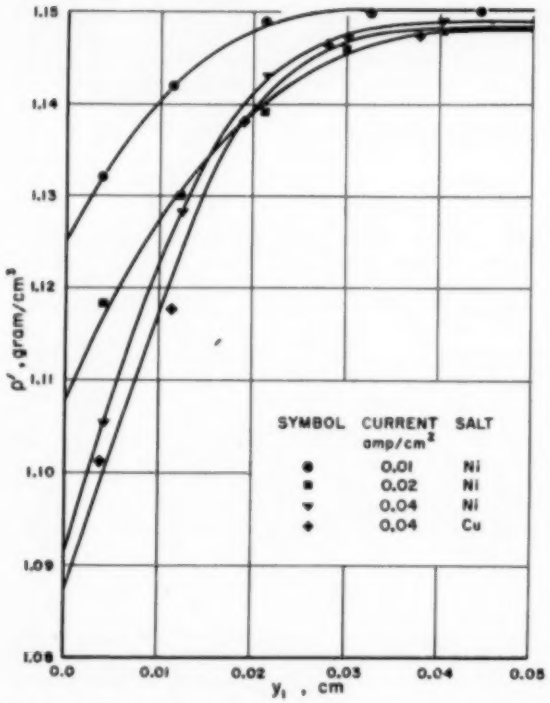

FIGURE 7. *Graphical representation of the data from Brenner's tests.*

in identifying the exact magnitude of the maximum layer thickness from the curves of figure 7. If this element of uncertainty be ignored, the agreement between the theoretical and observed values may be judged to be fairly satisfactory.

The second question to be considered is the distribution of the mean densities in the layer itself, that is the variation of $\Delta\rho'/\Delta\rho_m$ with y_1/y_{s1}. The observed proportional density reductions for a given relative distance are given in table 3. The method of determinations is obvious from the contents of the various columns. In forming the ratio y_1/y_{s1}, the theoretical values of y_{s1} are used. Values from the table are plotted in figure 8. The curve drawn is the theoretical distribution and is the plot of eq 117. Again the agreement between observation and theory may be judged to be fairly satisfactory.

The third question to be examined is the dependence of the average density gradient at the cathode surface upon the intensity of the electrical current. This question deals with the electrochemical boundary condition represented by eq 37. Since the average gradient according to eq 95 is

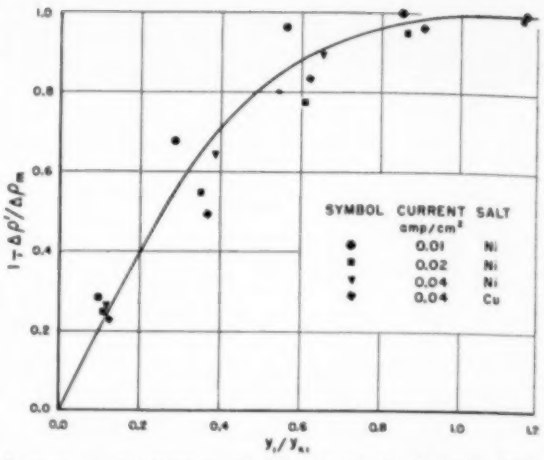

FIGURE 8. *Distribution of densities of the diffusion layer according to theory and observation.*

$$\overline{\left(\frac{\partial\alpha}{\partial y}\right)_0} = -\frac{2.1}{y_{s1}},$$

eq 37 may be changed to

$$\frac{2.1\,m\,D\Delta\rho_m}{y_{s1}} = \frac{U_2}{U_1+U_2}\,\frac{I}{F}. \tag{118}$$

This relation may be examined in two ways. If the transport number of the cations (nickel and copper) are known, the relation may be used in computing $\Delta\rho_m$, the average density reduction at the cathode. Or, using the observed value $\Delta\rho_m$, the transport number of the cations may be determined. The second method will be used here.

From the data in table 3 the ratios $\Delta\rho_m/y_{s1}$ are computed and these are plotted against current density in figure 9. The distribution of the points is linear, and the equation of the line drawn is

$$\Delta\rho_m/(y_{s1}I) = 0.5\times10^2. \tag{119}$$

TABLE 4.—*Theoretical and observed maximum diffusion layer thickness in the Brenner experiments*

Bath density, ρ_1	Cathode density, ρ_2	Reduction of density at cathode, $\Delta\rho_m$	Cathode immersion length, l_1	Observed maximum layer thickness, y_{s1}	Theoretical maximum layer thickness, y_{s1}	Current intensity, I	Metallic ion
g/cm^3	g/cm^3	g/cm^3	cm	cm	cm	amp/cm^2	
1.148	1.087	0.061	10	0.032	0.0302	0.04	Copper
1.150	1.125	.025	10	.032	.0382	.01	Nickel
1.148	1.108	.040	10	.037	.0347	.02	Do.
1.149	1.090	.059	10	.034	.0315	.04	Do.

We also have

$$F \cdot D = 2.56 \times 10^{-1}$$

and

$$m = 1.32 \times 10^{-2}.$$

Substituting these values in eq 118, it is seen that

$$\frac{U_2}{U_1 + U_2} = 0.356. \tag{120}$$

Accordingly, the transport of the cations, nickel, is $n_c = 0.644$, a value very close to the generally accepted value determined by other methods. Thus in this respect also there is agreement between theory and observation.

Another element of the theory that could be examined with considerable signficance is the question of the vertical velocities. Unfortunately in the experiments of Brenner this matter was not touched. To give an idea of the order of magnitude of the velocities involved, we may compute the maximum upward velocity in a normal section of the diffusion layer using eq 99. Consider the case of copper sulfate. Corresponding to the current intensity of $I = 4 \times 10^{-2}$ amp/cm^2, the density reduction at the cathode surface is $\Delta\rho_m/\rho_1 = 5.31 \times 10^{-2}$. Since $1/\gamma = 1.74 \times 10^{-4}$, the formula gives for maximum velocities

$$\frac{u_m}{\sqrt{gx}} = 2.50 \times 10^{-3}.$$

Thus at a point $x = 10$ cm, u_m equals 2.48 mm/sec.

The discussion presented above must lead one to the following conclusion. The approximate analytical theory of the diffusion layer based on the assumption of a uniform density reduction along the entire cathode surface gives fairly satisfactory results regarding the maximum width of the layer, the average densities in planes parallel to the cathode surface, and the transport number of ions. Brenner is now engaged in further work on the variation of densities in planes parallel to the cathode surface. Information of this kind may possibly point to defects in the present theory. In that event it might be necessary to base the theoretical investigation of the problem on the assumption that the gradient of the density and not the density is uniform along the cathode surface.

The author expresses his sincere appreciation to W. Blum for the guidance shown in the beginning of the investigation, and to A. Brenner for advice given during the progress of work. Thanks are due also to K. Hilding Beij, and to John L. French for reviewing the paper.

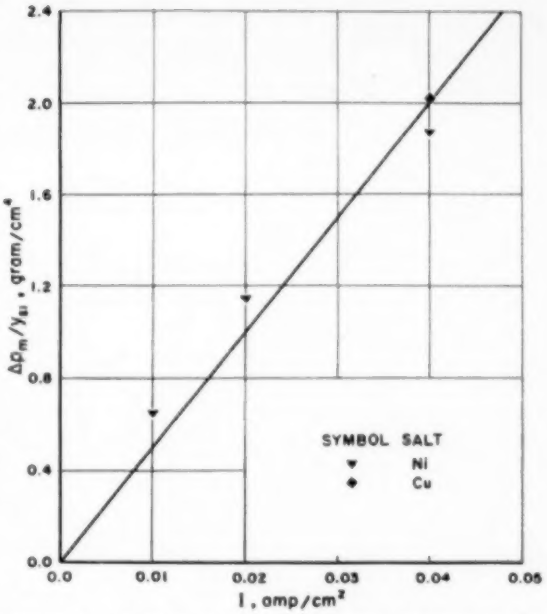

FIGURE 9. *Relation of maximum density reduction to the intensity of electric current.*

11. References

[1] J. N. Agar, Diffusion and convection at electrodes, Discussions of the Faraday Society, No. 1 (1947), Electrode Processes, p 26.
[2] Carl Wagner, The role of natural convection in electrolytic processes, J. Electrochem. Soc. **95,** 161 (1949).
[3] J. Larmor, Aether and matter, p. 289 (Cambridge University Press (Eng.), 1900).
[4] W. Nernst, Zur Kinetik der in Lösung befindlicher Körper, Z. Phys. Chem. **2** 613 (1888).
[5] S. Goldstein, Modern developments in fluid dynamics, **II,** 638 (Oxford, The Clarendon Press, 1938).
[6] Abner Brenner, Cathode films in electrodeposition, Proc. Educational Sessions of the Twenty-ninth Annual Convention, American Electroplaters Society, p. 28 (1941).
[7] Svante Arrhenius Über die innere Reibung verdünnter wässeriger Lösungen, Z. Phys. Chem. **1** 285 (1887).
[8] Julius Wagner, Über die innere Reibung verdünnter Saltzlösungen, Z. Phys. Chem. **5** 31 (1890).
[9] G. Thovert, Recherches sur la diffusion, Ann. Chem. Phys. [7] **26,** 366 (1902).

WASHINGTON, January 17, 1951.

Journal of Research of the National Bureau of Standards Vol. 47, No. 3, September 1951 Research Paper 2241

Absorption Spectra of Thioindigo Dyes in Benzene and Chloroform[1]

Wallace R. Brode and George M. Wyman

The spectral absorption curves of 10 purified thioindigo dyes, containing mostly methyl and ethoxyl groups or halogens as substituents, in benzene and chloroform solution were determined over the ultraviolet and visible parts of the spectrum. The existence of an equilibrium between *cis* and *trans* isomers was indicated by the study of the effect of light on the absorption spectra. Some of the results of this investigation have been published.[2] The present paper supplements the earlier paper and contains the spectral absorption curves that have not previously been published, along with the data on the purification of the three dyes that had not been reported there. In general, the first (long-wave) absorption band of the *cis*-form of each dye occurs at a shorter (by approximately 60 mμ) wavelength than that of the corresponding *trans* isomer. The spectra are displaced slightly toward longer wavelengths in chloroform solutions than in benzene. Substituents in the five and seven positions cause a bathochromic shift in the spectra of both isomers of each dye in each solvent without affecting the shape of the spectral absorption curves. The introduction of substituents in the four or six positions results in a change in the shape of the absorption curves and a shift of the absorption to shorter wavelengths.

1. Introduction

The absorption spectra of the 10 purified thioindigo dyes listed in table 3 were determined as a part of the National Bureau of Standards research project on the spectra of pure dyestuffs. It was observed that the absorption spectra of these dyes in organic solvents were a function of the wavelength range of the illumination to which the solutions had been exposed prior to the measurement of the spectrum. This phototropic behavior was attributed to the existence of a dynamic equilibrium between the *cis* and *trans* forms (as shown here for thioindigo):

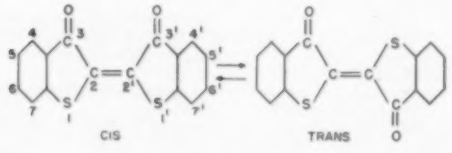

It was also possible to separate the two isomers in the case of two of these dyes. Some of the results of this investigation on seven of these dyes have been published (see footnote 2).

The object of this paper is to reproduce the complete spectral absorption curves of the dyes for which only the position of the absorption bands was reported in the earlier paper (cf. tables 2 and 3 of the reference cited in footnote 2); to describe the purification and the absorption spectra of three additional dyestuffs of this type; and to attempt to establish further correlations between the spectral absorption and the structure of these molecules.

[1] Paper XXIII in the series on "The relation between the absorption spectra and the chemical constitution of dyes" (Paper XXII is referred to in footnote 2).
[2] G. M. Wyman and W. R. Brode, J. Am. Chem. Soc. **73**, 1487 (1951).

2. Experimental Methods

2.1. Purification of Dyes

The dyes used in this work were commercial products of known structure. Each was purified by adsorption on silica gel followed by selective elution. The solutions were then evaporated to dryness and the residue recrystallized from benzene or chloroform. Table 1 lists the conditions of the purification of the three dyes that had not been reported previously.

TABLE 1. *Chromatographic purification of thioindigo dyes*

Dye	Adsorbed from—	Eluted with—	Crystallized from—
5,5′,7,7′-Tetramethylthioindigo.	CCl_4[a]	{33% of CCl_4[d] / 67% of C_6H_6[b]}	$CHCl_3$[c]
4,4′,5,5′,7,7′-Hexachlorothioindigo.	CCl_4	{87.5% of CCl_4 / 12.5% of C_6H_6}	$CHCl_3$
Vat Scarlet G	{50% of CCl_4 / 50% of C_6H_6}	C_5H_5N	$CHCl_3$

[a] Freshly distilled, technical.
[b] Freshly distilled, ACS grade.
[c] USP.
[d] By volume.

2.2 Preparation of Solutions

Approximately 0.01-g samples of each dye were weighed and dissolved in 600 to 700 ml of benzene or chloroform by heating at the boiling point of the solvent for several hours. The solutions were then cooled to room temperature and diluted to 1 liter.

2.3. Irradiation of Solutions

The dye solution contained in a fused quartz absorption cell was exposed for 5 to 10 min to colored light, using a 100-w Spencer microfilm projector with

Corning glass filters. These filters are listed in table 2, along with the manufacturer's numbers and the observed transmission cut-off (wavelength at which the transmission of light is less than 1%).

2.4. Measurement of Absorption Spectra

The absorption spectra were measured at room temperature by means of a Cary Recording Quartz Spectrophotometer (Model 12), using matched absorption cells equipped with fused quartz windows.

3. Results

Figures 1 to 16 show the experimentally determined absorption spectra of eight of these thioindigo dyes in benzene and in chloroform solutions under the stated conditions of irradiation. Figures 17 to 32 present the calculated probable absorption curves for each pair of pure *cis* and *trans* isomers of each dye, which had not previously been reported, in the two solvents (concentration: 0.0100 g/liter, cell length: 2.00 cm).[3] Table 2 lists the approximate amounts of each isomer present at equilibrium, under various conditions of illumination, for the three dyes that had not previously been reported.

The spectral absorption curves in figures 1 to 16 demonstrate graphically the phototropic effect discussed in the previous paper (see footnote 2). This effect, attributed to the existence of a dynamic equilibrium between the *cis* and *trans* forms of these dyes, is apparently common to all thioindigo dyes in benzene and in chloroform solutions, and it was observed that even the hemi-thioindigoid dye, Vat Scarlet G (Colour Index No. 1228), exhibited this behavior. It is believed that interconversion of *cis-trans* isomers in general can be effected by selective irradiation, provided that the first absorption bands (at the long-wave end of the spectrum) of the two isomers occur at appreciably different wavelengths. It can be readily seen from figures 17 to 32 that the *cis* isomers of these dyes have their first absorption bands at a considerably higher frequency than do the corresponding *trans* forms. This frequency difference is remarkably constant and ranges from 1,800 to 2,250 cm^{-1} in chloroform; and from 2,000 to 2,400 cm^{-1} in benzene solutions for the 10 dyes reported here, as shown in table 3.[4]

TABLE 2. *Approximate amounts of the two isomers of each dye*

Corning filter number	Wavelength region	In benzene		In chloroform	
		trans	*cis*	*trans*	*cis*
5,5′,7,7′-Tetramethylthioindigo (565 mμ)[a]					
	mμ	%	%	%	%
None		84	16	75	25
585	<495	89	11	78	22
351	>520	57	43	66	34
2424	>575	29	71	44	56
4,4′,5,5′,7,7′-Hexachlorothioindigo (565 mμ)[a]					
None		78	22	81	19
585	<495	82	18	84	16
351	>520	72	28	74	26
2424	>575	45	55	55	45
Vat Scarlet G (515 mμ)[a]					
None		58	42	57	43
585	<495	68	32	63	37
397	>550	50	50	51	49
351	>520	28	72	29	71

[a] Approximate wavelength of first absorption band.

The absorption spectra of each dye in the two solvents used appear strikingly similar. There is a slight displacement of the first absorption bands toward lower wave numbers in chloroform. This displacement amounts to less than 200 cm^{-1} for the *trans* isomers and 200 to 400 cm^{-1} for the *cis* forms. It seems probable that the more polar solvent (chloroform) lowers the energy of the first excited states (which are also polar, cf. the reference cited in footnote 2), and this effect is more pronounced for the relatively more polar *cis* form than for the corresponding *trans* isomer. The ratios of the absorption bands are constant for each isomer and, for each dye, independent of the solvent (cf. table 3).

It is interesting to note that, although in the *trans* isomers, the most intense ultraviolet absorption peak is always at slightly less than double the frequency of the first absorption band (corresponding to the second harmonic of that fundamental vibration), this ratio is diminished considerably (to approximately 1.6) in the *cis* isomers (cf. table 3). Substitution in the 6,6′-positions reduces these ratios considerably and, in addition, gives rise to new absorption bands in the near ultraviolet.

It is possible to evaluate the effect of substituents by comparing the calculated absorption curves for the pure *cis* and *trans* isomers (figs. 17 to 32). It is immediately apparent from such a comparison that that the introduction of substituents in thioindigo in the 5 and 7 positions causes the usual shift toward longer wavelengths in both isomers. The effect of a methyl group is approximately equal to that of a chlorine atom (cf. figs. 17 to 23). This bathochromic shift is also observed when two bromine atoms are substituted in the 5,5′-positions in 6,6′-diethoxythioindigo (cf. figs. 27 to 29).[5] 4,4′, 5,5′, 7,7′-Hexachlorothioindigo also shows this expected bathochromic shift in the ultraviolet region; the first absorption band in the visible region, however, is at about the same wavelength as that for tetramethylthioindigo. In its ultraviolet spectrum it shows the absence of the second, auxiliary absorption band in benzene solution only, thus contributing the sole

[3] The experimentally observed absorption curves for thioindigo and 6,6′-diethoxythioindigo in the two solvents and the calculated probable absorption curves for these two dyes and for 4,4′-dimethyl-6,6′-dichlorothioindigo and bis-4,5-benzothioindigo in chloroform were published in the previous paper (see footnote 2).

[4] For an interpretation of this frequency difference cf the reference in footnote 2.

[5] An explanation was suggested for these bathochromic shifts in the earlier paper (footnote 2).

TABLE 3. *Ratio of the frequency of each subsequent absorption band (in order of increasing wave numbers) to that of the first absorption band*

Dye	In chloroform						In benzene						$\nu'_{cis}-\nu'_{trans}$	
	Trans				*Cis*		*Trans*				*Cis*		In $CHCl_3$	In C_6H_6
Thioindigo			1.75	1.96		1.63			1.80	(a)		1.65	2100	2250
5,5′-Dichloro-7,7′-dimethyl thioindigo			1.75	1.93		1.62			1.75	1.94		1.62	2000	2300
5,5′-Dichloro-4,4′,7,7′-tetramethyl thioindigo			1.76	1.94		1.62			1.75	1.93		1.62	2000	2150
5,5′,7,7′-Tetramethyl-thioindigo			1.72	1.95		1.61			1.73	1.95		1.60	2100	2300
4,4′,5,5′,7,7′-Hexachloro-thioindigo			1.78	1.89		1.66			(b)	1.87		1.67	2100	2200
4,4′-Dimethyl-6,6′-dichlorothioindigo	1.57	1.71	1.75	1.91	1.44	1.60	1.56	(b)	1.76	1.90	1.46	1.63	1950	2150
6,6′-Diethoxythioindigo	1.35	1.40	1.75	1.88	1.29	1.54	1.33	1.41	1.76	(a)	1.29	1.53	2250	2400
5,5′-Dibromo-6,6′-diethoxythioindigo	1.37	1.41		1.83	1.30	1.53	1.35	1.43		1.83	1.30	1.51	2050	2400
bis-4, 5-Benzothioindigo	1.31	1.35			1.23	1.49	1.32	1.44			1.23	1.48	1800	2200
Vat Scarlet G			1.71			1.58			1.71			1.59	1800	2000

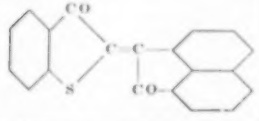

[a] Absorption band obscured by absorption due to solvent.
[b] Absorption band absent in benzene, although present in chloroform.

example in this series for a compound showing a significant difference in absorption spectrum in the two solvents used (cf. figs. 7 and 8, also 24 and 25).

It had been pointed out by Formanek [6] that the introduction of substituents in the 6,6′-positions in thioindigo causes a shift of the first absorption band toward higher frequencies. Although the existence of *cis* and *trans* isomers of thioindigo dyes was not known at that time, this statement has been shown to be applicable to the *cis* compounds also and an explanation for this, apparently anomalous, hypsochromic shift was suggested in the previous paper (see footnote 2). In general, the introduction of substituents in the 6,6′-position in the thioindigo nucleus gives rise to the appearance of new absorption peaks in the near ultraviolet region (cf. figs. 26 to 29). In addition, the most intense ultraviolet absorption band undergoes a slight shift toward lower frequencies in both isomers of each of these dyes (except *trans* 6,6′-diethoxythioindigo). Thus, it appears likely that in the second excited state, the 6,6′-positions are more strongly conjugated with the negatively polarizable oxygen atoms, than they are in the first excited state. A comparison of the spectra of 5,5′-dichloro-7,7′-dimethylthioindigo (figs. 17 and 18) and of 4,4′-dimethyl-6,6′-dichlorothioindigo (figure 26 and figure 7 in the reference cited in footnote 2 shows, however, that the bathochromic shift of the main ultraviolet absorption band in the case of the latter is still far less than in the case of its more "normal" isomer. It is interesting to note that the visible spectrum of bis-4,5-benzothioindigo (fig. 30 and fig. 9 in the reference cited in footnote 2 resembles the spectra of 6,6′-diethoxythioindigo and of 5,5′-dibromo-6,6′-diethoxythioindigo more closely than that of any of the other thioindigo dyes. This suggests that the two phenyl groups act as electron donors similar to (though not as strong as) the ethoxy groups; contributing structures of this type to the resonance hybrid of the ground state:

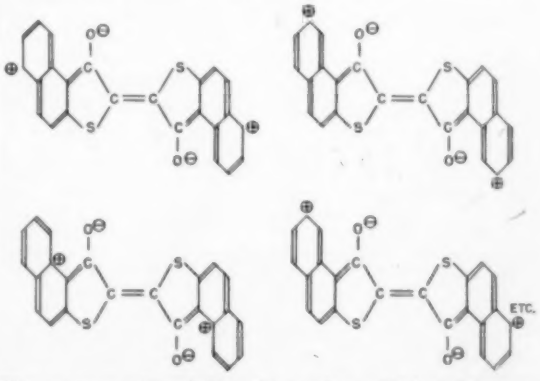

The strong ultraviolet absorption of bis-4,5-benzothioindigo (fig. 13) is probably due to the strong absorption normally associated with phenyl groups in this region of the spectrum.

[6] J. Formanek, Z. Angew. Chem. **41**, 1137 (1928).

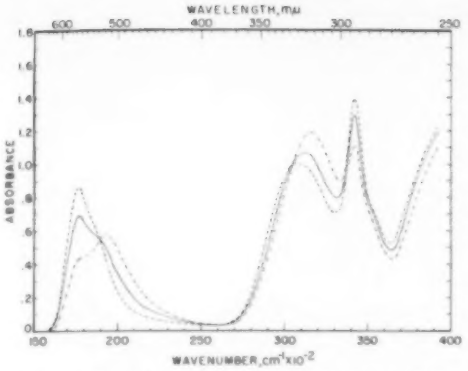

FIGURE 1. *Absorption spectra of 5,5′-dichloro-7,7′-dimethylthioindigo in chloroform.*

_____, Exposed to blue light (λ<495 mμ); _____, exposed to yellow light (λ>520 mμ); _ _ _ _ _, exposed to red light (λ>575 mμ). Concentration, 0.0053 g/liter. Cell length, 5.00 cm.

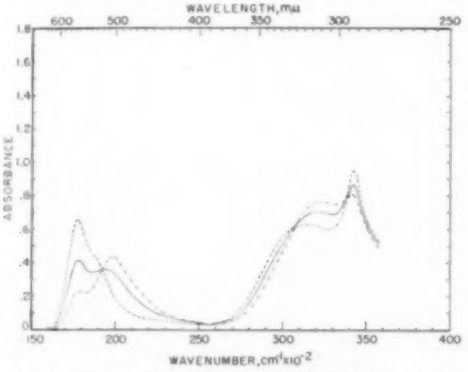

FIGURE 2. *Absorption spectra of 5,5′-dichloro-7,7′-dimethyl thioindigo in benzene.*

_____, Exposed to blue light (λ<495 mμ); _____, exposed to yellow light (λ>520 mμ); _ _ _ _ _, exposed to red light (λ>575 mμ). Concentration, 0.0091 g/liter. Cell length, 2.00 cm.

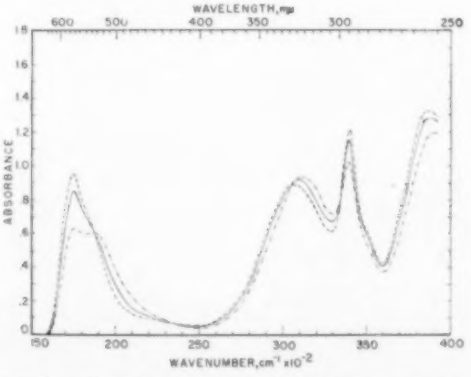

FIGURE 3. *Absorption spectra of 5,5′-dichloro-4,4′, 7,7′-tetramethylthioindigo in chloroform.*

_____, Exposed to blue light (λ<495 mμ); _____, exposed to yellow light (λ>520 mμ); _ _ _ _ _, exposed to red light (λ>575 mμ). Concentration, 0.0117 g/liter. Cell length, 2.00 cm.

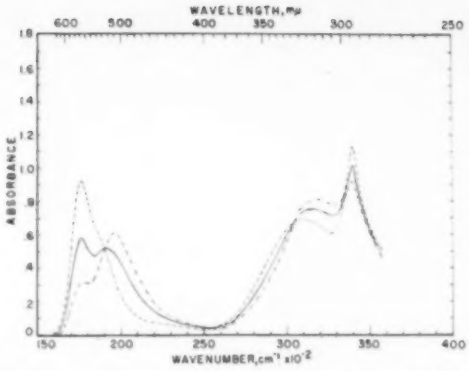

FIGURE 4. *Absorption spectra of 5,5′-dichloro-4,4′,7,7′-tetramethylthioindigo in benzene.*

_____, Exposed to blue light (λ<495 mμ); _____, exposed to yellow light (λ>520 mμ); _ _ _ _ _, exposed to red light (λ>575 mμ). Concentration, 0.0108 g/liter. Cell length, 2.00 cm.

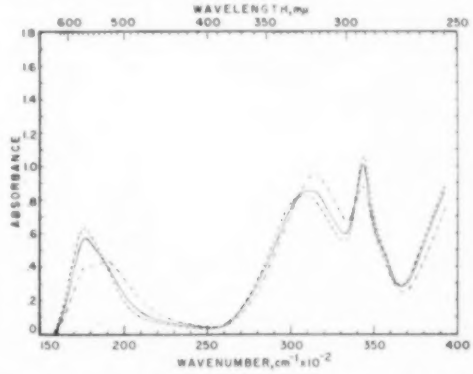

FIGURE 5. *Absorption spectra of 5,5′, 7,7′-tetramethylthioindigo in chloroform.*

_____, Exposed to blue light (λ<495 mμ); _____, exposed to yellow light (λ>520 mμ); _ _ _ _ _, exposed to red light (λ>575 mμ). Concentration, 0.0091 g/liter. Cell length, 2.00 cm.

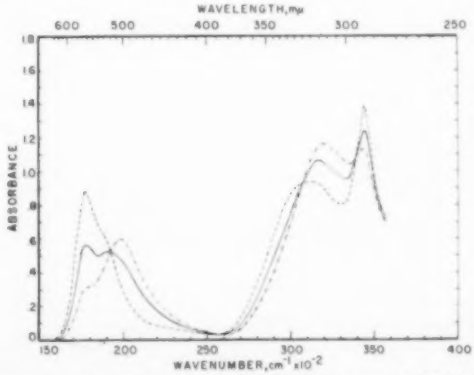

FIGURE 6. *Absorption spectra of 5,5′, 7,7′-tetramethylthioindigo in benzene.*

_____, Exposed to blue light (λ<495 mμ); _____, exposed to yellow light (λ>520 mμ); _ _ _ _ _, exposed to red light (λ>575 mμ). Concentration, 0.0107 g/liter. Cell length, 2.00 cm.

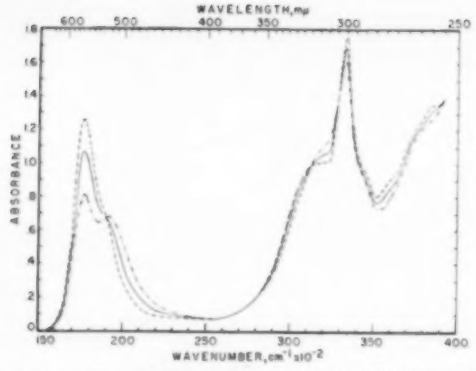

FIGURE 7. *Absorption spectra of 4,4′, 5,5′, 7,7′-hexachlorothioindigo in chloroform.*

_____, Exposed to blue light (λ<495 mμ); _____, exposed to yellow light (λ>520 mμ); _ _ _ _ _, exposed to red light (λ>575 mμ). Concentration, 0.0055 g/liter. Cell length, 5.00 cm.

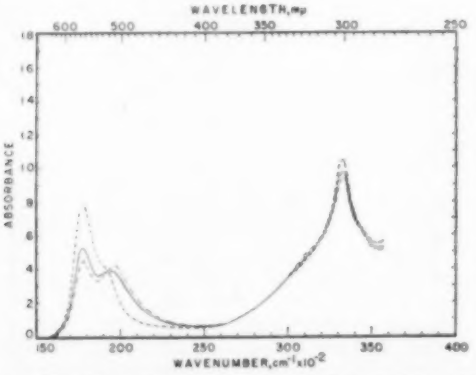

FIGURE 8. *Absorption spectra of 4,4′, 5,5′, 7,7′-hexachlorothioindigo in benzene.*

_____, Exposed to blue light (λ<495 mμ); _____, exposed to yellow light (λ>520 mμ); _ _ _ _ _, exposed to red light (λ>575 mμ). Concentration, 0.0096 g/liter. Cell length, 2.00 cm.

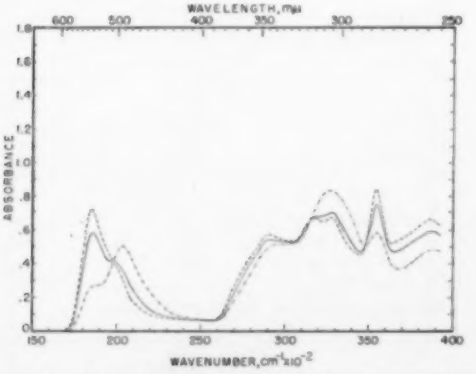

FIGURE 9. *Absorption spectra of 4,4′-dimethyl-6,6′-dichlorothioindigo in chloroform.*

_____, Exposed to blue light (λ<495 mμ); _____, exposed to green light (λ>350 mμ); _ _ _ _ _, exposed to yellow light (λ>520 mμ). Concentration, 0.0081 g/liter. Cell length, 2.00 cm.

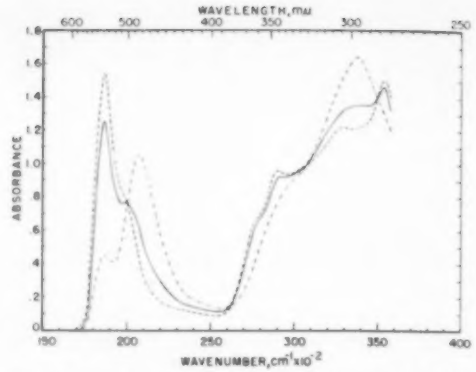

FIGURE 10. *Absorption spectra of 4,4′-dimethyl-6,6′-dichlorothioindigo in benzene.*

_____, Exposed to blue light (λ<495 mμ); _____, exposed to green light (λ>350 mμ); _ _ _ _ _, exposed to yellow light (λ>520 mμ). Concentration, 0.0144 g/liter. Cell length, 2.00 cm.

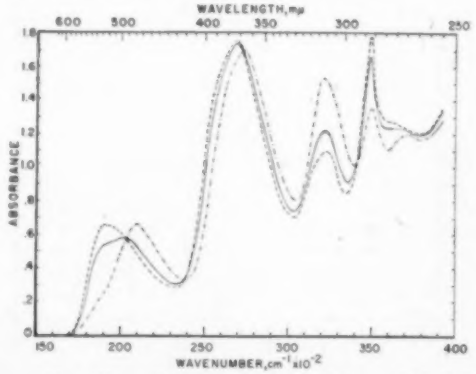

FIGURE 11. *Absorption spectra of 5,5′-dibromo-6,6′-diethoxythioindigo in chloroform.*

_ _ _ _ _, Exposed to blue light (λ<495 mμ); _____, exposed to daylight; _____, exposed to yellow light (λ>520 mμ). Concentration, 0.0092 g/liter. Cell length, 5.00 cm.

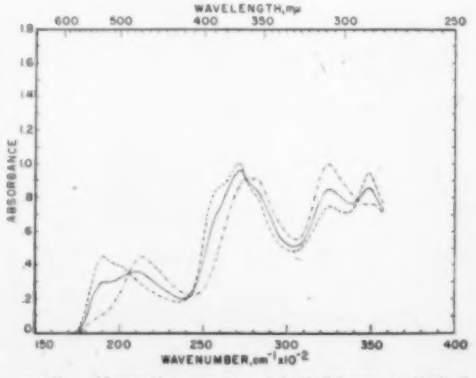

FIGURE 12. *Absorption spectra of 5,5′-dibromo-6,6′-diethoxythioindigo in benzene.*

_____, Exposed to blue light (λ<495 mμ); _____, exposed to green light (λ>350 mμ); _ _ _ _ _, exposed to yellow light (λ>520 mμ). Concentration, 0.0052 g/liter. Cell length, 5.00 cm.

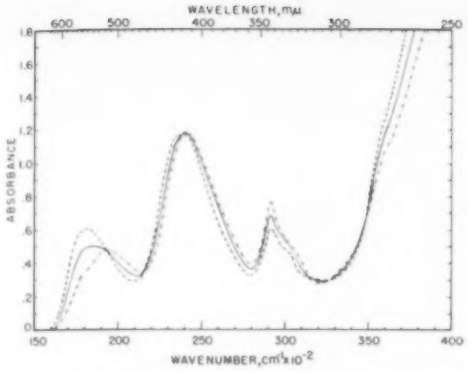

FIGURE 13. *Absorption spectra of bis-4,5-benzothioindigo in chloroform.*

_____, Exposed to blue light (λ<495 mμ); _____, exposed to yellow light (λ>470 mμ); _ _ _ _ _, exposed to red light (λ>575 mμ). Concentration, 0.0046 g/liter. Cell length, 5.00 cm.

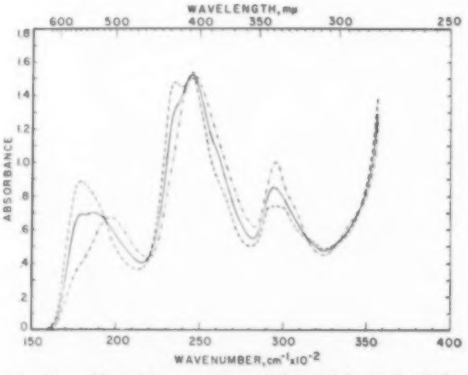

FIGURE 14. *Absorption spectra of bis-4,5-benzothioindigo in benzene.*

_____, Exposed to blue light (λ<495 mμ); _____, exposed to yellow light (λ>470 mμ); _ _ _ _ _, exposed to red light (λ>575 mμ). Concentration, 0.0064 g/liter. Cell length, 5.00 cm.

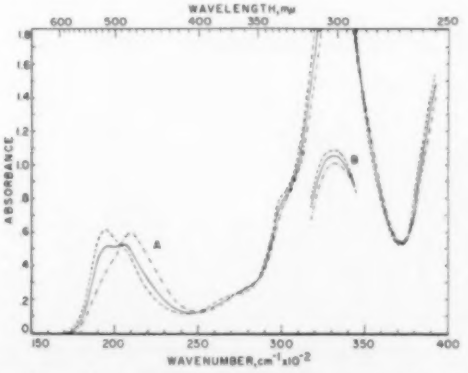

FIGURE 15. *Absorption spectra of Vat Scarlet G in chloroform.*

_____, Exposed to blue light (λ<495 mμ); _____, exposed to green light (λ>350 mμ); _ _ _ _ _, exposed to yellow light (λ>520 mμ). A, Concentration, 0.0109 g/liter. Cell length, 2.00 cm. B, Concentration, 0.0055 g/liter. Cell length, 2.00 cm.

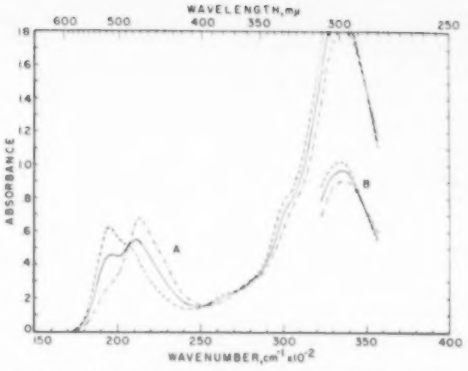

FIGURE 16. *Absorption spectra of Vat Scarlet G in benzene.*

_____, Exposed to blue light (λ<495 mμ); _____, exposed to green light (λ>350 mμ); _ _ _ _ _, exposed to yellow light (λ>520 mμ). A, Concentration, 0.0100 g/liter. Cell length, 2.00 cm. B, Concentration, 0.0050 g/liter. Cell length, 2.00 cm.

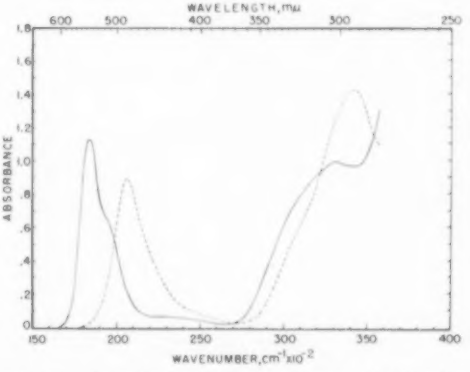

FIGURE 17. *Calculated absorption spectra of thioindigo in benzene.*

_____, *Trans*-form; _ _ _ _ _, *cis*-form.

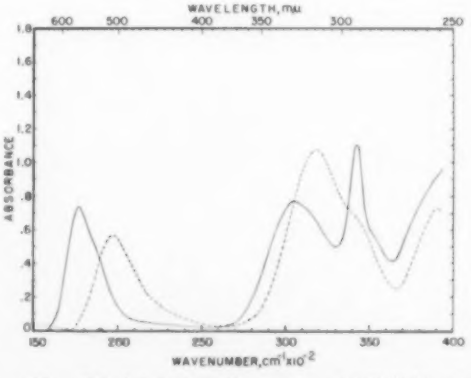

FIGURE 18. *Calculated absorption spectra of 5,5'-dichloro-7,7'-dimethylthioindigo in chloroform.*

_____, *Trans*-form; _ _ _ _ _, *cis*-form.

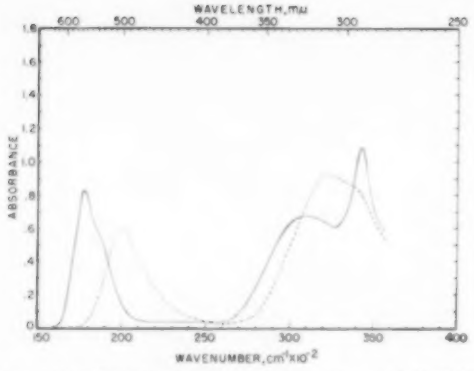

FIGURE 19. *Calculated absorption spectra of 5,5'-dichloro-7,7'-dimethylthioindigo in benzene.*

_____, *Trans*-form; _ _ _ _, *cis*-form.

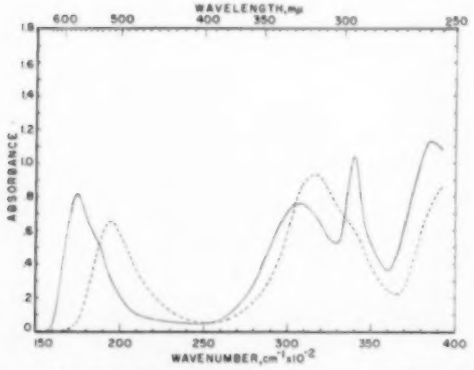

FIGURE 20. *Calculated absorption spectra of 5,5'-dichloro-4,4', 7,7'-tetramethylthioindigo in chloroform.*

_____, *Trans*-form; _ _ _ _, *cis*-form.

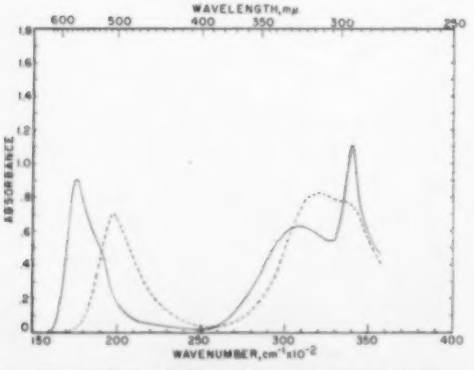

FIGURE 21. *Calculated absorption spectra of 5,5'-dichloro-4,4', 7,7'-tetramethylthioindigo in benzene.*

_____, *Trans*-form; _ _ _ _, *cis*-form.

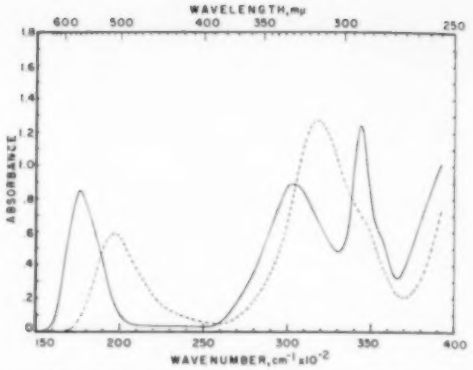

FIGURE 22. *Calculated absorption spectra of 5,5', 7,7'-tetramethylthioindigo in chloroform.*

_____, *Trans*-form; _ _ _ _, *cis*-form.

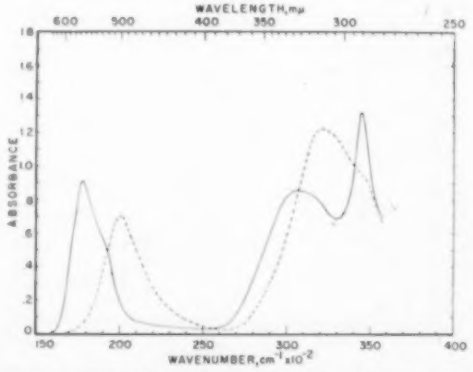

FIGURE 23. *Calculated absorption spectra of 5,5', 7,7'-tetramethylthioindigo in benzene.*

_____, *Trans*-form; _ _ _ _, *cis*-form.

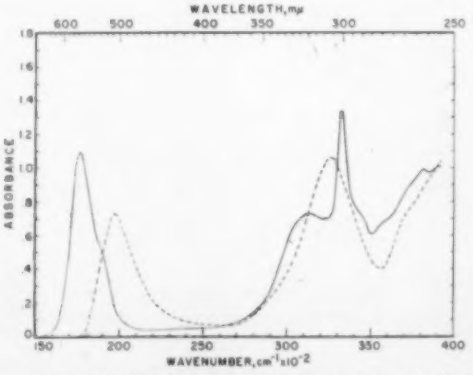

FIGURE 24. *Calculated absorption spectra of 4,4', 5,5', 7,7'-hexachlorothioindigo in chloroform.*

_____, *Trans*-form; _ _ _ _, *cis*-form.

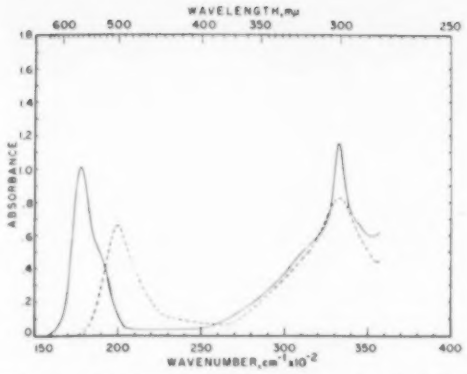

FIGURE 25. *Calculated absorption spectra of 4,4′, 5,5′, 7,7′-hexachlorothioindigo in benzene.*

_____, *Trans*-form; _ _ _ _ _, *cis*-form.

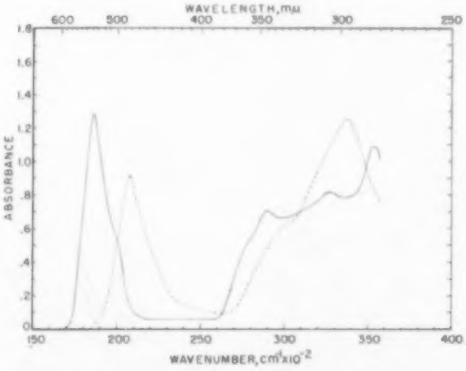

FIGURE 26. *Calculated absorption spectra of 4,4′-dimethyl-6,6′-dichlorothioindigo in benzene.*

_____, *Trans*-form; _ _ _ _ _, *cis*-form.

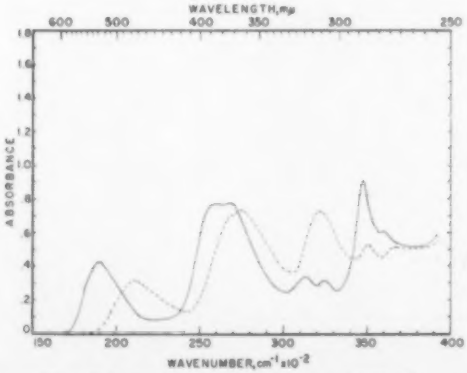

FIGURE 27. *Calculated absorption spectra of 5,5′-dibromo-6,6′-diethoxythioindigo in chloroform.*

_____, *Trans*-form; _ _ _ _ _, *cis*-form.

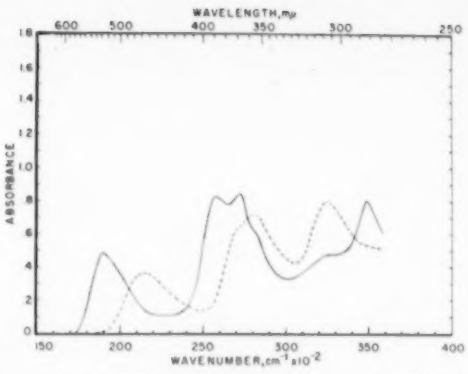

FIGURE 28. *Calculated absorption spectra of 5,5′-dibromo-6,6′-diethoxythioindigo in benzene.*

_____, *Trans*-form; _ _ _ _ _, *cis*-form.

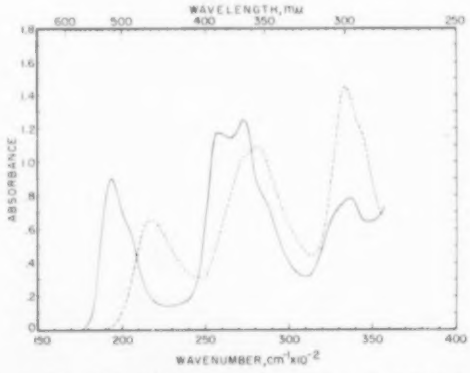

FIGURE 29. *Calculated absorption spectra of 6,6′-diethoxythioindigo in benzene.*

_____, *Trans*-form; _ _ _ _ _, *cis*-form.

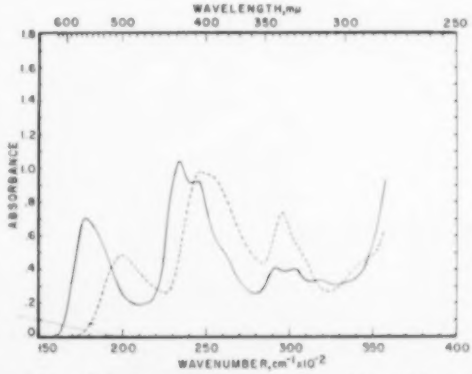

FIGURE 30. *Calculated absorption spectra of bis-4,5-benzothioindigo in benzene.*

_____, *Trans*-form; _ _ _ _ _, *cis*-form.

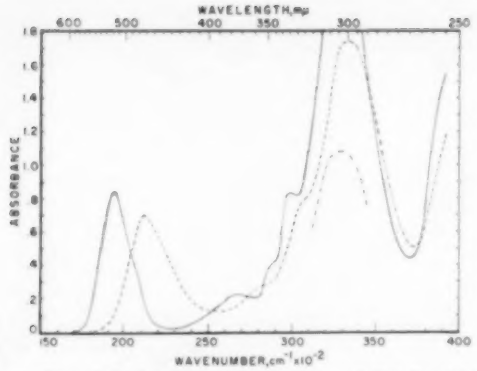

FIGURE 31. *Calculated absorption spectra of Vat Scarlet G in chloroform.*

_____, *Trans*-form; _ _ _ _ _, *cis*-form; _ . _ . _ . _ . , *trans*-form, concentration, 0.0050 g/liter.

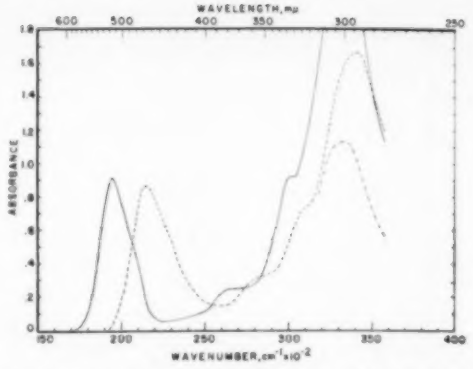

FIGURE 32. *Calculated absorption spectra of Vat Scarlet G in benzene.*

_____, *Trans*-form; _ _ _ _ _, *cis*-form; _ . _ . _ . _ . , *trans*-form, concentration, 0.0050 g/liter.

WASHINGTON, March 5, 1951.

Journal of Research of the National Bureau of Standards Vol. 47, No. 3, September 1951 Research Paper 2242

A Sonic-Flow Pyrometer for Measuring Gas Temperatures[1]

George T. Lalos

Evaluation of the performance of gas turbines and jet engines requires knowledge of the temperature of the working medium. Although conventional temperature-measuring instruments are adequate for some purposes, they possess a number of disadvantages that become more serious with increasing gas velocity and temperature. The most troublesome sources of error are the directed motion of the gas and the loss of heat to the surroundings by radiation and conduction. An instrument that is relatively free of these errors is described and evaluated. It has been called a sonic pyrometer because the measuring element is located in the throat of a nozzle through which the gas, whose temperature is to be measured, is caused to flow at sonic velocity. In accordance with theory and experiment, the total temperature of the gas is obtained by multiplying the temperature indicated by the measuring element by an essentially constant correction factor. Tests on experimental units indicate that these have many advantages over conventional instruments when used in the evaluation and control of gas turbines and jet engines.

1. Introduction

While conventional instruments for measuring the temperature of the working medium of gas turbines and jet engines are adequate for some purposes, they have certain inherent disadvantages that become more serious with increasing gas temperature and velocity. Particularly troublesome are the effects on temperature-sensing elements of directed motion of the gas and of heat loss to the surroundings by radiation and conduction.

As will be shown, these effects become negligibly small in an instrument of the type described. In such an instrument the measuring junction of a thermocouple is located within the throat of a small nozzle, through which the gas whose temperature is to be measured is caused to flow at sonic velocity. For the latter reason, such a modification of the familiar suction pyrometer is here called a sonic pyrometer.

When the velocity of the gas in the free-stream exceeds a few hundred feet per second, the kinetic energy of directed motion becomes an appreciable fraction of that due solely to random molecular motion. For a complete energy accounting under these conditions it is therefore necessary to recognize two temperatures, pressures, and enthalpies in specifying the energy state of the moving gas. These are frequently identified by the adjectives static and total. As an example, the static temperature would be indicated by an error-free thermocouple moving in the same direction and at the same velocity as the gas, that is, by one that is static with respect to the gas; the total temperature would be indicated by an error-free instrument immersed in the gas after the latter is brought to rest adiabatically.

The relation between these two temperatures of a flowing gas can be expressed by the well-known equations

$$T_t - T_s = V^2/2gJC_p, \tag{1}$$

and

$$T_t/T_s = 1 + (\gamma - 1)M^2/2, \tag{2}$$

in which T is absolute temperature (°R), V is velocity (ft/sec), g is the acceleration of gravity (ft/sec^2), J is the mechanical equivalent of heat (ft lb/Btu), C_p is heat capacity at constant pressure (Btu/lb deg R), γ is the specific heat ratio, M is Mach number, and the subscripts s and t signify static and total, respectively.

When an error-free, conventional temperature-sensing instrument is immersed in a flowing gas, it reaches and indicates a temperature (T_i) intermediate between T_t and T_s. Neither T_t nor T_s can be deduced from an observed value of T_i without further knowledge of the characteristics of the instrument.

Experiments have shown that each actual instrument, in the absence of other errors, attains a temperature that exceeds T_s by a nearly constant fraction of the interval $T_t - T_s$. This fraction, known as the recovery factor (r), is a function of the configuration of the instrument and changes little with the composition, temperature, pressure, or velocity of the flowing gas. The above definition of recovery factor is expressed by the equation

$$r = (T_i - T_s)/(T_t - T_s). \tag{3}$$

Combining eq 1 and 3 gives

$$T_i = T_s + (1 - r)V^2/2gJC_p, \tag{4}$$

from which it is seen that the actual temperature of a high-velocity gas stream can be calculated from the

[1] The material contained in this report has been accepted by the Catholic University of America in partial fulfillment of the requirements for the degree of Master of Science in Physics.

temperature indicated by a conventional instrument only when the velocity and heat capacity of the gas and the recovery factor of the instrument are known. This requirement obviously constitutes a serious limitation to the application of conventional sensing elements at high gas velocities.

It is to be noted that the higher the recovery factor of the instrument, the smaller is the difference between T_t and T_s, and the less is the need for accuracy in the values of V and C_p. Total-temperature probes, which indicate T_t directly, are in common use in the low-temperature range. However they are not practical at high temperatures and under the extreme mechanical stresses existing in gas turbines. Nevertheless, an instrument designed for engine applications should have the highest practicable recovery factor.

Conventional instruments have a second limitation that can be understood by considering the heat transfer to and from the surroundings. In most applications, the gas turbine being a common one, the retaining walls are colder than the gas. A measuring instrument immersed in the stream thus attains a steady temperature below that of the gas, because energy is lost by the sensing element to the walls by radiation and conduction. The temperature indicated by the element is determined by the relative rates of heat transfer from the gas by forced convection and to the surroundings by radiation and conduction. The heat exchange with the surroundings is a function of the temperatures of the element and the walls, and that part that is due to radiation increases approximately as the fourth power of the gas temperature. From the standpoint of thermometric error, it is obviously desirable that the rate of transfer to the element be high as compared with the rate of loss.

For a conventional element installed in a gas turbine, no independent control can be exercised over the mass rate at which gas flows over the instrument, which in turn determines the rate of heat transfer to the unit by forced convection. Actually this rate is a function of the operating conditions alone, and these, for aircraft gas turbines, involve flow rates that decrease with altitude. Thus, although the error of a conventional instrument due to radiation and conduction could be reduced by increasing the mass flow past the sensing element, not only is it impossible to exercise such control in an engine, but also the accuracy of the measured temperatures decreases with decreasing ambient pressure (i. e. with increasing altitude).

From the above facts, it is clear that improved performance and simplified over-all instrumentation may be possible by modifying conventional sensing elements so that (a) the recovery factor is increased; (b) the rate of heat loss from the sensing element by radiation and conduction is decreased; (c) the mass flow across the element is as high as practicable; and (d) the temperature indicated is independent of the free-stream velocity.

It will be shown that a sonic pyrometer can be designed to have most of these advantages, and that it therefore deserves careful consideration in the instrumentation of gas turbines. Previous reports on the sonic pyrometer appeared as classified documents, and more recently a paper published by Allen and Hamm [1] described one instrument of this type. The present detailed study was undertaken because none of the previous reports contain a careful evaluation of the several important design variables.

The present results, obtained with three experimental units, are in excellent agreement with theory, and indicate that a single calibration in air at a relatively low temperature, together with a knowledge of the γ of the gas in which the instrument is applied, suffices for calculating reliable values of T_t from observed values of T_s over the range experienced in gas turbines.

2. Theory of the Sonic Pyrometer

Sonic gas velocity (V_c) is always maintained over the measuring junction of the sonic pyrometer. This velocity may be expressed as follows in terms of the properties and state of the gas:

$$V_c^2=\gamma g R T_s, \tag{5}$$

in which R is the gas constant in ft lb/lb deg Rankine, and the other quantities have been defined previously.

Since $C_p-C_v=R/J$, eq 1 and 5 under conditions of sonic flow may be combined to give

$$T_s=2T_t/(\gamma+1). \tag{6}$$

Combining eq 4, 5, and 6 gives

$$T_t=(\gamma+1)T_t/[2+r(\gamma-1)]=\alpha T_t, \tag{7}$$

where $\alpha=(\gamma+1)/[2+r(\gamma-1)]$.

Calibration and use of the sonic pyrometer would be extremely simple if the α of a given instrument were completely independent of operating conditions. This cannot be so, because γ decreases somewhat with increasing temperature. Application of the instrument remains relatively simple if r is sensibly constant, even though the effect of changing γ must be taken into account. It is to be noted that both α and r approach unity simultaneously, and that the dependence of α upon γ becomes vanishingly small as r approaches unity.

To illustrate these points, assume that a sonic pyrometer, for which α has been determined by using air having a $\gamma=1.400$, is applied in high-velocity streams of air at elevated temperatures, and that the latter temperatures are calculated by multiplying each observed value of T_t by the same constant α. Under the calibration conditions, α is simply the ration T_t/T_s, of two measured quantities, and since the γ of the calibrating air is 1.400,

$$\alpha=6/(5+r). \tag{8}$$

This α is not exactly correct at any other tempera-

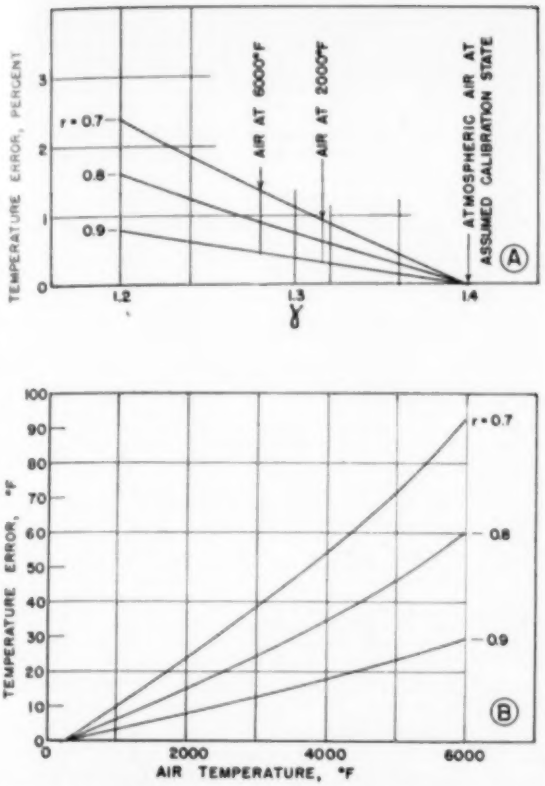

FIGURE 1. *Temperature errors that arise if the variation of γ with temperature is neglected, as calculated for sonic pyrometers having various values of recovery factor, r.*

ture, and from eq 7 and 8 the fractional error, E, of each observed value of T_t due to deviations in γ from the calibration value of 1.400 is

$$E=\frac{(r-1)(5\gamma-7)}{(r+5)(\gamma+1)}. \tag{9}$$

Such errors, expressed in percentage, are plotted in figure 1, A, as funcions of γ at assumed constant values of r over the range of the latter, which is to be expected from a thermocouple junction in a sonic pyrometer. Using tabulated values of the γ of air as a function of temperature [2], the percentage errors can be interpreted in terms of absolute error, as has been done in figure 1,B. It can be seen that changes in E due to changes in r and in γ are small, and that it is desirable to make r as high as is practicable.

In the preceding example it has been assumed that the recovery factor of a given instrument has the same value, $r=6/\alpha-5$, during the calibration and in actual use. If this assumption is correct, then the errors discussed in the foregoing example can be avoided as follows: In a calibration under convenient conditions (as with air at a relatively low temperature), determine r as $6T_t/T_s-5$; apply the instrument in any gas, and calculate T_t from eq 7, using the actual value of γ and the experimental value of r. One of the purposes of the present tests was to determine whether such a procedure was permissible with the sonic pyrometer.

It is to be expected that the recovery factor of a bare thermocouple junction located in a sonic stream and obstructing only a small fraction of the flow area will approach the theoretical value for a flat plate, which, according to Pohlhausen [3], and more recently to Emmons and Brainerd [4], approaches 0.87. Another purpose of the present tests was to determine how closely this theoretical value could be approached in a practical sonic pyrometer.

3. Apparatus and Results

Three experimental sonic pyrometers, designated as 1, 2, and 3, were built and evaluated. Unit 1 was designed for low temperatures only, with the idea that it would yield enough information to determine whether the construction of more elaborate instruments seemed worth while. Unit 2 was built for use up to 1,500° F, but without regard to its suitability for use in gas turbines, particularly as to its size. Unit 3 was designed on a smaller scale, and its performance was investigated in much greater detail than was that of the other two.

The calibration equipment, with the No. 1 unit mounted for test, is shown diagrammatically in figure 2. The sole purpose of the pressure taps was for initial evaluation of nozzle performance and to insure that the flow was sonic at station 2 during use. The flow area at station 1 was so large that the impact effect was negligible, and the thermocouple there served for the accurate measurement of $T_{1s}=T_{1t}$. From this chamber the gas passed to the nozzle of the sonic pyrometer and was accelerated to sonic velocity at station 2 by maintaining the ratio P_{2s}/P_{1s} always below the required critical value. This could be done in the test system either by compressing to increase P_{1s}, or by pumping to reduce P_{2s}. Since it would complicate a service instrument to install a pressure tap at the throat of the nozzle, a second downstream pressure tap was installed at station 3. If the flow area between stations 2 and 3 is made large as compared with the area of the throat, the pressures at these two stations are approximately equal, and only the tap at station 3 is needed. It is further advantageous to keep the pressure drop between stations 2 and 3 small in order that sonic flow may be maintained with a minimum of pressure at station 1 during discharge to the atmosphere or with a minimum of pumping on the discharge of the unit.

In tests at room temperature the heat loss between stations 1 and 2 is entirely negligible. Since air behaves nearly as a perfect gas, there is no change in total temperature between these stations, so that T_{2t} is identical with the measured T_{1t}. The calibration value of α is simply the ratio of the observed

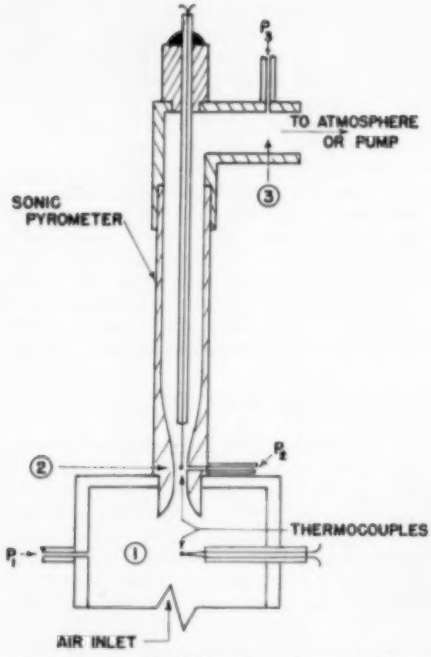

FIGURE 2. *Diagram of calibration equipment with sonic pyrometer 1 mounted for test.*

quantities $T_{1t}=T_{2t}$ and T_{2t}. The recovery factor of the unit is $6/\alpha-5$ when the γ of the calibrating air is 1.400.

3.1. Experimental Sonic Pyrometer 1

The first unit, designed for preliminary studies at temperatures below 400° F and shown in cross section in figure 2, had a convergent-divergent brass inlet nozzle with a cylindrical throat three-eighths in. long and 0.165 in. in diameter. A bare thermocouple junction of No. 28 gage Chromel and Alumel wire was located centrally at the downstream end of the throat (station 2), directly alongside a static pressure tap. The junction itself was approximately spherical and had a diameter about twice that of either thermocouple wire. An identical thermocouple was installed at station 1 in a comparatively large inlet chamber, for the measurement of $T_{1t}=T_{1s}=T_{2t}$. The static pressures in the inlet chamber, nozzle throat, and exit passage were measured with mercury manometers.

Air supplied to the inlet chamber could be maintained by electric heaters at any desired steady temperature in the range from room temperature to 400° F. Thermal electromotive forces were measured with a semiprecision potentiometer. Sonic flow through the nozzle could be maintained either by establishing the necessary pressure in the inlet chamber and discharging into the atmosphere, or by pumping at the exit when required.

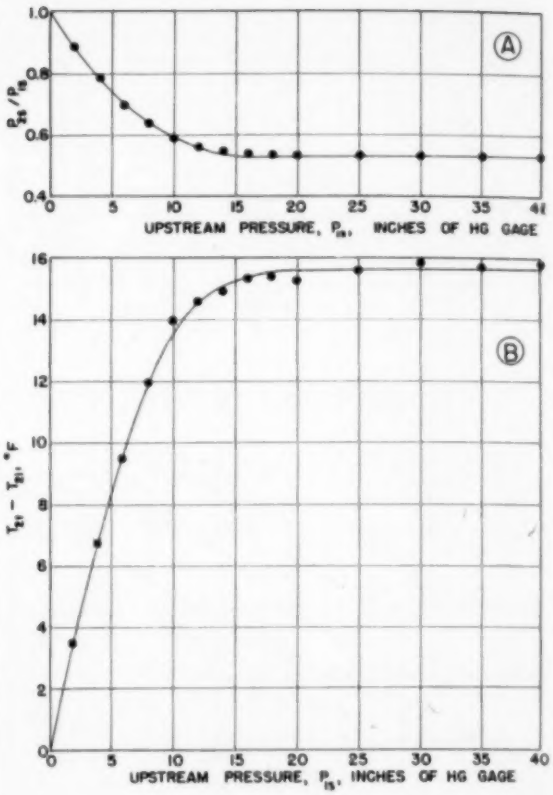

FIGURE 3. *Performance of sonic pyrometer 1.*

The characteristics of the instrument, as determined with atmospheric air (74° F; $\gamma=1.400$) and with $P_{2s}=1$ atm are shown in figure 3. Figure 3, A, in which the pressure ratio P_{2s}/P_{1s} is plotted against P_{1s} in inches of mercury gage, shows that the nozzle of the pyrometer behaves in accordance with theory, since P_{2s}/P_{1s} attains a constant value of 0.53. At all values of P_{1s} greater than 20 in. mercury gage, the flow is therefore sonic in the throat, and the desired condition for the operation of the pyrometer prevails. In figure 3, B, the observed difference in temperature $T_{2t}-T_{2t}$ is plotted against upstream static pressure. Again in accordance with theory, this difference increases with the velocity in the throat (i. e. with increasing P_{1s}) until this velocity becomes sonic at $P_{1s}=20$ in. mercury gage. For all higher values of P_{1s}, the total and indicated temperatures of the gas in the throat of the nozzle remain constant and differ by 15.6 deg F. The measured values of $T_{2t}=533.7°$ R and $T_t=518.1°$ R constitute a calibration of the unit. Inserting these values, and $\gamma=1.400$, in eq 7 gives $\alpha=1.030$ and $r=0.825$.

In all experiments of this type, the thermocouples at stations 1 and 2 were made from adjacent lengths of wire to avoid possible errors from inhomogeneities. The emfs of the thermocouples were always read

dividually and by bucking one against the other (i. e. differentially), and in no case did the observed difference in temperature depart more than 0.1 deg F from that obtained by subtraction.

Using eq 7, the results may be computed in the following ways: (a) on the assumption that α always has the same value as that determined in the calibration run; (b) on the assumption that r always has the same value as that determined in the calibration run, but that α varies with γ; or (c) the appropriate values of T_{2t}, T_{2s}, and γ may be used in solving for a value of r for each run. Table 1 summarizes the data for four runs made at initial temperatures of 74° (calibration), 279.0°, 395°, and 400° F, and of results calculated on the aforementioned bases. The next to the last column gives values of the static temperature (T_{2s}) in the nozzle throat, calculated from eq 2 for the condition of sonic flow, that is, when $M=1$.

The tabulated values show that the sonic pyrometer gives values of the total temperature of the high-velocity air that differ in no case from the value observed before the air is accelerated by more than 0.6 deg F, regardless of the assumptions made as to α and γ, and despite increasing differences between

TABLE 1. *Results obtained with sonic pyrometer 1*

Run No.	Observed temperatures		γ from tables	T'_{2t} (calc), assuming $\alpha=1.030$	$T_{2t}-T'_{2t}$ (calc)	T''_{2t} (calc), assuming $r=0.825$	$T_{2t}-T''_{2t}$ (calc)	r, from eq 7	Deviation from mean r	T_{2s}, from eq 2	$T_{2t}-T_{2s}$
	T_{2t}	T_{2t}									
	°R	°R		°R	°R	°R	°R		*Percent*	°R	°R
*1	533.7	518.1	1.400	533.7	0.0	533.7	0.0	0.825	+0.2	444.8	88.9
2	738.7	717.0	1.395	738.5	.2	738.3	.4	.822	−.2	616.9	121.8
3	854.7	830.4	1.388	855.3	−.6	854.7	.0	.825	+.2	715.8	138.9
4	859.7	834.8	1.388	859.8	−.1	859.2	.5	.822	−.2	720.0	139.7
							Mean	0.823$_5$			

* Calibration run, giving $\alpha=1.030$ and $r=0.825$.

T_{2t} and T_{2s}. The calculated values of recovery factor are sensibly constant, the maximum deviation from the mean value of r being only 0.2 percent.

Although the range of temperatures used in the tests described is very small, the tabulated results were believed to indicate that unit No. 1 showed sufficient promise to warrant the construction and evaluation of more practical units, designed for higher temperatures.

3.2. Experimental Sonic Pyrometer 2

In this unit, shown photographically in figure 4 and schematically in figure 5, the nozzle and supporting parts were made of 18–8 stainless steel, and the nozzle was surrounded by an outer tube (1⅛- in. outside diameter), which served as a radiation shield. To aid in bringing both the nozzle and its shield to the gas temperature, gas was brought to stagnation in the space between these parts, and small bleed holes were provided to renew this stagnant gas slowly.

The throat of the nozzle had a diameter of 0.21 in. and was cylindrical for a length of three-eighths in. A pressure tap in the throat was used only in preliminary tests made to show that sonic flow was attained at all pressure ratios below 0.53, in the manner already illustrated in figure 3.

A No. 22 gage Chromel-Alumel thermocouple junction, filed to the form of a flat disk having a thickness equal to and a diameter twice that of a single wire, was mounted centrally at the downstream end of the cylindrical throat. Thermal electromotive forces in the tests of sonic pyrometers 2 and 3 were measured with a Brown Electronik potentiometer.

After calibration in the manner already described, the instrument was tested in the exhaust gas stream from a Jumo 004 combustor, using the equipment

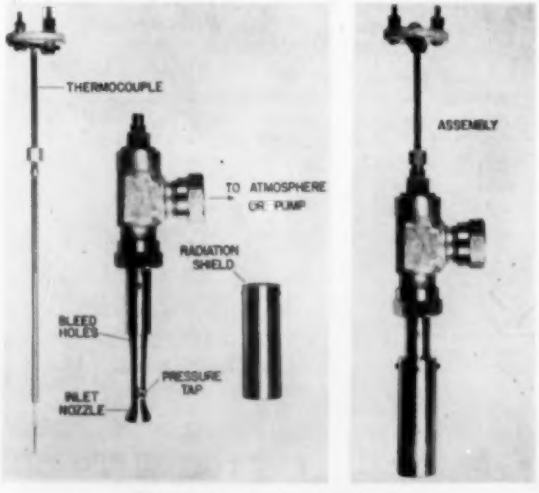

FIGURE 4. *Sonic pyrometer 2.*

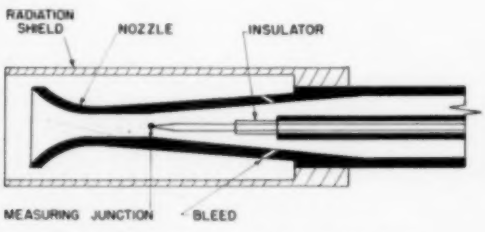

FIGURE 5. *Diagram of sonic pyrometer 2.*

shown diagrammatically in figure 6. A shielded thermocouple, for which radiation corrections [5] were known accurately, and the sonic pyrometer, were inserted radially to the center of the 6-in. test section. Gas velocities here did not exceed 300 ft/sec, so that the corrections for impact on the thermocouple were always less than 3 deg F.

Observations were made at gas temperatures from 400° to 1,300° F, in intervals of 100 deg F. In most runs, the temperature of the walls was made equal to that of the gas, so that radiation could not affect either the shielded thermocouple or the sonic pyrometer. In order to determine the effects of radiation on the latter, other runs were made with the walls cooler than the gas by measured amounts.

All of the results with sonic pyrometer 2 are summarized in table 2. The calibration data, obtained with air at about room temperature, are given in the first horizontal line. For this unit, the calibration gives $\alpha=1.0205$ and $r=0.8795$. Starting at the left, columns in the table show in order the values of gas temperature indicated by the shielded thermocouple (T_{1t}), the corrections applied to the shielded couple for radiation (ΔT_r) and impact (ΔT_r), the corrected total temperature ($T_{1t}=T_{1t}+\Delta T_r+\Delta T_r$) of the gas in the test system as determined with the radiation-shielded thermocouple, and the temperature indicated by the thermocouple of the sonic pyrometer (T_{2t}). Observed quantities not listed in table 2 are the pressure in the test section and the pyrometer discharge pressures.

The remaining columns of table 2 show the effects of various possible methods of computing T_{2t} from the observed values of T_{2t}. In the column marked

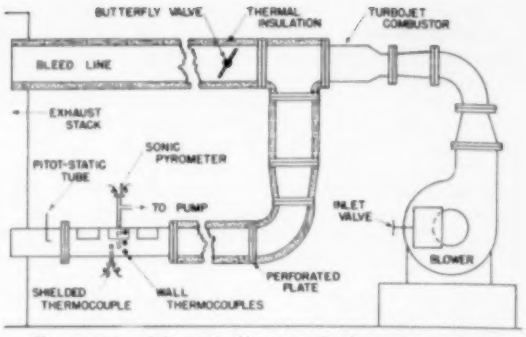

FIGURE 6. *Schematic diagram of exhaust-gas system.*

α(obs) the ratio T_{2t}/T_{1t} is given for each run. While the maximum spread in the observed values of this ratio is only 0.4 percent, the ratio shows a definite decrease as the gas temperature increases. As is evident from the last two columns of table 2, the ratio decreases linearly with temperature, in accordance with the empirical equation $T_{2t}/T_{1t}=\alpha$ (smoothed) $=1.0225-38\times10^{-7}T_{1t}$, in which T_{1t} is expressed in deg F.

If the value $\alpha=1.0205$, determined in the calibration with air at room temperature, is applied directly to the other runs, the temperatures listed in the column headed T''_{2t} are obtained. The corresponding errors, $T_{2t}-T''_{2t}$ include both the experimental errors and those introduced by neglecting changes in γ. Even so, the maximum error is less than 7 deg F, which is probably small enough for most purposes.

TABLE 2. *Results with sonic pyrometer 2*

Silver-shielded thermocouple						Sonic pyrometer, T_{2t}	α(obs) $=T_{2t}/T_{1t}$	$T''_{2t}=1.0205T_{1t}$	$T_{2t}-T''_{2t}$	γ	r (eq 7)	$T''_{2t}=\frac{(\gamma+1)T_{1t}}{2+0.8795(\gamma-1)}$	$T_{1t}-T''_{2t}$	α(sm)[a]	$\frac{\alpha(\text{obs})-\alpha(\text{sm})}{\alpha(\text{obs})}$
T_{1t}	ΔT_r	ΔT_r	$T_{1t}=T_{1t}+\Delta T_r+\Delta T_r$	$T_{1t}-T_w$											
Calibration run															
°F	°R	°R	°R	°R	°R	°R		°R	°R			°R	°R		*Percent*
109.0	568.7	0	0	568.7	0	557.3	1.0205	.....	.....	1.3986	0.8795	.....	.....	1.0221	−0.16
Runs without loss by radiation															
400.0	859.7	0	0.1	859.8	0	842.2	1.0209	859.4	0.4	1.384	0.873	859.0	0.8	1.0210	−0.01
500.0	959.7	0	0.7	960.4	0	941.7	1.0199	961.0	−.6	1.378	.877	959.6	.8	1.0206	−.07
590.0	1049.7	0	0.8	1050.5	0	1030.2	1.0197	1051.3	−.8	1.371	.877	1049.8	.7	1.0203	−.06
600.0	1059.7	0	1.0	1060.7	0	1039.9	1.0200	1061.2	−.5	1.371	.875	1059.7	1.0	1.0203	−.03
697.5	1157.2	0	1.0	1058.2	0	1135.5	1.0200	1158.6	−.6	1.363	.872	1157.1	1.1	1.0198	+.02
798.3	1258.0	0	1.3	1259.3	0	1234.6	1.0200	1260.9	−.6	1.357	.871	1257.6	1.7	1.0195	+.05
900.0	1359.7	0	1.6	1361.3	0	1333.9	1.0205	1361.2	.1	1.350	.865	1358.3	3.0	1.0191	+.14
1000.0	1459.7	0	1.8	1461.5	0	1432.4	1.0203	1461.8	−.3	1.343	.864	1458.1	3.4	1.0187	+.16
1080.0	1549.7	0	1.9	1551.6	0	1523.6	1.0184	1554.8	−3.2	1.337	.875	1550.5	1.1	1.0182	+.02
1100.0	1559.7	0	1.9	1561.6	0	1531.8	1.0194	1563.2	−1.6	1.337	.869	1558.9	2.7	1.0182	+.12
1200.0	1659.7	0	2.3	1662.0	0	1632.7	1.0179	1666.2	−4.2	1.331	.876	1661.1	0.9	1.0179	.00
1300.0	1759.7	0	2.6	1762.3	0	1733.5	1.0166	1769.0	−6.7	1.326	.883	1763.3	−1.0	1.0176	−.10
Runs to determine the effects of radiation															
900.0	1359.7	1.8	1.8	1363.3	378	1338.0	1.0189	1365.4	−2.1	1.350	0.874	1362.4	1.1	1.0191	−0.02
1110.0	1569.7	3.3	1.9	1574.9	408	1547.6	1.0176	1579.3	−4.4	1.337	.886	1575.0	−1.4	1.0182	−.06
1200.0	1659.7	4.5	2.1	1666.3	539	1638.6	1.0169	1672.2	−5.9	1.331	.881	1667.4	−0.6	1.0179	−.10
1310.0	1769.7	5.1	1.8	1776.6	506	1746.0	1.0175	1781.8	−5.2	1.326	.878	1776.0	.6	1.0176	−.01
										Avg....	0.875				

[a] α(smoothed) $=1.0225-38\times10^{-7}T_{1t}$(°F).

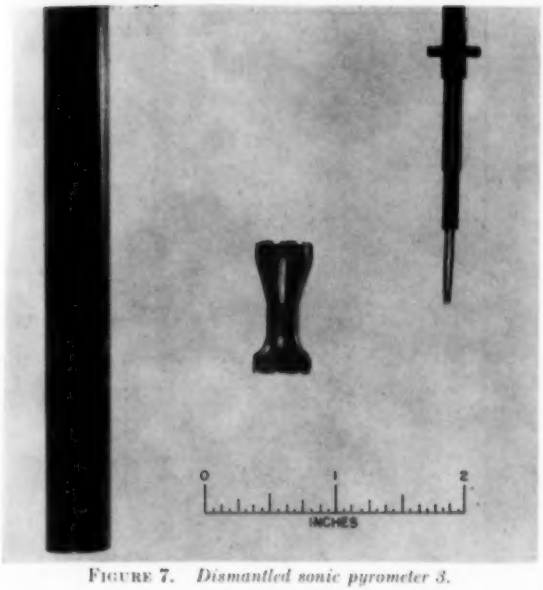

FIGURE 7. *Dismantled sonic pyrometer 3.*

A more accurate method of applying the calibration data is to calculate r for the calibration run, and to use this value with the appropriate values of γ in eq 7. This has been done in the column headed T''_{2t}, and the maximum error $(T_{2t}-T''_{2t})$ is found to be half as great as in the previous method of reduction. Furthermore $T_{2t}-T''_{2t}$ does not continue to increase with temperature. This merely shows that a small but definite improvement is made by taking the changes in γ into account. It also illustrates, once again, that the γ need not be known precisely, since a change from 1.400 to 1.326 alters the result by less than 6 deg F.

Most of the differences, $T_{2t}-T''_{2t}$, are of the same sign, and in a direction indicating that the recovery factor determined in the calibration run was higher than that for the other runs. This can be examined in more detail by substituting the measured values of T_{2t} and T_{2t}, along with appropriate values of γ, in eq 7 to calculate an individual value of r for each run. As the tabulated results show, the maximum spread in r is about 2.5 percent; the calibration r is higher than most of the others and about 0.5 percent higher than the average. Possible explanations for this are discussed later in connection with the results obtained with pyrometer 3.

If the effects of radiation and conduction on the performance of the sonic pyrometer are significant, these should be apparent in the last four horizontal lines of table 2. In these runs, the walls were from 378 to 559 deg colder than the gas, yet the differences $T_{2t}-T''_{2t}$ and $T_{2t}-T''_{2t}$ are no greater than they are at the same gas temperatures in the runs without heat losses. Hence it is concluded that the shielding features, plus the high mass flow rate over the measuring junction, combine to render the heat losses entirely negligible. It is obviously a great advantage

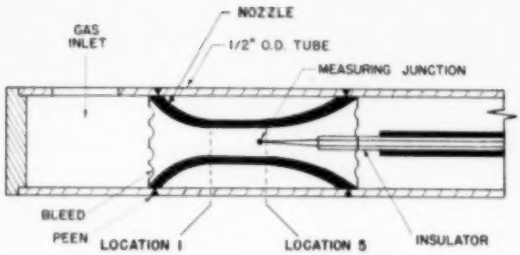

FIGURE 8. *Diagram of sonic pyrometer 3.*

of this type of instrument that this feature can be built in, so that no separate determination or evaluation of corrections is required.

On the basis of the highly encouraging results obtained with pyrometers 1 and 2, it was considered desirable to design and evaluate a smaller unit, which might be installed in a restricted passage without blocking off the flow area unduly. To this end, unit No. 3 was built within a cylindrical tube having an external diameter of ½ in. In addition to tests like those already described, the effects of the following features were investigated: axial location of the measuring junction; shape of the junction; the technique of calibration, with particular attention to the effect of moisture condensation if unheated and undried air is used; and the rate of response to sudden changes in temperature.

3.3. Sonic Pyrometer 3

In this unit, shown photographically in figure 7 and diagrammatically in figure 8, the nozzle was made of 18–8 stainless steel and the outer tube of ½-in. Inconel. The end of the latter was closed, and a 1/16-in. diameter hole was drilled near the closed end of the tube for admission of gas.

The nozzle, having a cylindrical throat 0.157 in. in diameter and ¼ in. long, was fitted snugly within the Inconel tube, except where notches were cut at either end to admit some gas to the intervening space. The tube was peened in to anchor the nozzle at both ends.

a. Effects of Axial Location of the Junction

During tests of this unit, various junctions of No. 22 gage Chromel and Alumel were mounted axially. Provision was made for locating the junction reproducibly at any one of the following positions:

Location No.	Distance from upstream end of cylindrical throat
	Inches
1	0
2	1/8
3	5/16
4	7/32
5	1/4
6	5/16
7	3/4

It was expected that sonic velocity would prevail at the downstream end of the cylindrical throat, but exact location of this plane in the hand-made nozzle is impossible. Hence tests were made with the measuring junction at locations only one thirty-second in. apart in this region.

The calibration results obtained with air initially at about 100° F. are presented in figure 9, in which the observed temperature differences ($T_{2t}-T_{2t}$) are plotted against the suction, in inches of Hg, applied at the outlet of the pyrometer, for each of the seven junction locations. The curves for locations 1 through 3 become horizontal after the critical pressure is reached. The plane of sonic velocity appears to be in the region between locations 3 and 5, and probably between 3 and 4, since the curve for location 4 continues to rise slightly as the suction is increased. The slope of the curves at higher suctions increases progressively at locations 5, 6, and 7, indicating supersonic flow there.

The curves of figure 9 indicate that the gas velocity increases progressively from location 1 to location 7. It is sonic somewhere in the one-sixteenth in. between locations 3 and 5. Only at this place do the equations for the sonic pyrometer apply exactly, because only here is the square of the gas velocity equal to γgRT_s. However, this means merely that the junction should not be located downstream from position 5, and not that locating it farther upstream is seriously disadvantageous. As will be shown later, the instrument performs equally well with the junction at locations 2, 3, 4, and 5, and it is believed that location 1 would also have been found satisfactory if runs had been made with that configuration. This is so because the Mach number at any upstream station remains constant when the critical pressure ratio is maintained across the nozzle, and because the effect on recovery factor of variations in velocity at constant M is insignificant.

Perhaps the most important conclusion to be drawn from figure 9 is that the junction should be kept at one and only one location during calibration and subsequent use. Full appreciation of the importance of junction location did not develop until after the tests of pyrometer 2 were completed. Therefore, some of the small variations in the ratio T_{2t}/T_{2t} noted with that unit may have been due to insufficient care in bringing the junction always to the same axial location.

b. Performance Tests

Tests of sonic pyrometer 3 in exhaust gas were made in the same manner and with the same equipment used for unit 2. A series of runs was made with the measuring junction at locations 2, 3, 4, and 5. Again, most of the runs were made with the gas and the walls at the same temperature, and a limited number were made with colder walls to see whether the heat loss affected the instrument significantly. All of the results are presented in table 3, which has the same general form as table 2, and therefore need not be described in detail.

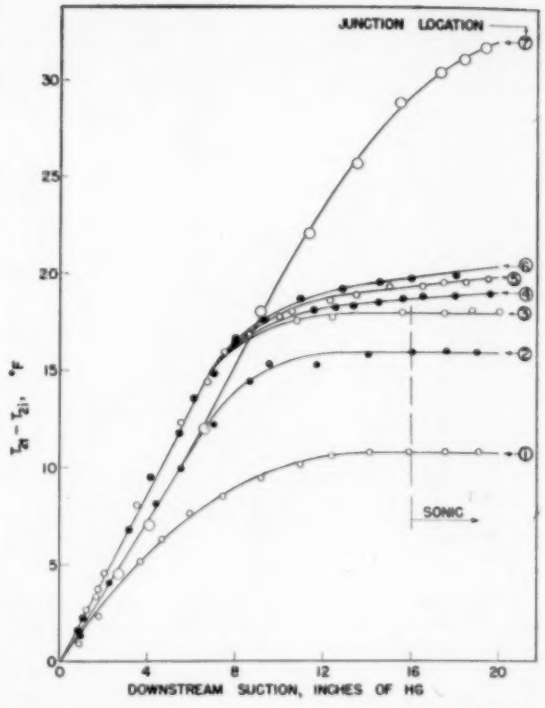

FIGURE 9. *Effect of axial location of the measuring junction on the calibration of unit 3 ($T_t=100°$ F.).*

In general, unit 3 showed the same characteristics as No. 2, namely that it was capable of measuring accurate values of the total temperature of streaming exhaust gas; that no corrections for radiation or conduction were required; and that the recovery factor determined with air at room temperature was slightly higher than the average of values determined at elevated temperatures.

In addition, the following characteristics are evident from the table. If an error of 15 deg F can be tolerated, it is necessary only to determine α with air at room temperature and to consider that α is constant. The total temperature is then the constant α times T_t, and γ need not be known. If the recovery factor is calculated from the calibration and this value is held constant for all other runs, the error is reduced to less than 3 deg F in the range up to 1,500° F when the appropriate values of γ are used. These need not be known precisely.

The error can be reduced to less than 2 deg F if the instrument is calibrated over the range of temperatures in which it is to be used, and the resulting values of r are used in conjunction with the proper values of γ. A separate accurate instrument is required for this kind of calibration, which is certainly not required for applications in engines where large temperature gradients are present normally.

TABLE 3. *Results with sonic pyrometer 3*

	T_D	ΔT_r	ΔT_s	$T_D=T_D+\Delta T_r+\Delta T_s$	T_D-T_w	T_D	$a(\text{obs})=T_D/T_D$	T_D'	T_D-T_D'	γ	r (eq 7)	T_D''	T_D-T_D''	$a(\text{sm})$	$\frac{a(\text{obs})-a(\text{sm})}{a(\text{obs})}$
Measuring Junction at Location 2															
Calibration run	°F 150	°R 609.7	°R 0	°R 0.1	°R 609.8	°R 0	°R 560.8	1.0322	..... $1.0322\,T_D$	°R	1.3978	0.812	°R $r=0.812$	°R		[a] 1.0342	*Percent* −0.22
Runs without loss by radiation	540	999.7	0	0.4	1000.1	0	969.8	1.0312	1001.0	0.1	1.374	0.808	999.4	0.7		1.0317	.05
	775	1234.7	0	.7	1235.4	0	1199.0	1.0304	1237.6	−2.2	1.356	.805	1234.0	1.4		1.0302	.02
	895	1354.7	0	.9	1355.6	0	1316.9	1.0294	1359.3	−3.7	1.350	.808	1354.8	0.8		1.0294	.00
	995	1454.7	0	1.1	1455.8	0	1414.9	1.0289	1460.4	−4.6	1.344	.807	1455.0	.8		1.0287	.02
	1080	1539.7	0	1.3	1541.0	0	1499.6	1.0276	1547.9	−6.9	1.338	.814	1541.5	−.5		1.0282	−.06
	1190	1649.7	0	1.3	1651.0	0	1606.7	1.0276	1658.4	−7.4	1.332	.811	1650.9	.1		1.0275	.01
	1290	1749.7	0	1.7	1751.4	0	1705.7	1.0268	1760.6	−9.2	1.326	.814	1751.8	−.4		1.0268	.00
Run to determine the effects of radiation	1445	1904.7	3.6	1.8	1910.1	195	1862.3	1.0257	1922.3	−12.2	1.318	.817	1911.6	−1.5		1.0258	−.01
											Avg..	0.811					
Measuring Junction at Location 3															
Calibration run	110	569.7	0	0.1	569.8	0	551.3	1.0336	..... $1.0336\,T_D$	.....	1.3986	0.804	..... $r=0.804$	.....		[b] 1.0366	−0.30
Runs without loss by radiation	550	1009.7	0	0.4	1010.1	0	977.8	1.0330	1010.6	−0.5	1.374	.797	1008.9	1.2		1.0337	−.07
	700	1159.7	0	.7	1160.4	0	1123.8	1.0326	1161.6	−1.2	1.363	.794	1158.6	1.8		1.0327	−.01
	790	1249.7	0	.8	1250.5	0	1211.4	1.0323	1252.1	−1.6	1.357	.793	1248.4	2.1		1.0322	.01
	890	1349.7	0	.9	1350.6	0	1309.6	1.0313	1353.6	−3.0	1.350	.796	1348.9	1.7		1.0315	−.02
	990	1449.7	0	1.1	1450.8	0	1407.1	1.0310	1454.4	−3.6	1.344	.795	1448.7	2.1		1.0309	.01
	1085	1544.7	0	1.2	1545.9	0	1501.0	1.0299	1551.4	−5.5	1.338	.799	1544.7	1.1		1.0303	−.04
	1195	1654.7	0	1.4	1656.1	0	1609.2	1.0291	1663.3	−7.2	1.332	.801	1655.3	0.8		1.0295	−.04
Runs to determine effects of radiation	1375	1834.7	3.5	1.8	1840.0	200	1789.0	1.0285	1849.1	−9.1	1.321	.800	1838.7	1.3		1.0284	.01
	1435	1894.7	4.0	1.8	1900.5	235	1849.2	1.0277	1911.3	−10.8	1.318	.804	1900.2	0.3		1.0280	−.03
											Avg..	0.798					
Measuring Junction at Location 4															
Calibration run	110	569.7	0	0.1	569.8	0	550.6	1.0349	..... $1.0349\,T_D$	.....	1.3986	0.797	..... $r=0.797$	.....		[c] 1.0380	−0.31
Runs without loss by radiation	490	979.7	0	.4	980.1	0	948.3	1.0346	950.3	−0.2	1.378	.790	948.9	1.2		1.0354	−.08
	605	1064.7	0	.6	1065.3	0	1030.3	1.0340	1066.2	−.8	1.370	.789	1064.0	1.3		1.0346	−.06
	705	1164.7	0	.7	1165.4	0	1127.2	1.0339	1166.5	−1.1	1.363	.786	1163.5	1.9		1.0339	.00
	790	1249.7	0	.8	1250.5	0	1210.1	1.0334	1252.3	−1.8	1.357	.787	1248.5	2.0		1.0333	.01
	880	1339.7	0	.9	1340.6	0	1298.2	1.0327	1343.5	−2.9	1.350	.787	1338.7	1.9		1.0326	.01
	985	1444.7	0	1.1	1445.8	0	1400.7	1.0322	1449.6	−3.8	1.344	.787	1443.7	2.1		1.0319	.03
	1050	1549.7	0	1.3	1551.0	0	1503.8	1.0314	1556.3	−5.3	1.338	.789	1549.2	1.8		1.0312	.02
	1185	1644.7	0	1.3	1646.0	0	1597.4	1.0304	1653.1	−7.1	1.332	.793	1644.9	1.1		1.0305	−.01
Runs to determine effects of radiation	1420	1879.7	3.5	1.8	1885.0	209	1832.4	1.0287	1896.4	−11.4	1.319	.797	1885.0	0.0		1.0289	−.02
	1435	1894.7	3.0	1.8	1899.5	165	1847.5	1.0281	1912.0	−12.5	1.318	.801	1900.4	−.9		1.0288	−.07
	1500	1959.7	5.9	2.0	1967.6	350	1913.8	1.0281	1980.6	−13.0	1.310	.796	1967.4	.2		1.0283	−.02
											Avg..	0.792					
Measuring Junction at Location 5															
Calibration run	100	559.7	0	0.1	559.8	0	539.5	1.0376	..... $1.0376\,T_D$	.....	1.3988	0.782	..... $r=0.782$	.....		[d] 1.0395	−0.19
Runs without loss by radiation	530	989.7	0	.4	990.1	0	954.7	1.0371	990.6	−0.5	1.376	.774	988.8	1.3		1.0370	.01
	575	1034.7	0	.4	1035.1	0	999.0	1.0361	1036.6	−1.5	1.372	.778	1034.4	0.7		1.0367	−.06
	715	1174.7	0	.6	1175.3	0	1134.6	1.0359	1177.3	−2.0	1.362	.774	1173.8	1.5		1.0359	.00
	805	1264.7	0	.8	1265.5	0	1222.4	1.0352	1268.4	−2.9	1.356	.775	1264.0	1.5		1.0354	−.02
	895	1354.7	0	.9	1355.6	0	1309.5	1.0352	1358.7	−3.1	1.350	.772	1353.4	2.2		1.0348	.04
	1000	1459.7	0	1.1	1460.8	0	1412.9	1.0339	1466.0	−5.2	1.343	.776	1459.5	1.3		1.0342	−.03
	1085	1544.7	0	1.3	1546.0	0	1495.8	1.0336	1552.0	−6.0	1.338	.775	1544.5	1.5		1.0337	−.01
	1185	1644.7	0	1.3	1646.0	0	1593.5	1.0329	1653.4	−7.4	1.331	.776	1644.4	1.6		1.0331	−.02
	1280	1739.7	0	1.5	1741.2	0	1686.4	1.0325	1749.8	−8.6	1.326	.775	1739.5	1.7		1.0325	.00
Runs to determine effects of radiation	1320	1779.7	2.6	1.6	1783.9	170	1730.2	1.0310	1795.2	−11.3	1.324	.784	1784.4	−0.5		1.0323	−.13
	1465	1924.7	3.2	1.9	1929.8	165	1871.4	1.0312	1941.8	−12.0	1.317	.779	1928.9	.9		1.0315	−.03
	1483	1942.7	2.6	1.9	1947.2	143	1889.6	1.0305	1960.6	−13.4	1.316	.783	1947.5	−.3		1.0314	−.09
											Avg..	0.777					

[a] $a(\text{smoothed})=1.0352-65\times10^{-7}\,T_D(°\text{F})$. [b] $a(\text{smoothed})=1.0373-65\times10^{-7}\,T_D(°\text{F})$. [c] $a(\text{smoothed})=1.0388-7\times10^{-6}\,T_D(°\text{F})$. [d] $a(\text{smoothed})=1.0401-59\times10^{-7}\,T_D(°\text{F})$.

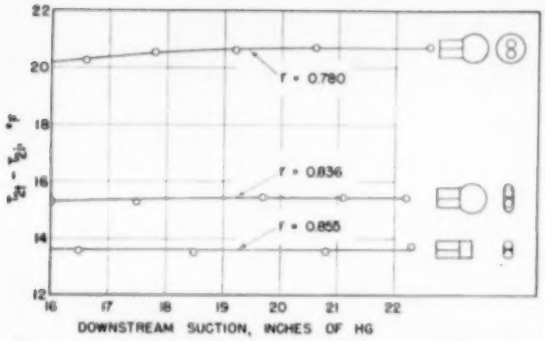

FIGURE 10. *Effects of the shape of the measuring junction.*

c. Effects of the Shape of the Junction

The measuring junction used in obtaining the results shown in table 3 was approximately spherical. This accounts for the fact that its recovery factor is lower than that of the flat junction used in unit 2. To further check on the effects of junction shape, unit 3 was calibrated with a junction in the form of a spherical bead, with one having the bead filed to a disk with thickness equal to the wire diameter, and with a third dressed until the upstream end had the area of the two thermocouple wires plus the two small welding fillets. These junction shapes can be visualized from the diagrams in figure 10, which also shows the results obtained with each of these junctions at location 4. The recovery factor of the junctions increase in the order in which they have been described, so that the junction with most of the bead filed away is best for use in a sonic pyrometer.

d. Effect of Moisture Condensation on Recovery Factor

As stated previously, each value of recovery factor determined with air at room temperature was slightly higher than the average of values determined at elevated temperatures. It was thought that this might be caused by condensation of water vapor during expansion through the nozzle, which is accompanied by a decrease of about 100 deg F in the static temperature of the gas. To check this hypothesis, a calibration system was devised whereby the temperature of the calibration air could be increased at will from ambient to about the boiling point of water. Depending upon the relative humidity of the ambient air, somewhere in this range the temperature becomes high enough that the dew point will not be reached in the throat of the nozzle.

The results of this calibration, made with a junction of minimum size at location 4 in pyrometer 3, are shown by the open circles in figure 11, in terms of recovery factor as a function of upstream temperature. The filled circles were obtained in a series of runs to be described later. The observed values of r decrease as the temperature of the inlet air rises and seem to approach a constant minimum value Effects of moisture condensation are believed responsible for the initial marked decrease in r. It is recognized also that changes in the axial location of the junction may result from differential expansion, though these are surely small because Chromel, Alumel, and Inconel have nearly identical coefficients of thermal expansion.

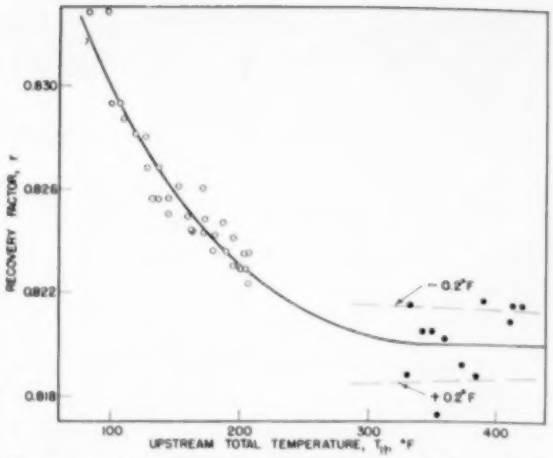

FIGURE 11. *Variation in recovery factor at low inlet temperatures, showing the effect of moisture condensation in the nozzle.*

Actually the curve of figure 11 is of more importance in showing how small, rather than how large, are the changes in r. The converging dashed lines at the right of the figure show the variation in r, which would produce an error of ± 0.2 deg F. As another example, at 400° F a change in r over the entire range covered by the curve, that is from 0.820 to 0.833, would introduce an error of only 1.9 deg F.

e. Effect of Free-Stream Velocity

Although the free-stream velocity was not expected to affect the performance of a sonic pyrometer, this was checked in simple tests with available equipment. Compressed air, heated in an exchanger, was passed through a 4-in. tube and discharged through a 2-in. nozzle into the atmosphere. A total-temperature probe was installed at the center of the 4-in. tube just upstream of the nozzle. The $\frac{5}{16}$-in. gas inlet to pyrometer 3 was placed in the axis of the jet, about 2 in. from the nozzle. As in the tests just described, the measuring junction had a minimum area and was at location 4. The total temperatue of the air was varied from about 330° to 420° F, and its velocity at the pyrometer from about 260 to 1,260 ft/sec. The results are presented in table 4.

The average value of the recovery factor over the range of these tests was 0.820, as can be seen from the filled circles in figure 11, as well as from table 4. In the next to the last column of this table, it can be seen that the gas temperatures observed with the total temperature probe and those calculated from the sonic pyrometer by eq 7 with r=0.820 are practically identical. This agreement at all velocities

through sonic is proof that the performance of the sonic pyrometer is completely independent of the free-stream velocity.

f. Rate of Response

When a temperature-sensing instrument immersed in the gas stream of an engine is to be used for control purposes, its rate of response to sudden changes in temperature is of greater importance than its absolute accuracy. It was therefore of interest to determine the characteristic time (τ) of sonic pyrometer 3. Using a method that has been described elsewhere [6], this pyrometer, with a spherical measuring junction at location 5, was found to have a characteristic time of 0.65 sec at several free-stream mass flow rates (G) between 3 and 5 lb/sec ft^2. Under the conditions of these measurements, the mass flow rate in the throat of the sonic nozzle was approximately 30 lb/sec ft^2. From previous tests, the bare junction alone in the free stream was known to have a characteristic time of 1.1 sec at a mass flow rate of 3 lb/sec ft^2. Thus the sonic pyrometer tested has a characteristic time approximately six-tenths as great as that which its measuring junction alone would have in the same free stream. This advantage is greatest at low stream velocities, and decreases to zero when the free-stream velocity is sonic, as may be seen in figure 12. In this example, it is assumed that a given thermocouple junction has a τ of 1.0 sec at a mass flow rate of 4 lb/sec ft^2; that τ is inversely proportional to $G^{n/2}$ that the volume of gas within the pyrometer and upstream of the junction is zero; and that the total temperature and static pressure of the free stream are held constant at 2,000° R and 1 atm, respectively, as the stream velocity is varied.

The observed advantage of the sonic pyrometer as to the rate of response is not as great as might be expected from a consideration of the mass flow rates alone. On this basis, the τ of the junction used during the determinations of characteristic time should be about 0.4 sec at a mass flow rate of 30 lb/sec ft^2. Since the τ of the complete instrument was 0.65 sec, the difference must be due to the time required for the displacement of gas already within the pyrometer. It was therefore of interest to determine whether the τ of the instrument could be decreased materially by removing the stagnation chamber, that is, that portion of the Inconel tube that projected upstream from the nozzle.

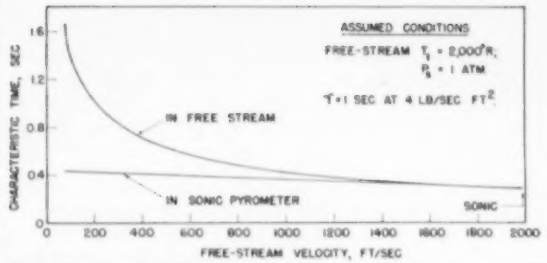

FIGURE 12. *Comparison of the characteristic times of a No. 22 gage bare junction in the free stream and within a sonic pyrometer in the same stream.*

g. Effects of Removing the Stagnation Chamber

Actually this modification reduced the characteristic time of the pyrometer by only about 10 percent. In addition, the unit became sensitive to the free-stream velocity, as can be seen in figure 13. Here the apparent recovery factor of the modified unit, plotted in terms of stream velocity, is seen to decrease to about 0.38 at sonic velocity. This cannot be a real recovery factor, and must reflect the effect of velocity. It is concluded that the stagnation chamber performs an essential function in a practical instrument, and cannot be dispensed with for the sake of a slight decrease in characteristic time.

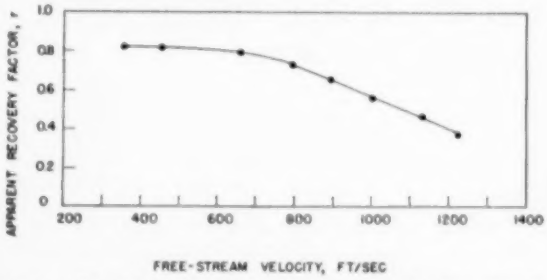

FIGURE 13. *Effect of removing the stagnation chamber of sonic pyrometer 3.*

TABLE 4. *Effect of free-stream velocity on sonic pyrometer 3*

$T_{1t}=T_{2t}$		T_{2t}	$\alpha=T_{2t}/T_{2t}$	γ	r	T_{1t}^m, eq 7, $r=0.820$	$T_{1t}-T_{1t}^m$	Velocity, V
°F	°R	°R				°R	°R	ft/sec
353.6	813.3	789.0	1.0308	1.391	0.817	812.9	0.4	260
385.0	844.7	819.8	1.0304	1.389	.819	844.5	.2	352
414.0	873.7	848.4	1.0298	1.387	.822	873.9	−.2	452
420.7	880.4	854.9	1.0298	1.387	.822	880.6	−.2	646
412.5	872.2	846.9	1.0299	1.387	.821	872.4	−.2	848
390.7	850.4	825.7	1.0299	1.389	.822	850.6	−.2	982
373.5	833.2	808.6	1.0304	1.390	.819	833.1	.1	1,089
360.3	820.0	795.9	1.0303	1.391	.820	820.0	.0	1,160
349.8	809.5	785.7	1.0303	1.392	.820	809.6	−.1	1,223
343.2	802.9	779.3	1.0303	1.392	.820	803.0	−.1	1,257
336.7	796.4	772.9	1.0304	1.392	.822	796.4	.0	Supersonic
331.0	790.7	767.2	1.0306	1.392	.819	790.5	.2	Do.
				Avg....	0.820			

4. Conclusion

The so-called sonic pyrometer is an instrument in which a thermocouple junction is located in the axis of a critical-flow nozzle, at or near the plane of sonic flow. Adequate shielding from radiation is simple to accomplish, and the entire instrument can be built within a tube ½ in. in outside diameter. As compared with a bare thermocouple in a free stream, the sonic pyrometer has the following advantages:

(a) Errors due to heat loss by radiation can be made negligible under normal engine operating conditions.

(b) It measures free-stream total temperatures, regardless of free-stream velocity, so that the latter need not be known.

(c) It is relatively simple to calibrate, and accurate to within about 3 deg F up to 1,500° F when approximate values of γ are known and used in calculating total temperatures from indicated values.

(d) Calibration with air at room temperature, and the application of a constant correction factor so determined, gives turbine exhaust gas temperatures that are accurate to within about 15 deg F up to 1,500° F, without any knowledge of or corrections for the γ of the gas.

(e) Because the velocity over the measuring junction is always sonic, the mass flow rate past the junction is greater than that of the free stream until the latter also becomes sonic. Hence a given junction in a sonic pyrometer responds more rapidly to sudden changes in temperature than would the same junction in the free stream. This advantage becomes greater as the free-stream velocity decreases.

As compared with a bare thermocouple in the free stream, the sonic pyrometer has the following disadvantages:

(a) It is more complicated and expensive to build.

(b) A pump is required whenever the ratio of the pressure in the throat of the nozzle to the free-stream total pressure is greater than 0.53, and in this case the sonic pyrometer is not convenient for flight tests.

(c) The bare thermocouple can be made smaller.

The following precautions in the design and use of sonic pyrometers are suggested by the present results:

(a) The measuring junction should consist of a bead of the smallest practicable dimensions. Such a junction has a higher recovery factor than any larger beads that were tried; one which, in fact, is within a few percent of the theoretical value for a flat plate.

(b) The throat of the nozzle should be large enough, and the thermocouple junction small enough, that the blocked area is not excessive. In the present unit No. 3, the smallest and the largest junctions blocked about 6 and 11 percent of the area of the throat, respectively. Both configurations of the device functioned in accordance with theory.

(c) The measuring junction should be located as near the plane of sonic flow as is practicable. Location somewhat upstream of this plane is satisfactory, but the junction should never be located downstream, in a region where the flow may be supersonic.

(d) The measuring junction should be fixed axially so that its location cannot change during calibration and subsequent use.

(e) When rapid response to sudden changes in temperature is desired, the volume within the pyrometer and upstream from the measuring junction should be kept to a practicable minimum.

(f) The resistance to flow between the discharge of the nozzle and the external port of the unit should be kept low, in order that sonic velocity may be attained in the nozzle with a minimum of pumping effort.

(g) Use of a convergent-divergent nozzle is also advantageous in reducing the pumping effort.

(h) The sonic pyrometer should never be used for measuring gas temperature unless it is known that critical flow prevails in the nozzle.

(i) Where high accuracy is required, it is recommended that the sonic pyrometer be calibrated with air initially at or above 200° F. In this way errors due to condensation of water vapor during the expansion through the nozzle are avoided.

Characteristics of the sonic pyrometer that have not been investigated include the following:

(a) Its ability to withstand mechanical vibration.

(b) The minimum practicable size.

(c) The maximum permissible throat area that may be blocked by the measuring junction.

(d) The effect of lateral displacement of the measuring junction from the axis of the nozzle.

(e) The effect of using dry air for calibration.

Each of these items can be treated more logically if and when practical needs arise that cannot be met by the instruments and test methods described above.

5. References

[1] S. Allen and J. R. Hamm, A pyrometer for measuring total temperature in low density gas streams, Trans. ASME **72,** 851 (1950).

[2] J. H. Keenan and J. Kaye, Thermodynamic properties of air (John Wiley and Son, Inc., New York, N. Y., 1945).

[3] E. Pohlhausen, Heat exchange between solid bodies and liquids of low viscosity and low thermal conductivity, Z. angew. Math. u. Mech. **1,** 115 (1921).

[4] H. W. Emmons and J. G. Brainerd, Temperature effects in a laminar compressible fluid boundary layer along a flat plate, Trans. ASME **63,** A–105 (1941).

[5] A. I. Dahl and E. F. Fiock, Shielded thermocouples for gas turbines, Trans. ASME **71,** 153 (1949).

[6] A. I. Dahl and E. F. Fiock, Response characteristics of temperature-sensing elements for use in the control of jet engines, J. Research NBS **45,** 292 (1950) RP2136.

WASHINGTON, February 16, 1951.

Journal of Research of the National Bureau of Standards Vol. 47, No. 3, September 1951 Research Paper 2243

Convergence of Cauchy-Riemann Sums to Cauchy-Riemann Integrals[1]

Otto Szász and John Todd

Two general theorems giving conditions to insure the truth of the relation

$$\lim_{h\to 0}\sum_{n=1}^{\infty} f(nh)=\int_0^{\infty} f(x)\,dx$$

are established. In addition, several cases involving Bessel functions are discussed.

1. Introduction

We are concerned with the validity of the equation

$$\lim_{h\to+0} h\sum_{\nu=1}^{\infty} f(\nu h)=\int_0^{\infty} f(x)dx, \tag{1}$$

where the integral is taken in the Cauchy-Riemann sense, that is,

$$\int_0^{\infty} f(x)dx=\lim_{\substack{\epsilon\to 0\\ \omega\to\infty}}\int_{\epsilon}^{\omega} f(x)dx.$$

There are cases when (1) is meaningless if the sum and the integral are interpreted in the ordinary way, but it becomes meaningful and correct if suitable summability methods are employed. A very simple case is when

$$f(x)=\sin x,$$

in which (1) is true if both the series and the integral are interpreted in the (C,1) sense. We do not propose to consider such cases at present. We shall also concern ourselves mainly with the case when the integrand has no singularity at the origin. Detailed investigations of the case when there is a singularity at the origin have been carried out by A. Wintner [8][2] and A. E. Ingham [3].

The problem was studied by Bromwich and Hardy [1] in 1908, and some of the results they obtained are now found in textbooks. Their results are of the following type:

If $f(x)$ decreases steadily and if the integral exists, then the series converges and (1) holds. (2)

If $\varphi(x)$ is continuous and decreases steadily to zero then (1) is true for $f(x)=\varphi(x)\sin x$. (3)

If $\varphi(x)$ is continuous and decreases steadily to zero and if $\int_0^{\infty}\varphi(x)dx$ exists, if furthermore $F(x)$ is a bounded continuous function, then (1) is true for $f(x)=\varphi(x)F(x)$. (4)

We note that (2) covers such cases as $f(x)=xe^{-x}$, where $f'(x)<0$ for $x>1$; that (3) covers such cases as $\varphi(x)=x^{-\alpha}$, $0<\alpha\leq 1$ (which is continuous except at $x=0$) and that (4) covers such cases as $\varphi(x)=x^{-2}$, $F(x)=\sin^2 x$.

The result (2) has been generalized to the quasi-monotone case by O. Szász [6] as follows:

If for some $\alpha\geq 0$, for $x\geq 1$ and $0<y<1$, we have (5)

$$0<f(x+y)\leq\left(1+\frac{\alpha}{x}\right)f(x),$$

and if the integral exists, then (1) holds.

Krishnan [9] has pointed out that in certain (non-trivial) cases a stronger result than (1) is true, namely,

$$h\sum f(\nu h)=\int_0^{\infty} f(x)dx \tag{6}$$

for *all* sufficiently small positive h; indeed:

If $f(x)$ is a function whose Fourier transform vanishes outside a finite interval $[-a, a]$ and if the Poisson formula can be applied, then we have (for all θ) (7)

$$h\sum_{\nu=-\infty}^{\infty} f(\nu\alpha+\theta)=h\sum_{\nu=-\infty}^{\infty} f(\nu h)=\int_{-\infty}^{+\infty} f(x)dx,$$

provided $0<h<2\pi/a$.

A simple case when this applies is when $f(x)=x^{-2}\sin^2 x$. We use this technique to give an alternative proof of one of our results on Bessel functions.

In sections 2 and 3 we give two sets of conditions that are sufficient to insure the truth of (1) and that include many of the known cases. The remainder of the paper, which is independent of these two sections, gives discussions, by various methods, of special cases, mainly involving Bessel functions, in which (1) is true.

2. $xf(x)=\psi(x)$, a Periodic Function

Our first theorem asserts the truth of (1), where $f(x)=x^{-1}\psi(x)$ under certain conditions on $\psi(x)$. The simplest case is that when $\psi(x)=\sin x$.

[1] The preparation of this paper was sponsored (in part) by the Office of Naval Research.

[2] Figures in brackets indicate the literature references at the end of this paper.

Theorem 1. *Let*

$$\psi(x)=\sum_{n=1}^{\infty} b_n \sin nx, \quad \sum |b_n|<\infty. \tag{8}$$

Let the Cauchy-Riemann integral

$$\int_{-\infty}^{x} \frac{\psi(t)}{t}\,dt \tag{9}$$

exist. Then (1) *holds for* $f(x)=x^{-1}\psi(x)$, *i. e., we have*

$$\lim_{h\to+0} h \sum_{n=1}^{\infty} \frac{\psi(nh)}{nh}=\int_{-\infty}^{\infty} \frac{\psi(x)}{x}\,dx. \tag{10}$$

Proof. We begin by establishing convergence of the series on the left of (10). We do this by first establishing that it is summable-A and then noticing that since ψ is bounded, its general term is $O(n^{-1})$, and we can therefore use a standard Tauberian theorem [10, p. 501]. We therefore consider

$$\left.\begin{aligned}\sum_{n=1}^{\infty} \frac{\psi(nh)}{n} r^n &= \sum_{n=1}^{\infty} \frac{r^n}{n} \sum_{\nu=1}^{\infty} b_\nu \sin \nu nh \\ &= \sum_{\nu=1}^{\infty} b_\nu \sum_{n=1}^{\infty} \frac{r^n}{n} \sin \nu nh.\end{aligned}\right\} \tag{11}$$

This interchange of summation being permissible because of the absolute convergence of the double series

$$\sum\sum |b_\nu|(r^n/n)=\sum |b_\nu| \sum (r^n/n)$$

whenever $0\le r<1$. We now require some elementary properties of the inner series in (11). It is well known [11, p. 285] that

$$\sum_{n=1}^{\infty} \frac{r^n}{n} \sin nx=\arctan \frac{r \sin x}{1-r \cos x}$$

when $0\le r<1$. This gives

$$\sum_{n=1}^{\infty} \frac{r^n}{n} \sin \nu nh=\arctan \frac{r \sin \nu h}{1-r \cos \nu h}$$

when $0\le r<1$. Since for $r=0$, the left-hand side is zero, we must choose that determination of the arctan that vanishes for $r=0$. Since the denominator $1-r \cos \nu h$ never vanishes ($0\le r<1, h\to+0, \nu=1, 2, \ldots$) we cannot leave this branch and, in particular, we have

$$\left|\sum_{n=1}^{\infty} \frac{r^n}{n} \sin \nu nh\right|=\left|\arctan \frac{r \sin \nu h}{1-r \cos \nu h}\right| \le \tfrac{1}{2}\pi.$$

Hence, we have

$$\sum_{n=1}^{\infty} \frac{\psi(nh)}{n} r^n=\sum_{\nu=1}^{\infty} b_\nu \arctan \frac{r \sin \nu h}{1-r \cos \nu h}$$

where the series on the right is, for fixed $h>0$, uniformly and absolutely convergent in $0\le r<1$, being majorized by $\frac{1}{2}\pi \sum_{\nu=1}^{\infty} |b_\nu|$.

Hence, as $r\to 1$, we have [10, p. 339]

$$\sum_{\nu=1}^{\infty} b_\nu \arctan \frac{r \sin \nu h}{1-r \cos \nu h} \to \sum_{\nu=1}^{\infty} b_\nu \arctan \frac{\sin \nu h}{1-\cos \nu h}$$

$$=\sum_{\nu=1}^{\infty} b_\nu \arctan (\cot \tfrac{1}{2}\nu h).$$

This means that $\sum_{n=1}^{\infty} \psi(nh)/n$ is, for all $h>0$, summable-A, and therefore convergent, to the sum

$$\sum_{\nu=1}^{\infty} b_\nu \arctan (\cot \tfrac{1}{2}\nu h).$$

We shall now show that, as $h\to 0$,

$$\sum_{\nu=1}^{\infty} b_\nu \arctan\left(\cot \frac{1}{2}\nu h\right) \to \frac{1}{2}\pi \sum_{\nu=1}^{\infty} b_\nu. \tag{12}$$

The difference between these two expressions can be written as

$$\sum_{\nu=1}^{N} \left\{ b_\nu \arctan\left(\cot \frac{1}{2}\nu h\right)-\frac{1}{2}\pi b_\nu \right\}+$$

$$\sum_{\nu=N+1}^{\infty} b_\nu \arctan\left(\cot \frac{1}{2}\nu h\right)-\frac{1}{2}\pi \sum_{N+1}^{\infty} b_\nu. \tag{13}$$

We first choose N so large that $\frac{1}{2}\pi \sum_{N+1}^{\infty} b_\nu$ (and therefore also $\sum_{\nu=N+1}^{\infty} b_\nu \arctan\left(\cot \frac{1}{2}\nu h\right)$ is small. With N fixed we then can choose h so small that the first sum in (13) is small. This establishes (12). To complete the proof of Theorem 1 we have first to establish the existence of the integral on the right of (10) and then show that its value is $\frac{1}{2}\pi \sum_{\nu=1}^{\infty} b_\nu$. Our hypothesis (9) insures convergence at the lower limit. Integrating by parts, we see that

$$\int_{\pi}^{u} \frac{\psi(x)}{x}\,dx=\frac{\psi_1(u)}{u}+\int_{\pi}^{u} \frac{\psi_1(x)}{x^2}\,dx, \tag{14}$$

where

$$\psi_1(u)=\int_{\pi}^{u} \psi(x)\,dx.$$

Since $\psi_1(x)=O(1)$ by periodicity, and since $\int^{\infty} x^{-2}dx$ is convergent, we can let $u\to\infty$ in (14) to obtain

$$\int_{\pi}^{\infty} \frac{\psi(x)}{x^2}\,dx=\int_{\pi}^{\infty} \frac{\psi_1(x)}{x^2}\,dx.$$

Thus the existence of

$$\int_{-1}^{\infty} \frac{\psi(x)}{x}\,dx$$

is established.

We now consider

$$\left.\begin{aligned}\int_t^{\infty} \frac{\psi(x)}{x}\,dx &= \int_t^{\infty} \frac{\sum_{\nu=1}^{\infty} b_\nu \sin \nu x}{x}\,dx \\ &= \sum_{\nu=1}^{\infty} b_\nu \int_t^{\infty} \frac{\sin \nu x}{x}\,dx.\end{aligned}\right\} \tag{15}$$

This inversion may be justified as follows. We use the fact that

$$Si(x)=\int_x^{\infty} \frac{\sin t}{t}\,dt=\left[\frac{-\cos t}{t}\right]_x^{\infty}-\int_x^{\infty} \frac{\cos t\,dt}{t^2}=O(x^{-1})$$

as $x\to\infty$. What we have to show is that

$$I_1=\int_t^T \sum_{\nu=N}^{\infty} \frac{b_\nu \sin \nu x}{x}\,dx=\int_t^T \frac{1}{x}\sum_{\nu=N}^{\infty} b_\nu \sin \nu x\,dx$$

and

$$I_2=\sum_{\nu=1}^{N} b_\nu \int_T^{\infty} \frac{\sin \nu x}{x}\,dx$$

are both small for N, T sufficiently large. Since $\sum b_\nu$ is absolutely convergent, and since for all ν, $\int_T^{\infty} \frac{\sin \nu x}{x}\,dx=O(T^{-1})$, it follows that $I_2=O(T^{-1})$, i. e., small if T is large uniformly for all N. Fixing T we can choose N so large that I_1 is small. This establishes (15).

We can let $t\to 0$ in (15) since the series on the right is uniformly convergent in t. This gives

$$\int_{-0}^{\infty} \frac{\psi(x)}{x}\,dx=\sum_{\nu=1}^{\infty} b_\nu \int_0^{\infty} \frac{\sin \nu x}{x}\,dx=\frac{1}{2}\pi\sum_{\nu=1}^{\infty} b_\nu$$

and thereby completes the proof of Theorem 1.

Remark: An example that is *not* covered by this theorem is the case when $b_n=(-1)^n/n$. Here

$$\psi(t)=\sum b_n \sin nt=\pi\left\{\left[t+\frac{1}{2}\right]-t\right\}$$

if $t+\frac{1}{2}$ is not an integer and $\psi(t)=0$ if $t+\frac{1}{2}$ is an integer, and although it is clear that $\int_0^{\infty} f(x)\,dx$ exists, the question of the truth or falsity of (1) seems to be rather deep.

3. $xf(x)=\psi(x)$, a Fourier Integral

Our second theorem asserts the truth of (1) when $xf(x)$ is the sine transform of an absolutely integrable function $\eta(t)$. This, when we take

$$\eta(t)=0,\quad t<0,\quad \eta(t)=\tfrac{1}{2},\quad 0\le t\le 2,\quad \eta(t)=0,\quad t>2$$

reduces to the case

$$f(x)=\sin^2 x/x^2,$$

which has been mentioned by Hardy and Bromwich [1] and by Krishnan [9].

Theorem 2. Let

$$f(x)=\frac{1}{x}\int_0^{\infty} \eta(t)\sin xt\,dx,$$

where

$$\int_0^{\infty} |\eta(t)|dt$$

is finite. Then (1) *is true.*

Proof. We have

$$\begin{aligned}h\sum_{\nu=1}^{\infty} f(\nu h)&=\sum_{\nu=1}^{\infty}\frac{1}{\nu}\int_0^{\infty} \sin \nu ht\,\eta(t)dt \\ &=\int_0^{\infty}\sum_{\nu=1}^{\infty}\frac{1}{\nu}\sin \nu ht\,\eta(t)dt.\end{aligned}$$

This interchange of summation and integration is legitimate because $\sum \nu^{-1}\sin \nu ht$ is convergent and its partial sums are uniformly bounded.

It is well known [10, p. 523] that for x positive and not an integer,

$$\sum_{\nu=1}^{\infty} \nu^{-1}\sin 2\pi\nu x=-\pi\{x-[x]-\tfrac{1}{2}\},$$

where $[x]$ denotes the integral part of x. This gives

$$\sum \nu^{-1}\sin \nu ht=-\pi\left\{\frac{ht}{2\pi}-\left[\frac{ht}{2\pi}\right]-\frac{1}{2}\right\}.$$

Substituting, we find

$$\begin{aligned}&\int_0^{\infty}\left\{\sum_{\nu=1}^{\infty}\nu^{-1}\sin \nu ht\right\}\eta(t)dt \\ &=-\pi\int_0^{\infty}\left\{\frac{ht}{2\pi}-\left[\frac{ht}{2\pi}\right]-\frac{1}{2}\right\}\eta(t)dt \\ &=\frac{1}{2}\pi\int_0^{\infty}\eta(t)dt-\pi\int_0^{\infty}\left\{\frac{ht}{2\pi}-\left[\frac{ht}{2\pi}\right]\right\}\eta(t)dt.\end{aligned}$$

We shall show that the second term on the right tends to zero with h. To do this, write

$$\begin{aligned}&\int_0^{\infty}\left\{\frac{ht}{2\pi}-\left[\frac{ht}{2\pi}\right]\right\}\eta(t)dt \\ &=\int_0^{\omega}\left\{\frac{ht}{2\pi}-\left[\frac{ht}{2\pi}\right]\right\}\eta(t)dt+\int_{\omega}^{\infty}\left\{\frac{ht}{2\pi}-\left[\frac{ht}{2\pi}\right]\right\}\eta(t)dt \\ &=I_1(h)+I_2(h),\end{aligned}$$

say. We can choose and fix ω so large that

$$|I_2(h)| \leq \int_\omega^\infty |\eta(t)|dt$$

is small for all h. Then we can choose h so small that

$$\frac{ht}{2\pi} - \left[\frac{ht}{2\pi}\right] \leq \frac{ht}{2\pi}$$

is itself small enough to insure that $|I_1(h)|$ is small.

Hence

$$h\sum_{\nu=1}^{\infty} f(\nu h) \to \tfrac{1}{2}\pi \int_0^\infty \eta(t)dt.$$

To complete the proof we have to show that

$$\int_0^\infty f(x)dx = \tfrac{1}{2}\pi \int_0^\infty \eta(t)dt;$$

but this follows easily, since

$$\int_0^\infty f(x)dx = \int_0^\infty \int_0^\infty \frac{\sin xt}{x}\eta(t)dt\,dx$$

$$= \int_0^\infty \left[\int_0^\infty \frac{\sin xt}{x}dx\right]\eta(t)dt$$

$$= \tfrac{1}{2}\pi \int_0^\infty \eta(t)dt,$$

the change of order of integration being permissible, since $\int_0^\infty \eta(t)dt$ is, by hypothesis, absolutely convergent.

4. The Cases $f(x) = J_0(x)$ and $f(x) = K_0(x)$

It is known [5, p. 336] that

$$\sum_{n=0}^{\infty} J_0(nh) = \tfrac{1}{2} + h^{-1} \tag{16}$$

and so, as $h \to 0$,

$$h\sum_{n=0}^{\infty} J_0(nh) \to 1.$$

Since also [2, p. 96]

$$\int_0^\infty J_0(x)dx = 1,$$

the relation (1) is true in this case.

The result (16) can be established directly in the following manner. From the asymptotic formula

$$J_0(x) = \left(\frac{2}{\pi x}\right)^{\frac{1}{2}} \sin\left(x + \frac{1}{4}\pi\right) + O(x^{-3/2}),$$

using partial summation, it can be shown that the series $\sum_{n=0}^{\infty} J_0(nh)$ converges for $0 < h < \pi$ (and, indeed, converges uniformly in every closed subinterval). We evaluate the sum of this series by determining its $(C,1)$ sum, using the integral representation

$$J_0(x) = \frac{2}{\pi}\int_0^{\pi/2} \cos(x\cos t)\,dt, \tag{17}$$

and the facts that

$$C_n(x) \equiv \sum_{\nu=0}^{n} \cos \nu x = \frac{1}{2} + \frac{\sin\left(n+\frac{1}{2}\right)x}{2\sin\frac{1}{2}x}, \tag{18}$$

$$\frac{1}{n+1}\sum_{\nu=0}^{n} C_\nu(x) = \frac{1}{2} + \frac{\sin^2\left(n+\frac{1}{2}\right)x}{2(n+1)\sin^2\frac{1}{2}x}. \tag{19}$$

From (17), (18), and (19) we obtain

$$s_n(h) = \sum_{\nu=0}^{n} J_0(\nu h) = \frac{2}{\pi}\int_0^{\pi/2} \left\{\frac{1}{2} + \frac{\sin\frac{1}{2}(n+1)h\cos t}{2\sin\left(\frac{1}{2}h\cos t\right)}\right\} dt$$

$$\sigma_n(h) \equiv \frac{1}{n+1}\sum_{\nu=0}^{n} s_\nu(h)$$

$$= \frac{1}{\pi}\int_0^{\pi/2} \left\{1 + \frac{\sin^2\left[\frac{1}{2}\left(n+1\right)h\cos t\right]}{(n+1)\sin^2\left(\frac{1}{2}h\cos t\right)}\right\} dt.$$

Now $\sin^{-2}x = (1/x^2) + O(1)$ as $x \to 0$, and so, for fixed $h > 0$ we find

$$\sigma_n(h) = \frac{1}{2} + \frac{4}{\pi(n+1)h^2}\int_0^{\pi/2} \frac{\sin^2\left[\frac{1}{2}\left(n+1\right)h\sin t\right]}{\sin^2 t}dt + O\left(\frac{1}{n}\right)$$

$$= \frac{1}{2} + R_1(n) + R_2(n) + O(n^{-1}),$$

where R_1 and R_2 are the contributions from the ranges $(0, \pi/4)$ and $(\pi/4, \pi/2)$, respectively. Clearly,

$$R_2(n) < \frac{4}{\pi n h^2 \sin^2\frac{\pi}{4}} = O(n^{-1}).$$

To deal with R_1 we change the variable t to $u = \frac{1}{2}(n+1)h\sin t$; we find, writing $h(n+1)2^{-3/2} = k$, that

$$R_1(n)=\frac{2}{\pi h}\int_0^k \frac{\sin^2 u\,du}{u^2\left\{1-\left(\frac{2u}{(n+1)h}\right)^2\right\}^{\frac{1}{2}}}$$

$$=\frac{2}{\pi h}\int_0^k\left(\frac{\sin u}{u}\right)^2 du+$$

$$\frac{2}{\pi h}\int_0^k\left(\frac{\sin u}{u}\right)^2\left\{\left[1-\left(\frac{2u}{(n+1)h}\right)^2\right]^{-\frac{1}{2}}-1\right\}du.$$

As $n\to\infty$, $k\to\infty$ and the first term tends to h^{-1} and is indeed $h^{-1}+O(n^{-2})$.

Let $v=[2u/(n+1)h]^2$; then in the range $0\le u\le k$ we have $0\le v\le\frac{1}{2}$, and

$$(1-v)^{-\frac{1}{2}}-1=\frac{(1-v)^{-1}-1}{1+(1-v)^{-\frac{1}{2}}}$$

$$=\frac{v}{(1-v)\{1+(1-v)^{-\frac{1}{2}}\}}$$

$$<2v=\frac{8u^2}{(n+1)^2h^2}.$$

This means that the second term is $O(n^{-2})$ as $n\to\infty$.

Gathering our results together, we have

$$\sigma_n(h)=\frac{1}{2}+h^{-1}+O(n^{-1}).$$

This means that the series $\sum J_0(nh)$ is summable $(C,1)$ to the sum $\frac{1}{2}+h^{-1}$, when $h>0$. This completes the sketch of the proof of (16).

To deal with the case $f(x)=K_0(x)$ we use the formula [13, p. 301]

$$\sum_{n=1}^{\infty}K_0(nh)=\frac{\pi}{2h}+\pi\sum_{n=1}^{\infty}\left\{\frac{1}{\sqrt{h^2+4n^2\pi^2}}-\frac{1}{2n\pi}\right\}+\frac{1}{2}\gamma+$$

$$\frac{1}{2}\ln h-\frac{1}{2}\log 4\pi,$$

which leads to

$$\lim_{h\to 0}h\sum_{n=1}^{\infty}K_0(nh)=\frac{1}{2}\pi.$$

Since [12, p. 388] we have

$$\int_0^{\infty}K_0(x)dx=\frac{1}{2}\pi$$

(1) is true in this case. We note that here we have a (logarithmic) singularity at the origin, and have used a summation starting at 1 and not at 0 to avoid trouble.

5. The Cases $f(x)=J_0(x)\cos xt$ and $f(x)=J_0(x)\sin xt$

It is known [4, p. 59] that for $h>0$, $0\le t<1$, we have

$$\sum_{n=1}^{\infty}J_0(nh)\cos(nht)=-\frac{1}{2}+\frac{1}{h\sqrt{1-t^2}}.$$

Multiplying by h and then letting $h\to 0$ we find, for $0\le t<1$,

$$h\sum_{n=1}^{\infty}J_0(nh)\cos(nht)\to\frac{1}{\sqrt{1-t^2}}.$$

On the other hand [4, p. 51], we have, for $0\le t<1$,

$$\int_0^{\infty}J_0(x)\cos xt\,dx=\frac{1}{\sqrt{1-t^2}}$$

and so (1) is true.

The case when we consider

$$f(x)=J_0(x)\sin xt$$

is slightly more complicated. It is known [4, p. 59] that for $h>0$, $0\le t<1$, we have

$$\sum_{n=1}^{\infty}J_0(nh)\sin(nht)$$

$$=\sum_{n=1}^{\infty}\left\{[(2\pi n+th)^2-h^2]^{-\frac{1}{2}}-[(2\pi n-th)^2-h^2]^{-\frac{1}{2}}\right\}$$

$$=-\sum_{n=1}^{\infty}\{8\pi nth/D\},$$

where

$$D=[(2\pi n+th)^2-h^2]^{\frac{1}{2}}[(2\pi n-th)^2-h^2]^{\frac{1}{2}}\times$$
$$\{[(2\pi n+th)^2-h^2]^{\frac{1}{2}}+[(2\pi n-th)^2-h^2]^{\frac{1}{2}}\}.$$

Now for small h and fixed t

$$\frac{nth}{D}=O\left(\frac{h}{n^2}\right).$$

Hence, as $h\to 0$,

$$h\sum_{n=1}^{\infty}J_0(nh)\sin(nht)\to 0.$$

On the other hand, it is known [4, p. 51] that for $0\le t<1$

$$\int_0^{\infty}J_0(x)\sin xt\,dx=0.$$

Thus (1) holds in this case also.

6. The Case $f(x)=\Lambda_\mu(x)=(2^\mu x^{-\mu})\Gamma(\mu+1)J_\mu(x)$, $\mu>-\frac{1}{2}$

It is known [2, p. 91] that

$$\sum_{n=0}^{\infty}\Lambda_\mu(nh)=\frac{\sqrt{\pi}}{h}\,\frac{\Gamma(\mu+1)}{\Gamma\left(\mu+\frac{1}{2}\right)}\qquad(20)$$

and so, as $h \to 0$,

$$h\sum_{n=0}^{\infty} \Lambda_\mu(nh) \to \frac{\sqrt{\pi}\Gamma(\mu+1)}{\Gamma\left(\mu+\frac{1}{2}\right)}.$$

The convergence of this series can be established in a similar manner to that used in the case $\mu = 0$.

Since also [12, p. 391] or [7, p. 182]

$$\int_0^{\infty} \Lambda_\mu(x)\,dx = \frac{\sqrt{\pi}\Gamma(\mu+1)}{\Gamma\left(\mu+\frac{1}{2}\right)},$$

the relation (1) is true in this case, and is a generalization of that discussed in section 4. This case, when $\mu = \frac{1}{2}$, reduces to the case $f(x) = \sin x/x$.

We shall now discuss this case using the Poisson summation formula

$$\sqrt{\beta}\left\{\frac{1}{2}F_c(0) + \sum_{n=1}^{\infty} F_c(n\beta)\right\} = \sqrt{\alpha}\left\{\frac{1}{2}f(0) + \sum_{n=1}^{\infty} f(n\alpha)\right\}, \tag{21}$$

where $\alpha\beta = 2\pi$, $\alpha > 0$ and F_c is the cosine transform of f defined by

$$F_c(x) = \sqrt{\frac{2}{\pi}}\int_0^{+\infty} f(t)\cos xt\,dt.$$

This formula is true, for instance [7, p. 60 to 64], provided that $f(x)$ is continuous and of bounded variation in $0 \leq x < \infty$, that $f(x) \to 0$ as $x \to \infty$ and that the Cauchy-Riemann integral $\int_0^{+\infty} f(t)dt$ exists.

These conditions are satisfied when $\mu > \frac{1}{2}$ if

$$f(x) = \frac{2^{\frac{1}{2}-\mu}}{\Gamma\left(\mu+\frac{1}{2}\right)}(1-x^2)^{\mu-1}, \qquad 0 < x < 1$$

$$f(x) = 0, \qquad x \geq 1$$

so that [7, p. 65]

$$F_c(x) = \frac{J_\mu(x)}{x^\mu} = \frac{2^{-\mu}}{\Gamma(\mu+1)}\Lambda_\mu(x).$$

In this case (21) gives

$$\frac{1}{2^\mu\Gamma(\mu+1)}\left\{\frac{1}{2} + \sum_{n=1}^{\infty}\Lambda_\mu(n\beta)\right\} =$$

$$\left(\frac{\alpha}{\beta}\right)^{\frac{1}{2}}\frac{2^{\frac{1}{2}-\mu}}{\Gamma\left(\mu+\frac{1}{2}\right)}\left\{\frac{1}{2} + \sum_{n\alpha\leq 1}(1-n^2\alpha^2)^{\mu-\frac{1}{2}}\right\}. \tag{22}$$

This formula is true as it stands for $\mu > \frac{1}{2}$; if $\mu = \frac{1}{2}$ and a term on the right corresponding to $n = \alpha^{-1}$ occurs, it must be halved; if $-\frac{1}{2} < \mu < \frac{1}{2}$, the formula remains true, provided that α is not the reciprocal of an integer.

We now assume $\alpha > 1$, so that the sum on the right is empty; this means that

$$\beta = 2\pi\alpha^{-1} < 2\pi.$$

In these circumstances (22) gives

$$\frac{1}{2^\mu\Gamma(\mu+1)}\left\{\frac{1}{2} + \sum_{n=1}^{\infty}\Lambda_\mu(n\beta)\right\} = \left(\frac{2\pi}{\beta^2}\right)^{\frac{1}{2}}\frac{1}{2^{\mu+1}\Gamma\left(\mu+\frac{1}{2}\right)},$$

that is,

$$\sum_{n=1}^{\infty}\Lambda_\mu(n\beta) = \frac{\sqrt{\pi}}{\beta}\frac{\Gamma(\mu+1)}{\Gamma\left(\mu+\frac{1}{2}\right)} - \frac{1}{2},$$

which is (20).

7. References

[1] T. J. I'A. Bromwich and G. H. Hardy, The definition of an infinite integral as the limit of a finite or infinite series, Quart. J. Math. **39,** 222 to 240 (1908).

[2] G. Doetsch, Summatorische Eigenschaften der Besselschen Funktionen, Compositio Mathematica **1,** 85 to 97 (1935).

[3] A. E. Ingham, Improper integrals as limits of sums, J. London Math. Soc. **24,** 44 to 50 (1949).

[4] W. Magnus and F. Oberhettinger, Formeln und Sätze für die speziellen Funktionen der mathematischen Physik 2d ed. (1948).

[5] N. Nielsen, Handbuch der Theorie der Cylinderfunktionen (Leipzig, 1904).

[6] O. Szász, Quasi-monotone series, Am. J. Math. **70,** 203 to 206 (1948).

[7] E. C. Titchmarsh, Introduction to the theory of Fourier integrals (Oxford, 1948).

[8] Aurel Wintner, The sum formula of Euler-Maclaurin and the inversions of Fourier and Möbius, Am. J. Math. **69,** 685 to 708 (1947).

[9] K. S. Krishnan, On the equivalence of certain infinite series and corresponding integrals, J. Indian Math. Soc. (New Series) **12,** 79 to 88 (1948).

[10] K. Knopp, Theory and application of infinite series (London and Glasgow, 1928).

[11] T. J. I'A. Bromwich, Theory of infinite series (London, 1926).

[12] G. N. Watson, Bessel functions (Cambridge, 1948).

[13] G. N. Watson, Oxford Quart. J. **2,** 298 to 309 (1931).

Los Angeles, July 20, 1950.

Journal of Research of the National Bureau of Standards Vol. 47, No. 3, September 1951 Research Paper 2244

Maximum Likelihood Estimates of Position Derived From Measurements Performed by Hyperbolic Instruments[1]

Eugene Lukacs

Certain electronic surveying instruments—referred to as hyperbolic instruments—determine the difference between the distances from two fixed stations to a moving object. Data obtained from a single observation yield one relation between the three coordinates of the moving object and restrict it to a hyperboloid of revolution. To locate a position in space, observations from at least three pairs of stations are needed. If more than three observations are taken, more than three equations for the three coordinates are obtained. In general these equations will not be compatible; it is then a statistical problem to find an estimate for the unknown position. In this paper maximum likelihood estimates are obtained for positions in space derived from such hyperbolic data.

1. Introduction

Several electronic surveying instruments have been developed in recent years. These instruments utilize the Doppler effect [2 3] and are designed to locate the position of a moving object. In this paper we are considering measurements obtained by using certain types of these instruments, which are often referred to as hyperbolic instruments. Hyperbolic instruments, such as Raydist (see footnote 2), determine the difference between the distances from two stations to a moving object. Data obtainable from one observation (using one pair of stations) yield one relation among the three coordinates of the moving object. To locate a position in space from hyperbolic data, at least three observations are needed. If more than three observations are taken, more than three equations for the three coordinates are obtained. In general, these equations will not be compatible; it is then a statistical problem to find an estimate for the unknown position. The use of exactly three observations is justified if it can be assumed that the data are not affected by any observational errors. In general, this assumption is not realistic and should not be made without a thorough investigation. It appears desirable, therefore, to use more than the minimum number of observations and to estimate the location of the moving object by statistical methods. The purpose of this paper is to obtain maximum likelihood estimates for positions in space derived from hyperbolic data.

2. Formulation of the Assumptions and the Problem

We denote by $N \geq 4$ the number of stations $S_\alpha (\alpha = 1,2, \ldots N)$ and by $(a_{\alpha 1}, a_{\alpha 2}, a_{\alpha 3})$ the known coordinates of the station S_α. Let P be the unknown position of the moving object and $(\theta_1, \theta_2, \theta_3)$ be the coordinates of P. A single observation based on the stations S_α and S_β gives then a determination of the distance $\overline{PS}_\alpha - \overline{PS}_\beta$. If N stations are available it is possible to make at most

$$\binom{N}{2} = \frac{N(N-1)}{2}$$

observations based on different pairs of stations. However, not all these observations will be used in practice. Let $n \leq [N(N-1)]/2$ be the number of observations actually taken. We make the following assumptions:

(I) The hyperbolic measurements $z_{\alpha\beta}$ are observations on n independent random variables $Z_{\alpha\beta}$. The variates $Z_{\alpha\beta}$ have rectangular distributions with mean $\mu_{\alpha\beta}$ and common range $2r$. Further $Z_{\beta\alpha} = -Z_{\alpha\beta}$ and $z_{\beta\alpha} = -z_{\alpha\beta}$.

(II) The parameters of the n rectangular distributions may be expressed in terms of the coordinates of the unknown point by means of the formula

$$E(Z_{\alpha\beta}) = \mu_{\alpha\beta} = \sqrt{\sum_{i=1}^{3} (\theta_i - a_{\alpha i})^2} - \sqrt{\sum_{i=1}^{3} (\theta_i - a_{\beta i})^2}. \qquad (1)$$

(III) The distances d_α and d_β from the position of the moving object at time $t=0$ to the stations S_α and S_β, respectively, satisfy the inequality

$$d_\alpha - d_\beta > r. \qquad (2)$$

The nature of the problem, as well as its solution are to a great extent determined by assumption (I). To justify this assumption it is necessary to describe briefly how hyperbolic data are obtained.

It is desired to determine the instantaneous location of a moving object. A transmitter is carried in the object and emits a continuous signal of frequency f_0. A second transmitter (the reference transmitter) emits a signal of a frequency f'_0, slightly different from f_0. Each station receives both signals simultaneously. A certain beat frequency n_α is

[1] An unclassified treatment of the mathematical portion of a classified Navord-report written by the author while a member of the staff of the U. S. Naval Ordnance Test Station, Inyokern, Calif.

[2] J. F. McAllister, Measuring velocity of V-2 rockets by Doppler effect, Tele-Tech. **6**, No. 2, p. 56 to 59 and 129 (1947).

[3] Charles E. Hastings, Raydist—a radio navigation and tracking system, Tele-Tech. **6**, No. 6, p. 30 to 33 and 100 to 103 (June 1947).

thus associated with each station S_α; n_α depends on the velocity component of the object away from S_α and on the frequencies f_0 and f'_0. To obtain an observation two stations S_α and S_β have to be linked by wire or by radio The frequencies n_α and n_β give then a beat frequency; the quantity recorded is the number of cycles $n_{\alpha\beta}$ of the beat frequency signal occurring during the time of observation. It can be assumed that the observation $z_{\alpha\beta}$ on $Z_{\alpha\beta}$ can be satisfactorily approximated by a linear function of $n_{\alpha\beta}$ given by

$$z_{\alpha\beta}=\frac{c}{f_0}n_{\alpha\beta}+d_\alpha-d_\beta. \tag{3}$$

In this formula c is the speed of light. The frequency $n_{\alpha\beta}$ may be recorded continuously to permit reading $n_{\alpha\beta}$ to fractions of a cycle. Alternatively it is possible to devise a counter that registers full cycles only.[4] In either case it is easily possible to determine a range for the reading error of $n_{\alpha\beta}$ (and therefore also of $z_{\alpha\beta}$). Moreover, the recording devices are of such a nature that any error within the possible range is equally likely to occur. It seems, therefore, quite realistic to assume that the errors have a rectangular distribution about zero with a certain range. This, however, is equivalent to assumption (I). Equation (2) is a condition imposed on the location of the stations. As the half range r is rather small (2) implies hardly more than $d_\alpha > d_\beta$. This consideration shows that (2) is not a very serious restriction. The aim of this paper is the determination of a maximum likelihood estimate of the unknown position. That is, the unknown coordinates θ_1, θ_2, θ_3 have to be determined so that the greatest possible probability is given to the actual observations. This discussion will be based on assumptions (I), (II), and (III).

3. The Maximum Likelihood Estimate

Let $f_{\alpha\beta}(z)$ be the frequency function of the random variable $Z_{\alpha\beta}$. According to assumption (I)

$$f_{\alpha\beta}(z)=\begin{cases}\frac{1}{2r} \text{ if } \mu_{\alpha\beta}-r\leqq z\leqq\mu_{\alpha\beta}+r.\\ 0 \text{ otherwise}\end{cases}$$

The likelihood function[5] assumes, therefore, also only two values, the value $(1/2r)^n$ and the value zero. If one wants to determine the unknown parameters θ_1, θ_2, θ_3 so that the greatest possible probability is given to the actual observations, one has only to chose the parameters so that the likelihood function is not zero. This is the case if and only if each observation $z_{\alpha\beta}$ falls within the range of $Z_{\alpha\beta}$. That is, the likelihood condition

$$\mu_{\alpha\beta}-r\leqq z_{\alpha\beta}\leqq\mu_{\alpha\beta}+r, \tag{4}$$

must be satisfied for the n pairs (α,β) used. From (1) it is seen that the likelihood condition (4) consists of a set of inequalities involving θ_1, θ_2, θ_3. A point $(\theta_1, \theta_2, \theta_3)$ of the parameter space is said to be a maximum likelihood estimate if its coordinates satisfy the maximum likelihood condition. In general, inequalities (4) will not have a unique solution. Either all the points of a certain region in the parameter space will satisfy (4), or it may happen that no maximum likelihood estimate exists. If maximum likelihood estimates exist, one may consider the set of all the maximum likelihood estimates. This set will be called the maximum likelihood region. Any point in the interior of the maximum likelihood region may be used as an estimate for the unknown position. The most important problem is the determination of the maximum likelihood region. This problem will be solved by expressing the boundaries of this region in terms of the actual observations. This requires certain transformations of the likelihood condition (4). If we substitute the value of $\mu_{\alpha\beta}$ from (1) and transpose we obtain

$$z_{\alpha\beta}-r\leqq\sqrt{\sum_{i=1}^{3}(\theta_i-a_{\alpha i})^2}-\sqrt{\sum_{i=1}^{3}(\theta_i-a_{\beta i})^2}\leqq z_{\alpha\beta}+r \tag{4a}$$

We next introduce the following notation

$$\left.\begin{aligned}n_0&=-\frac{f_0}{c}(d_\alpha-d_\beta-r)\\ n_1&=-\frac{f_0}{c}(d_\alpha-d_\beta+r)\end{aligned}\right\} \tag{4b}$$

From (4a) we see $n_1=n_0-2rf_0/c<n_0$.
In the following we distinguish three cases, namely,

Case (A): $n_{\alpha\beta}>n_0$
Case (B): $n_{\alpha\beta}<n_1$
Case (C): $n_1\leqq n_{\alpha\beta}\leqq n_0$.

From (3) it is seen that

$$\left.\begin{aligned}&z_{\alpha\beta}-r>0 \text{ and a fortiori } z_{\alpha\beta}+r>0 \text{ in case (A)}\\ &z_{\alpha\beta}+r<0 \text{ and a fortiori } z_{\alpha\beta}-r<0 \text{ in case (B)}\\ &z_{\alpha\beta}+r\geqq 0\geqq z_{\alpha\beta}-r \text{ in case (C)}.\end{aligned}\right\} \tag{5}$$

We first consider the conditions imposed by a single observation $z_{\alpha\beta}$ based on an arbitrary pair of stations. It is no loss in generality if we assume $\alpha=1$ and $\beta=2$. To simplify the discussion we choose an appropriate system of coordinates. Let the position of the moving object at time $t=0$ be the origin O and choose the θ_1-axis so as to be parallel to the line joining S_1 and S_2 the θ_2-axis should be in the plane OS_1S_2 and per-

[4] Hastings Bulletin R-23, Complete Raydist tracking system for missiles (Sept. 1947).
[5] A description of the maximum likelihood method and a description of the likelihood function may be found in, H. Cramér, Mathematical Methods of Statistics, p. 498 (Princeton Univ. Press, Princeton, 1946).

pendicular to S_1S_2.[6] The θ_3-axis is perpendicular to the $\theta_1\theta_2$-plane; finally some orientation is given to the axes. With this choice of coordinates, we have

$$\left.\begin{aligned} a_{11} &\neq a_{21} \\ a_{12} &= a_{22} \\ a_{13} &= a_{23} = 0 \end{aligned}\right\} \tag{6}$$

We shall write $a_{11}=a_1$, $a_{21}=a_2$; $a_{12}=a_{22}=b$.

To make the formulae more concise, we introduce the following notation:

$$\underline{z}=|z_{12}-r|; \qquad \underline{z}^*=|z_{21}-r|, \tag{7}$$

$$\overline{z}=|z_{12}+r|; \qquad \overline{z}^*=|z_{21}+r|, \tag{7a}$$

$$R_i=\overline{PS}_i=\sqrt{(\theta_1-a_i)^2+(\theta_2-b)^2+\theta_3^2} \text{ for } i=1,2, \tag{7b}$$

$$m=(a_1+a_2)/2, \tag{7c}$$

$$d=(a_1-a_2)/2; \qquad d^*=(a_2-a_1)/2, \tag{7d}$$

$$T_1=m-\frac{\overline{z}^2}{4d}; \qquad T_1^*=m-\frac{(\overline{z}^*)^2}{4d^*}, \tag{7e}$$

$$T_2=m-\frac{\underline{z}^2}{4d}; \qquad T_2^*=m-\frac{(\underline{z}^*)^2}{4d^*}, \tag{7f}$$

$$A_1=\frac{2d}{\overline{z}}; \qquad A_1^*=\frac{2d^*}{\overline{z}^*}, \tag{7g}$$

$$A_2=\frac{2d}{\underline{z}}; \qquad A_2^*=\frac{2d^*}{\underline{z}^*}. \tag{7h}$$

Considering that according to assumption (I) $z_{21}=-z_{12}$, we obtain from (7) and (7a)

$$\underline{z}^*=\overline{z} \text{ and } \overline{z}^*=\underline{z}. \tag{8}$$

We see also

$$d^*=-d, \tag{8a}$$

and therefore

$$T_1^*+T_2=T_1+T_2^*=2m, \tag{8b}$$

from these relations we see

$$A_1^*=-A_2 \text{ and } A_2^*=-A_1. \tag{8c}$$

A simple computation gives $R_1^2-R_2^2=-4d(\theta_1-m)$ so that we have with the aid of (7e) and (7f)

$$\left.\begin{aligned} R_1^2-R_2^2-\underline{z}^2 &= 4d\,(T_2-\theta_1) \\ R_1^2-R_2^2-\overline{z}^2 &= 4d\,(T_1-\theta_1) \\ R_2^2-R_1^2-\underline{z}^2 &= 4d(\theta_1-T_1^*) \\ R_2^2-R_1^2-\overline{z}^2 &= 4d(\theta_1-T_2^*) \end{aligned}\right\} \tag{9}$$

We next rewrite the maximum likelihood condition for each of the three cases (A), (B) and (C).

Case (A)

From (5), (7) and (7a) it is seen that $\underline{z}=z_{12}-r$, $\overline{z}=z_{12}+r$. It follows then from (4a) that $0<\underline{z}+R_2\leqq R_1\leqq\overline{z}+R_2$. By squaring and transposing we obtain the inequalities

$$R_2\leqq\frac{R_1^2-R_2^2-\underline{z}^2}{2\underline{z}} \text{ and } R_2\geqq\frac{R_1^2-R_2^2-\overline{z}^2}{2\overline{z}}.$$

Considering (9), (7g), and (7h), we obtain from these relations the final form for the maximum likelihood conditions

(A.1) $R_2\leqq A_2(T_2-\theta_1)$ and (A.2) $R_2\geqq A_1(T_1-\theta_1)$.

In an analogous manner we obtain the likelihood conditions in Case (B).

(B.1) $R_1\leqq A_2^*(T_2^*-\theta_1)$ and (B.2) $R_1\geqq A_1^*(T_1^*-\theta_1)$.

It is seen that the inequalities (B.1) and (B.2) may be obtained from (A.1) and (A.2) by writing R_1 instead of R_2 and by attaching an asterisk to the A and T symbols.

Case (C) Similarly, we obtain the likelihood conditions

(C.1) $R_2\geqq A_1(T_1-\theta_1)$ and (C.2) $R_1\geqq A_1^*(T_1^*-\theta_1)$.

It is seen that (C.1) $\equiv$ (A.2) and (C.2) $\equiv$ (B.2)

4. Discussion of the Likelihood Condition

Before discussing the likelihood condition, it is desirable to derive a simple relation.

From (2) we have $d_1>d_2$; in our coordinate system this means

$$a_1^2>a_2^2 \text{ or } |a_1|>|a_2|.$$

From this we see easily

$$\text{sign } d=\text{sign } (a_1-a_2)=\text{sign } a_1=-\text{sign } d^*. \tag{10}$$

Here sign x stands for "the sign of x", that is, sign $x=+1$ if $x>0$ and sign $x=-1$ if $x<0$.

We first discuss the case (A) and start with condition (A.1). It is seen immediately that (A.1) can only be satisfied if $A_2(T_2-\theta_1)\geqq 0$.

Considering (7h) and (10) this necessary condition can be written

$$T_2 \text{ sign } a_1\geqq\theta_1 \text{ sign } a_1. \tag{11}$$

This condition restricts the point P to a half space determined by the observations and the location of the stations. In the following we assume that (11) is satisfied. We can, therefore, square (A.1) and obtain

[6] If the origin is located on the line S_1S_2 the three points OS_1S_2 do not determine a plane. In this case the θ_2-axis may be chosen in an arbitrary plane so as to intersect the θ_1-axis perpendicularly.

$R_2^2 \leqq A_2^2(T_2-\theta_1)^2$. As $R_2^2=(\theta_1-a_2)^2+(\theta_2-b)^2+\theta_3^2$,

it follows that

$$(\theta_2-b)^2+\theta_3^2 \leqq (A_2^2-1)\theta_1^2-2(A_2^2T_2-a_2)\,\theta_1+(A_2^2T_2^2-a_2^2). \tag{12}$$

We have to distinguish two possibilities (a) If $A_2^2=1$ then from (7h) and (7f) $T_2=m-d=a_2$. The right-hand side of (12) is then zero so that (12) can only be satisfied for the points of the line $\theta_2=b$, $\theta_3=0$.

We consider next the case where (b) $A_2^2\neq 1$. From (7f) and (7h) it is seen easily that

$$A_2^2T_2-a_2=m(A_2^2-1). \tag{12a}$$

Using this formula we obtain by a simple computation from (12)

$$(A_2^2-1)(\theta_1-m)^2-(\theta_2-b)^2-\theta_3^2 \geqq \frac{A_2^2(T_2-a_2)^2}{A_2^2-1}. \tag{12b}$$

The equality sign in (12b) determines a quadric surface of revolution Q_1. The center of this quadric is the point $(m,b,0)$; the axis of revolution is parallel to the θ_1-axis and is therefore the line joining the two stations S_1 and S_2. The surface Q_1 is a hyperboloid if $A_2^2>1$ and an ellipsoid if $A_2^2<1$. Denote by u the real (resp. major) semiaxis and by v the imaginary (resp. minor) semiaxis of Q_1. Then it is seen from (12b), (7h), and (7f) that

$$u^2=\frac{\bar{z}^2}{4} \text{ and } v^2=\frac{\bar{z}^2}{4}\,|A_2^2-1|. \tag{13}$$

Let $2e$ be the distance between the two focal points of Q_1, then $e^2=u^2+v^2\text{sign}(A_2^2-1)$ or from (13), e=d and u=$\underline{z}$/2.

$$e=d \text{ and } u=\frac{1}{2}\,\underline{z}. \tag{13a}$$

The focal points of the quadric Q_1 are therefore the stations S_1 and S_2. The quadric surface Q_1 divides the space into two regions, we call the region containing the center the interior of Q_1 and its complement the exterior of Q_1. We can then say that condition (A.1) is satisfied outside Q_1 if $A_2^2>1$ and inside Q_1 if $A_2^2<1$. If $A_2^2=1$ then (A.1) is satisfied only on points of the line $\theta_2=b$, $\theta_3=0$ for which $A_2=\text{sign}(T_2-\theta_1)$.

We next consider condition (A.2). This inequality is satisfied in two different regions. In the first region the right-hand side of (A.2) is positive, in the second the right-hand side of (A.2) is negative or zero. We assume first that the right-hand side of (A.2) is positive. By squaring and transposing we obtain then

$$(\theta_2-b)^2+\theta_3^2 \geqq (A_1^2-1)\theta_1^2-2(A_1^2T_1-a_2)\theta_1+A_1^2T_1^2-a_2^2. \tag{14}$$

Again we distinguish two possibilities: (a) If $A_1^2=1$ then from (7e) and (7g) $T_1=m-d=a_2$. The right-hand side of (14) is then zero; in this case (14) is satisfied for all points; (b) if $A_1^2\neq 1$ we see easily from (7e) and (7g) that

$$A_1^2T_1-a_2=m(A_1^2-1). \tag{14a}$$

Using this formula (14) reduces by a simple computation to

$$(A_1^2-1)(\theta_1-m)^2-(\theta_2-b)^2-\theta_3^2 \leqq \frac{A_1^2(T_1-a_2)^2}{A_1^2-1}. \tag{14b}$$

The equality sign in (14b) determines again a quadric surface of revolution Q_2. The center of this quadric is the point $(m, b, 0)$; the axis of revolution is again the line joining the stations S_1 and S_2. The surface Q_2 is a hyperboloid if $A_1^2>1$ and an ellipsoid if $A_1^2<1$. Denote by p the real (major) semiaxis and by q the imaginary (minor) semiaxis of Q_2. Then it is seen from (14b), (7g) and (7e) that

$$p^2=\frac{\bar{z}^2}{4} \text{ and } q^2=\frac{\bar{z}^2}{4}\,|A_1^2-1|. \tag{15}$$

Let $2f$ be the distance between the two focal points of Q_2. By an argument similar to the one used before, we obtain

$$f=d \text{ and } p=\frac{\bar{z}}{2}, \tag{15a}$$

so that the quadrics Q_1 and Q_2 are confocal. We summarise these results in the following statement.

If the right-hand side of (A.2) is positive, the condition (A.2) is satisfied inside the quadric Q_2 when $A_1^2>1$, but outside Q_2 when $A_1^2<1$. In case $A_1^2=1$, condition (A.2) is satisfied for all points for which $A_1=\text{sign}\,(T_1-\theta_1)$.

We investigate next the second region in which (A.2) is valid by assuming that the right-hand side of (A.2) is nonpositive; that is

$$A_1(T_1-\theta_1) \leqq 0. \tag{15b}$$

From (7g) and (10) we see that sign A_1=sign a_1 so that (A.2) is satisfied if

$$T_1 \text{ sign } a_1 \leqq \theta_1 \text{ sign } a_1. \tag{15c}$$

From (15c) and the necessary condition (11) it is seen that (A.2) is satisfied if θ_1 belongs to the interval (T_1, T_2) in case (15b) holds. Therefore, (A.2) is satisfied either in the above-mentioned region determined by Q_2 respectively in a half space or in a region bounded by two planes perpendicular to the line joining S_1 and S_2.

In case (A) we have $\underline{z}=z_{12}-r>0$ so that $\bar{z}>z$. Therefore, we see from (7g) and (7h) that $A_2^2>A_1^2$ and using also (11a) and (15a), $u<p$. We are now ready to determine the region where (A.1) and (A.2)

are satisfied simultaneously. We have to distinguish five possibilities.

1. $A_2^2 > A_1^2 > 1$. It is easily seen that the point $(T_2,b,0)$ [resp. the point $(T_1,b,0]$ is on the line segment joining the vertices of Q_1 (resp. Q_2). From our previous results we see that (A.1) and (A.2) are satisfied in one-half of the hyperbolic shell bounded by Q_1 and Q_2.

2. $A_2^2 > 1 = A_1^2$. The point $(T_1,b,0)$ coincides with S_2, while $(T_2,b,0)$ is on the line segment joining the vertices of Q_1. Conditions (A.1) and (A.2) are satisfied in one-half of the outside of the hyperboid Q_1.

3. $A_2^2 > 1 > A_1^2$. The point $(T_1,b,0)$ is then outside Q_1 and outside Q_2, while $(T_2,b,0)$ is inside Q_1. The region consists again of one-half of the outside of the hyperboloid Q_1.

4. $A_2^2 = 1 > A_1^2$. In this case conditions (A.1) and (A.2) are satisfied only by points of the line S_1S_2, which obey (11).

5. If $1 > A_2^2 > A_1^2$ no region exists where (A.1) and (A.2) are simultaneously satisfied. It is worth while to remark that cases (2), (3), (4), and (5) are of little practical interest. From (7g), (7h), and (10) it is seen that $A_1^2 \leqq 1$ (respectively $A_2^2 \leqq 1$) is equivalent to

$$|2d| \leqq |z_{12} - r| \quad \text{(respectively } |2d| \leqq |z_{12} + r|\text{)}.$$

A situation where these relations hold is conceivable but unlikely as long as r is small. This is seen if we remember that the difference between two sides of a triangle is always less than its third side.

Case (B) can be discussed independently by repeating the arguments used for case (A).

We can then summarize the results by distinguishing the following five cases:

1. $A_1^2 > A_2^2 > 1$. In this case (B.1) and (B.2) are satisfied in one half of the hyperbolic shell bounded by Q_1 and Q_2.

2. $A_1^2 > 1 = A_2^2$.
3. $A_1^2 > 1 > A_2^2$.

conditions (B.1) and (B.2) are satisfied in one half of the outside of Q_2.

4. $A_1^2 = 1 > A_2^2$. Then (B.1) and (B.2) are satisfied only by points of the line S_1S_2 that obey (11).

5. If $1 > A_1^2 > A_2^2$ no region exists where both (B.1) and (B.2) are simultaneously satisfied. Cases (2), (3), (4), and (5) offer again little practical interest.

We finally consider Case (C) with the conditions (C.1) $\equiv$ (A.2) $R_2 \geqq A_1(T_1 - \theta_1)$ and (C.2) $\equiv$ (B.2) $R_1 \geqq A_1^*(T_1^* - \theta_1)$. It is seen that (C.1) is identical with (A.2) and (C.2) with (B.2), therefore, the previous results can be applied immediately. It is advisable to remark that no necessary conditions [similar to (11)] exist; however, (C.1) as well as (C.2) are satisfied if the right-hand sides are nonpositive. Considering the previous results, case (C) may be summarized by distinguishing the following five cases.

1. $A_2^2 > A_1^2 > 1$ [or $A_1^2 > A_2^2 > 1$]. Conditions (C.1) and (C.2) are satisfied in a simply connected region bounded by one nappe of Q_1 and by one nappe of Q_2 so that the convex side of one nappe is turned toward S_1, while the convex side of the other nappe is turned toward S_2.

2. $A_2^2 > A_1^2 = 1$ [or $A_1^2 > A_2^2 = 1$]. The conditions (C.1) and (C.2) are satisfied in the region that is bounded by one nappe of one of the quadrics and that contains the center.

3. $A_2^2 > 1 > A_1^2$ [or $A_1^2 > 1 > A_2^2$]. The conditions are again satisfied in the region that is bounded by one nappe of one of the quadrics and that contains the center.

4. $A_2^2 = 1 > A_1^2$ [or $A_1^2 = 1 > A_2^2$]
5. $1 > A_2^2 > A_1^2$ [or $1 > A_1^2 > A_2^2$]

the conditions are everywhere satisfied.

In case (C) the observation gives only little information about the location of the moving object. However, case (C) can occur only if $|z_{12}| < r$. This will happen only for a small portion of the path of the moving object if r is small. Moreover, it should be possible to locate the stations in such a way that case (C) occurs only for one observation at a time so that this possibility should not cause any difficulty in locating the moving object.

5. The Maximum Likelihood Region

In section 2, it was assumed that n hyperbolic observations (based on n pairs of stations) were taken to determine the position of the moving object. In section 3 we derived the likelihood condition imposed by a single observation and discussed in section 4 the resulting information on the location of the moving object. It was shown that the moving object was confined to a certain region in space with known boundaries. We finally consider all the n observations. Each observation determines a region; if there exists a point set in the parameter space common to all these regions then a maximum likelihood region R exists and is identical with this point set. The boundaries of R are hyperboloids of revolution. Any point inside the region R can be considered to be a maximum likelihood estimate.[7]

With an appropriate choice of stations it is easy to devise a computational procedure that leads always to an interior point of R. If the maximum likelihood region becomes small, then it is practically possible to use any point interior to R as an estimate for the unknown position of the moving object.

[7] The maximum likelihood region cannot increase in size when the number of observations increases. On the contrary, it is to be expected that it will decrease.

WASHINGTON, August 18, 1950.

Journal of Research of the National Bureau of Standards Vol. 47, No. 3, September 1951 Research Paper 2245

Infrared Spectra of Eighteen Halogen-Substituted Methanes

Earle K. Plyler and W. S. Benedict

In order to study how the vibrational frequencies of methane vary with halogen substitutions, the infrared spectra of the following halogen-substituted methanes have been studied with a prism spectrometer between 2 and 38 microns: Carbon tetrafluoride, chlorotrifluoromethane, dichlorodifluoromethane, trichlorofluoromethane, carbon tetrachloride, trichlorobromomethane, dichlorodibromomethane, fluoroform, difluorochloromethane, dichlorofluoromethane, chloroform, dichlorobromomethane, chlorodibromomethane, bromoform, iodoform, methylene fluoride, methylene chloride, and methylene iodide. Spectra are presented as obtained at room temperature in the vapor and liquid states, and in a few cases in solution. The bands are interpreted as fundamentals, overtones, combination, and difference bands. Tables and graphs display the regularities existing among the various fundamentals of these molecules and other halogen-substituted methanes. Force-constant calculations, using an approximate potential function with general constants transferred from one molecule to another are reported.

1. Introduction

The infrared absorption spectra of various halogen derivatives of methane have been studied by several investigators in various regions of the spectrum, and under varying degrees of dispersion [1].[1] The Raman spectra of these compounds have also been extensively studied [2]. The gradual improvement in infrared techniques, in particular the development of prism spectrographs using thallium bromide-iodide (KRS–5) as the dispersing medium, and the increasing practical importance of the fluorine-containing compounds (Freons) have made it seem worth while to carry out a comprehensive reinvestigation of these compounds over the wide spectral range of 2 to 38 μ, using prism spectrographs of various dispersing intervals, so that good dispersion is obtained throughout the entire region. Compounds were studied both in the vapor and liquid states, using in many cases comparatively thick cells in order to develop bands of low intensity.

A listing of the compounds studied, together with their boiling points and the phases in which they were observed, is given in table 1. Representatives of all types of halogen-substituted methanes except the methyl halides, which have been extensively studied under high resolution, were included.

Since the spectra were recorded with prism spectrographs, it was not possible to resolve the rotational fine-structure.

It should be possible to account for the observed absorption bands in terms of transitions among the various vibrational states of the molecules. The bands will be of three types: fundamentals, in which transition occurs from the ground vibrational level to a state in which one mode of vibration is singly excited; overtones and combinations, from the ground level to states in which there are two or three quanta of vibrational energy in one or more modes; and difference bands, in which transition is from one singly excited vibrational mode to other higher vibrational levels. In general the fundamentals will be the most intense bands, although in certain of the molecules, because of symmetry considerations, the intensity in the vapor phase should become zero. The combinations and overtones, lying at shorter wavelengths than the fundamentals, will be weaker, and the difference bands, which, in general, will be at longer wavelengths, will be very weak, except in the heavier molecules, where the fundamentals will be of such low energy that appreciable percentages of the molecules will be in excited states at room temperature. The following sections describe the experimental method, present the results, and discuss further the vibrational assignments.

[1] Figures in brackets indicate the literature references at the end of this paper.

2. Experimental Methods and Results

The infrared absorption spectra of 18 substituted methanes have been measured in the region 2 to 38 μ. They were measured in the liquid state, at room temperature whenever possible, and also several of the compounds, as listed in table 1, have been measured in both the liquid and vapor state. The eight Freons have been measured as gases, except trichlorofluoromethane, in the 23- to 38-μ region. In order to observe the bands of low intensity in liquids, a cell with a thickness of 1.6 mm was used. For the intense bands a film of liquid between windows constituted the cell. In such cases the cell thickness was of the order of 0.01 mm. For the measurement of the gases and vapors the cell thickness varied from 5 cm to 1 m. The pressure of the vapors was that of the saturated vapor at room temperature (approximately 25° C). For the Freons the pressure was atmospheric or less for the different cell lengths. The liquid-cell thickness, gas-cell length, and gas pressure are given on graphs of the results. The spectra were recorded on a Perkin-Elmer spectrometer.

In order to cover the region from 2 to 38 μ with good resolution, prisms of lithium fluoride, sodium chloride, potassium bromide, and thallium bromide-iodide were used. Sharp bands could be measured

with an accuracy of 5 cm^{-1} or less for the entire region. The general method of measurement was the same as that used in previous studies [3].

The eight fluorinated methane derivatives were supplied by W. S. Murray, of Kinetic Chemicals, Wilmington, Del. They were all above 99 percent in purity, except carbon tetrafluoride, whose spectrum showed one band that could not be accounted for by combination or overtone bands. It appeared in the same position as an intense band in chlorotrifluoromethane at about 9 μ. The carbon tetrafluoride gas was tested for purity by F. L. Mohler on the mass spectrometer and found to be 98.2 percent pure. The Michigan Chemical Co. supplied the chlorodibromomethane, dichlorobromomethane, trichlorobromomethane, and dichlorodibromomethane, and some of the others were from Dow Chemical Co. The bromoform and chloroform were obtained from Eastman Kodak Co. and were purified by W. Harold Smith, of the Organic Chemistry Section. After the first purification, the chloroform showed a band in the 3.4-μ region in addition to the intense band at 3.3 μ. After the second purification, the band at 3.4 μ disappeared.

The results are presented as graphs of percentage absorption against wavelength and wave number in figures 1 to 12, inclusive. The conditions of measurement are stated on each graph. In general, the spectra are presented in groups of five molecules of similar structure, and the spectrum is divided into two portions, 2 to 15 μ, corresponding to measurements with sodium chloride and lithium fluoride prisms, and 15 to 38 μ, corresponding to measurements with potassium bromide and thallium bromide-iodide prisms.

Numerical values of the positions of maximum absorption that may be identified as band centers, and further data pertaining to their interpretation, are presented in tables 2 to 6, inclusive. These include the band centers in wave numbers; the approximate intensity, characterized as weak, strong, etc. (for a more quantitative estimate, the graphs should be consulted); the vibrational transition; and the symmetry of the transition. In addition to bands that appear in the infrared spectrum, there are given in parentheses the fundamental frequencies that do not appear, either because they fall outside the range of wavelengths studied, or because they have zero or very weak intensities. These frequencies are obtained either from the Raman effect or from combination and difference bands. The values given refer in general to the liquid state, except for compounds that are gaseous at room temperature. Cases where there is a pronounced difference between the two states will be mentioned in the discussion.

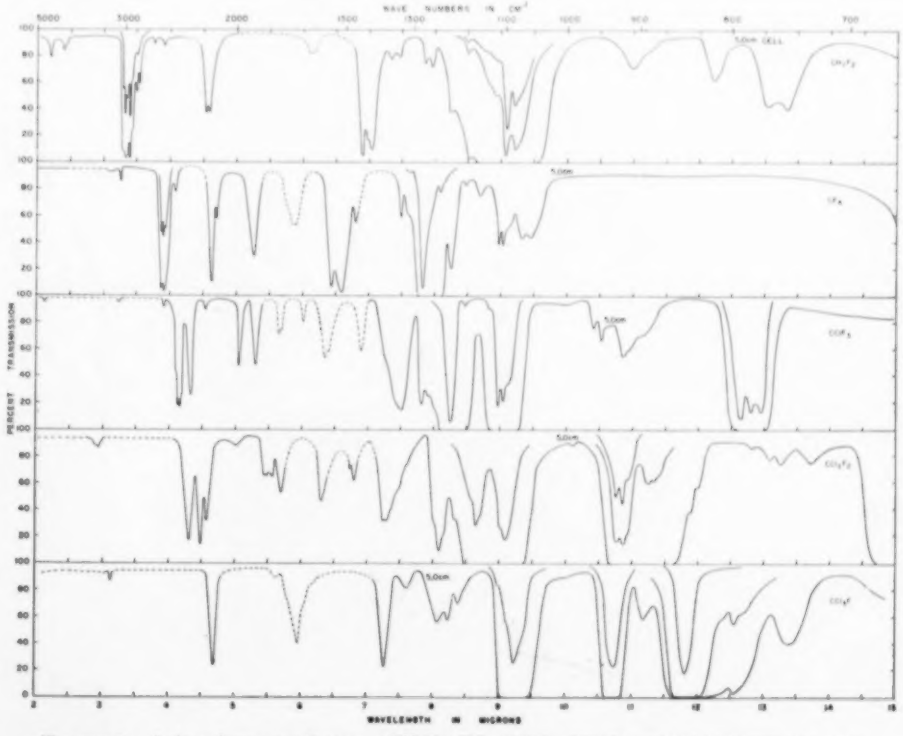

FIGURE 1. *Infrared spectra of gaseous* CH_2F_2, CF_4, $CClF_3$, CCl_2F_2, *and* CCl_3F *from 2 to 15* μ.

The pressure is atmospheric. The insert was measured at reduced pressures.

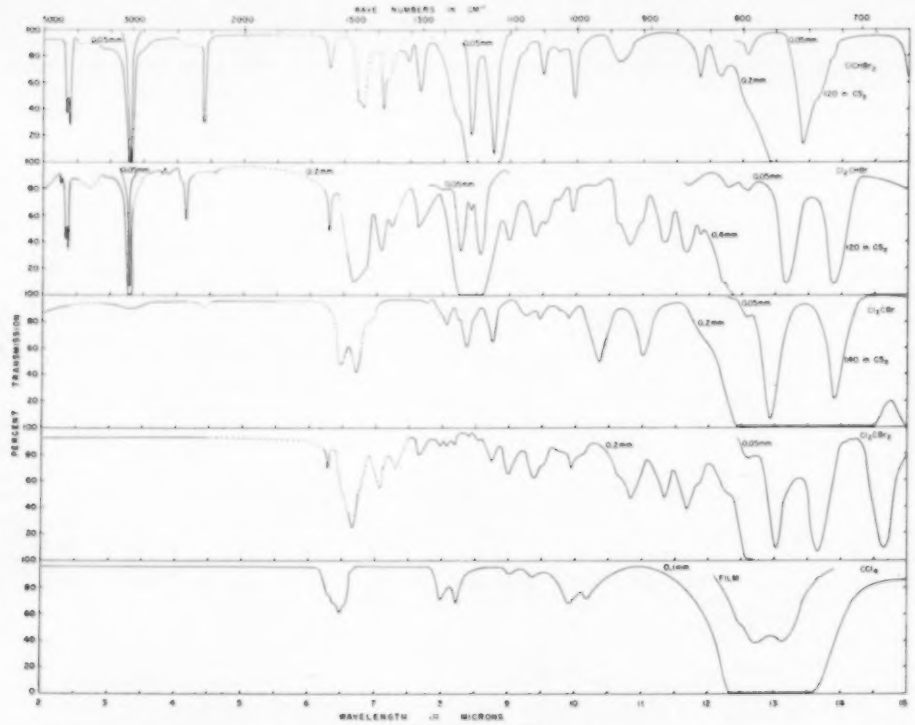

FIGURE 2. *Infrared spectra of* $CHBr_2Cl$, $CHBrCl_2$, $CBrCl_3$, CBr_2Cl_2, *and* CCl_4 *in the liquid state.*

Some strong bands near 14 μ were measured in solution.

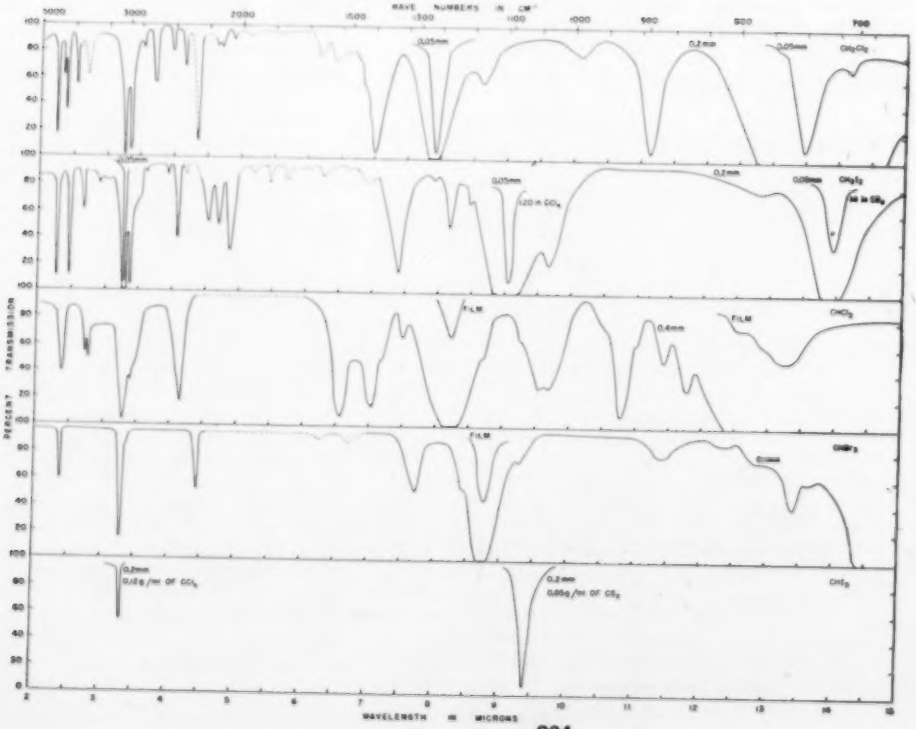

FIGURE 3. *Infrared spectra of* CH_2Cl_2, CH_2I_2, $CHCl_3$, $CHBr_3$, *in the liquid state and* CHI_3 *in solution from 2 to 15 μ.*

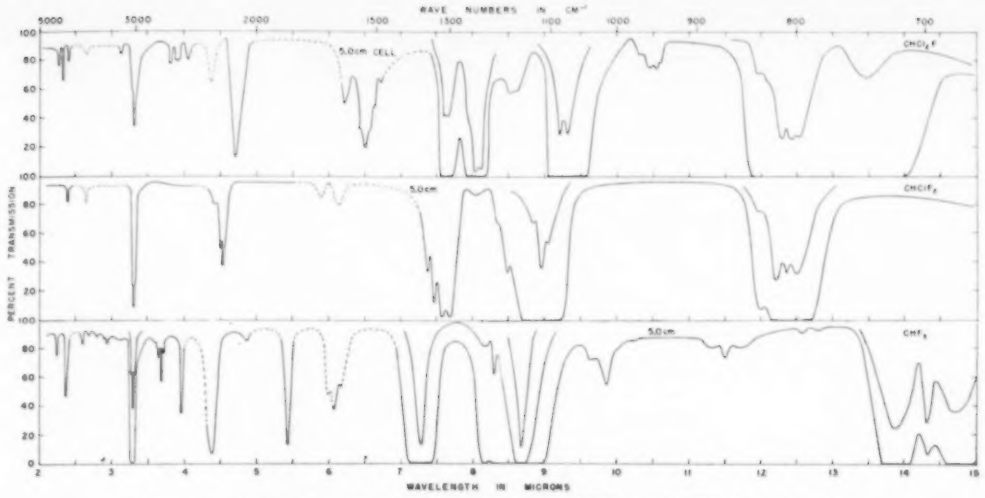

FIGURE 4. *Infrared spectra of gaseous* $CHCl_2F$, $CHClF_2$, *and* CHF_3 *from 2 to 15 μ.*

Pressure is atmospheric. Insert graphs are for pressures less than atmospheric.

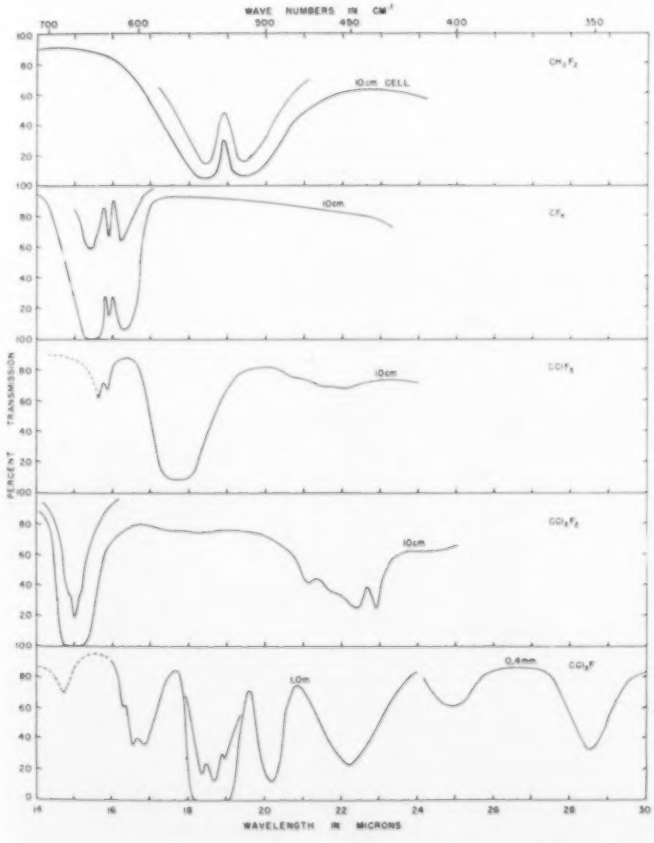

FIGURE 5. *Infrared spectra of gaseous* CH_2F_2, CF_4, $CClF_3$, CCl_2F_2, *and* CCl_3F *from 14 to 30 μ.*

Insert graphs are for pressures less than atmospheric. For CCl_3F the 0.4-mm cell refers to the liquid state.

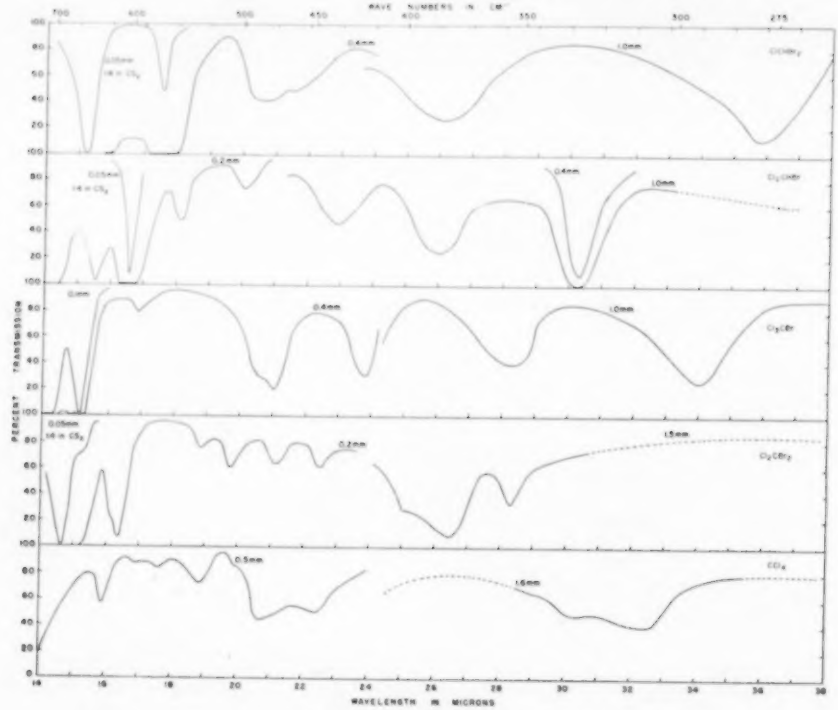

FIGURE 6. *Infrared spectra of* $CHBr_2Cl$, $CHBrCl_2$, $CBrCl_3$, CBr_2Cl_2, *and* CCl_4 *from 14 to 38 μ in the liquid state.*

The stronger bands near 16 μ were measured in solution.

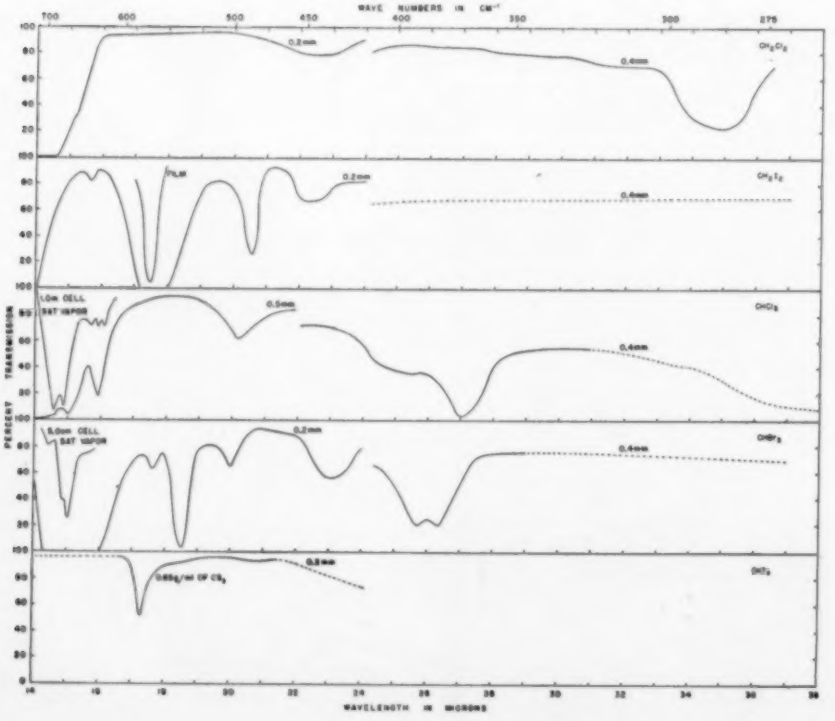

FIGURE 7. *Infrared spectra of* CH_2Cl_2, CH_2I_2, $CHCl_3$, $CHBr_3$, *in the liquid state, and* CHI_3 *in solution from 14 to 38 μ.*

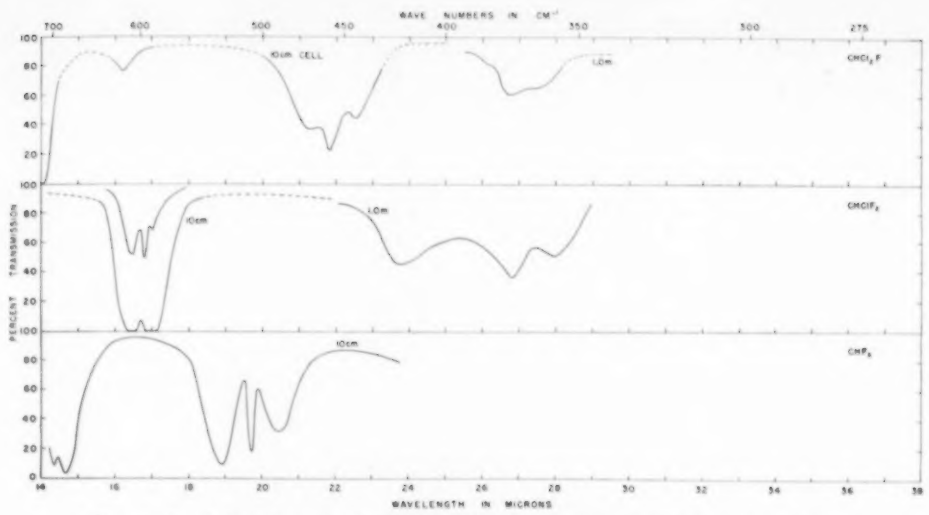

FIGURE 8. *Infrared spectra of gaseous* $CHCl_2F$, $CHClF_2$, *and* CHF_3 *from 14 to 38 μ.*
Pressure is atmospheric. Insert graph is for a pressure less than atmospheric.

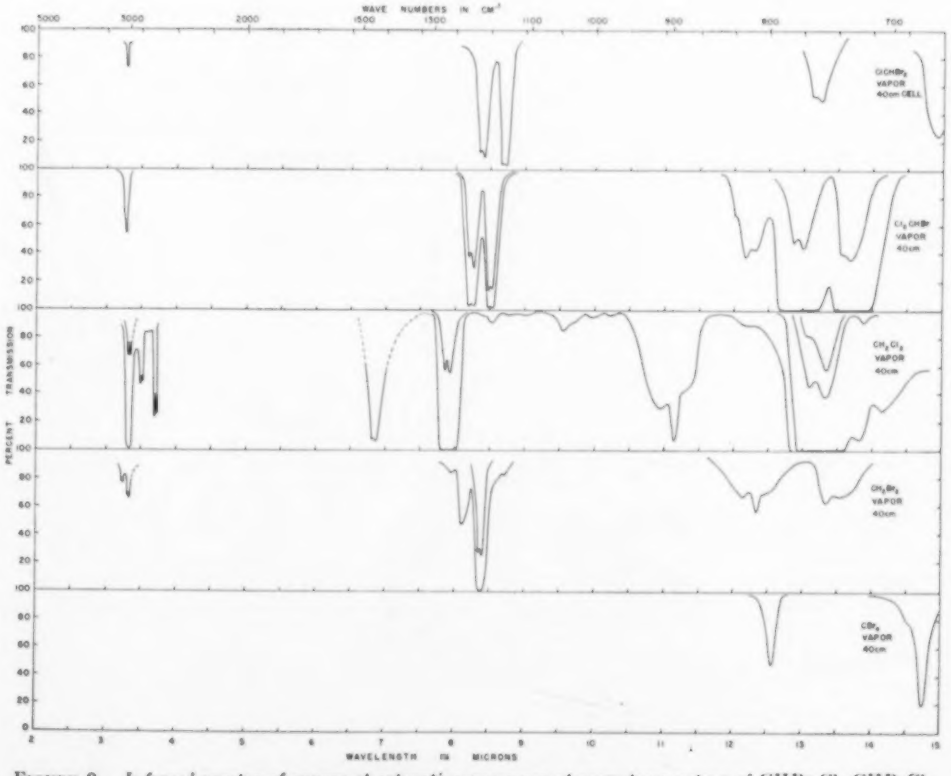

FIGURE 9. *Infrared spectra of vapors at saturation pressures at room temperature of* $CHBr_2Cl$, $CHBrCl_2$, CH_2Cl_2, CH_2Br_2, *and* CBr_4, *from 2 to 15 μ.*
The insert curves are for reduced vapor pressures.

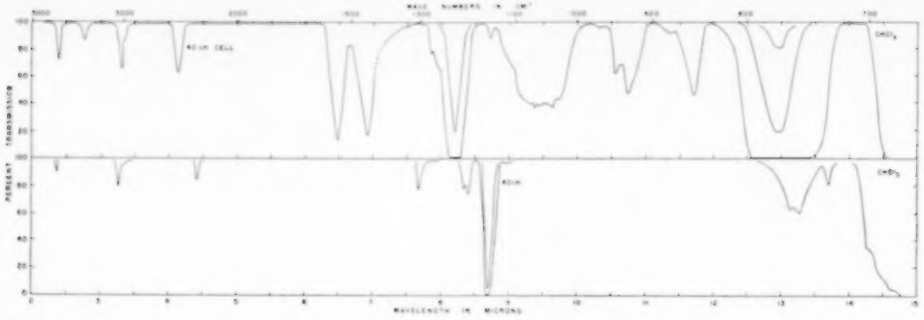

FIGURE 10. *Infrared spectra of vapors saturated at room temperature of* $CHCl_3$, *and* $CHBr_3$ *from 2 to 15 μ.*

The inserts are for reduced pressure.

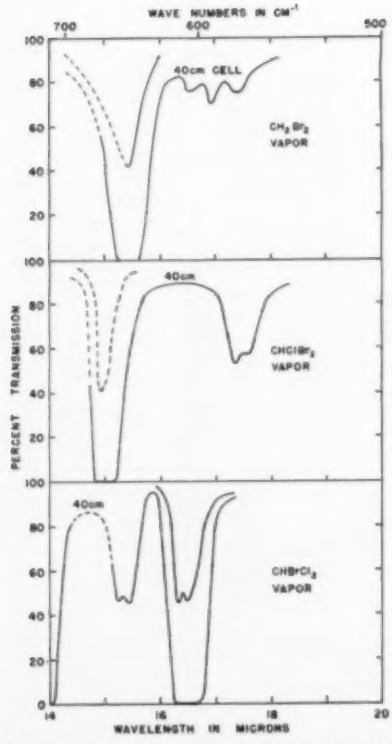

FIGURE 11. *Infrared spectra of saturated vapors of* CH_2Br_2, $CHBr_2Cl$, *and* $CHBrCl_2$ *from 14 to 20 μ.*

Insert curves are for reduced pressure.

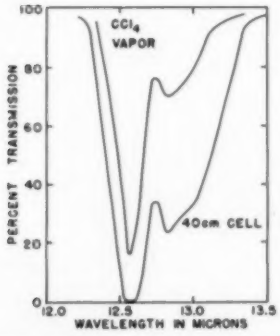

FIGURE 12. *Infrared absorption spectra of saturated vapor of* CCl_4 *at room temperature.*

Insert curve is for reduced pressure.

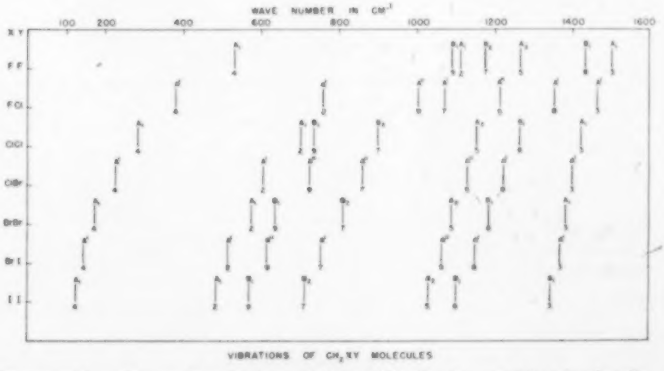

FIGURE 13. *Comparison of the positions of the fundamental bands of molecules of type* CH_2XY.

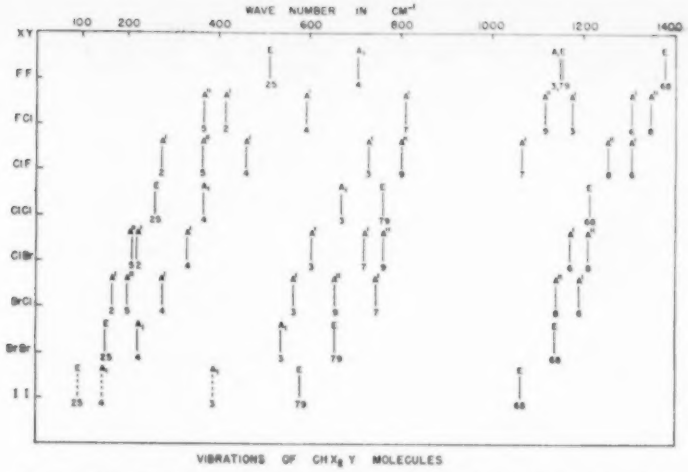

FIGURE 14. *Comparison of the positions of the fundamental bands of molecules of type* CHX_2Y.

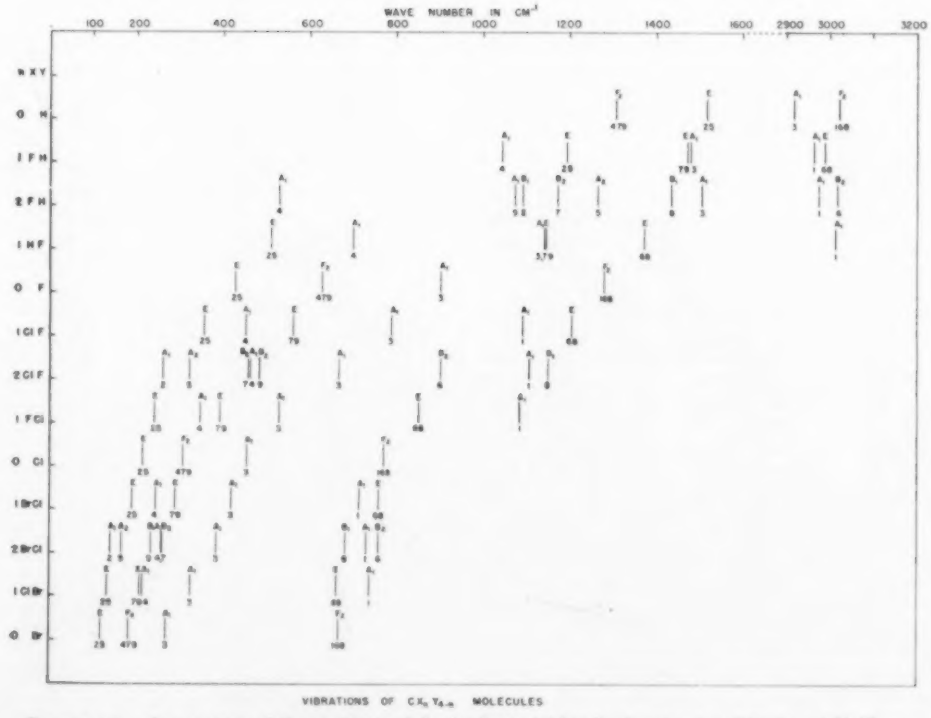

FIGURE 15. *Comparison of the positions of the fundamental bands of molecules of the type* CX_2Y_{4-2}.

TABLE 1. *Some physical properties of the compounds measured*

Compound	Formula	Boiling point *	Observed as—		
			Gas	Liquid	Solution
		°C			
Carbon tetrafluoride (Freon 14)	CF_4	−128	×		
Chlorotrifluoromethane (Freon 13)	CF_3Cl	−80	×		
Dichlorodifluoromethane (Freon 12)	CF_2Cl_2	−28	×		
Trichlorofluoromethane (Freon 11)	CCl_3F	24.1	×		
Carbon tetrachloride	CCl_4	76.77	×	×	
Trichlorobromomethane	CCl_3Br	104.07		×	×
Dichlorodibromomethane	CCl_2Br_2	135±		×	×
Fluoroform (Freon 23)	CHF_3	−82.2	×		
Difluorochloromethane (Freon 22)	CHF_2Cl	−40.8	×		
Dichlorofluoromethane (Freon 21)	$CHFCl_2$	8.9	×		
Chloroform	$CHCl_3$	61.26 58 to 61.5	×	×	
Dichlorobromomethane	$CHCl_2Br$	91 to 92	×	×	×
Chlorodibromomethane	$CHClBr_2$	120	×	×	×
Bromoform	$CHBr_3$	149.5	×	×	
Iodoform	CHI_3	Sublimes			×
Methylene fluoride (Freon 32)	CH_2F_2	−51.6	×		
Methylene chloride	CH_2Cl_2	40.1	×	×	×
Methylene iodide	CH_2I_2	Decomposes 180	×	×	×

* These values are principally from the Handbook of Physics and Chemistry.

3. Discussion

3.1. The Fundamental Frequencies

Each of the related methane derivatives reported in this paper has nine fundamental frequencies of vibration. The general theory of the vibrations of such molecules has been discussed in many places and need not be repeated here. It will suffice to recall that when there are atoms of different kinds joined to the carbon atom, the symmetry of the molecule is less than when all four linked atoms are alike, and that the particular degree of symmetry governs the degeneracy of the vibrations, the general form of the molecular motions, and the resulting activity in both the infrared and the Raman spectrum. The pertinent information derivable from such symmetry considerations is summarized in table 7. The symmetry class of overtones, combinations, and difference bands of the various fundamentals follow well-known rules and are given in tables 2 to 6.

The numerical values of the fundamentals show regular variations when going from one molecule to another in which a single substituent has been altered. This is a qualitative consequence of the facts that in all these substituted methanes the forces between the central atom and a particular peripheral atom are to a first approximation independent of the other peripheral atoms, and that these forces vary regularly with the mass of the peripheral atom. A more quantitative discussion will be given later. The relative positions and groupings of the numerical values are also affected by the symmetry. The conventional system of numerical identification of the fundamentals is based on the symmetry. This system fails to display the regularities existing among molecules of different symmetry. Accordingly, in this paper, one purpose of which was to show the consistency of all the frequencies of a large number of related compounds of different symmetry, use is made of an unconventional numbering system. The system closely resembles the conventional one for molecules of the type CH_2X_2, where there are no degeneracies. For molecules of higher symmetry than C_{2v}, where degeneracy occurs, the degenerate frequencies have been assigned two or three numbers, so that all nine frequencies may be identified. The relation between the numbers adopted here and those that would follow from application of the conventional rules is shown in table 8. This table also collects in one place the numerical values of the fundamentals of all the molecules, the spectra of which are reported in this paper, as well as of related molecules that have recently been studied in this laboratory [4].

TABLE 2. *The observed bands and their assignments of* CF_4, CF_3Cl, CF_2Cl_2, *and* $CFCl_3$

ν	Intensity	Band	Symmetry
Molecule CF_4 (Freon 14) molecular symmetry T_d			
cm^{-1}			
[437](R)	----	ω_{25}	E
630	s	ω_{479}	F_2
[904](R)	----	ω_1	A_1
1067	w	$\omega_{25}+\omega_{479}$	$F_2(+F_1)$
1277	s	$2\omega_{479}$ ω_{125}	$F_2(+A_1+E)$ F_2
1468	w	$2\omega_{125}+\omega_{479}$	$2F_2(+F_1)$
1517	m	$\omega_{479}+\omega_1$	F_2
1555	m	----------	----------
1698	w	$\omega_{125}+\omega_{160}$	$F_2(+F_1)$
1901	m	$3\omega_{479}$ $\omega_{479}+\omega_{125}$	$2F_2(+A_1+F_1)$ $F_2(+A_1+E+F_1)$
2123	w	$2\omega_{479}+\omega_1$	$F_2(+A_1+E)$
2160	m	$\omega_1+\omega_{160}$	F_2
2447	vw	$\omega_{479}+2\omega_{25}$	F_2
2565	m	$2\omega_{125}$	$F_2(+A_1+E)$
3081	vw	$2\omega_{25}+\omega_{125}$	F_2
Molecule CF_3Cl (Freon 13) molecular symmetry C_{3v}			
[356](R)	----	ω_{26}	E
[470](R)	----	----------	----------
450?	vw	ω_4	A_1
563	m	ω_{79}	E
635	w	$\omega_{26}-\omega_{79}$? $\omega_1-\omega_4$	A_1
781	s	ω_1	A_1
921	w	$\omega_{23}+\omega_{19}$	$E+A_1(+A_2)$
950	w	$2\omega_{79}$	A_1
1105	s	ω_3	A_1
1132?	w	$2\omega_{79}$	$2E+A_1$
1181?	w	----------	----------
1212	s	ω_{23}	E
[1279]	m	$\omega_3+\omega_4$	A_1
1335	m	$\omega_{79}+\omega_{23}$	E
1451?	m	$\omega_{23}+\omega_1$	E
1575	w	$2\omega_{23}$ $\omega_3+\omega_{23}$ $\omega_{23}+\omega_{19}$	$3A_1+E(+A_2)$
1067	vw	$\omega_4+\omega_{23}$	E
1887	w	$\omega_3+\omega_4$	A_1
1984	w	$\omega_3+\omega_{23}$	E
2208	vw	$2\omega_4$	A_1
2315	m	$\omega_1+\omega_{23}$	E
2417	m	$2\omega_{23}$	$E+A_1$
2554	vw	$\omega_{79}+\omega_3+\omega_{23}$	$E+A_1(+A_2)$
3104	vw	$\omega_3+\omega_1+\omega_{23}$	E

TABLE 2. *The observed bands and their assignments of* CF_4, CF_3Cl, CF_2Cl_2, *and* $CFCl_3$—Continued

ν	Intensity	Band	Symmetry
Molecule CF_2Cl_2 (Freon 12) molecular symmetry C_{2v}			
cm^{-1}			
[261](R)	----	ω_2	A_1
[318](R)	----	ω_5	A_2
437	w	ω_7	B_1
[455](R)	----	ω_4	A_1
446	w	ω_6	----------
473	w	ω_9	B_2
667	s	ω_3	A_1
728	w	$\omega_2+\omega_9$	B_2
755	w	$\omega_5+\omega_7$	B_2
781	vw	$\omega_3+\omega_9$	B_1
837	w	$\omega_6-\omega_5$	A_1
		$\omega_4-\omega_2$	A_1
882	s	$\omega_4+\omega_7$	B_1
922	vs	ω_6	B_1
987?	vw	$\omega_3+\omega_5$	A_2
1101	s	$\omega_3+\omega_4$	A_1
		ω_1	A_1
1159	s	ω_5	B_2
1236	m	$\omega_5+\omega_6$	B_2
1335	w	$2\omega_3$	A_1
1372	w	$\omega_7+\omega_9$	A_1
		$\omega_4+\omega_6$	B_1
		$\omega_9+\omega_6$	A_2?
1473	vw	$\omega_3+\omega_9$	B_1
1587	w	$\omega_9+\omega_1$	B_2
		$\omega_4+\omega_5$	B_2
		$\omega_7+\omega_6$	A_2
1754	w	$\omega_3+\omega_1$	A_1
		$2\omega_4+2\omega_7$	A_1
1795	w	$\omega_4+\omega_6+\omega_7$	A_1
1832	w	$2\omega_6$	A_1
1996	vw	$\omega_4+\omega_7+\omega_1$	B_1
		$\omega_6+\omega_1$	
2188	w	$2\omega_1$	A_1
2242	m	$\omega_1+\omega_5$	B_2
2325	m	$2\omega_5$	A_1
3413	vw	$\omega_1+2\omega_6$	A_1
Molecule $CFCl_3$ (Freon 11) molecular symmetry C_{3v}			
[248](R)	----	ω_{10}	E
350	w	ω_4	A_1
401	vw	ω_{19}	E
451	w	$\omega_{16}-\omega_{19}$?	A_1
495	w	$\omega_{16}-\omega_4$?	E+A_1
		$2\omega_{23}$	
535	m	ω_3	A_1
603	w	$\omega_{23}+\omega_4$	E
		$\omega_{16}-\omega_{23}$	
680	w	$2\omega_4$	A_1
748	w	$\omega_4+\omega_{19}$	E
797	m	$\omega_{23}+\omega_3$	E
847	vs	ω_{16}	E
895	w	$\omega_4+\omega_3$	A_1
932	s	$\omega_{19}+\omega_3$	E
1085	s	ω_1	A_1
		$2\omega_3$	
1115?	m	$\omega_{23}+\omega_{16}$	E+A_1+A_2
1193	w	$\omega_4+\omega_{16}$	E
1215	w	$\omega_{19}+\omega_{16}$	E+A_1(+A_2)
1239	w		
1317	w	$\omega_{23}+\omega_1$	E
1376	m	$\omega_3+\omega_{16}$	E
1678?	w	$2\omega_{16}$	E+A_1
		$2\omega_4+\omega_1$	A_1
1775?	vw	$\omega_{19}+\omega_3+\omega_{16}$	E+A_1+A_2
2132	m	$2\omega_3$	A_1
3195	vw	$3\omega_3$	A_1

TABLE 3. *The observed bands and their assignments of* CCl_4 CCl_3Br, *and* CCl_2Br_2

ν	Intensity	Band	Symmetry
Molecule CCl_4 molecular symmetry T_d			
cm^{-1}			
[218](R)	----	ω_{25}	(E)
309	w	$\omega_3+\omega_{419}-\omega_3$	F_2
319		ω_{419}	
329			
446	w	$\omega_{168}-\omega_{419}$	F_2
482	w	$\omega_3+\omega_{419}-\omega_{419}$	F_2
[458](R)	----	ω_1	(A_1)
501	vw	$\omega_{419}+\omega_{25}$	F_2(+F_1)
531	w	$\omega_{168}-\omega_{25}$	F_2
569	vw	$\omega_3+\omega_{419}-\omega_{25}$	F_2
635	w	$2\omega_{419}$	F_2(+E+A_1)
762	s	ω_{168}	F_2
785	s	$\omega_3+\omega_{419}$	F_2
982	w	$\omega_{168}+\omega_{25}$	F_2(+F_1)
1096	w	$\omega_3+\omega_{419}+\omega_{25}$	F_2(+F_1)
1068	vw	$\omega_{168}+\omega_{419}$	F_2(+F_1+E+A_1)
1107	vw	$\omega_3+2\omega_{419}$	F_2(+E+A_1)
1218	w	$\omega_{168}+\omega_3$	F_2
1253	w	$2\omega_3+\omega_{419}$	F_2
1529	w	$2\omega_{168}$	F_2(+E+A_1)
1546	w	$\omega_{168}+\omega_3+\omega_{419}$	F_2(+F_1+E+A_1)
1575	w	$2\omega_3+2\omega_{419}$	F_2(+E+A_1)
Molecule CCl_3Br molecular symmetry C_{3v}			
[187](R)	----	ω_{23}	E
[243](R)	----	ω_4	A_1
294	w	ω_{19}	E
353	w	$\omega_{16}-\omega_3$	E
		$2\omega_{23}$	E+A_1
420	w	ω_3	A_1
475	m	$2\omega_4$	A_1
		$\omega_1-\omega_4$	A_1
490	w	$\omega_{19}+\omega_{23}$	E+A_1(+A_2)
592	vw	$2\omega_{19}$	E+A_1
		$\omega_3+\omega_{23}$	E
		$\omega_{16}-\omega_{23}$	A_1
664	s	$\omega_3+\omega_4$	A_1
719	vs	ω_1	A_1
773	vs	ω_{16}	E
796	m	$2\omega_{19}+\omega_{23}$	2E+A_1(+A_2)
908	w	$\omega_1+\omega_{23}$	E
966	w	$\omega_1+\omega_4$	A_1
		$\omega_{16}+\omega_{23}$	E+A_1(+A_2)
1010	vw	$\omega_{16}+\omega_4$	E
1046	vw	$\omega_4+2\omega_{23}$	E+A_1
1080	vw	$2\omega_3+\omega_4$	A_1
1143	w	$\omega_1+\omega_3$	A_1
1193	w	$\omega_{16}+\omega_3$	E
1242	vw	$\omega_1+\omega_{16}-\omega_4$	E
1440	w	$2\omega_1$	A_1
1493	w	$\omega_1+\omega_{16}$	E
1545	w	$2\omega_{16}$	E+A_1
2270	vw	$2\omega_{16}+\omega_1$	E+A_1

TABLE 3. *The observed bands and their assignments of* CCl_4, CCl_2Br, *and* CCl_2Br_2—Continued

ν	Intensity	Band	Symmetry
Molecule CCl_2Br_2 molecular symmetry C_{2v}			
cm^{-1}			
[141](R)	----	ω_8	A_1
[164](R)	----	ω_9	(A_2)
[230](R)	----	ω_6	B_1
[252](R)	----	ω_7	B_2
[252](R)	----	ω_4	A_1
353	w	$\omega_6+\omega_{12}$	B_1
377	w	ω_3	A_1
398	w	$\omega_7+\omega_{12}$ $\omega_8+\omega_5$	B_2 B_2
443	w	$2\omega_{10}$ $\omega_5-\omega_{14}$	A_1 $B_1(+A_2)$
472	w	$\omega_6+\omega_{14}$	$B_1(+A_2)$
505	w	$2\omega_{14}$	$2A_1+B_2$
529	w	$\omega_3+\omega_{12}$ $\omega_3+\omega_5$	A_1 A_2
610	m	$\omega_1+\omega_{14}$ $\omega_5-\omega_{12}$	$A_1+B_1+B_2$ B_2
683	vs	ω_6	B_1
733	vs	ω_1	A_1
768	vs	ω_5	B_2
793	m	$\omega_5+\omega_5-\omega_3$	B_1
818	w	$\omega_6+\omega_{12}$	B_1
844	vw	$\omega_8+\omega_5$	B_2
858	w	$\omega_1+\omega_{12}$	A_1
882	w	$\omega_8+\omega_{12}$ $\omega_1+\omega_5$	B_2 (A_2)
923	w	$\omega_3+\omega_9$ $\omega_6+\omega_5$	A_1 B_1
939	vw	$\omega_9+\omega_{17}$	$B_1(+A_2)$
991	vw	$\omega_1+\omega_{15}$	A_1+B_2
1005	w	$\omega_5+\omega_{17}$	$(A_2)+A_1+B_2$
1067	w	$\omega_6+\omega_3$	B_1
1112	w	$\omega_1+\omega_3$	A_1
1144	w	$\omega_8+\omega_3$	B_2
1171	vw	$\omega_5+\omega_5+\omega_3$	A_1
1190	vw	$\omega_1+2\omega_9$	A_1
1221	vw	$\omega_8+\omega_3+\omega_5$	B_2
1241	vw	$\omega_1+\omega_3+\omega_2$	A_1
1256	vw	$\omega_5+\omega_3+\omega_2$	B_2
1307	w	$\omega_8+\omega_3+\omega_5$	A_1
1362	w	$2\omega_6$	A_1
1416	w	$\omega_1+\omega_6$	B_1
1470	vw	$2\omega_1$	A_1
1503	m	$\omega_1+\omega_5$	B_2
1540	vw	$2\omega_5$	A_1
1592	w	$2\omega_9+\omega_9$	B_1

TABLE 4. *The observed bands and their assignments of* CHF_3, CHF_2Cl, $CHFCl_2$, *and* $CHCl_3$

ν	Intensity	Band	Symmetry
Molecule CHF_3 (Freon 23) molecular symmetry C_{3v}			
cm^{-1}			
507	m	ω_{10}	E
700	m	ω_4	A_1
870	w	$\omega_{16}-\omega_{15}$	A_1
1014 1035	w vw	$2\omega_{15}$	$E+A_1$
1150?	vs	ω_3	A_1
1152	vs	ω_{19}	E
1206	s	$\omega_{15}+\omega_4$	E
1372	m	ω_{16}	E
1647	m	$\omega_{15}+\omega_{19}$	$2E+A_1(+A_2)$

TABLE 4. *The observed bands and their assignments of* CHF_3, CHF_2Cl, $CHFCl_2$, *and* $CHCl_3$—Continued

ν	Intensity	Band	Symmetry
Molecule CHF_3 (Freon 23) molecular symmetry C_{3v}			
cm^{-1}			
1842	m	$(\omega_{15}+\omega_{18}?)$ $\omega_1+\omega_3$ $\omega_4+\omega_{19}$	$E+A_1(+A_2)$ A_1 E
2045	vw	$\omega_3+\omega_{16}$	E
2278	m	$\omega_3+\omega_{19}$ $2\omega_{19}$	2E A_1
2523	m	$\omega_3+\omega_{15}$ $\omega_{19}+\omega_{15}$	2E $A_1(+A_2)$
2716	w	$2\omega_{16}$	$E+A_1$
3031	s	ω_1	A_1
3407 3445	vw vw	$2\omega_{15}+\omega_4$ $3\omega_{19}$	$E+A_1$
4212	w	$\omega_3+\omega_1$ $\omega_{19}+\omega_1$	A_1 E
4448	vw	$\omega_{16}+\omega_1$	E
Molecule CHF_2Cl (Freon 22) molecular symmetry C_s			
365	w	ω_{15}	A''
422	w	ω_{14}	A'
595	s	ω_4	A'
809	vs	ω_7	A'
833	m	$2\omega_{12}$	A'
1116	vs	ω_8	A''
1178	m	ω_3 $\omega_3+\omega_7$	A' A'
1198	w	$2\omega_{14}$	A'
1244	vw	$\omega_{12}+\omega_7$	A'
1311	s	ω_3	A'
1347	m	ω_5	A''
1625?	w	$2\omega_7$	A'
1695?	vw	$\omega_5+\omega_5$ $\omega_5+\omega_8$ $\omega_6+\omega_8$	A'' A' A'
2222	m	$2\omega_9$	A'
3023	m	ω_1	A'
3769?	vw	$\omega_7+\omega_1$?	A'
4167	vw	$\omega_8+\omega_1$	A''
Molecule $CHFCl_2$ (Freon 22) molecular symmetry C_s			
[276](R)	----	ω_{12}	A'
368	w	ω_{15}	A''
458	w	ω_4	A'
742	s	$\omega_5+\omega_5$?	A''
		$(\omega_{12}+\omega_4)$ ω_3?	A'
804	vs	ω_8	A''
835	s	$\omega_3+\omega_4$	A''
955?	w	$\omega_5-\omega_3$ $\omega_5-\omega_{12}$	A'' A''
1079	s	$\omega_5+\omega_{12}$ ω_7	A'' A'
1106	w	$\omega_3+\omega_{12}$	A'
1242	s	ω_5	A''
1260	w	$\omega_4+\omega_{12}$	A''
1304	s	ω_8	A'
1494	w	$\omega_5+\omega_8$	A''
1536	m	$\omega_4+\omega_7$	A'
1608	w	$2\omega_{12}$ $\omega_5+\omega_8$	A' A'
2123	m	$2\omega_7$ $\omega_8+\omega_8$	A' A''
2280?	w	$\omega_5+\omega_7$	A''
2463	w	$2\omega_8$	A'

TABLE 4. *The observed bands and their assigments of* CHF_3, CHF_2Cl, $CHFCl_2$, *and* $CHCl_3$—Continued

ν	Intensity	Band	Symmetry
Molecule $CHFCl_2$ (Freon 21) molecular symmetry C_s			
cm^{-1}			
2557	vw	$\omega_5+\omega_8$	A″
2616	vw	$2\omega_6$	A′
3023	m	ω_1	A′
3184	vw	$3\omega_7$	A′
3780?	vw	$\omega_1+\omega_3$	A′
4144	vw	$\omega_7+\omega_1$	A′
4303	w	$\omega_6+\omega_3$	A′
4398	vw	$4\omega_7$?	A′
Molecule $CHCl_3$ molecular symmetry C_{3v}			
[261](R)	----	ω_{12}	E
370	m	ω_4	A_1
392	w	$\omega_3-\omega_{12}$	$E+A_1$
488	w	$2\omega_{12}$	$E+A_1$
		$\omega_{79}-\omega_{12}$	A_1
629	m	$\omega_3+\omega_{12}$	E
667	s	ω_5	A_1
755	vs	ω_{79}	E
		$2\omega_4$	A_1
849	m	$\omega_{68}-\omega_4$	E
929	m	$\omega_3+\omega_{12}$	E
951	w	$\omega_{68}-\omega_{12}$	A_1
1031	m	$\omega_5+\omega_4$	A_1
1049	m	$\omega_{79}+\omega_{12}$	$E+2A_1$
1145	w	$\omega_{79}+\omega_4$	E
1214	s	ω_{68}	E
1333	w	$2\omega_5$	A_1
1393	m	$\omega_{79}+\omega_4+\omega_{12}$	$E+2A_1$
1420	m	$\omega_3+\omega_{79}$	E
1524	m	$2\omega_{79}$	$E+A_1$
2410	m	$2\omega_{68}$	$E+A_1$
3040	m	ω_1	A_1
3597	w	$3\omega_{68}$	$E+A_1+A_2$
3663	w	$\omega_1+\omega_5$	A_1
4202	m	$\omega_1+\omega_{68}$	E

TABLE 5. *The observed bands and their assignments of* $CHCl_2Br$, $CHClBr_2$, $CHBr_3$, *and* CHI_3

ν	Intensity	Band	Symmetry
Molecule $CHCl_2Br$ molecular symmetry C_s			
cm^{-1}			
[215](R)	----	ω_9	A″
220 (R)	----	ω_2	A′
330	m	ω_8	A′
383	w	$\omega_3-\omega_{23}$	A′+A″
437	w	$2\omega_{23}$	2A′+A″
495	w	$\omega_7-\omega_{23}$	A′+A″
552	w	$\omega_8+\omega_{23}$	A′+A″
		$\omega_9-\omega_{23}$	A′+A″
604	s	ω_3	A′
643	m	$2\omega_8$	A′
719	vs	ω_7	A′
760	vs	ω_9	A″
795	m	$\omega_3+\omega_9$	A″
814	w	$\omega_3+\omega_2$	A′
843	vw	----------	----------
858	w	$\omega_9-\omega_8$	A″
884	w	$\omega_9-\omega_8$	A′

TABLE 5. *The observed bands and their assignments of* $CHCl_2Br$, $CHClBr_2$, $CHBr_3$, *and* CHI_3—Continued

ν	Intensity	Band	Symmetry
Molecule $CHCl_2Br$ molecular symmetry C_s			
cm^{-1}			
916	w	$\omega_7+\omega_{23}$	A′+A″
924	w	$\omega_3+\omega_8$	A′
942	w	$\omega_9+\omega_{23}$	A′+A″
		$\omega_8-\omega_{23}$	A′+A″
1004	vw	$\omega_8-\omega_{23}$	A′+A″
1052	w	----------	----------
1066	w	$\omega_7+\omega_8$	A′
1114	w	$\omega_9+\omega_8$	A″
1168	s	ω_9	A′
1189	m	$2\omega_3$	A′
1211	s	ω_8	A″
1312	w	$\omega_3+\omega_7$	A′
1385	vw	$\omega_3+\omega_9$	A″
		$\omega_9+\omega_{23}$	A′+A″
1414	vw	$2\omega_7$	A′
		$\omega_8+\omega_{23}$	A′+A″
1506	w	$2\omega_9$	A′
1592	w	$\omega_{68}+\omega_4$	A′+A″
2421	w	$2\omega_{68}$	2A′+A″
3040	s	ω_1	A′
3077	vw	$2\omega_8+\omega_7$	A′
3802	vw	$\omega_1+\omega_9$	A″
4237	m	$\omega_1+\omega_8$	A′
4291	w	$\omega_1+\omega_8$	A″
4504	vw	$\omega_1+2\omega_9$	A′
Molecule $CHClBr_2$ molecular symmetry C_s			
[168](R)	----	ω_2	A′
[201](R)	----	ω_9	A″
278	w	ω_8	A′
383	w	$\omega_3-\omega_{23}$	A′+A″
		$2\omega_{23}$	2A′+A″
460	w	$\omega_8+\omega_2$	A′
		$\omega_9-\omega_8$	A′
492	w	$\omega_8+\omega_9$	A″
		$\omega_9-\omega_2$	A″
570	s	ω_3	A′
657	vs	ω_9	A″
733	m	$\omega_3+\omega_2$	A′
746	s	ω_7	A′
796	m	$\omega_3+\omega_9$	A″
821	w	$\omega_2+\omega_9$	A″
844	w	$\omega_3+\omega_8$	A′
		$\omega_9+\omega_9$	A′
937	w	$\omega_7+\omega_{23}$	A′+A″
		$\omega_9+\omega_8$	A″
1004	w	$\omega_7+\omega_8$	A′
1029	vw	$\omega_8-\omega_2$	A′
1053	w	$\omega_2+\omega_9+\omega_9$	A′+A″
1144	vs	ω_8	A″
		$2\omega_3$	A′
1189	s	ω_9	A′
1218	w	$\omega_3+\omega_9$	A″
1309	w	$2\omega_9$	A′
1340	vw	$\omega_8+\omega_8$	A″
		$\omega_9+\omega_2$	A″
1410	w	$\omega_7+\omega_9$	A″
1473	w	$\omega_9+\omega_8$	A′
1488	w	$2\omega_7$	A′
15927	w	$\omega_3+\omega_7+\omega_9$	A″
2278	m	$2\omega_{68}$	2A′+A″
3034	s	ω_1	A′
4203	m	$\omega_1+\omega_9$	A″
4257	w	$\omega_1+\omega_8$	A′

TABLE 5. *The observed bands and their assignments of* $CHCl_2Br$, $CHClBr_2$, $CHBr_3$, *and* CHI_3—Continued

ν	Intensity	Band	Symmetry
Molecule $CHBr_3$ molecular symmetry C_{3v}			
cm^{-1}			
[154](R)	....	ω_{10}	E
[222](R)	....	ω_4	A_1
[300?](R)	....	$2\omega_{10}$	$E+A_1$
380	m	$\omega_6+\omega_{10}$	E
389	m	$\omega_5-\omega_{10}$	E
435	w	$2\omega_4$	A_1
501	w	$\omega_9-\omega_{10}$	A_1
541	m	ω_3	A_1
668	vs	ω_9	E
6947	m	$\omega_5+\omega_{10}$	E
762	w	$\omega_3+\omega_4$	A_1
873	w	$\omega_9+\omega_4$	E
1078	w	$2\omega_5$	A_1
1142	vs	ω_6	E
1188	m	$\omega_3+\omega_9$	E
1295	m	$2\omega_9$ $\omega_6+\omega_{10}$	$E+A_1$ $E+2A_1$
14937	vw	$2\omega_9+\omega_{10}$	$2E+A_1$
15977	vw	$\omega_5+\omega_6$	E
2257	w	$2\omega_6$	$E+A_1$
3040	m	ω_1	A_1
4202	w	$\omega_1+\omega_6$	E
Molecule $CHBr_3$ molecular symmetry C_{3v}			
[92]?(R)	....	ω_{12}	E
[145]?(R)	....	ω_4	A_1
[385](R)	....	ω_5	A_1
581	m	ω_{11}	E
1064	m	ω_{12}	E
[3040](R)	....	ω_1	A_1

TABLE 6. *The observed bands and their assignments of* CH_2F_2, CH_2Cl_2, *and* CH_2I_2

ν	Intensity	Band	Symmetry
Molecule CH_2F_2 (Freon 32) molecular symmetry C_{2v}			
cm^{-1}			
529	s	ω_4	A_1
757	w	$\omega_{12}-\omega_4$	A_2
816	w	.....	.....
910	w	$\omega_{12}-\omega_4$	B_1
1090	vs	ω_9	B_1
1116	s	ω_3	A_1
1176	m	ω_7	B_2
1262	w	ω_5	A_2
1349	w	.....	.....
1435	s	ω_6	B_1
(1508)	....	ω_2	A_1
1623	vw	$\omega_4+\omega_{12}$	A_1+B_1
2183	m	$2\omega_{12}$	$2A_1+B_1$
2551	vw	$2\omega_3$ $\omega_7+\omega_{12}$	A_1 A_1+B_1
2838	m	$2\omega_6$	A_1
2945	m	$\omega_6+\omega_9$	B_1
2989	s	ω_1	A_1
3012	s	ω_8	B_2
4161	w	$\omega_1+\omega_7$ $\omega_8+\omega_{12}$	$2B_2+A_2$
4550	w	$\omega_8+\omega_6$	B_2

TABLE 6. *The observed bands and their assignments of* CH_2F_2, CH_2Cl_2, *and* CH_2I_2—Continued

ν	Intensity	Band	Symmetry
Molecule CH_2Cl_2 molecular symmetry C_{2v}			
cm^{-}			
286	w	ω_4	A_1
444	w	$\omega_9-\omega_4$	B_1
706	m	ω_2	A_1
742	vs	ω_9	B_1
898	m	ω_7	B_2
991	w	$\omega_2+\omega_4$	A_1
1159	vw	ω_5	A_2
1262	s	ω_8	B_1
1424	m	ω_3	A_1
1562	vw	$\omega_4+\omega_8$	B_1
1621	vw	$\omega_7+\omega_{12}$	A_1+B_2
1945	vw	$\omega_2+\omega_8$	B_1
2053	vw	$\omega_5+\omega_7$	B_1
2132	vw	$\omega_3+\omega_2$	A_1
2155	vw	$\omega_3+\omega_9$	B_1
2304	m	$\omega_7+\omega_8$	B_2
2410	w	$\omega_8+\omega_5$	B_2
2525	w	$2\omega_{12}$	A_1
2688	m	$\omega_1-\omega_4$ $\omega_3+\omega_8$	A_1 B_2
2833	vw	$2\omega_3$	A_1
2985	s	ω_1	A_1
3048	s	ω_8	B_2
3690	w	$\omega_3+\omega_2$	A_1
3952	w	$\omega_8+\omega_7$	A_1
4219	m	$\omega_8+\omega_5$	B_1
4273	w	$\omega_8+\omega_8$	B_1
4464	m	$\omega_8+\omega_3$	B_2
Molecule CH_2I_2 molecular symmetry C_{2v}			
[128](R)	....	ω_4	A_1
444	w	$\omega_9-\omega_4$	B_1
486	m	ω_2	A_1
572	s	ω_8	B_1
639	w	$\omega_2+\omega_4$	A_1
717	m	ω_7	B_2
1035	w	ω_5	A_2
1107	vs	ω_9	B_1
1182	vw	$\omega_2+\omega_7$	B_2
1225	w	$\omega_4+\omega_9$	B_1
1351	m	ω_3	A_1
1435	vw	$2\omega_7$	A_1
1597	w	$\omega_2+\omega_9$	B_1
1748	w	$\omega_3+\omega_7$	B_1
1842	w	$\omega_3+\omega_2$	A_1
1923	vw	$\omega_3+\omega_9$	B_1
2062	m	$2\omega_5$ $\omega_3+\omega_7$	A_1 B_2
2132	m	$\omega_3+\omega_8$	B_2
2204	m	$2\omega_9$	A_1
2390	vw	$\omega_3+\omega_5$	A_2
2456	m	$\omega_3+\omega_8$	B_1
2551	vw	$\omega_8-\omega_7$	B_2
2850	w	$\omega_1-\omega_4$	A_1
2967	s	ω_1	A_1
3049	vs	ω_8	B_2
3450	vw	$\omega_1+\omega_2$	A_1
3759	m	$\omega_8+\omega_7$	A_1
4065	m	$\omega_1+\omega_8$ $\omega_8+\omega_5$	B_1 B_1
4397	m	$\omega_3+\omega_8$	B_2

TABLE 7. *Symmetry effects in the vibrations of molecules of the type* $C-X_1X_2X_3X_4$ *having tetrahedral symmetry when* $X_1=X_2=X_3=X_4$

Structure	Typical molecule	Molecular symmetry group	Vibrational subgroups	Number and degeneracy of vibrations in each subgroup	Infrared activity	Raman activity	
						Polarized	Depolarized
$X_1=X_2=X_3=X_4$	CF_4	T_d	A_1	1 1	0	×	
			E	1 2	0	×	
			F_2	2 3	×		×
$X_1=X_2=X_3\neq X_4$	CF_3Cl	C_{3v}	A_1	3 1	×	×	
			E	3 2	×		×
$X_1=X_2\neq X_3=X_4$	CF_2Cl_2	C_{2v}	A_1	4 1	×	×	
			A_2	1 1	0		×
			B_1	2 1	×		×
			B_2	2 1	×		×
$X_1=X_2\neq X_3\neq X_4$	$CHFCl_2$	C_s	A′	6 1	×	×	
$X_1\neq X_2\neq X_3\neq X_4$	$CHFClBr$		A″	3 1	×		×
				9 1	×		×

Degradation of the symmetrical vibrations in structures of lower symmetry

$$T_d \longrightarrow C_{3v} \longrightarrow C_{2v} \longrightarrow C_s$$

$$6F_2 \longrightarrow \begin{Bmatrix}4E\\2A_1\end{Bmatrix} \longrightarrow \begin{Bmatrix}2B_1\\2B_2\\2A_1\end{Bmatrix} \longrightarrow \begin{Bmatrix}2A''\\4A'\end{Bmatrix}$$

$$2E \longrightarrow 2E \longrightarrow \begin{Bmatrix}A_1\\A_2\end{Bmatrix} \longrightarrow \begin{Bmatrix}A'\\A''\end{Bmatrix}$$

$$A_1 \longrightarrow A_1 \longrightarrow A_1 \longrightarrow A'$$

TABLE 8. *Fundamental frequencies of methane derivatives, numbered and characterized in different ways*

Conventional No.	Methane derivative												
	CF_4	CF_3Cl	CF_2Cl_2	$CFCl_3$	CCl_4	CCl_3Br	CCl_2Br_2	$CClBr_3$	CBr_4	CHF_3	CHF_2Cl	$CHFCl_2$	$CHCl_3$
1 ν, cm^{-1}	904	1105	1101	1085	458	719	733	747	267	3031	3023	3023	3040
1 Adopted No.	3	1	1	1	3	1	1	1	3	1	1	1	1
1 Character	$\nu_{F,s}$	$\nu_{F,s}$	$\nu_{F,s}$	ν_F	$\nu_{Cl,s}$	$\nu_{Cl,s}$	$\nu_{Cl,s}$	ν_{Cl}	$\nu_{Br,s}$	ν_H	ν_H	ν_H	ν_H
2 ν, cm^{-1}	437	781	667	535	218	420	377	329	123	1150	1311	1304	667
2 Adopted No.	25	3	3	3	25	3	3	3	25	3	6	6	3
2 Character	δ_F	ν_{Cl}	$\nu_{Cl,s}$	$\nu_{Cl,s}$	δ_{Cl}	ν_{Br}	$\nu_{Br,s}$	$\nu_{Br,s}$	δ_{Br}	$\nu_{F,s}$	δ_H	δ_H	$\nu_{Cl,s}$
3 ν, cm^{-1}	1277	470	455	350	773	243	252	215	669	700	1178	1079	370
3 Adopted No.	168	4	4	4	168	4	4	4	168	4	3	7	4
3 Character	$\nu_{F,s}$	$\delta_{F,s}$	$\delta_{F,s}$	$\delta_{Cl,s}$	$\nu_{Cl,s}$	$\delta_{Cl,s}$	$\delta_{Cl,s}$	$\delta_{Br,s}$	$\nu_{Br,s}$	$\delta_{F,s}$	$\nu_{F,s}$	ν_F	$\delta_{Cl,s}$
4 ν, cm^{-1}	630	1212	261	847	319	773	141	675	183	1372	869	742	1214
4 Adopted No.	479	68	2	68	479	68	2	68	479	68	7	3	68
4 Character	$\delta_{F,s}$	$\nu_{F,s}$	$\delta_{Cl,s}$	$\nu_{Cl,s}$	$\delta_{Cl,s}$	$\nu_{Cl,s}$	$\delta_{Br,s}$	$\nu_{Br,s}$	$\delta_{Br,s}$	$\nu_{F,s}$	ν_{Cl}	$\nu_{Cl,s}$	δ_H
5 ν, cm^{-1}		563	318	401		294	164	214		1152	595	458	755
5 Adopted No.		79	5	79		79	5	79		79	4	4	79
5 Character		$\delta_{F,s}$	δ	δ_F		$\delta_{Cl,s}$	δ	δ_{Cl}		δ_H	$\delta_{F,s}$	δ_F	$\nu_{Cl,s}$
6 ν, cm^{-1}		356	906	248		187	768	141		507	422	276	261
6 Adopted No.		25	6	25		25	6	25		25	2	2	25
6 Character		δ_{Cl}	$\nu_{Cl,s}$	$\delta_{Cl,s}$		δ_{Br}	$\nu_{Cl,s}$	$\delta_{Br,s}$		$\delta_{F,s}$	δ_{Cl}	$\delta_{Cl,s}$	$\delta_{Cl,s}$
7 ν, cm^{-1}			437				252				1347	1242	
7 Adopted No.			7				7				8	8	
7 Character			δ_{Fl}				$\delta_{Cl,s}$				δ_H	δ_H	
8 ν, cm^{-1}			1159				683				1116	804	
8 Adopted No.			8				8				9	9	
8 Character			$\nu_{F,s}$				$\nu_{Br,s}$				$\nu_{F,s}$	$\nu_{Cl,s}$	
9 ν, cm^{-1}			473				230				365	368	
9 Adopted No.			9				9				5	5	
9 Character			δ_{Fl}				$\delta_{Br,s}$				δ_{Fl}	δ_{Fl}	

TABLE 8. *Fundamental frequencies of methane derivatives, numbered and characterized in different ways*—Continued

Conventional No.		Methane derivative											
		$CHCl_2Br$	$CHClBr_2$	$CHBr_3$	CHI_3	CH_2F_2	CH_2ClF	CH_2Cl_2	CH_2ClBr	CH_2Br_2	CH_2I_2	CH_3F	CH_4
1	ν,cm^{-1}	3040	3034	3040	(3040)	2949	2993	2985	2987	2988	2967	2964	2915
	Adopted No.	1	1	1	1	1	1	1	1	1	1	1	3
	Character	ν_H	ν_H	ν_H	ν_H	$\nu_{H,s}$	$\nu_{H,s}$	$\nu_{H,s}$	$\nu_{H,s}$	$\nu_{H,s}$	$\nu_{H,s}$	$\nu_{H,s}$	$\nu_{H,s}$
2	ν,cm^{-1}	1168	1189	541	385	1508	1470	1424	1402	1385	1351	1475	1533
	Adopted No.	6	6	3	3	3	3	3	3	3	3	3	25
	Character	δ_H	δ_H	$\nu_{Br,s}$	$\nu_{I,s}$	$\delta_{H,s}$	$\delta_{H,s}$	$\delta_{H,s}$	$\delta_{H,s}$	$\delta_{H,s}$	$\delta_{H,s}$	$\delta_{H,s}$	δ_H
3	ν,cm^{-1}	719	746	222	145	1116	1351	706	1225	579	486	1048	3020
	Adopted No.	7	7	4	4	2	8	2	8	2	2	4	168
	Character	$\nu_{Cl,s}$	ν_{Cl}	$\delta_{Br,s}$	$\delta_{I,s}$	$\nu_{F,s}$	δ_{HF}	$\nu_{Cl,s}$	δ_{HCl}	$\nu_{Br,s}$	$\nu_{I,s}$	ν_F	$\nu_{H,s}$
4	ν,cm^{-1}	604	570	1142	1064	529	1068	286	728	174	128	2982	1304
	Adopted No.	3	3	68	68	4	7	4	9	4	4	68	479
	Character	ν_{Br}	$\nu_{Br,s}$	δ_{Br}	δ_H	$\delta_{F,s}$	ν_F	$\delta_{Cl,s}$	ν_{Cl}	δ_{Br}	δ_I	$\nu_{H,s}$	$\delta_{H,s}$
5	ν,cm^{-1}	330	278	668	581	1262	760	1159	606	1066	1035	1471	.....
	Adopted No.	4	4	79	79	5	2	5	2	5	5	79	.....
	Character	$\delta_{Cl,s}$	δ_{Cl}	$\nu_{Br,s}$	$\nu_{I,s}$	δ	ν_{Cl}	δ	ν_{Br}	δ	δ	$\delta_{H,s}$	.....
6	ν,cm^{-1}	220	168	154	92	3012	385	3048	226	3065	3049	1196	.....
	Adopted No.	2	2	25	25	6	4	6	4	6	6	25	.....
	Character	δ_{Br}	$\delta_{Br,s}$	$\delta_{Br,s}$	$\delta_{I,s}$	$\nu_{H,s}$	δ_{Cl}	$\nu_{H,s}$	δ_{Br}	$\nu_{H,s}$	$\nu_{H,s}$	δ_{HF}	.....
7	ν,cm^{-1}	1211	1144	.....	.....	1176	3048	898	3060	813	717	.....	.....
	Adopted No.	8	8	.....	.....	7	6	7	6	7	7	.....	.....
	Character	δ_H	δ_H	.....	.....	δ_{HF}	$\nu_{H,s}$	δ_{HCl}	$\nu_{H,s}$	δ_{HBr}	δ_{HI}	.....	.....
8	ν,cm^{-1}	760	657	.....	.....	1435	1236	1262	1130	1190	1107	.....	.....
	Adopted No.	9	9	.....	.....	8	5	8	5	8	8	.....	.....
	Character	$\nu_{Cl,s}$	$\nu_{Br,s}$	.....	.....	δ_{HF}	δ_{HF}	δ_{HCl}	δ_{HCl}	δ_{HBr}	δ_{HI}	.....	.....
9	ν,cm^{-1}	215	201	.....	.....	1080	1004	742	852	639	572	.....	.....
	Adopted No.	5	5	.....	.....	9	9	9	7	9	9	.....	.....
	Character	δ_{ClBr}	δ_{ClBr}	.....	.....	$\nu_{F,s}$	δ_{HCl}	$\nu_{Cl,s}$	δ_{HBr}	$\nu_{Br,s}$	$\nu_{I,s}$	.....	.....

The regularities mentioned in the preceding paragraph are displayed in figures 13 to 15, inclusive. In these graphs the frequencies of related molecules are plotted, the molecules being arranged vertically in order of increasing molecular weight. The regular decrease in frequency with increasing weight of the substituent, and the way in which the degenerate frequencies in the more symmetrical molecules break up in the less symmetrical ones and then regroup, is to be noted.

Another often-used method of identifying the fundamentals, which also possesses a degree of physical significance, is to characterize them by the type of intramolecular motion involved. In this method, ν_x signifies the stretching of a bond connecting the carbon atom with the x substituent, and δ_x signifies the bending of such a bond. All the molecules considered will have four ν's and five δ's. When there are several identical bonds, the suffix *s* or *a* may be added, according to whether the motion of the identical atoms is symmetrically toward the central atom or otherwise. In molecules as light as those considered here, this method often has limited meaning, since the motions in each fundamental mode cannot be localized as closely as the method would imply; in the δ modes in particular all the atoms participate in the motion. Nevertheless, a characterization of the fundamentals by this method is also included in table 8 and will be referred to in later discussion. For some such cases no suffix can be given; in others, a double suffix identifies the two atoms most prominently involved.

The relative intensity of the various fundamentals is not displayed in figures 13 to 15. The intensity depends on a number of factors, principally the symmetry of the motion and the distribution of electrical charge within the molecule. From the spectral graphs and tables it will be noted that there is a general parallelism in the intensities of corresponding bands in the various molecules of like symmetry. It should be noted that, although for molecules of symmetry C_{2v}, the A_2 frequency ω_9 should be inactive, it does appear in all the molecules considered, if it falls in the observable frequency range. It is always quite weak, however, and its appearance may readily be explained as due to a breakdown of the strict selection rules because of intermolecular forces, particularly in the liquid state, or to Coriolis interactions with nearby active frequencies, or to a combination of these causes.

3.2. Force Constant Calculations

For a quantitative verification of the assignment of fundamentals, recourse must be had to a calculation in terms of the atomic masses, atomic dimensions, and a suitable set of force constants of the potential energy. In the most general potential function there are many more disposable constants than there are observed frequencies, so that various approximations must be introduced. Certain of the constants, especially those involving interactions between motions of different types, may be set equal to zero; other constants may be assumed to have the

ame numerical value in different molecules. Many such treatments have been reported for most of the molecules considered here. One of the more successful of the recent simpler calculations was that of Decius [5], who was able to calculate 82 frequencies in 14 normal and deuterated chloro-bromo-methanes from 28 constants, with a mean accuracy of 1.1 percent.

In order to substantiate some of our assignments, and to determine whether a similar treatment may be applied to compounds containing fluorine, the calculations of Decius have been extended to the molecules CF_4, CF_3H, CF_2H_2, CFH_3, CF_3Cl, CF_2Cl_2, $CFCl_3$, CCl_3Br, CCl_2Br_2, and $CClBr_3$, for which all nine frequencies were computed; and to the less symmetrical molecules CHF_2Cl, $CHFCl_2$, $CHCl_2Br$, $CHClBr_2$, CH_2FCl, and CH_2ClBr, for which only the three frequencies of symmetry A'' were computed. (To evaluate the remaining six frequencies of the latter molecules would involve the expansion and solution of a sixth-order determinant.) In these calculations the constants and molecular dimensions of Decius were adopted when applicable (one apparent numerical error or misprint, for f^1_β in C—Cl, was corrected). New values for the corresponding constants involving fluorine were adopted, which gave a fair over-all fit of the data considered. It is probable that additional computations would yield somewhat better values of these constants, but this does not seem useful, in view of the approximations involved. The constants used are listed in Decius' notation in table 9. Calculations on "mixed" molecules, that is, those containing more than one halogen, require additional constants. For these are used the geometric mean of the corresponding constants involving a single halogen. For example, since the constant f^2_{C-X}, corresponding to the interaction of motion along two $C-X^1$ bonds, $C-X^1_j \cdot C-X^1_k$, is 0.96 (in units of 10^5 dyne/cm) for $X^1=F$ and 0.332 for $X^1=Cl$, the constant for interaction of motion along C—F and C—Cl would be $[(0.96)\cdot(0.332)]^{1/2}=0.565$. The constants involving

TABLE 9.—*Force constants for halomethanes (after Decius)*

The following constants are assumed to be zero: f^1_{hr}, $f^1_{h\gamma}$, f^2_{rr}, $f^1_{r\alpha}$, $f^2_{r\alpha}$, $f^1_{r\beta}$, $f^1_{r\gamma}$, $f^1_{r\gamma}$, $f^1_{\alpha\beta}$, $f^2_{\alpha\beta}$, $f^2_{\beta\gamma}$, f^2_{γ}, and f^3_{γ}.

The numerical units are 10^5 dyne cm^{-1} for two stretching coordinates, 10^{-5} dyne for bending and stretching, and 10^{-11} dyne cm for two bending coordinates. r_0C—F=1.35 A, r_0C—Cl=1.75 A, r_0 C—Br=1.88 A, r_0C—H=1.093 A, all $\alpha_0=\beta_0=\gamma_0=109°28'$

Constant	Terms involved	$X^1=F$	$X^1=Cl$	$X^1=Br$
f^1_k	$C-X^1_j \cdot C-X^1_j$	6.26	3.383	2.840
f^2_k	$C-X^1_j \cdot C-X^1_k$	0.96	0.332	0.186
f^1_r	$C-H_i \cdot C-H_i$	5.04	5.04	5.04
$f^1_{k\alpha}$	$C-X^1_j \cdot H-C-X^1_j$	0.40	0.340	0.305
$f^2_{k\alpha}$	$C-X^1_j \cdot H-C-X^1_k$	−.21	−.164	−.152
$f^1_{k\beta}$	$C-X^1_j \cdot X^1_j-C-X^1_k$	.34	.338	.342
$f^2_{k\beta}$	$C-X^1_j \cdot X^1_k-C-X^1_j$	−.34	−.249	−.190
f^1_α	$H_i-C-X^1_j \cdot H_j-C-X^1_j$	.875	.687	.589
f^2_α	$H_i-C-X^1_j \cdot H_j-C-X^1_k$	.050	.009	−.005
f^3_α	$H_i-C-X^1_j \cdot H_k-C-X^1_j$	−.048	−.034	−.026
f^4_α	$H_j-C-X^1_j \cdot H_k-C-X^1_k$	−.145	−.065	−.060
f^1_β	$X^1_j-C-X^1_k \cdot X^1_j-C-X^1_k$	1.75	1.236	1.061
f^2_β	$X^1_j-C-X^1_k \cdot X^1_j-C-X^1_j$	0.17	0.092	0.134
f^3_β	$X^1_j-C-X^1_k \cdot X^1_j-C-X^1_m$	−.10	−.037	.039
f^1_γ	$H_j-C-H_k \cdot H_j-C-H_k$	.530	.530	.530

TABLE 10. *Comparison of calculated and observed frequencies* $\left(\Delta=\frac{100(\nu_{obs}-\nu_{calc})}{\nu_{obs}}\right)$

ω	$\nu_{calc.}$	Δ
CF_4		
3	904	0.0
25	437	.0
168	1234	3.4
479	613	2.7
CF_2H_2		
1	3005	1.9
3	1466	2.8
4	1154	−3.0
2	537	−1.5
5	1262	0.0
6	3082	−2.3
7	1108	5.8
8	1475	−2.8
9	1150	−5.5
CF_3Cl		
1	1096	0.8
3	744	4.7
4	480	2.2
68	1191	1.8
79	562	0.2
25	358	−.5
$CFCl_3$		
1	1125	−3.7
3	524	2.1
4	363	−3.7
68	813	4.0
79	420	−4.8
25	243	2.0
CCl_2Br_2		
1	734	−0.1
3	364	3.5
4	251	0.4
2	147	−4.3
5	168	−2.5
6	772	−0.5
7	260	−3.2
8	676	1.0
9	229	0.4
CHF_2Cl		
8	1366	−1.4
9	1132	−1.4
5	391	−7.1
$CHFCl_2$		
8	1221	−1.8
9	791	1.6
5	392	−6.6
$CHCl_2Br$		
8	1221	−4.4
9	749	1.5
5	219	−1.9

ω	$\nu_{calc.}$	Δ
CF_3H		
1	3047	−0.5
3	1139	1.0
4	665	5.0
68	1369	0.2
79	1140	−1.2
25	532	−4.8
CFH_3		
1	2960	0.1
3	1452	1.6
4	1125	7.3
68	3072	−3.0
79	1479	0.5
25	1181	1.3
CF_2Cl_2		
1	1126	−2.3
3	648	2.8
4	463	−1.8
2	282	−0.4
5	331	−4.1
6	867	4.3
7	433	0.9
8	1168	−.8
9	469	2.8
CCl_3Br		
1	699	−2.9
3	450	−7.1
4	235	−3.3
68	768	0.7
79	294	.0
25	174	6.9
CBr_3Cl		
1	751	−0.5
3	324	1.6
4	215	0.0
68	678	−.5
79	215	−.4
25	137	2.8
$CHBr_2Cl$		
8	1135	0.8
9	651	.9
5	205	−2.0
CH_2FCl		
6	3080	−1.1
5	1214	1.8
9	1005	−0.1
CH_2ClBr		
6	3077	−0.6
5	1142	−1.1
7	846	−0.7

bending of X^1-C-X^1 bonds and their interactions are obtained similarly, without introducing further new constants.

The resulting computed frequencies are compared with the observed fundamentals in table 10. It is seen that, in general, the agreement is good. The greatest deviation is 7.3 percent, and the average deviation of 85 frequencies in 16 molecules is 2.22 percent. This degree of fit was obtained by introducing 13 new constants, in addition to the 28 taken from Decius. Better agreement is not to be expected in view of the approximations introduced. Inasmuch as the very accurate results of microwave spectroscopy show that the interatomic distances are not constant, particularly for the C—F bond, and that the angles are not tetrahedral, it is clear that the force constants must vary to some extent. The interaction constants are relatively large: the particularly high value of f_R^a for C—F (0.96×10^5 dyne cm^{-1}) is to be noted. This is a further reflection of the importance of specific forces arising from the highly polar C—F linkage, and indicates that for a truly accurate calculation, one should take into account all the ignored interactions, perhaps basing them on some more general force field [6]. The present comparison serves merely to confirm the choice of fundamentals and to demonstrate the approximate similarity of the carbon-halogen bonds in a large number of halomethanes.

It should be noted that the C—F constants, particularly the major ones involving the stretching, are in good agreement with a very recently published calculation based on much the same data and methods [7]. It should also be mentioned that preliminary calculations indicate that the C—F constants used also give adequate agreement with observation in such molecules as C_2F_6, CF_3-CH_3, CF_3-CCl_3, etc.

There are not enough data on the iodine compounds to derive constants for this bond, but approximate values extrapolated from the series F→Cl→Br→I may be seen to give adequate agreement with the few observations.

3.3. Overtone, Combination, and Difference Bands

In addition to the fundamentals, the bands that appear in the spectrum must be attributed to overtones, combinations, and differences of the fundamentals. They have been so assigned in tables 2 to 6. The assignments appear eminently reasonable, in that the selection rules are obeyed, in the molecules of higher symmetry, with the exception of an occasional weak combination of symmetry A_2 in C_{2v}; that binary combinations are in general much stronger than those involving three frequencies; and that difference bands arise only from relatively low vibrational frequencies.

Under the dispersion of prism instruments, it is not always possible to make an unambiguous assignment of these higher-order bands. As will be noted in tables 2 to 6, there are many instances in which two or more combinations can be offered as probable, and many other such have not been listed separately. The magnitude of the anharmonic corrections, by which the frequencies of the overtones and combinations differ from the sum of the fundamentals, ranges from +10 to −50 cm^{-1}, and, with nine fundamentals, such overlapping is common. Unless much higher resolution is available, it is unprofitable to attempt to distinguish between the possibilities, except to note that the assignments that are set forth show a consistent behavior in a large number of molecules. Indeed, because of the possibility of Fermi resonance among levels of like symmetry, it is often meaningless to distinguish between close-lying levels. Some of the more striking and definite examples of this effect occur in CCl_4 and CCl_2F_2 and will be discussed in more detail later. In a very heavy molecule of low symmetry, such as CCl_2Br_2, the number of possible difference bands of appreciable intensity arising from the five fundamentals below 300 cm^{-1} is particularly large. It will be noted in figure 6 that in these molecules there is a rather strong background of structureless absorption throughout the region 280 to 500 cm^{-1}, which undoubtedly arises from such overlappings.

It should be mentioned that a number of the overtone and combination bands of the methylene-halide compounds CH_2F_2, CH_2FCl, CH_2Cl_2, CH_2ClBr, and CH_2Br_2 have been studied under very high resolving power in the region 1.6 to 2.5 μ. The results will be reported separately. They show the expected large number of bands, with the rotational structure partially resolved, and further confirm the vibrational assignments reported in this paper.

3.4. Liquid-Vapor Shifts

As mentioned above, a number of the compounds of low boiling point have been studied both as liquids and as vapors, at room temperature. As is commonly observed, the vapor spectra show more indications of partially resolved rotational structure (P, Q, and R branches), but otherwise do not differ appreciably from those of the liquids, except for slight shifts of the central absorption frequencies. Some of these shifts are listed in table 11. It will be noted that the frequencies for the vapor are consistently higher than for the liquid, and that the magnitude of the shift is in general greater, especially on a percentage basis, for the stretching frequencies involving the halogens (ν_x's) than for the bending frequencies or for the hydrogen-stretching frequencies. This is undoubtedly due to the fact that the shifts result from partial association in the liquid, which is predominantly due to forces between the dipoles localized in the carbon-halogen bonds.

The fluorine compounds CH_2F_2 and CHF_3 were studied in this research only in the gaseous state. Their Raman spectra have, however, been studied in the liquid. Since the C—F bond is considerably more polar than C—Cl, one might expect the ν_F frequencies to show quite large liquid-vapor shifts, and these have been observed. These two molecules have also been listed in table 11, the Δ now referring to the shift between our adopted infrared frequencies and the most recent Raman data [8].

TABLE 11. *Frequency differences ($\nu_{vapor} - \nu_{liquid}$) for some halomethanes*

Vibration	$\Delta\nu$ cm^{-1}	Vibration	$\Delta\nu$
$CHCl_3$		$CHCl_2Br$	
$\omega_2\nu Cl_3$	+13	$\omega_2\nu Cl_2$	+12
$\omega_5\nu Cl_3$	+17	$\omega_5\nu Cl_2$	+13
$\omega_6\delta H$	+5	$\omega_6\delta H$	+8
$\omega_1\nu H$	+15	$\omega_1\delta H$	+6
$CHClBr_2$		$CHBr_3$	
$\omega_2\nu Br_2$	+14	$\omega_6\delta H$	+7
$\omega_5\nu Cl$	+12	$\omega_1\nu H$	+18
$\omega_6\delta H$	+7		
$\omega_1\delta H$	+5		
CH_2Cl_2		CH_2F_2	
$\omega_2\nu Cl_2$	+9	$\omega_6\delta F_2$	−3
$\omega_5\nu Cl_2$	+15	$\omega_5\nu F_2$	+35
$\omega_7\delta HCl$	0	$\omega_2\nu F_2$	+38
$\omega_6\delta HCl$	+4	$\omega_7\delta HF$	+6
$\omega_3\delta H_2$	+38	$\omega_6\delta HF$	0
$\omega_1\nu H_2$	+14	$\omega_3\nu H_2$	−14
		$\omega_1\nu H_2$	−18
CHF_3			
$\omega_{12}\delta F_3$	+1		
$\omega_6\delta F_3$	+3		
$\omega_5\nu F_3$	+33		
$\omega_7\delta F_3$	−7		
$\omega_8\nu H$	−6		
$\omega_1\nu H$	−26		

3.5. Discussion on Particular Molecules

It does not seem necessary to discuss all the assignments for each molecule, since in most cases the assignments are in substantial agreement with the work of other investigators who have studied these molecules, either by the infrared or Raman spectra. In a few instances, however, where certain points have been discussed in the literature, it seems desirable to justify our choices further. It should be pointed out that in many cases final decisions can hardly be reached until the rotational fine structure of the bands in question is studied under very high resolution.

3.6. CF_4

The bands may all be assigned as F_2 combinations or overtones of the two infrared active frequencies 629 cm^{-1} and 1,277 cm^{-1}, and the Raman-active 437 cm^{-1} (E) and 904 cm^{-1} (A_1). The fact that these pairs are each nearly in the ratio 1:2 would make it possible for Fermi resonance to appear in many of the combinations; however, as the observations give a band of high intensity at each position, it appears that the interactions are not strong, and that the resonance is only partial. There is a very weak peak at ~1,238 cm^{-1}, which may correspond to the weaker component of the $2\nu_{479}$, ν_{168} F_2 pair; the corresponding combinations with ν_1 also appear at 2,123 and 2,160 with a relative intensity of about 1:5. The unresolved rotational envelopes of the 629 and 1,277 cm^{-1} fundamentals are quite different, the former showing well separated P, Q, and R branches, with a $P-R$ distance of ~33 cm^{-1}, whereas in the latter this distance is much less and unresolved. This is due to the interaction with the rotation of angular momentum of vibration, and is in qualitative agreement with calculation: the ζ-factor for the valence vibration ν_{168} should be about +0.68 and for ν_{479} about −0.18, so that the rotational spacings for the two bands should be in the ratio (0.32/1.18) ~0.3. The combination bands of these fundamentals with ν_3 show the same behavior; for example, 1,532 is found with a $P-R$ spacing of ~38 cm^{-1}, whereas 2,160 is narrow and unresolved.

3.7. CF_3Cl

The two lowest-frequency fundamentals, ω_{25}(E) and $\omega_4(A_1)$ are very weak in the infrared, but appear strongly in the Raman spectrum of the liquid. Although a weak band appears at 450 cm^{-1}, in the infrared spectrum, it seems preferable to adopt 470 cm^{-1} of the Raman spectra for the vapor-phase frequency of ω_4, as this accounts for the weak absorption at 635 cm^{-1} as a difference band and gives satisfactory agreement in a number of combinations.

3.8. CF_2Cl_2

The force-constant calculations definitely require that there be five (deformation) frequencies below 500 cm^{-1} and only four above 600 cm^{-1}. Hence the assignment of both the strong bands at 882 and 922 cm^{-1} as fundamentals cannot be correct; it is very reasonable to consider this a case of Fermi resonance, with the original ω_6 fundamental (B_1) at 906 cm^{-1} split by interaction with the combination $\omega_4(A_1)455+\omega_7(B_1)437$. The region from 420 to 480 cm^{-1} must be studied under higher resolution before the values for the three overlapping frequencies ω_6, ω_4, and ω_9 can be considered certain. The value of 455 cm^{-1} for ω_4 is from the Raman effect.

3.9. $CFCl_3$

As in the other chloro-fluoromethanes, the deformation fundamentals are very weak, but Raman-effect measurements enable a choice to be made between the fundamentals and the equally intense difference bands at wavelengths greater than 20μ. The combination band at 932 cm^{-1} is more intense than the fundamentals on which it is based. This may result from a partial Fermi resonance with the very intense ω_{68}. The ν_F frequency shows a +17 cm^{-1} shift from the liquid value found in the Raman effect [9].

3.10. CCl_4

This much-studied molecule shows one of the earliest-recognized examples of Fermi resonance in the strong pair at 762 to 785 cm^{-1}. The unsplit position of the ω_{168} is taken as the exact center, 773 cm^{-1}, since the two bands are nearly of equal intensity, in the liquid. In the vapor the resonance with 319+458 is less exact, the intensity ratio now being about 4:1, the higher frequency component being the stronger. This is in accord with the general observation that the vapor-liquid shift is greatest for the asymmetric valence vibrations. It is of consider-

able interest that the doubling also appears in two difference bands, arising from ω_{25} and ω_{479}.

3.11. CCl_3Br and CCl_2Br_2

In these heavy molecules many fundamentals lie beyond the limit of our observation, but are known from the Raman effect. There is considerable absorption without definite structure beyond 20 μ, corresponding to many possible overlapping difference and combination bands of the deformation frequencies.

3.12. CHF_3

This molecule has been studied under very high resolution in the photographic infrared [10]. We have also examined a number of the combination bands under high resolution. The only question in the frequency assignment concerns the value of ω_3, the $\nu_{F,s}$ fundamental. Its intensity and polarization in the Raman spectrum definitely prove that in the liquid it falls at 1,116 cm^{-1}. In the infrared spectrum of the gas there is no indication of any weak absorption to longer wavelengths of the 1,152 cm^{-1} peak. It is therefore believed that the $\nu_{F,s}$ and $\nu_{F,a}$ fundamentals overlap at this point, the difference from the Raman effect being due to the vapor-liquid shift, whereas the weak band at 1,209 cm^{-1} is a combination tone. A high-resolution study of this region would be of interest. Our force-constant calculations, in agreement with those of Rank, Shull, and Pace, confirm the assignments of 700 cm^{-1} to A_1 and 507 cm^{-1} to E symmetry, although the rotational envelopes of the two bands are nearly identical.

3.13. CHF_2Cl

The assignment of the $\omega_3(\nu_{F,s})$ fundamental differs from that of Glockler, Edgell, and Leader [11] obtained from the Raman effect. There are two medium-intensity bands to choose between, at 833 and 1,178 cm^{-1}. The higher value fits much better with the related molecules. The low frequency, which is fairly strong in the Raman effect, and which may well be accounted for as 2×422 cm^{-1}, undoubtedly gains in intensity by partial Fermi resonance with ω_7, at 809 cm^{-1}.

3.14. $CHFCl_2$, $CHCl_3$, $CHCl_2Br$, $CHClBr_2$, $CHBr_3$

In all these molecules, there is little question as to the assignment of fundamentals, when the infrared and Raman results are both considered. All show absorption in the long-wavelength region. The 262 cm^{-1} fundamental of $CHCl_3$ is relatively strong, but occurs just at the long-wavelength limit of the TlBr-I prism.

3.15. CHI_3

The results for this molecule are quite incomplete. Because of its physical properties (solid at room temperature and above, subliming with decomposition) it could be studied only in solution. Its chemical instability prevented the use of high concentration, and rapid surveys of the spectrum were required. The Raman frequencies, and rough force-constant calculations, show that two of the fundamentals lie at very long wavelengths. The few bands observed find a natural interpretation by analogy with the corresponding molecules.

3.16. CH_2F_2

This molecule has been investigated recently under high resolution [12]. As mentioned above, high-resolution studies in the 1.6 to 2.5 μ, region have also been made in the radiometry laboratory of the Bureau. The assignment of fundamentals differs from that of the above authors, but is in agreement with the one very recently offered by Rank, Shull, and Pace, [8] and with the force-constant calculations. The Raman-effect data leave no doubt that in the liquid ω_3 is at 1,508 cm^{-1}. This $\nu_{H,s}$ frequency might well be very weak in the infrared and escape detection, since it falls in a region where the H_2O absorption masks weak bands. The band structures found by Stewart and Nielsen are equally well accounted for by the assignment, since the B_1 combination at 2,945 cm^{-1} can be ascribed to $\omega_3+\omega_8$. As mentioned above in connection with table 11, a relatively large liquid-vapor shift may be invoked to reconcile the Raman and infrared measurements in the region of 1,100 cm^{-1}. The depolarized Raman line at 1,054 cm^{-1} can be attributed to ω_9, rather than to $2\omega_4$ which should be polarized. The ω_5 frequency, whose A_2 symmetry should make it inactive, appears weakly at 1,262 cm^{-1}, presumably due to Coriolis interaction with ω_7 (B_2) at 1,176 cm^{-1}, or to breakdown of the strict selection rules induced by the strong polar intermolecular forces. There are two weak bands, at 816 and 1,349 cm^{-1} which cannot be assigned. They may be due to impurities.

3.17. CH_2Cl_2 and CH_2I_2

These molecules show no unexpected effects. There is a close parallelism among the spectra of all the methylene halides. These will be discussed at greater length in connection with high-resolution studies in the overtone region.

The authors are indebted to N. Acquista and Mary A. Lamb for assistance in the observations of the spectra.

4. References

[1] G. Herzberg, Infrared and Raman spectra of polyatomic molecules (D. van Nostrand Co., Inc., New York, N. Y., 1945).
[2] K. W. F. Kohlrausch, Ramanspektren (Becker & Erler, Leipzig, 1943).
[3] E. K. Plyler, R. Stair, and C. J. Humphreys, J. Research NBS **38**, 211 (1947) RP1769.
[4] E. K. Plyler, H. W. Smith, and N. Acquista, J. Research NBS **44**, 503 (1950) RP2097.
[5] J. C. Decius, J. Chem. Phys. **16**, 214 (1948).
[6] T. Simanouti, J. Chem. Phys. **17**, 245 (1949).
[7] E. L. Pace, J. Chem. Phys. **18**, 881 (1950).
[8] D. H. Rank, E. R. Shull, and E. L. Pace, J. Chem. Phys. **18**, 885 (1950).
[9] J. P. Zietlow, F. F. Cleveland, and A. G. Meister, J. Chem. Phys. **18**, 1076 (1950).
[10] H. J. Bernstein and G. Herzberg, J. Chem. Phys. **16**, 30 (1948).
[11] G. Glockler, W. F. Edgell, and G. R. Leader, J. Chem. Phys. **9**, 224 (1941).
[12] H. B. Stewart and H. H. Nielsen, Phys. Rev. **75**, 640 (1949).

Washington, January 16, 1951.